

**Remote refocusing
light-sheet fluorescence microscopy
for high-speed 2D and 3D imaging
of calcium dynamics in cardiomyocytes**

**Thesis submitted for the degree of
Doctor of Philosophy (PhD)**

Liuba Alexandra Dvinskikh

Photonics group, Department of Physics

National Heart and Lung Institute, Faculty of Medicine

Institute of Chemical Biology, Department of Chemistry

Imperial College London

Abstract

The high prevalence and poor prognosis of heart failure are two key drivers for research into cardiac electrophysiology and regeneration. Dyssynchrony in calcium release and loss of structural organization within individual cardiomyocytes (CM) has been linked to reduced contractile strength and arrhythmia. Correlating calcium dynamics and cell microstructure requires multidimensional imaging with high spatiotemporal resolution. In light-sheet fluorescence microscopy (LSFM), selective plane illumination enables fast optically sectioned imaging with lower phototoxicity, making it suitable for imaging subcellular dynamics. In this work, a custom remote refocusing LSFM system is applied to studying calcium dynamics in isolated CM, cardiac cell cultures and tissue slices.

The spatial resolution of the LSFM system was modelled and experimentally characterized. Simulation of the illumination path in Zemax was used to estimate the light-sheet beam waist and confocal parameter. Automated MATLAB-based image analysis was used to quantify the optical sectioning and the 3D point spread function using Gaussian fitting of bead image intensity distributions. The results demonstrated improved and more uniform axial resolution and optical sectioning with the tighter focused beam used for axially swept light-sheet microscopy.

High-speed dual-channel LSFM was used for 2D imaging of calcium dynamics in correlation with the t-tubule structure in left and right ventricle cardiomyocytes at 395 fps. The high spatio-temporal resolution enabled the characterization of calcium sparks. The use of para-nitro-blebbistatin (NBleb), a non-phototoxic, low fluorescence contraction uncoupler, allowed 2D-mapping of the spatial dyssynchrony of calcium transient development across the cell.

Finally, aberration-free remote refocusing was used for high-speed volumetric imaging of calcium dynamics in human induced pluripotent stem-cell derived cardiomyocytes (hiPSC-CM) and their co-culture with adult-CM. 3D-imaging at up to 8 Hz demonstrated the synchronization of calcium transients in co-culture, with increased coupling with longer co-culture duration, uninhibited by motion uncoupling with NBleb.

Table of contents

Abstract.....	2
Table of contents.....	3
Supervisors and examiners	6
Statement of originality.....	7
Copyright declaration.....	7
Acknowledgements.....	8
List of videos.....	9
List of figures.....	10
List of tables.....	12
List of abbreviations	13
1 Introduction.....	15
1.1. Fluorescence microscopy	16
<i>Challenges of live-cell fluorescence microscopy</i>	18
1.2. Optically sectioned imaging.....	20
<i>Confocal microscopy</i>	20
<i>Multiphoton microscopy</i>	21
<i>Structured illumination microscopy</i>	22
<i>TIRFM, deconvolution and other approaches</i>	22
1.3. Light-sheet fluorescence microscopy.....	23
<i>Light-sheet illumination</i>	24
<i>LSFM image acquisition and system configurations</i>	25
1.4. Heart function, disease and regenerative therapy	26
<i>Cardiac anatomy and function</i>	26
<i>Heart disease</i>	28
<i>Treatment and stem cell regenerative therapy</i>	28
<i>Imaging calcium dynamics in cardiomyocytes</i>	29
1.5. Summary	29
2 Design and operation of remote refocusing LSFM system.....	31
2.1. Introduction to high-speed volumetric imaging.....	31
2.1.1. Lateral scanning-based approaches.....	31
2.1.2. Camera-based approaches.....	32
2.1.3. Aberration-free remote refocus	36
2.1.4. Alternatives to 3D imaging.....	40
2.2. System description	43
2.2.1. Optomechanical design	44

2.2.2.	Spatiotemporal imaging modes.....	51
2.3.	Variable-angle projection imaging.....	54
2.3.1.	Shear geometry	54
2.3.2.	Potential implementation	55
2.4.	Summary	58
3	Characterizing the spatial resolution.....	59
3.1	Introduction.....	59
3.1.1.	Resolution definition and criteria.....	59
3.1.2.	Image formation in incoherent imaging.....	61
3.1.3.	Resolution enhancement	63
3.1.4.	Characterizing optical sectioning.....	66
3.1.5.	Measuring spatial resolution	68
3.1.6.	Resolution in SPIM.....	70
3.2.	Modelling the system resolution	77
3.2.1.	System PSF for uniformly filled illumination and detection pupils.....	77
3.2.2.	Modelling the illumination path in Zemax.....	81
3.3.	Experimental resolution measurement.....	87
3.3.1.	Method	87
3.3.2.	Results.....	92
3.4.	Discussion and conclusion.....	99
4	High-speed 2D imaging of calcium dynamics in ventricular cardiomyocytes	101
4.1	Introduction.....	101
4.1.1	Calcium regulation of excitation contraction coupling.....	101
4.1.2	Desynchronization of calcium dynamics	102
4.1.3	Differences in left and right ventricle cardiomyocytes	103
4.1.4	Multidimensional imaging of calcium dynamics: approaches and challenges	104
4.1.5	Experimental objectives.....	105
4.2	Experimental methods.....	107
4.3	Image analysis.....	110
4.3.1	Data pre-processing.....	110
4.3.2	T-tubule detection and nuclear segmentation	112
4.3.3	Spark analysis	115
4.3.4	Transient analysis.....	117
4.4	Results.....	122
4.4.1	Calcium spark morphology and correlation with t-tubule structure	122
4.4.2	Calcium transient dyssynchrony and correlation with t-tubule structure.....	125
4.4.3	Comparison for left and right ventricle cardiomyocytes.....	129

4.5	Discussion & conclusion.....	133
5	High-speed 3D imaging of calcium dynamics in stem-cell derived and adult cardiomyocytes.	136
5.1	Introduction.....	136
5.1.1	Stem cell regenerative therapy and hiPSC-CM	136
5.1.2	Excitation-contraction coupling in hiPSC-CM	136
5.1.3	Electromechanical coupling of hiPSC-CM and adult-CM.....	138
5.1.4	Living myocardial slices	138
5.1.5	Experimental objectives	139
5.2	Experiment outline and methods.....	141
5.3	Results.....	147
5.3.1	Exp. 1-2: Imaging calcium dynamics in hiPSC-CM in 2D and 3D.	147
5.3.2	Exp. 3: Imaging coupling of hiPSC-CM and adult-CM	150
5.3.3	Exp. 4: Influence of co-culture duration and decoupling with NBleb	155
5.3.4	Exp. 5: Imaging live myocardial slices	161
5.4	Discussion and conclusion.....	163
6	Conclusion	165
7	Research outputs	169
	Publications.....	169
	Conference presentations	169
8	References.....	170
9	Appendix.....	192
A1.	Video captions.....	192
A2.	System design and operation.....	193
A3.	Resolution characterization.....	196
A4.	Single-cell 2D imaging	198
A5.	Permission to reproduce third-party works	200

Supervisors

Professor Chris Dunsby

Photonics Group, Department of Physics, Imperial College London

Professor Ken MacLeod

National Heart and Lung Institute, Department of Medicine, Imperial College London

Professor Sian Harding

National Heart and Lung Institute, Department of Medicine, Imperial College London

Examiners

Professor Godfrey Smith

Institute of Cardiovascular & Medical Sciences, University of Glasgow

Professor Dan Elson

Department of Surgery & Cancer, Faculty of Medicine, Imperial College London

Statement of originality

I confirm that the work presented in this thesis is my own, and all contributions of others have been appropriately identified and attributed.

Liuba Dvinskikh

March 2022

Copyright declaration

The copyright of this thesis rests with the author. Unless otherwise indicated, its contents are licensed under a Creative Commons Attribution-Non Commercial 4.0 International Licence (CC BY-NC).

Under this licence, you may copy and redistribute the material in any medium or format. You may also create and distribute modified versions of the work. This is on the condition that: you credit the author and do not use it, or any derivative works, for a commercial purpose.

When reusing or sharing this work, ensure you make the licence terms clear to others by naming the licence and linking to the licence text. Where a work has been adapted, you should indicate that the work has been changed and describe those changes.

Please seek permission from the copyright holder for uses of this work that are not included in this licence or permitted under UK Copyright Law.

Acknowledgements

I am very grateful to my PhD supervisor, Chris Dunsby – for giving me the opportunity to pursue this work and discover the world of optical microscopy, and for supporting me from start to finish, and beyond. Thank you for your patience and for teaching me an invaluable amount of imaging optics, scientific principles, and how to tighten a bolt. I would also like to thank my co-supervisors Sian Harding and Ken MacLeod for their enthusiasm, support, scientific expertise and guidance.

I would like to thank my examiners, Prof. Dan Elson and Prof. Godfrey Smith, for agreeing to read this thesis and take part in my PhD viva - I am looking forward to discussing my work.

Thank you to the members of the Cardiac function group at NHLI: Alice, Jahn, Tamzin, Laura, José, Najah and Roman, for helping me navigate the biological lab. Additionally, I am grateful to Liliana and Thusharika for providing the hiPSC-CM samples. I would also like to thank Simon, Martin and John in the optics workshop for help with optomechanical system development, and the helpful and friendly optics administrators Marcia and Judith for the continuous support.

I want to thank all past and present PhD students from our Biophotonics group for contributing to the fun environment in the office. A big thank you to Jonny and Connor, with whom I shared most of my PhD journey, for your friendship and support. Thank you to previous and current PhD's: Terry, Daniel, Sam, Riccardo, Jack, Leo, Zhonghe, Meizhu, Mi Qi, Dan, Bill, Huihui, Matt, Wenzhi and Karishma. Our pub trips, badminton games and laughs have created fun memories.

Thank you for the guidance of the post-docs in our group: Hugh, for the support both in and out of the lab, Sunil, for your enthusiasm and willingness to help, Edwin, for advice on biology labwork, and previous postdocs: Nathan, Nils, Hai, and Wenjun. Thank you to Mark Neil and Kenny Weir for excellent teaching and organization of the postgraduate optics course, and to Paul French, for the leadership of our group. I am hopeful that the Wednesday Journal Club, Christmas dinners in April and other group traditions that have made my time in the group special will remain strong in the future.

Thank you to the ICB CDT and the Chemistry Department for academic and administrative support throughout my degree, and to the BHF and EPSRC for co-funding my PhD and making this work possible.

Finally, I am grateful for the encouragement of my friends, and the patience and unwavering support of my family and partner.

List of videos

1. **Video 4.3:** 2D LSFM timelapse of calcium transients and sparks in a cardiomyocyte.
2. **Video 5.5:** 3D LSFM timelapse of hiPSC-CM undergoing spontaneous calcium transients.
3. **Video 5.6:** Widefield transillumination timelapse of hiPSC-CM and adult-CM co-culture.
4. **Video 5.7:** Widefield epifluorescence timelapse of hiPSC-CM and adult-CM co-culture
5. **Video 5.8:** 3D LSFM timelapse of synchronized transients in hiPSC-CM and adult-CM co-culture.
6. **Video 5.10a:** 3D LSFM timelapse of hiPSC-CM and adult-CM co-culture, without NBleb.
7. **Video 5.10b:** 3D LSFM timelapse of hiPSC-CM and adult-CM co-culture, with NBleb.
8. **Video 5.11:** 3D LSFM timelapse of live myocardial slices undergoing stimulated contraction.

The videos can be found online via the following URL (Dvinskikh, 2022):

<https://doi.org/10.5281/zenodo.6917163>

The video captions are presented in **Appendix A1**.

List of figures

Figure 1.1 Fluorescence energy level transitions and spectra	16
Figure 1.2 Widefield epifluorescence microscope layout	18
Figure 1.3 The “pyramid of frustration”	19
Figure 1.4 Laser scanning confocal fluorescence microscope layout	21
Figure 1.5 Basic light-sheet fluorescence microscope layout	23
Figure 1.6 Examples of different LSFM configurations.	26
Figure 1.7 Diagram of the human heart.	27
Figure 2.1 3D data acquisition modes	31
Figure 2.2 Microscope system for remote refocusing or EDOF-imaging with a DM.	34
Figure 2.3 Scan geometries in single-objective light-sheet approaches.....	34
Figure 2.4 Defining the ray angles and the normalized pupil radius in an imaging system.	37
Figure 2.5 Remote refocusing imaging system in unfolded geometry.....	38
Figure 2.6 Folded configuration for aberration-free remote refocusing system	39
Figure 2.7 Axial plane optical microscopy	41
Figure 2.8 Equivalence of the scaled projections of rotated and sheared volumes	42
Figure 2.9 Optical system layout diagram.	44
Figure 2.10 DSLM and mSPIM illumination path optical relays	45
Figure 2.11 Detection path optical relay	47
Figure 2.12 Relevant spectra for simultaneous dual-channel imaging.	48
Figure 2.13 Image of test chart before and after Fluo-4 defocus correction..	49
Figure 2.14 Fluo-4 channel defocus correction using a pair of lenses.	50
Figure 2.15 Hardware timing diagram for volumetric acquisition with remote refocus.....	52
Figure 2.16 Stage-scan and remote-refocus volumetric data acquisition modes.	53
Figure 2.17 Multi-angle projection viewing through lateral shearing.....	55
Figure 2.18 Projections of sheared image stack and rotated image stacks.....	57
Figure 3.1 Gaussian illumination beam focused by a lens.....	72
Figure 3.2 Detection, illumination and system PSF modelled for uniformly filled pupils	77
Figure 3.3 Spatially varying axial resolution in LSFM simulated using image formation..	78
Figure 3.4 POP simulation of beam waist at focus for the DSLM and mSPIM illumination.	82
Figure 3.5 POP simulation of on-axis intensity for DSLM and mSPIM illumination	83
Figure 3.6 Calculated beam width variation with defocus for the DSLM and mSPIM illumination... ..	84
Figure 3.7 Theoretical axial system PSF FWHM dependence on illumination and detection NA.....	85
Figure 3.8 Modulation of the axial resolution at different points along the illumination beam.....	86
Figure 3.9 Experimental PSF characterization workflow	87
Figure 3.10 Data acquisition for varying remote refocus and positions along the light-sheet.	89

Figure 3.11	Sum intensity projections of the de-sheared bead sample image stack	90
Figure 3.12	Subsection of the sum intensity projections (SIP) along the X' -axis of bead images.....	91
Figure 3.13	1D intensity profiles with Gaussian fits through representative bead images	93
Figure 3.14	Histograms of measured bead image X' -, Y' -, Z' -, and Z^{*} '-FWHM.....	94
Figure 3.15	Three-way orthoslices through representative bead images	95
Figure 3.16	Comparison of modelled and measured axial FWHM along the illumination axis.....	98
Figure 4.1	Calcium regulation during excitation-contraction coupling in cardiomyocytes.....	101
Figure 4.2	Top view of the pacing chamber prototype.	108
Figure 4.3	Pre-processing of the dual-channel data	111
Figure 4.4	Extraction of tubular microstructure from the CMO-channel fluorescence	113
Figure 4.5	T-tubule maps with the membrane outline and identified nuclei.	114
Figure 4.6	T-tubule and distance to nearest tubule (DNT) maps	114
Figure 4.7	Spark detection and correlation with cell structure	117
Figure 4.8	Pixel-wise determination of transient T50.....	120
Figure 4.9	T50 maps averaged over three consecutive transients for a selection of cells.....	121
Figure 4.10	Spark count histograms for a selection of calculated parameters	122
Figure 4.11	Spark parameters compared for epitubular and paratubular regions of the cell	124
Figure 4.12	Comparison of transient T50 for different regions of the cell	126
Figure 4.13	Correlation of the t-tubule structure with transient time-to-half-maximum	127
Figure 4.14	Transient T50 and T50/DNT slope for different DNT regions.....	128
Figure 4.15	Spark and transient parameter correlation with imaging time for LV and RV CM.....	131
Figure 4.16	Correlation of spark amplitude with the relative time of imaging for LV and RV CM .	131
Figure 4.17	Spark and transient parameter comparison for LV and RV CM for restricted dataset..	132
Figure 5.1	hiPSC-CM and adult CM co-culture and pacing chamber.	144
Figure 5.2	LMS sample mounting for imaging.....	145
Figure 5.3	Adult-CM on top of weakly-scattering hiPSC-CM, as seen in transillumination..	146
Figure 5.4	2D LSFM imaging of spontaneous and stimulated calcium transients in hiPSC-CM.....	148
Figure 5.5	3D LSFM imaging of spontaneous and stimulated calcium transients in hiPSC-CM.....	149
Figure 5.6	Synchronized contraction in co-culture imaged under widefield transillumination.....	151
Figure 5.7	Widefield epifluorescence imaging of transients in co-culture	152
Figure 5.8	Synchronized spontaneous transients in 24 hour co-culture.....	154
Figure 5.9	Counting adult-CM with transients and contraction from widefield co-culture imaging.	156
Figure 5.10	Synchronized spontaneous transients in co-culture, with and without NBleb.....	159
Figure 5.11	Stimulated LMS imaged over time in 3D	162

List of tables

Table 3.1	Comparison of resolution simulations models	80
Table 3.2	Estimated illumination beam waists, Rayleigh ranges and confocal parameters	84
Table 3.3	Modelled system resolution at the beam waist.....	85
Table 3.4	Measured FWHM of the bead image intensity distributions.....	96
Table 3.5	Estimated lateral and axial system PSF FWHM for DSLM and mSPIM illumination.....	96
Table 4.1	Total spark number per cell in each distance to nearest tubule category	123
Table 4.2	Spark parameter comparison for epitubular and paratubular sparks	123
Table 4.3	Comparison of average T50 for different regions of the cell	125
Table 4.4	Transient T50 variation with DNT.....	127
Table 4.5	Comparison of T50/DNT slopes in tubulated and detubulated cell areas.....	128
Table 4.6	Comparison of the spark and transient parameters calculated for LV and RV CM.....	129
Table 4.7	Correlation of the spark and transient parameters with relative imaging time.....	130
Table 4.8	Comparison of the spark parameters and transient T50 calculated for LV and RV CM ...	133
Table 5.1	Overview of imaging experiments with hiPSC-CM and their co-culture with adult-CM..	141
Table 5.2	Summary of 2D timelapse acquisitions of unpaced and paced hiPSC-CM culture	147
Table 5.3	Summary of dynamics identified from widefield co-culture imaging	153
Table 5.4	Summary of the 3D LSFM imaging of of hiPSC-CM and adult-CM co-culture.....	155
Table 5.5	Results from widefield imaging of co-cultures with and without NBleb.....	157
Table 5.6	Summary of the LSFM imaging of co-culture for Experiment 4.....	160

List of abbreviations

ASLM – axially swept light-sheet microscopy

BFP – back focal plane

CICR – calcium-induced calcium release

CM – cardiomyocyte

CMO – CellMask Orange

COM – centre of mass

CTF – contrast transfer function

DHPR – dihydropyridine receptor

DNT – distance to the nearest tubule

DOF – depth of focus

DSLM – digitally-scanned light-sheet microscopy

EC – excitation-contraction

EDOF – extended depth-of-field

EHT – engineered heart tissue

ESC – embryonic stem cells

F50 – half of the peak amplitude

FDHM – full-duration half-maximum

FOV – field of view

FWHM – full-width at half-maximum

HF – heart failure

(h)iPSC – (human) induced pluripotent stem cells

LMS – live myocardial slices

LSFM – light-sheet fluorescence microscopy

LV – left ventricle

MI – myocardial infarction

(m)SPIM – multi-directional selective plane illumination microscopy

NA – numerical aperture

NBleb – para-Nitroblebbistatin

NCX – sodium-calcium exchanger

OPM – oblique plane microscopy

OTF – optical transfer function

POP – physical optics propagation

PSF – point spread function

RI – refractive index

RF – remote refocus

ROI – region of interest

RV – right ventricle

RyR – Ryanodine receptor

sCMOS – scientific complementary metal-oxide semiconductor

SERCA – Sarcoplasmic reticulum Ca^{2+} ATP-ase

SNR – signal-to-noise ratio

SOLS – single-objective light-sheet

SR – sarcoplasmic reticulum

T50 – time to half maximum of the peak amplitude (F50)

1 Introduction

“By the help of microscopes, there is nothing so small, as to escape our inquiry; hence there is a new visible world discovered to the understanding” – Robert Hooke (Hooke, 1665).

The fundamental structural and functional unit of life is the cell. Hence, the study of any biological system inevitably needs understanding of this basic building block. However, around a tenth of a millimetre in size, most cells are invisible without the help of the optical microscope. While the use of lenses for focusing light can be traced back several millennia (Sines & Sakellarakis, 1987), some of the first compound microscopes are thought to have been built in the late 16th century by spectacle maker Hans Janssen and his son Zacharias. In the early 17th century, Galileo Galilei converted one of his telescopes into a two-lens compound microscope.

One of the first applications of microscopes to study the microscopic world is credited to Robert Hooke. In his publication “Micrographia” (Hooke, 1665), he described his observations of various biological objects viewed through the compound microscope, and originated the word “cell”, used to describe walled plant cells that resembled the cells in a honeycomb. The application of microscopes to biology was further popularized by Antonie van Leeuwenhoek, who used single lens microscopes with over 200× magnification to observe living cells (Lane, 2015). In the early 19th century, improvements in glass quality by Joseph von Fraunhofer and Otto Schott reduced optical aberrations, improving lens performance. Developments in compound microscope instrumentation by Carl Zeiss, in collaboration with the theoretical work on optical resolution and aberrations by Ernst Abbe, revolutionized the design and manufacturing process of microscopes (Feffer, 1996).

Since then, the field of optical microscopy has undergone an extensive transformation, with technological progress driving biological discovery, and biological needs defining the directions of technical innovation. The development of fluorescent labelling allowed non-destructive and quantitative imaging of biological structures with high specificity. Optically sectioned imaging techniques enabled three-dimensional fluorescence microscopy by reducing out-of-focus background light emission or detection. The design of microscopes capable of gentle imaging of live cells with high spatial and temporal resolution has permitted the visualization, quantification, and, ultimately, understanding of biological structures and dynamics on scales too small for the naked human eye.

As a result of its orthogonal and decoupled illumination-detection geometry, light-sheet fluorescence microscopy (LSFM) enables optically sectioned parallelized plane imaging with low phototoxicity, and is compatible with the study of a range of biological systems. In the work described in this thesis, high-speed LSFM is applied to imaging calcium dynamics in heart muscle cells to study their function and

interaction with stem cell-derived heart muscle cells, with the aim of evaluating the potential of the latter for regenerative therapy for heart disease. This introduction chapter will present relevant background and concepts including the principles of fluorescence microscopy and the challenges of live cell imaging, approaches to optically sectioned imaging, light-sheet fluorescence microscopy, as well as the biological background of cardiac function, disease and stem cell regenerative therapy.

1.1. Fluorescence microscopy

Fluorescence is used as the main contrast mechanism in many modern optical microscopes. Unlike bright-field imaging, where the contrast mechanism is absorption by the sample, or dark field microscopy, where contrast is caused by scattering, fluorescence imaging allows the visualization of individual components of biological samples with high specificity and low background (Lakowicz, 2006). Fluorescence occurs when a molecule in an excited electronic energy level relaxes to a lower energy level through the emission of a fluorescence photon. In fluorescence microscopy, the molecule is generally excited through the absorption of a photon with a higher energy – or shorter wavelength – than the emitted photon. The process can be visualized on a Jablonski diagram (Jabłoński, 1935), as shown in **Figure 1.1a**.

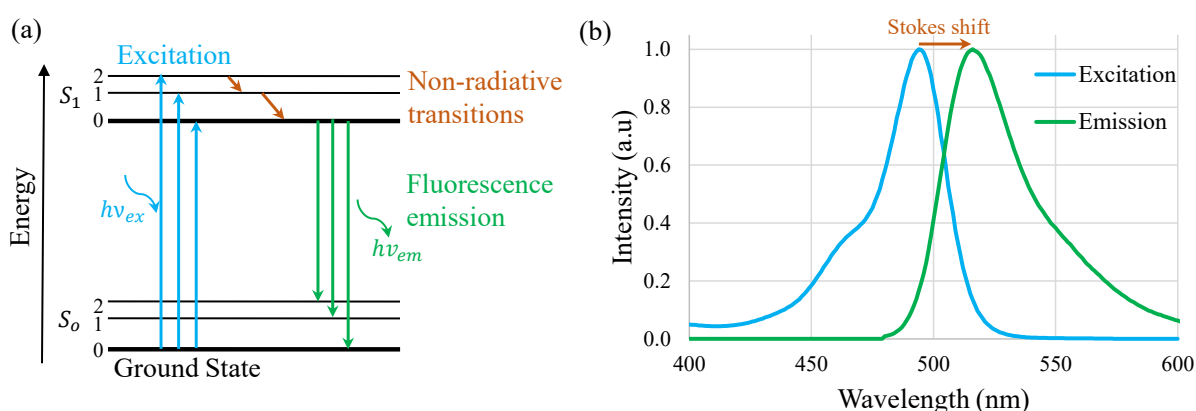


Figure 1.1 Fluorescence energy level transitions and spectra. (a) Simplified Jablonski diagram of energy level transitions involved in fluorescence, including fluorophore excitation through photon absorption, non-radiative transitions to lower vibrational energy levels of the first electronic excited state, and relaxation to the ground electronic state through emission of a fluorescence photon. (b) Excitation and emission spectra for Fluo-4 AM, a cell permeant calcium indicator. The Stokes shift between excitation and emission peaks is indicated by the red arrow. Excitation and emission spectral profiles obtained from the Fluorescence SpectraViewer (ThermoFisher Scientific).

The energy level structure of a fluorescent molecule determines the shape of its fluorescence excitation and emission spectra. The absorption of a photon with energy $E = h\nu_{ex}$, where ν_{ex} is the excitation frequency and h is Planck's constant, results in the fluorophore's excitation from ground state S_0 to a higher electronic energy state, such as one of the vibrational levels within the first electronic state S_1 . Non-radiative transitions to lower vibrational levels occur orders of magnitude faster than the fluorescence lifetime of $\sim 10^{-8}$ s. Hence, absorption and emission typically occur from the lowest

vibrational energy states (Kasha's rule), (Kasha, 1950), as at room temperature there is typically not enough thermal energy to fill the higher vibrational levels (Lakowicz, 2006).

The difference in electronic energy states is greater than that between vibrational levels, and hence an external source of energy – such as the absorption of a photon – is normally required to excite fluorescence. As the fluorophore relaxes to one of the vibrational levels within S_0 , a photon with energy $E = h\nu_{em}$ is emitted, where ν_{em} is the emission frequency. Due to loss of excitation energy through transitions to lower vibrational states, as well as the prevalence of decay to higher vibrational levels of S_0 , fluorescence typically occurs at longer wavelengths than that used to excite the molecule (**Fig. 1.1b**) – a phenomenon known as the Stokes shift (Stokes, 1852).

The Vavilov rule, a corollary of Kasha's rule, states that fluorescence emission spectra are typically independent of the excitation wavelength (Klán & Wirz, 2009). Organic fluorophores in solution have broad bands of vibrational and rotational states, which provide a range of possible excitation and emission pathways, which results in continuous spectral profiles. For many fluorescent molecules, the emission and absorption spectra are mirror images (Levshin's Rule and Francis-Condon principle) (Lakowicz, 2006; Vilkov & Pentin, 1987).

Another relevant property of fluorescence is the effect of polarised excitation light and the degree of emission polarization. For randomly oriented fluorophore molecules, polarised excitation light will preferentially excite fluorophores with transition moments co-aligned with the electric field vector of the excitation, resulting in partially polarised parallel emission. The degree of polarisation of the emitted fluorescence can be parameterised by the fluorescence anisotropy (Lakowicz, 2006).

The basic layout of a widefield epifluorescence microscope is shown in **Fig. 1.2**, with sample illumination and fluorescence detection performed through the same objective lens. The separation of excitation and emission light in a fluorescence microscope is achieved using spectral filters to select a range of wavelengths for excitation and detection, and to spatially separate the two beams. The design of the three filters is crucial for the suppression of unwanted light, however, for fluorophores that have significant excitation and emission spectra overlap, this reduces the fraction of detected photons from those emitted, and hence the achieved signal-to-noise ratio (SNR).

The main types of fluorophores used for fluorescence microscopy are synthetic dyes and fluorescent proteins. The former can attach to proteins through specific functional amino-, carboxyl- and other groups, and be used as a marker for bioactive reagents such as antibodies or nucleic acids. Techniques for DNA modifications allow the exogenous expression of fluorescent proteins such as green fluorescent protein (GFP), yellow fluorescent protein (YFP) and red fluorescent protein (RFP), enabling their use as protein location reporters and in gene expression quantification *in vivo* (Lakowicz, 2006). Calcium indicators dyes such as Fluo-4 (Gee et al., 2000) and genetically encoded calcium indicators

such as GCaMP (Nakai, Ohkura & Imoto, 2001) can be used to measure and monitor changes in intracellular calcium concentration.

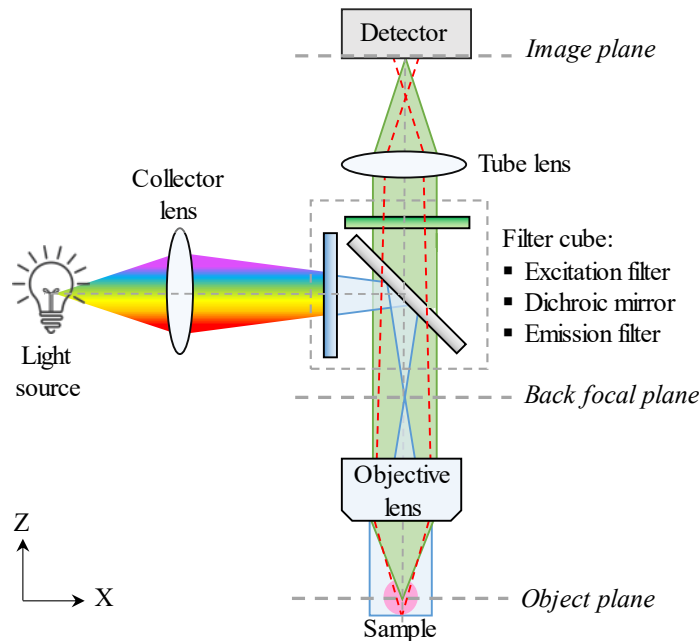


Figure 1.2 Widefield epifluorescence microscope layout. A collector lens is used to focus the light from the source (broadband spectrum indicated by rainbow pattern) onto the back focal plane of the objective lens, achieving even and collimated Kohler illumination of the sample (Köhler, 1894). The emitted fluorescence collected by the same objective is focused onto a detector by the tube lens. The excitation and emission light are separated using a filter cube containing a dichroic mirror, an excitation filter and an emission filter. In a widefield fluorescence microscope, fluorescence from out-of-focus planes (red dashed line) is also collected by the detector.

Autofluorescence from naturally fluorescent structures such as collagen or NADH (reduced nicotinamide adenine dinucleotide) which exists in all living cells, can be used for label-free diagnostic imaging, but can be problematic when interfering with the detection of low-intensity fluorescent signals from exogenous fluorophores (Monici, 2005). Since the number of fluorophores within any part of the sample is finite, and excited fluorophores may degrade, fluorescence microscopy is a photon-limited imaging modality (Stelzer, 2015).

Challenges of live-cell fluorescence microscopy

Live-cell imaging, or time-lapse microscopy of living cells, presents a unique set of challenges and trade-offs. These are sometimes summarized in the “*pyramid of frustration*” (Fig. 1.3), where sample health considerations introduce an additional dimension to the classical photon-limited triangle: spatial resolution, temporal resolution (or imaging speed), and signal-to-noise ratio (SNR) and contrast (Lemon & McDole, 2020). Fundamental limitations make it impossible to achieve full optimization of all parameters without compromising on others, and hence the imaging approach and priorities are tailored to the experimental aim. The imaging method and acquisition parameters need to consider the sample size, sensitivity, and the speed and duration at which the relevant biological dynamics unfold.

A fundamental challenge in fluorescence microscopy is light attenuation through absorption and scattering: inhomogeneous biological tissue interacts strongly with visible light, with more scattering at shorter wavelengths. Light scattering by the sample of both the excitation light and the fluorescence emission can result in signal attenuation and increased background, degrading image quality, and limiting the imaging depth. One way to mitigate this is by rejecting scattered fluorescence through spatial filtering. Light scattering can also be reduced by matching the refractive index of the sample and the surrounding medium through optical clearing (Costa et al., 2019), however, existing techniques are not compatible with live cell imaging.

While increasing sample illumination can improve the signal-to-noise ratio, excessive light exposure can cause cellular damage to biological samples. Photodamage is more severe for illumination with light of shorter wavelengths, which carries higher energy and is absorbed more strongly by biological molecules. Phototoxicity increases in the presence of exogenous fluorophores (Wagner et al., 2010): the photo-induced fluorophore toxicity can damage sample physiology and introduce experimental artefacts. The non-phototoxic light dose for fluorescently labelled cells was estimated to be around 10 J/cm^2 , which is equivalent to 100 seconds of solar irradiance (at around 100 mW/cm^2 or $1 \text{ nW}/\mu\text{m}^2$) (Schneckenburger & Richter, 2021).

The main cause of phototoxicity in live cell imaging is the generation of reactive oxygen species (ROS) – free radicals and reactive molecules produced from molecular oxygen (Icha et al., 2017). When excited by ultraviolet and visible light, both fluorophores introduced into cells as probes or labels, and naturally occurring organic molecules can undergo non-radiative transitions into a triplet state. Energy or electron transfer from the triplet state to molecular oxygen can lead to the formation of a singlet oxygen or a superoxide radical respectively (Zheng et al., 2014). These oxidizing species can damage the cell through oxidative stress of DNA, lipids and proteins (Icha et al., 2017).

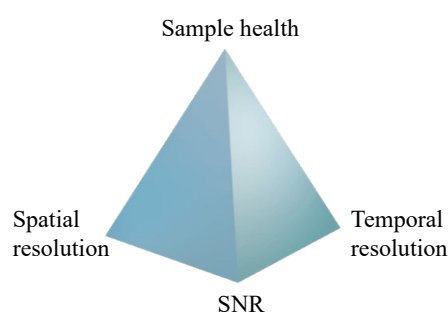


Figure 1.3 The “pyramid of frustration” (or, more geometrically accurate, the tetrahedron of frustration) illustrating the trade-offs in live cell imaging: spatial and temporal resolution, signal-to-noise ratio (SNR) and sample health.

In addition to phototoxicity, prolonged or high intensity illumination can also cause fluorophore photobleaching – a process which involves accumulated chemical photodamage in the form of covalent bond modification or reactions between the fluorophore and other surrounding molecules

(Demchenko, 2020). This photochemical effect involves irreversible loss of fluorescence ability, which can prevent quantitative analysis of the recorded fluorescence signal. Photobleaching and phototoxicity can be reduced by confining fluorescence excitation to the focal plane of the sample, adjusting the imaging buffer composition to include ROS scavengers and antioxidants, reducing the peak intensity, illuminating with longer wavelengths, using pulsed instead of constant illumination, and improving the detection efficiency. Implementing controls that monitor viability and check for any changes in sample morphology and physiology is important for reducing the influence of phototoxicity on sample behaviour and hence experimental conclusions (Icha et al., 2017).

A further important aspect of live cell imaging is appropriate physiological environmental control: the biological behaviour and health of cells and tissues will depend on factors such as temperature, imaging media composition and pH (Ettinger & Wittmann, 2014). Finally, biology takes place in 3D. As three-dimensional culture models are increasingly replacing monolayer sample architecture, visualizing these structures and their dynamics requires techniques capable of optically sectioned and volumetric imaging.

1.2. Optically sectioned imaging

In a widefield fluorescence microscope, in-focus two-dimensional imaging is achieved at the front focal plane of the objective, and over a specific axial range determined by the depth-of-focus (DOF). Imaging sub-micron biological structures requires objectives with a high numerical aperture (NA), which in turn have a small depth-of-focus, with $\text{DOF} \propto 1/\text{NA}^2$. Light from out-of-focus planes is also detected, contributing to background fluorescence and reduced contrast. Since the detected intensity value within each pixel on the detector cannot be directly mapped to a small volume in the sample, out-of-focus contributions limit the ability to achieve quantitative analysis of widefield fluorescence images of three-dimensional samples.

In contrast to physical sectioning of samples, such as that used in histology, where preparation of thin tissue slices often requires destructive methods incompatible with live imaging, optical sectioning allows the in-focus imaging of a single plane within the sample. This enables the acquisition and quantitative analysis of 3D data acquired by recording a stack of images at different focal planes (Agard, 1984). In fluorescence microscopy, out-of-focus light is only contributed by emitting fluorophores, and hence fluorescence microscopy modalities enable optically sectioned imaging through either optical or computational rejection of out-of-focus light, or by not exciting it in the first place.

Confocal microscopy

Confocal scanning microscopy (Minsky, 1961) improves spatial resolution and contrast by using a tightly focused illumination spot to only excite and detect fluorescence from a small focal area, hence blocking out-of-focus light. The emitted fluorescence is imaged onto a pinhole in the image plane (**Fig. 1.4**), with only light within the area of the pinhole collected by an integrating point detector such

as an avalanche photodiode or photomultiplier tube (PMT). An image of a volume is built up by scanning the illumination and detection spot in three-dimensions. The development of laser-scanning confocal microscopes (LSCM) (Davidovits & Egger, 1969), enabled improved excitation efficiency and faster acquisition times compared to earlier non-laser-based systems.

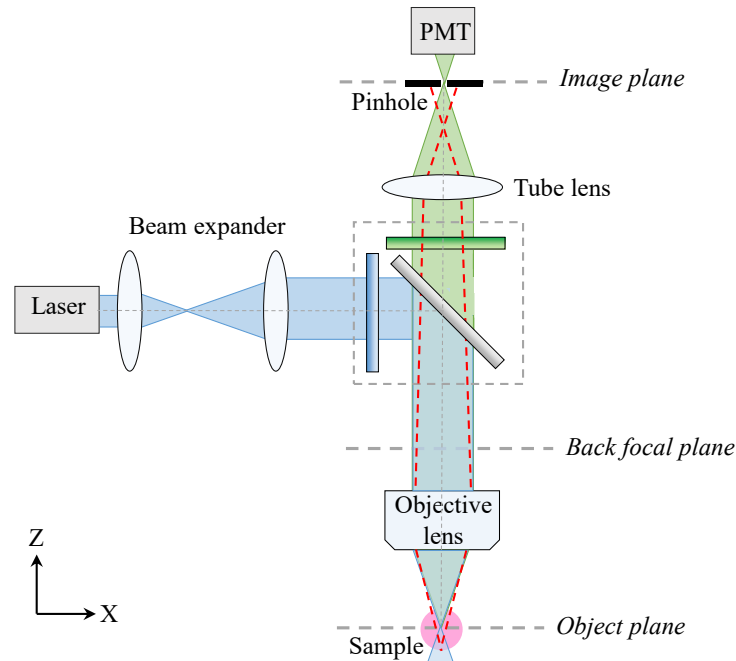


Figure 1.4 Laser scanning confocal fluorescence microscope layout. The laser beam is expanded to fill the back focal plane of the objective, illuminating a small focal volume within the sample. The emitted fluorescence, collected by the same objective, is transmitted through the dichroic and emission filter. A pinhole placed in the image plane in front of the photomultiplier tube (PMT) rejects out-of-focus light (dashed red lines).

Multiphoton microscopy

Another method for optically sectioned imaging is multiphoton microscopy. Two-photon absorption was first described in (Göppert-Mayer, 1931) and demonstrated in (Garrett & Kaiser, 1961) using laser excitation. The simultaneous (on the order of femtoseconds) absorption of two photons results in fluorescence emission at around twice the excitation frequency: $\nu_{em} \lesssim 2 \times \nu_{ex}$. The longer excitation wavelengths in the near-IR are scattered and absorbed less, allowing deeper tissue penetration (Helmchen & Denk, 2005). However, the low probability of near-simultaneous absorption of two (or more) photons means that multiphoton fluorescence requires high excitation intensities, with the two-photon and three-photon fluorescence intensity proportional to the square and cube, respectively, of the excitation intensity. This intensity dependence confines fluorescence to the focal volume, generating inherent optical sectioning, with reduced out-of-plane photobleaching and phototoxicity. However, the generation of high excitation power requires expensive ultra-fast pulsed laser sources, and the high photon flux required for excitation can contribute to non-linear phototoxicity and photobleaching effects in the focal plane (Patterson & Piston, 2000).

Structured illumination microscopy

While standard confocal and multiphoton microscopes require lateral scanning of the focal point to build up a two-dimensional image, wide-field optically sectioning techniques enable parallelized plane acquisition (Conchello & Lichtman, 2005). One such technique is structured illumination microscopy (SIM), where a sinusoidal illumination pattern is imaged onto the sample, and the final image is recovered from multiple frames acquired with laterally shifted illumination patterns. Neil et al. used spatially incoherent structured illumination in the form of a projected grid pattern to obtain an optically sectioned image I_{OS} by combining three images I_1 , I_2 , and I_3 , each with the grid pattern shifted by a third of the grid cycle period, through (Neil, Juškaitis & Wilson, 1997):

$$I_{OS} = \sqrt{(I_1 - I_2)^2 + (I_2 - I_3)^2 + (I_3 - I_1)^2} \quad (1.1)$$

This technique, also known as optically sectioning SIM (OS-SIM) does not use phase information in the reconstruction. Including the phase information in the reconstruction process can be used to enhance the resolution beyond the diffraction limit – this technique is known as super-resolution structured illumination microscopy (SR-SIM) (Gustafsson, 2000; Heintzmann & Cremer, 1999), in which the sample is excited with structured illumination generated by the interference of multiple laser beams. While the wide-field modality of SR-SIM can enable faster image acquisition and less photobleaching than point-scanning, the complex reconstruction is sensitive to motion and noise, and requires the acquisition of multiple frames for each reconstructed image.

TIRFM, deconvolution and other approaches

Optically sectioned two-dimensional imaging can be achieved using total internal reflection fluorescence microscopy (TIRFM) (Ambrose, 1956; Axelrod, 1981). In this technique, fluorescence of a thin slice of a sample directly adjacent to a supporting glass surface is excited by an evanescent wave. The evanescent wave is created when the illuminating beam incident on a refractive index (RI) interface undergoes total internal reflection at an angle of incidence exceeding the critical angle $\theta_c = \arcsin(n_2/n_1)$, where n_1 and n_2 are the RIs of the media before and after the interface. The evanescent wave decays exponentially with distance away from the solid surface, hence confining the excitation to ~ 100 nm in depth. This allows imaging of a thin optical section; however, observation is restricted to the surface layer of the sample (Fish, 2009).

Out-of-focus background can also be removed computationally in postprocessing through deconvolution – an algorithm that uses a priori information about the optical system to reverse the distortion introduced by the imaging process. By emphasizing higher spatial frequencies, the deconvolution process can computationally reduce lower-order out-of-focus background, enable 3D reconstruction from 2D images and improve the image quality (Conchello & Lichtman, 2005; McNally et al., 1994).

The resolution enhancement of some of these optically sectioning microscopy techniques are discussed in **Section 3.1.3**. Another “widefield” optically sectioning modality is light-sheet fluorescence microscopy (LSFM), where excitation is confined to a single plane within the sample, eliminating fluorescence from outside of the illuminated plane – this technique is covered in the following section.

1.3. Light-sheet fluorescence microscopy

Light-sheet fluorescence microscopy implements selective illumination of a thin slice of the sample that is orthogonal to the direction of observation. As a result, fluorophore excitation is confined to the focal plane, enabling optically sectioned imaging. As the focal plane is scanned through the sample for three-dimensional acquisition, each part of the specimen is only illuminated once per acquired volume, and hence the photodose is 3-5 orders of magnitude lower than in confocal microscopy (Stelzer et al., 2021), reducing phototoxicity and photobleaching (Jemielita et al., 2013; Reynaud et al., 2008). The basic layout of a selective plane illumination microscope (SPIM) is shown in in **Fig 1.5**. In this figure the expanded laser beam is propagating along the x-axis and is focused by a cylindrical lens in the z-direction to create a static light sheet. The excited fluorescence is detected perpendicularly to the illumination axis and focused onto a camera such as a charge-coupled device (CCD) or a scientific complementary metal-oxide-semiconductor (sCMOS) camera. The parallelized widefield detection enables fast acquisition at up to thousands of voxels per second (Stelzer et al., 2021).

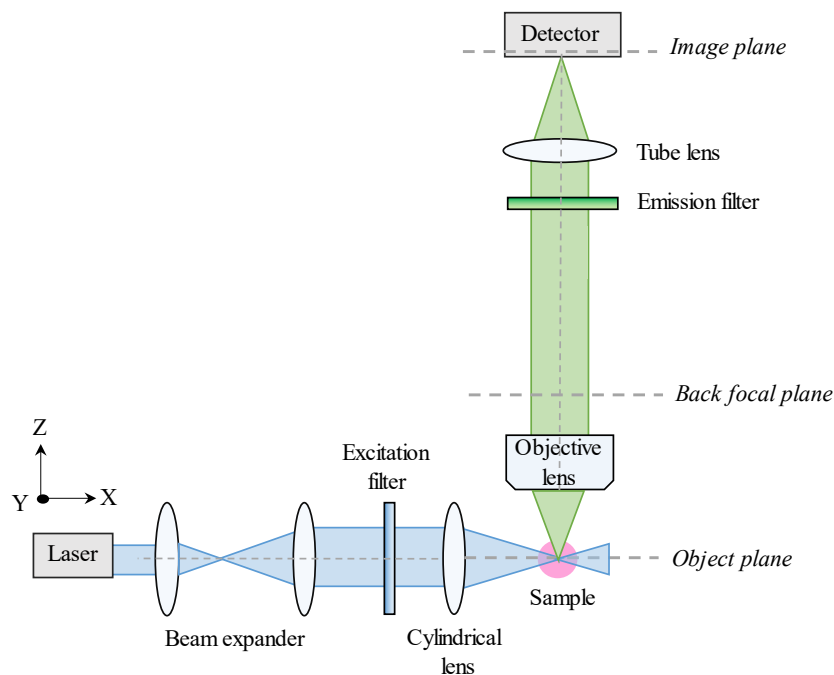


Figure 1.5 Basic light-sheet fluorescence microscope layout. Collimated and expanded laser light is focused in the z-direction, to generate a static light sheet. Sample fluorescence is collected by the detection objective positioned orthogonally to the illuminated plane and focused onto the detector by a tube lens. Widefield detection enables parallelized imaging of the entire illuminated field of view. Volumetric acquisition is achieved by the relative translation of the sample with respect to the co-aligned illumination and detection planes.

The first known implementation of orthogonal illumination-detection scheme was in the form of the ultramicroscope (Siedentopf & Zsigmondy, 1902), where a precision slit was imaged onto the sample, forming a light sheet, allowing the observation of sub-diffraction scattering particles. Orthogonal-plane fluorescence optical sectioning (OPFOS) (Voie, Burns & Spelman, 1993), was the first application of the perpendicular illumination-detection geometry to fluorescence microscopy, with a cylindrical lens used to focus the illumination. Building on the concept of the confocal theta microscope (Stelzer & Lindek, 1994), where confocal illumination and detection are done at an angle, the first diffraction-limited SPIM system was built (Huisken et al., 2004).

Since then, the extensive development of LSFM technology has both been driven by and enabled wide application within the life sciences, across a range of spatiotemporal scales. For example, within vertebrate developmental biology, the multidirectional acquisition capability and low phototoxicity of LSFM has enabled long-term observation of embryonic development in mice (McDole et al., 2018). The LSFM capacity for high-speed imaging through parallelized acquisition of entire optical sections has been used to capture rapid biological events on the millisecond timescale, such as calcium signalling in individual neurons (Keller & Ahrens, 2015).

Light-sheet illumination

The illumination confinement in LSFM enables optical sectioning as well as improvement in the axial resolution (discussed in detail in **Chapter 3**). Static light-sheets are commonly produced by focusing a Gaussian beam in one direction, with a cylindrical lens either directly before the sample or earlier in the illumination path. An alternative approach is digitally-scanned light-sheet microscopy (DSLM) (Keller et al., 2008), where the light sheet is generated through rapid scanning of a pencil-like beam along the y-axis. The fast scanning can be achieved with motorized mirrors, forming a virtual (or dynamic) incoherent light-sheet, with sample fluorescence excited line-by-line within the exposure time of the detector.

While the ideal light-sheet would be infinitely broad and thin, diffraction introduces a trade-off between the light-sheet thickness and length. For Gaussian beams, the beam radius increases with distance away from the focus along the illumination axis. The beam divergence is faster for more tightly focused beams, which reduces the optical sectioning away from the beam waist, and hence limits the useable field of view (FOV) range along the illumination axis.

One way of maintaining axial resolution over a larger FOV in a DSLM implementation is by using propagation-invariant illumination profiles such as Bessel beams (Fahrbach & Rohrbach, 2010; Planchon et al., 2011) or Airy beams (Vettenburg et al., 2014). However, while these beam profiles maintain a tight beam waist over longer axial distances than a Gaussian beam, part of the energy is distributed in side-lobe structures, which introduce out-of-focus light that reduces optical sectioning and contributes to photobleaching and phototoxicity outside of the imaged plane. The effects of

side-lobe excitation can be removed through deconvolution in postprocessing, or reduced in multiphoton fluorescence microscopy, where fluorescence intensity varies nonlinearly with the excitation intensity, however, the usual drawbacks of multiphoton fluorescence microscopy apply.

Another way to extend the range of the useable FOV is through axially swept light-sheet microscopy (ASLM) (Dean et al., 2015), where the beam waist is swept along the illumination axis. The axial sweeping of the light-sheet can be performed within the camera exposure or synchronously with the rolling shutter of the sCMOS detector (Dean & Fiolka, 2014), hence maintaining the axial resolution over the whole field of view. Alternatively, instead of generating uniformly thick light-sheets, large FOV's can be imaged by tiling the excitation light-sheet within the focal plane, acquiring images at each position, and stitching them together (Gao, 2015), however, the improved axial resolution without the trade-off of a limited FOV comes at the cost of reduced imaging speed and increased photodose to the sample. ASLM approaches are particularly compatible with larger fixed or cleared samples (Chakraborty et al., 2019), where the acquisition speed and phototoxicity are of less concern.

The directionality of light-sheet illumination can cause dark stripe artefacts due to shadows cast by parts of the sample with higher scattering and absorption. These can be overcome by light-sheet pivoting, or angular dithering of the light-sheet, or multi-directional sample illumination (mSPIM) (Huisken & Stainier, 2007), which provides more uniform fluorescence excitation.

LSFM image acquisition and system configurations

Volumetric acquisition in LSFM is achieved by the relative translation or rotation of the sample with respect to the co-aligned illumination and detection planes. This can be implemented through mechanical scanning of the sample using a piezo-electric motor; however, stage scanning is slow and can introduce motion artefacts and disturbance to the sample. Another approach is remote refocusing of the detection plane synchronously with the scanning of the light-sheet, where the sample remains stationary. Approaches to high-speed volumetric image acquisition are discussed in detail in **Chapter 2**.

Today, a multitude of LSFM illumination-detection configurations exist (Albert-Smet et al., 2019), some of which are shown in **Figure 1.6**. In inverted SPIM (Wu et al., 2011) (**Fig. 1.6a**), fluorescence illumination and detection are orthogonal, both at a 45° angle to the horizontal surface, which can simplify sample mounting and reduce the optical path for excitation and emission light through the sample. The shorter working distance of high-NA objectives can limit optical access to parts of the specimen further away from the objective. In open-top SPIM (McGorty et al., 2015) configurations, the illumination and detection objectives are located underneath the sample and are compatible with multi-well plate sample mounting and microfluidic devices. A water-filled refractive prism is used to reduce aberrations caused by imaging through a tilted refractive index boundary.

In dual-illumination SPIM (Wu et al., 2013), two orthogonally positioned objectives are used for both illumination and detection (**Fig. 1.6b**). Two sequentially acquired views are merged into a single 3D image in postprocessing through multiview image fusion, which can be achieved either using content-based transformation (Swoger et al., 2007) or bead image-based co-registration (Preibisch et al., 2010), achieving more isotropic resolution across the sample. In oblique plane microscopy (OPM) (Dunsby, 2008), illumination and detection are achieved through the same objective (**Fig. 1.6d**), making it compatible with conventional microscope sample mounting. More recently, the OPM concept has been extended to acquiring two views through the same objective (Sparks, Dent et al., 2020).

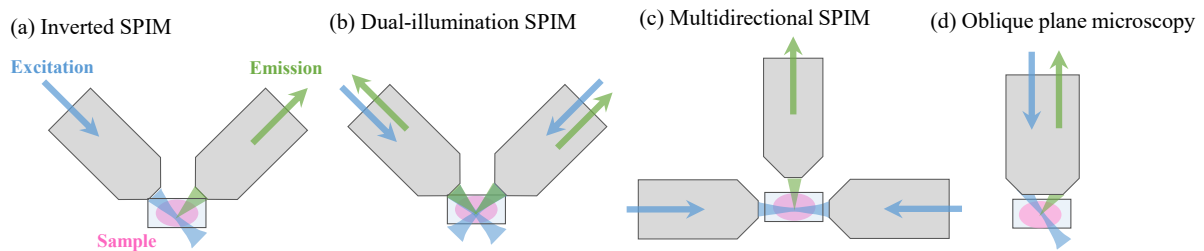


Figure 1.6 Examples of different LSFM configurations: (a) Inverted SPIM (iSPIM), (b) dual-illumination SPIM (diSPIM), (c) multidirectional SPIM (mSPIM) and (d) oblique plane microscopy (OPM).

Depending on the application, acquired LSFM data can extend to up to three spatial dimensions, with timelapse acquisitions sampled at thousands of timepoints, involve multiple spectral channels, and include datasets for multiple conditions, controls, and repeats. As a result, organization, storage, processing and visualization solutions need to be adapted to the extensive multidimensional output, with single experiments producing terabytes of data (Reynaud et al., 2015). In recent years, both customized processing pipelines tailored to the needs of individual experiments and standardized frameworks have been developed (Amat et al., 2015). After acquisition, pre-processing of LSFM data often includes background subtraction and lossless or lossy compression. Next, advanced processing may be implemented, including steps such as multiview fusion, stitching of overlapping FOV for imaging of larger samples, deconvolution and other corrections.

1.4. Heart function, disease and regenerative therapy

Cardiac anatomy and function

Heart contraction is responsible for pumping blood through the blood vessels, delivering oxygen and nutrients around the body and transporting carbon dioxide to the lungs. The human heart is located in the central compartment of the chest and divided into four chambers (**Fig. 1.7**): the larger pair are the left and right ventricles (LV and RV), and the two smaller chambers are the left and right atria (LA and RA). Deoxygenated blood enters the right atrium through the superior and inferior venae cavae and the right ventricle pumps the blood to the lungs (pulmonary circulation), where it releases carbon dioxide, and receives oxygen through respiration. Oxygenated blood then returns to the heart through the

pulmonary vein into the left atrium. It then passes into the left ventricle, which pumps the blood through the aorta to the rest of the body (systemic circulation). The cardiac cycle consists of two stages: diastole, during which the heart relaxes and refills with blood, and systole, where the heart contracts and pumps the blood. Heart valves at the ventricle openings prevent back flow.

The cardiac wall has three layers: the inner endocardium, the thick layer of myocardium (heart muscle) and a thinner outer epicardium. The myocardium tissue contains layers of *cardiomyocytes* – the contractile cells of cardiac muscle, within an extracellular matrix generated by fibroblasts. Blood flow to and from the muscle cells is provided by a capillary network extending throughout the myocardium, with coronary arteries and the smaller arterioles providing oxygen and nutrients, and coronary veins and venules draining away waste products.

Cardiac muscle contraction is triggered by the conversion of an electrical signal into a mechanical response through a series of events collectively known as excitation-contraction coupling (EC-coupling) (Bers, 2002). The heart's electrical activity is initiated by the sinoatrial node that lies at the junction of the right atrium and superior vena cava and generates currents that spread through the heart, passing from one cell to another through gap junction structures (Kurtenbach, Kurtenbach & Zoidl, 2014), usually in a coordinated manner. Each heart cell receives the electrical excitation in the form of an action potential, triggering calcium release from internal stores in the cell, resulting in contraction of specialized contractile fibres.

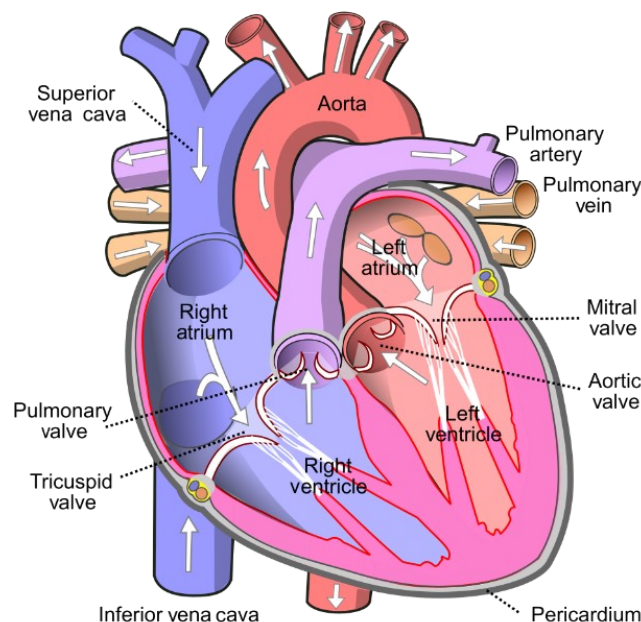


Figure 1.7 Diagram of the human heart illustrating the four chambers, arteries, veins and valves. The normal direction of blood flow is shown with white arrows. Reproduced under creative commons license CC BY-SA 3.0 from Wikimedia commons (Wapcaplet, 2006).

Heart disease

Cardiovascular diseases (CVD) are heart and circulatory diseases that can be either inherited or developed later in life. With 1 in 14 people in the world living with CVD, heart and circulatory disease is the leading cause of death, responsible for around 1 in 3 deaths globally (British Heart Foundation, 2021). Half of the CVD mortality rate is attributed to coronary heart disease (CHD), also known as ischaemic heart disease, which involves a reduced blood supply to the cardiac muscle as a result of an accumulation of a mixture of cholesterol, other fats, calcium and fibrin in the arteries of the heart. This plaque build-up can lead to full or partial occlusion of the vessels supplying the heart muscle, leading to myocardial infarction (MI), or a “heart attack”, where the lack of oxygen delivery leads to cardiac tissue damage.

Myocardial infarction and hypertension are the two main causes of heart failure (HF) (Metra & Teerlink, 2017), a complex syndrome that includes changes in the function and structure of the heart that compromise adequate blood circulation around the body, leading to insufficient blood supply to vital organs. Highly prevalent in the Western world, heart failure affects up to 10% of people over 65 (Mosterd et al., 1999), with 5-year survival reached by only around a third of patients with HF diagnosis (Mosterd & Hoes, 2007). The high prevalence and poor prognosis of heart failure have driven the pursuit for a better understanding of the electrophysiology and contractile function of healthy and damaged cardiac tissue. At the cellular level, HF has been shown to cause loss of structural organization (Lyon et al., 2009) and desynchronization of calcium release (Louch et al., 2006). These morphological and functional changes within single cardiomyocytes have been linked to reduced contractile function and arrhythmia (Hammer et al., 2015; Louch et al., 2006).

Treatment and stem cell regenerative therapy

While there is some research supporting the idea of cardiomyocyte renewal (Bergmann et al., 2009) through cell division (Senyo et al., 2013), the cardiomyocyte turnover rate is estimated to be < 1% in adults (Bergmann et al., 2015), and hence the natural regenerative capacity of the cardiac muscle is thought to be limited, and unable to compensate for damage after MI (Breckwoldt, Weinberger & Eschenhagen, 2016; Kikuchi & Poss, 2012). The main non-pharmacological treatment for heart-attack patients is revascularization, which involves restoration of blood perfusion of the heart either through coronary artery bypass surgery, transmyocardial laser revascularization, or other means. While these treatments can effectively reduce the mortality rate (Fisher et al., 2014), some heart tissue damage will be serious enough to advance into HF. Pharmaceutical interventions such as beta blockers mainly help manage symptoms but not prevent disease progression (Liew, Ho & Soh, 2020).

Stem-cell therapy has shown potential for therapeutic effects (Eschenhagen et al., 2017), but so far the benefits have been limited (Fisher et al., 2015), predominantly by high levels of early-stage cell washout and death in existing delivery methods such as direct myocardial injection (Chong & Murry, 2014) with

the marginal improvement attributed to paracrine effects promoting repair and regeneration. In order to better improve cardiac function, the transplanted cells need to integrate structurally and functionally with the host tissue, such that their individual contraction enhances the overall cardiac contractile function. When these functions are not fulfilled, stem-cell transplantation can result in independent contraction of the graft cells, leading to arrhythmia-based complications (Shiba et al., 2016). The observation and characterization of electromechanical interaction between graft and host tissues are crucial for the evaluation of stem-cell integration and the potential of stem cell regenerative therapy.

Imaging calcium dynamics in cardiomyocytes

Calcium cycling in cardiomyocytes is a central element to cardiac EC-coupling, and the creation of contraction and relaxation. Hence, optical mapping of calcium dynamics in cardiac cells, tissues and entire hearts is a useful tool for studying the function of the heart in health and disease (Jaimes et al., 2016). For example, fluorescence imaging with calcium-sensitive probes has facilitated the understanding of the mechanism of EC-coupling (Fabiato & Fabiato, 1979) and showed how it is modified in HF (Song et al., 2006). Despite the many technical developments helping advance optical mapping of calcium changes in the heart, many challenges remain, such as motion artefacts from contraction, imaging limitations such as scattering, SNR and resolution (Herron, Lee & Jalife, 2012; Muellenbroich et al., 2021).

The visualization and quantitative analysis of fast calcium dynamics in correlation with the cell microstructure requires imaging methods capable of high-speed multidimensional imaging at subcellular resolution. Imaging calcium dynamics in multicellular culture and tissue necessitates techniques capable of achieving high and isotropic spatial resolution, and the ability of rapid volumetric imaging. The optical sectioning capabilities, low phototoxicity and parallelized widefield acquisition of light-sheet fluorescence microscopy make it a suitable technique for these applications.

1.5. Summary

The aim of this introductory chapter was to provide the general background for the key topics and themes of this thesis. While fluorescence microscopy has found wide use across biology, its application to live cell imaging comes with a range of challenges. These include sample health considerations, practical constraints related to availability, accessibility or quality of required technology and equipment, and fundamental optical limitations, such as diffraction and the restricted photon budget from fluorescence.

Light-sheet fluorescence microscopy tackles many of these challenges to provide gentle, optically sectioned imaging, and the flexibility of the technique has enabled its application to a range of biological systems. Having already been applied to imaging whole beating hearts and calcium dynamics within single cardiomyocytes, it has the potential to not only help address unanswered questions about cell and tissue physiology in health and disease, but also study the mechanism and efficiency of regenerative

therapy. However, the acquisition speed, optical efficiency and resolution of previous systems limited its applicability for fast multidimensional imaging at sufficiently high resolution, FOV and SNR for quantitative analysis of dynamics.

This thesis describes the concepts, design and function of remote-refocusing light-sheet fluorescence microscopy and its application to high-speed imaging of calcium dynamics in cardiomyocytes. In the next chapter (**Chapter 2**), various approaches to high-speed volumetric imaging are introduced, the advantages of aberration-free remote refocusing are presented, and the system design and operation are described in detail. **Chapter 3** characterizes the system's spatial resolution and optical sectioning, comparing the experimental quantification with the theoretical and simulated performance.

Next, the thesis describes two biological applications of the system and the resultant findings. In **Chapter 4**, high-speed two-dimensional LSFM is used for imaging calcium dynamics in left and right ventricle cardiomyocytes in correlation with the cell structure, and in **Chapter 5**, remote refocusing LSFM is used for high-speed volumetric imaging of calcium dynamics in induced pluripotent stem cell-derived cardiomyocytes (iPSC-CM), iPSC-CM co-culture with adult cardiomyocytes, and in live myocardial tissue slices (LMS).

2 Design and operation of remote refocusing LSFM system

2.1. Introduction to high-speed volumetric imaging

Achieving an understanding of the function of biological systems requires observation of the complex sub- and inter-cellular dynamics. One of the key goals of modern optical microscopy is to enable gentle high-speed volumetric imaging of living cells with sufficiently high spatio-temporal resolution and signal-to-noise ratio to allow visualization and quantitative analysis of these dynamics.

Three-dimensional data acquisition can be done using conventional or scanning microscopes, whose equivalence is a consequence of the Helmholtz principle of reciprocity (Sheppard & Wilson, 1986). Faster 3D acquisition can be achieved by increasing the scanning speed of a point-, line-, or plane-scanning probe, or by parallelizing the acquisition of the whole volume (Fig. 2.1). Hence, broadly, fluorescence microscopes designed for multidimensional image acquisition can be grouped into two main categories of increasing scan dimensionality: those implementing sequential data acquisition using a scanner, and those implementing camera-based parallelized data acquisition (Mertz, 2019).

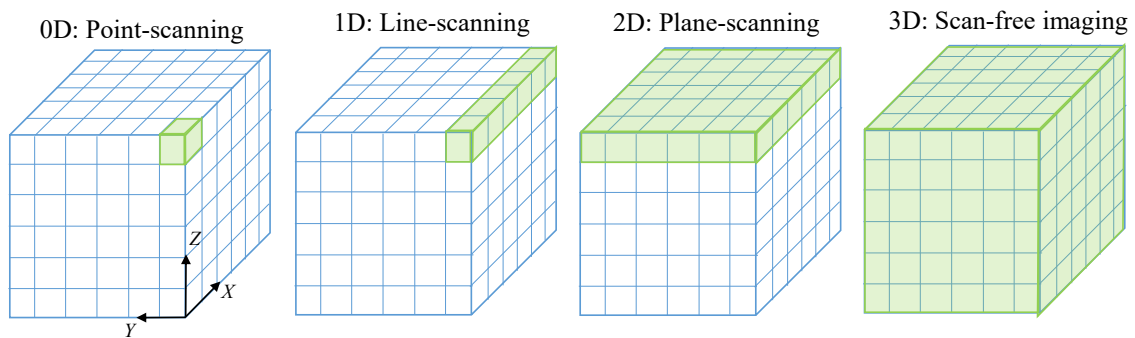


Figure 2.1 3D data acquisition modes using point-, line-, plane-scanning and scan-free volumetric imaging.

2.1.1. Lateral scanning-based approaches

Scanning-based approaches build up 3D images through the lateral and axial translation of a probe volume in object space. Methods such as confocal and multi-photon microscopy benefit from inherent optical sectioning by rejecting or not exciting out-of-focus fluorescence, however, achieving high-speed volumetric imaging requires technology enabling fast scanning in 3D. The lateral pixel-by-pixel scan of the illumination and simultaneous “descan” of the detection in a point-scanning microscope is typically achieved through beam deflection with resonant galvanometric scanners or inertia-free acousto-optic deflectors (AODs) (Im et al., 2005).

In line-scanning confocal microscopy (Maurice, 1974), point illumination and detection is extended to a line, hence eliminating the need for scanning in one of the two lateral directions. This parallelization comes at the cost of confocal rejection of out-of-focus fluorescence and the improvement in lateral resolution being limited to only one of the two lateral dimensions. In addition to 2D-image acquisition,

line-scanning can also be used to acquire x-t data without any lateral scanning for faster imaging within a fixed line.

To achieve faster imaging rates, confocal acquisition has been parallelized in standard (Egger & Petráň, 1967), and microlens-enhanced (Favro et al., 1992) spinning disc-based systems, where the simultaneous scanning of a series of pinholes enables imaging rates at several hundred frames per second (fps). However, the fixed pinhole dimensions in spinning disk confocal microscopes makes them less flexible for varying imaging conditions.

Programmable array microscopes (PAM) (Vliet, 1998) use electronically controlled digital micromirror devices (DMDs) (Hanley et al., 1999) or liquid crystal spatial light modulators (SLMs) (Smith et al., 2000) to generate arbitrary illumination and detection patterns equivalent to scanned pinholes, without any moving parts for the 2D image acquisition. Fiolka et al. (2007) extended the virtual pinhole concept to line-scanning confocal microscopy by implementing a scanned virtual slit aperture on a CCD camera in a slit-scanning confocal microscope (Fiolka, Stemmer & Belyaev, 2007). Confocal slit detection has also been implemented with scanned light-sheet fluorescent excitation by synchronizing it with the “rolling shutter” on a sCMOS camera for improved optical sectioning and SNR (Baumgart & Kubitscheck, 2012; Silvestri et al., 2012).

For sparse fluorescent samples, data acquisition can be sped up through random access microscopy, where only regions of interest (ROI) are imaged. This method has proven useful for imaging neurons, with the fast switching between the ROIs achieved using AODs (Reddy et al., 2008), however, the approach requires a preliminary overview of the sample to locate relevant ROI. When the fluorescent object distribution is not sparse, or changes with time, it is preferable to acquire data from the full FOV.

2.1.2. Camera-based approaches

Camera-based strategies for fluorescence microscopy involve the projection of 2D object planes orthogonal to the optical axis onto the 2D camera sensor. Sample information along the axial dimension can then be obtained by axial scanning of the focus (refocusing), by multiplexing several focal planes at the same time, or implementing extended DOF strategies.

Axial refocusing

The straight-forward method for axial refocusing through the relative translation of the sample with respect to the detection objective is limited in speed due to the inertia of the scanned element(s) and the power of the actuator. Additionally, mechanical movement of the sample or primary objective can introduce unwanted disturbance of the specimen. These challenges can be overcome by introducing additional elements in a remote location of the optical path that achieve refocusing with little or no associated inertia. Transmissive variable optical elements such as electrically tuneable lenses (ETLs) can reach kHz refocusing rates (Oku, Hashimoto & Ishikawa, 2004) and have been used for fast remote

refocusing light-sheet fluorescence microscopy at 30 Hz (Fahrbach et al., 2013). Tunable acoustic gradient (TAG) index of refraction lenses have also achieved refocusing with $\sim 1\mu\text{s}$ switching times (Mermillod-Blondin, McLeod & Arnold, 2008), however, both ETLs and TAG lenses only apply lower order defocus of the wavefront and are unable to correct for the higher order aberrations introduced with high-NA defocus (Kang, Duocastella & Arnold, 2020), hence limiting the axial refocus range for diffraction-limited imaging.

As an alternative to transmissive elements, refocusing can be achieved using reflective elements such as liquid crystal SLMs (Dal Maschio et al., 2011) placed in the Fourier plane. However, their wavefront phase modulation is limited up to 2π , and hence larger amounts of defocus requires phase wrapping, which introduces discontinuities between adjacent pixels, reducing the optical efficiency. In a more recent implementation by Yang et al. (Yang et al., 2021), the same SLM as used to achieve remote refocusing in a two-photon fluorescence microscope was also used for aberration correction to compensate for the reduced brightness at larger defocus. The use of liquid crystal SLMs for remote refocusing in the detection path is further limited by their polarization and chromatic dependence, making them more suitable for wavefront shaping and refocus of polarized and narrowband laser illumination, rather than of fluorescence emission.

Deformable mirror (DM) micro-electro-mechanical systems (MEMS) are continuous or segmented reflective surfaces whose shape can be changed to control the wavefront of the reflected light. Unlike ETLs and most TAG designs, DMs are capable of producing more complex wavefronts suitable for refocusing in high-NA systems. Additionally, the minimal light loss, polarization invariance and compatibility with broadband fluorescence emission have enabled the use of DMs for extended depth-of-field (EDOF) imaging (Shain et al., 2017) simultaneous motionless focusing and aberration correction in the detection path (Kner et al., 2010), active focus locking in a confocal microscope (Poland, Wright & Girkin, 2008) and remote-refocusing for fast volumetric imaging in a two-photon microscope (Žurauskas et al., 2017). Using a configuration similar to that by Shain et al. with the DM placed in the pupil plane (Shain et al., 2017) (**Fig. 2.2**), Wright et al. demonstrated rapid remote refocusing at 26.3 Hz over a 100 μm defocus range through continuous mirror oscillation (Wright et al., 2021), with potential for faster sweep rates and implementation for high-speed remote refocusing in light-sheet fluorescence microscopy for video-rate volumetric imaging.

In addition to the rapid remote refocusing enabled by the DM's low inertia and fast update rates, deformable mirrors can simultaneously correct aberrations (Žurauskas et al., 2017). However, a more direct way of achieving remote-refocusing and simultaneously cancelling defocus-induced aberrations was proposed and first implemented by Botcherby et al., where a second microscope relay is used to form an intermediate image, that is then reimaged onto the detector (Botcherby et al., 2007). Refocusing

is done in remote image space, without any direct disturbance of the sample. The concept, advantages and limitations of aberration-free remote refocusing are further discussed in **Section 2.1.3**.

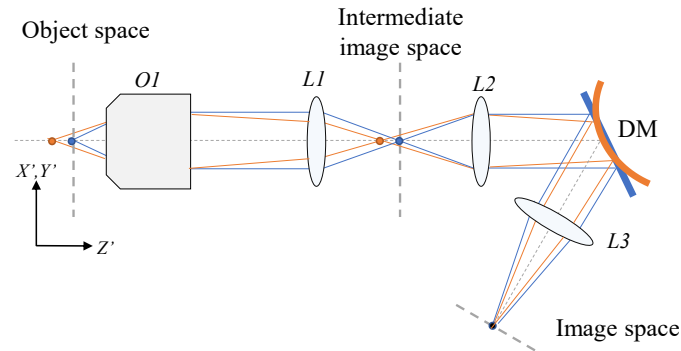


Figure 2.2 Microscope system for remote refocusing or EDOF-imaging with a DM. Applying a high numerical aperture defocus (orange, in bold) to the DM, placed in the Fourier plane, achieves refocusing of the emission from sample planes outside of the native focal plane of the primary detection objective onto the detector plane in image space.

Synchronized scanning of illumination and detection

In LSFM implementations, volumetric acquisition requires the co-registration of the light-sheet and the detection focal plane. For these applications, scanning geometries that enable automatic synchronization of the illumination and detection planes are advantageous. Implementations of single objective light-sheet (SOLS) approaches such as oblique plane microscopy (OPM) (Dunsby, 2008) achieve this using the same scanning optics for excitation and emission light: the original configuration achieves tilt-invariant axial scan through axial translation of the remote objective with a piezo-electric actuator (**Fig. 2.3a**) (Kumar et al., 2011; Sikkell et al., 2016a).

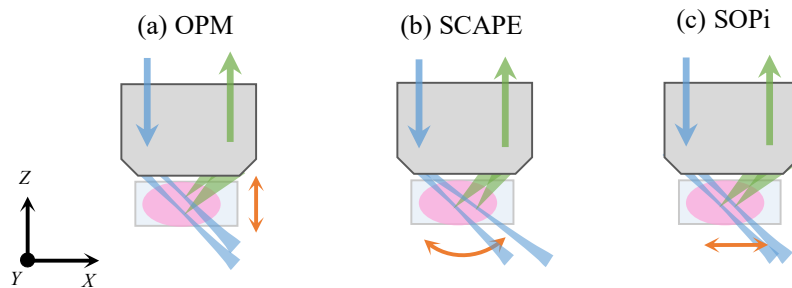


Figure 2.3 Scan geometries in single-objective light-sheet approaches. (a) Tilt-invariant z-scan in OPM. (b) Tilt-variant x-scan in SCAPE. (c) Tilt-invariant x-scan in SOPi, SCAPE 2.0 and other SOLS configurations. Light-sheet illumination is indicated in blue, and the detected fluorescence in green.

Lateral scanning of the illuminated and detected plane in a SOLS configuration was first implemented using a reflective polygon scanner in swept confocally-aligned planar excitation (SCAPE) (Bouchard et al., 2015), however, this introduced a position-dependant tilt variation in the light sheet (**Fig. 2.3b**), leading to non-isotropic FOV and resolution. Scanned oblique plane illumination (SOPi) microscopy (Kumar et al., 2018) implements synchronized tilt-invariant lateral scanning of the illumination and detection planes in a SOLS system (**Fig. 2.3c**) using a plane mirror scanner, positioned with its rotation

axis intersecting the scan lens' principal axis and the back focal plane (BFP). This tilt-invariant scanning configuration (Kumar & Kozorovitskiy, 2020) has also been implemented in diffractive OPM (Hoffmann & Judkewitz, 2019) and SCAPE 2.0 (Voleti et al., 2019).

Multifocus, extended depth-of-field and light field microscopy

Unlike the sequential acquisition of a stack of images through the axial scanning of focus, multi-focus approaches achieve simultaneous acquisition of different planes within the sample. This concept has been realized through a variety of implementations, including using one or multiple beamsplitters in the emission path to image different planes within the sample with axially displaced cameras (Prabhat et al., 2004), and by multiplexing axially displaced focal planes onto the same detector with lateral displacement introduced using a diffractive optical element (DOE) (Blanchard & Greenaway, 1999). Chromatic correction for the dispersion introduced by the DOE can be achieved using a second chromatic correction grating together with a refractive prism (Abrahamsson et al., 2013).

Extended depth-of-focus (EDOF) imaging is an alternative to axial scanning of the focal plane, or simultaneous acquisition at multiple depths in cases where a projection of the sample, rather than a 3D volume, is required. In EDOF microscopy, the focus is elongated in the axial direction, and 2D images acquired at different depths are super-imposed, losing all axial resolution. EDOF imaging can be achieved either by scanning the focus within the camera exposure time (Shain et al., 2017) or by extending the point-spread function (PSF) axially by modulating the detected wavefront using annular masks in the pupil plane (Welford, 1960). EDOF imaging suffers from accumulating out-of-focus fluorescence with increasing axial range, which can be suppressed using 3D deconvolution, or by combining the EDOF detection with SPIM illumination (Duocastella et al., 2017).

A different approach to obtaining 3D data with a 2D sensor is through light-field microscopy, which is typically implemented with a microlens array placed an intermediate image plane, and a camera in the Fourier plane of the lens array (Levoy et al., 2006). The recorded light-field distribution containing both the spatial location and propagation direction of the object's fluorescence can be used to compute the intensity distribution of the object with axial displacement, allowing computational focusing and generation of a 3D dataset. However, the directional information comes at the cost of lateral spatial resolution: acquiring more angular resolution for each sampled point requires a larger diameter for each lenslet, hence reducing the spatial sampling of the object (Broxton et al., 2013).

Both for approaches that use lateral scanning to build up each image, and those that employ parallelized camera-based acquisition, the development of techniques for faster imaging will need to tackle the more fundamental issue of signal-to-noise ratio in fluorescence imaging. This challenge can be tackled from multiple directions, including through the development of brighter, non-phototoxic and photostable fluorescent probes, improved computational reconstruction, techniques for increased optical

throughput, development of detectors with improved quantum efficiency and application of computational techniques for targeted data processing and analysis.

2.1.3. Aberration-free remote refocus

In a radially symmetrical optical system, perfect three-dimensional imaging is achieved when the system can form a stigmatic (aberration-free) image of any point within a 3D volume, such that all rays from that point converge to a single point in image space (Botcherby et al., 2008). For an optical system where the immersion media of object and image space have refractive indices (RI) n_1 and n_2 respectively (**Fig. 2.4a**), this requires the magnification in all directions to have a magnitude of (Maxwell, 1858):

$$|m| = \frac{n_1}{n_2} \quad (2.1)$$

It has been shown (Born & Wolf, 1980), that in a perfect imaging system, this means the ray originating from a single point in object space, and its conjugate ray going through the image origin, travel with the same angle w.r.t the optical axis, i.e., that:

$$\theta_2 = \pm \theta_1 \quad (2.2)$$

Most microscope are designed to obey the sine condition (Abbe, 1881), which ensures perfect imaging of on- and off-axis points within a small region of the focal plane, and states that the sine of the object-space angle θ_1 is proportional to the sine of the image-space angle θ_2 such that:

$$n_1 \sin \theta_1 = m_l \times n_2 \sin \theta_2 \quad (2.3)$$

where m_l is the lateral magnification from object space to image space. For ideal 3D imaging, points along the optical axis that are displaced from the focal plane need to be imaged perfectly. This is fulfilled for a system obeying the Herschel condition (Born & Wolf, 1980; Steward, 1927), which imposes a complementary relation between the conjugate ray angles w.r.t the optical axis:

$$n_1 \sin^2(\theta_1/2) = m_a \times n_2 \sin^2(\theta_2/2) \quad (2.4)$$

Here, m_a is the axial magnification from object to image space. For a system obeying the sine condition, if the lateral magnification is equal to $m_l = n_1/n_2$, Eq. 2.3 reduces to Eq. 2.2. Similarly, for a system designed to fulfil the Herschel condition, if the axial magnification is equal to $m_a = n_1/n_2$, Eq. 2.4 simplifies to Eq. 2.2. In both cases, this enables perfect imaging of the 3D object space.

The conventional arrangement for a high-NA microscope, consisting of a high-NA objective lens, tube lens and a detector, is commonly designed to satisfy the sine condition (Born & Wolf, 1980), which ensures perfect imaging of points within the focal plane of the objective (orthogonal to the optical axis).

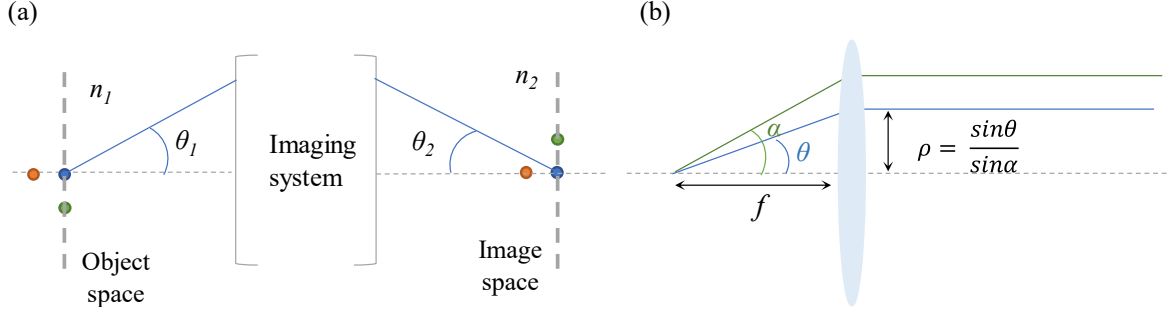


Figure 2.4 (a) Imaging system with refractive indices n_1 and n_2 and ray angles θ_1 and θ_2 in object and image space respectively. (b) Definition of the normalized pupil radius ρ in terms of the ray angle θ and maximum acceptance angle α .

Axial translation of the detector to image out-of-focus planes in a high-NA system introduces spherical aberration which increases rapidly with defocus (Sheppard & Gu, 1991). For a point source on the optical axis located a distance z away from the focal plane, the phase term of the wavefront in the pupil can be written as a spherical function (Sheppard, 1997):

$$\varphi = nkz\sqrt{1 - \rho^2 \sin^2 \alpha} \quad (2.5)$$

where n is the refractive index of the immersion media, $k = 2\pi/\lambda$ is the free-space wavenumber, and ρ is the normalized pupil coordinate, which under the sine condition equates to:

$$\rho = \frac{\sin\theta}{\sin\alpha} \quad (2.6)$$

where θ is the angle of the ray from the sample relative to the optical axis, α is the semi-aperture angle of the objective with a numerical aperture of $NA = n\sin\alpha$ (Fig. 2.4b). Expanding the term in the square root in Eq. 2.5 shows that the high-NA defocus phase profile is composed of a paraxial term ρ^2 and decreasing amounts of primary and higher-order spherical aberration (Botcherby et al., 2008):

$$\varphi = nkz \left(1 - \frac{\rho^2 \sin^2 \alpha}{2} + \frac{\rho^4 \sin^4 \alpha}{8} + \dots \right) \quad (2.7)$$

Only the paraxial ρ^2 term can be compensated by defocusing from the conventional image plane of the tube lens. The higher order terms in high-NA defocus cannot be focused by the tube lens, which leads to loss of stigmatic imaging for points in the sample away from the focal plane. Hence, achieving remote refocusing in a high-NA system requires an equal but opposite phase term to Eq. 2.7 in order to compensate for the high-NA defocus aberrations.

The odd parity property of the pupil function states that the phase distribution for a source placed at point \vec{r} will be equal and opposite to that from a source at $-\vec{r}$. Combining this property with the reciprocity of ray optics, it can be inferred that, if the pupil function of a first lens is imaged onto the pupil function of a second reversed lens, then the rays from any point source (displaced from object

space origin by distances much smaller than the focal length) in object space would converge stigmatically to a point (Botcherby et al., 2008).

These concepts lie at the foundation of system configuration capable of high-NA aberration-free remote refocusing, demonstrated in **Fig. 2.5**. For a perfect imaging system consisting of two microscope systems M1 and M2 arranged to create an isotropically magnified sample volume intensity distribution in remote image space, a third microscope M3 can be used to re-image the copy onto a detector in image space. Axial translation of the third microscope achieves refocusing to different planes within the object, without any disturbance near the sample.

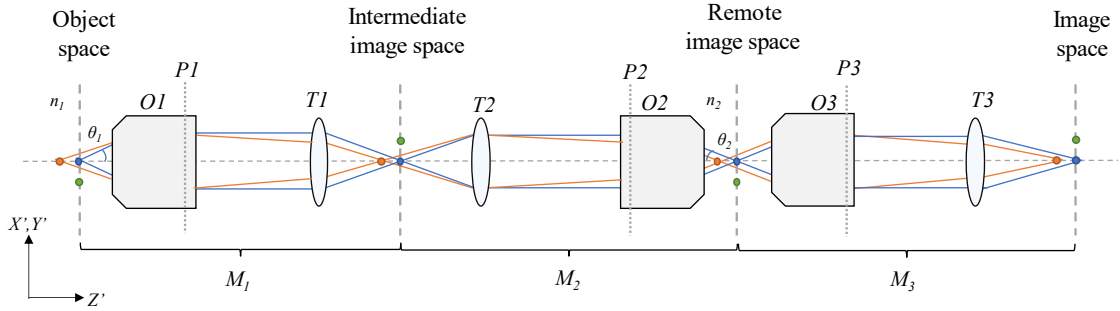


Figure 2.5: Remote refocusing imaging system in unfolded geometry imaging points on (blue, green) and off (orange) the focal plane of the primary objective. The relay consists of three microscope systems M1-3, each composed of objectives O1-3 with back focal planes P1-3 and tube lenses T1-3 respectively. The first microscope M1 forms an intermediate image of the object with magnification m_1 , which is reimaged by the second microscope M2 at magnification m_2 . The third microscope M3 forms the final image on the detector, with the overall magnification equal to $m_1 \times m_2 \times m_3$. Figure has been adapted from similar schematics used by (Mohan & Corbett, 2021) and (Botcherby et al., 2008).

While the magnification from object space to remote image space must be equal to the ratio of the refractive indices of the respective immersion media (Eq. 2.1), the objectives O1 & O2, tube lenses T1 & T2 and immersion media n_1 and n_2 of microscopes M1 & M2 don't have to be identical. When the lenses are set up in a 4f arrangement such that the pupil plane P1 of objective O1 is mapped onto P2, the pupil plane of O2, we have (Botcherby et al., 2008):

$$\frac{\rho_2}{\rho_1} = \frac{\sin \alpha_1}{\sin \alpha_2} \quad (2.8)$$

This arrangement is not always possible with commercially available microscopes objectives and tube lenses. A further complication is that while certain objectives are designed for optimal performance together with a specific tube lens, jointly achieving correction of specific aberrations, this may interfere with stigmatic imaging of the first pupil onto the second. The overall resolution of the refocusing system will be set by the limiting angular aperture of the system α_{max} . The effective system NA is then related to this angular aperture by projecting it back into object space: $NA_{eff} = n_1 \sin \alpha_{max}$.

A limitation in the three-objective configuration demonstrated in **Fig. 2.5** for remote refocusing is the speed with which O3 can be axially translated. The work by Botcherby et al. (Botcherby et al., 2008) also presented an alternative, optically equivalent folded remote refocusing arrangement (**Fig 2.6**), where a mirror is placed in the focal plane of the second objective O2, and a beam splitter is introduced before O2. The second objective is then used twice: as part of M2, to cancel the aberrations introduced by O1 and form a perfect image in remote space, and as part of M3, forming the final image on the detector. Since the image formed in remote image space will be of comparable dimensions to the object, the remote refocusing mirror can be small, enabling faster axial scanning than by translating O3, and hence more rapid remote refocusing. The speed improvement comes at the cost of lower collection efficiency from the introduction of a beam splitter: for a polarized beam splitter used together with a quarter waveplate, the maximum light throughput for unpolarized fluorescence signal during double-pass through the beam splitter is 50%.

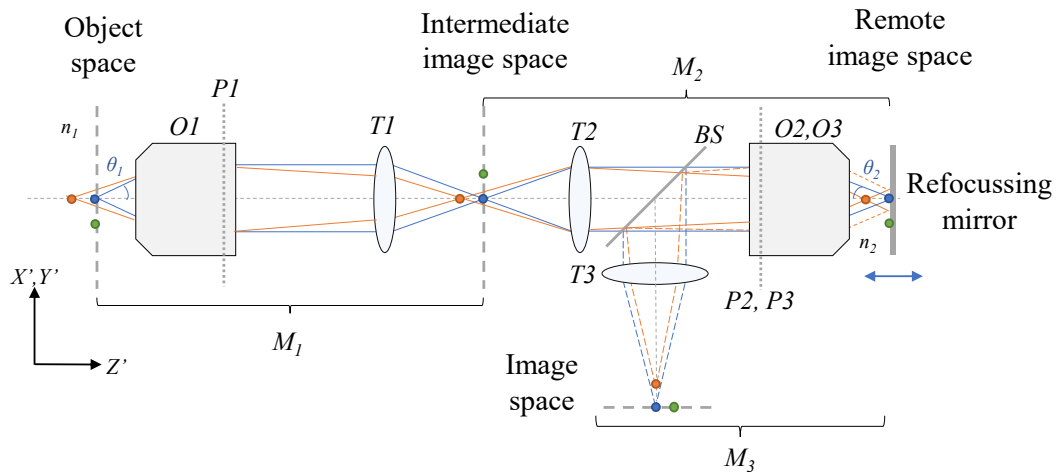


Figure 2.6 Folded configuration for aberration-free remote refocusing system, imaging points on (blue, green) and off (orange) the focal plane of the primary objective O1. In this geometry, a mirror is introduced into remote refocusing space. Objective O2 is used twice, first to cancel aberrations introduced by O1, forming an image in remote image space, and then as part of the third microscope together with tube lens T3, forming the final image on the detector in image space. Axial translation of the refocusing mirror allows imaging of different planes within the sample, building up a 3D volume.

A further limitation is the operational range of the remote refocus: for larger displacements, higher order terms within the expansion of the phase contribution of each objective lead to loss of stigmatic imaging (Botcherby et al., 2008). Theoretical calculations for a 60 \times 1.4 NA oil immersion objective, for a wavelength of 633 nm demonstrated a Strehl ratio > 0.8 for $\pm 70 \mu\text{m}$ axial displacement of a point source, while experimental PSF intensity measurements gave a constant Strehl ratio over $\pm 35 \mu\text{m}$ in object space (Botcherby et al., 2008).

A practical difficulty in the implementation of the remote-refocusing system proposed by Botcherby et al. is the challenge of optimal alignment of high-NA objectives. Recent work by Mohanan and Corbett investigated the sensitivity of remote refocusing performance to magnification mismatch through

computational modelling and experimental measurement of residual first order spherical aberration (Mohanani & Corbett, 2021). The results indicated a high sensitivity of remote refocus performance to magnification mismatch, with a 1% difference in the ratio of the actual lens magnification to ideal magnification resulting in a 50% drop of the dynamic range (defined as the axial range with a Strehl ratio greater than 0.8). Lower NA objectives will tolerate higher levels of magnification mismatch. The sign of spherical aberration from measured axial PSF profiles on either side of the focal plane can be used to identify whether ideal magnification conditions are satisfied, with the sign of spherical aberration on either side of the axial focus remaining unchanged for a system with ideal magnification (Mohanani & Corbett, 2021).

Aberration-free remote refocus has been implemented for fast axial scanning in multiphoton fluorescence microscopy of neuronal activity (Botcherby et al., 2012), spinning disc confocal microscopy (Gintoli et al., 2020), OPM (Dunsby, 2008) and other techniques – see (Millett-Sikking, et al., 2018) for a comprehensive review.

2.1.4. Alternatives to 3D imaging

While 3D imaging provides a more complete representation of the studied object, for certain applications, 2D imaging can be sufficient and preferable due to less data volume and faster acquisition speed. Since planes perpendicular to the optical axis are imaged with higher resolution than those parallel to it, conventional 2D scanning microscopes typically image the focal plane of the objective. However, for some types of samples, the plane of interest is orthogonal to the tissue surface. Accessing this plane in a conventional optical system configured for 2D image acquisition would require sample re-orientation, which can be incompatible with its viability or structural integrity, and result in reduced imaging quality due to sample induced aberrations from the longer optical path.

Direct imaging of the meridional plane has been achieved using a modified configuration of the folded aberration-free remote refocusing layout of the scanning confocal (Botcherby et al., 2009). This implementation combined line illumination with slit scanning along the optical axis through axial remote refocusing by mirror translation in refocusing space. The synchronized tilt of a galvo mirror conjugate to the BFP of the detection objective allowed lateral translation of the slit image onto a 2D CCD detector, achieving line-by-line imaging of the meridional plane onto the camera.

In axial plane optical microscopy (APOM), direct meridional plane imaging is combined with light-sheet illumination through the same lens as the detection (Li et al., 2014). A mirror tilted by 45° placed in remote refocusing space achieved 90° rotation of the 3D image (**Figure 2.7**). The axial cross-section of the sample is transformed into a lateral plane with respect to the remote refocusing lens, and can be directly imaged onto the detector, without the need for line scanning. The mirror tilt can be adjusted for imaging arbitrary planes within the sample, at the cost of resolution and collection efficiency and an asymmetric PSF due to image rotation and reduction in effective NA.

Digital confocal light-sheet axial plane optical microscopy (DC-APOM) (Yordanov et al., 2021), a recent extension of the above technique, uses digitally scanned Bessel and Gaussian light-sheet illumination with confocal slit sCMOS detection, demonstrating 3D live-cell imaging with conventional sample mounting. However, the drawback of signal and resolution loss as a result of aperture clipping remains, and the system geometry is highly sensitive to misalignment and RI mismatch in the sample medium.

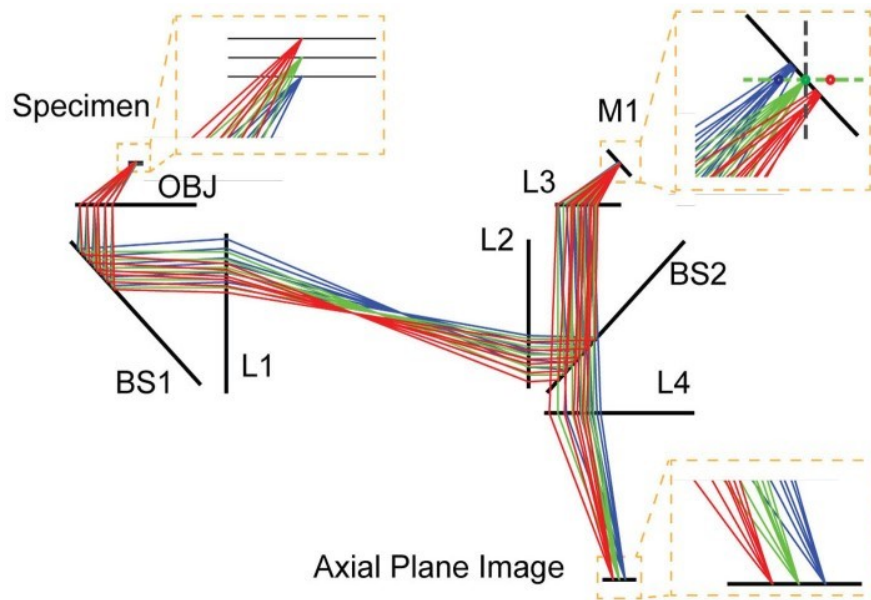


Figure 2.7 Axial plane optical microscopy. Ray tracing optical diagram for the detection path in APOM. An aberration-free intermediate image of the fluorescence emission from different points along the meridional plane of the specimen is formed by the optical relay consisting of the detection objective (OBJ) and lenses L1-3. A mirror tilted at 45 degrees w.r.t the optical axis of LS reflects the intermediate image, with lenses L3-L4 imaging the axial plane onto the detector. Beam splitter BS1 is used to couple in the illumination, and BS2 enables folded reflection of the meridional plane. Reproduced under CC-NC-ND 4.0 International License from (Li et al., 2014).

Multi-angle Projection Imaging

Another alternative to volumetric imaging is multi-angle projection imaging. In the work by (Chang et al., 2021), optical shearing of a 3D data stack laterally across the detector during a single camera exposure achieves projected 2D-viewing of the 3D object from a variable angle perspective. The main working principle of the projection method is an adaptation of the shear-warp transform (Lacroute & Levoy, 1994) – an algorithm in computer vision for faster volume rendering which makes use of the mathematical equivalence between the scaled two-dimensional projections of a rotated and sheared volume (**Fig. 2.8**). The transformations can be modelled as a series of matrix operations. Using the same coordinate geometry and variables as the authors (Chang et al., 2021) we consider a volume projected along the y-axis, and rotated about the z-axis by θ . The projection P of the rotation matrix R can be written as

$$PR = \begin{bmatrix} 1 & 0 \\ 0 & 0 \end{bmatrix} \begin{bmatrix} \cos\theta & -\sin\theta \\ \sin\theta & \cos\theta \end{bmatrix} = \begin{bmatrix} \cos\theta & -\sin\theta \\ 0 & 0 \end{bmatrix} \quad (2.9)$$

The principle behind the shear-warp transform states that this should be equivalent to the scaled projection along the y-axis of a volume sheared along the x-axis by the shear factor α . The projection P of the shear matrix S , scaled in x by S_x and in y by S_y through multiplication with scaling matrix M can be written as (Chang et al., 2021):

$$MPS = \begin{bmatrix} S_x & 0 \\ 0 & S_y \end{bmatrix} \begin{bmatrix} 1 & 0 \\ 0 & 0 \end{bmatrix} \begin{bmatrix} 1 & \alpha \\ 0 & 1 \end{bmatrix} = \begin{bmatrix} S_x & \alpha S_x \\ 0 & 0 \end{bmatrix}. \quad (2.10)$$

The two expressions (Eq. 2.9 and Eq. 2.10) will be equal when $S_x = \cos\theta$, and $\alpha = -\tan\theta$. In one of the authors' implementations, the lateral shearing is realized using a lens-less scan unit consisting of two galvanometric mirrors positioned directly in front of the sCMOS detector. Synchronous rotation of the two mirrors results in lateral sweeping of the image across the sensor without introducing any overall angular change in the beam path. By synchronizing the lateral sweeping with the axial scanning of the focal plane, the sheared image stack is acquired during a single exposure, with the resultant 2D projection of the sheared image stack equivalent to a stretched projection of the rotated 3D volume. The viewing angle θ can be adjusted by modifying the amount of shear by changing the amplitude of the galvo mirror sweep. Correction of the introduced one-dimensional stretch of $1/\cos\theta$ can be implemented computationally and can be considered negligible for small angles where $\cos\theta \sim 1$.

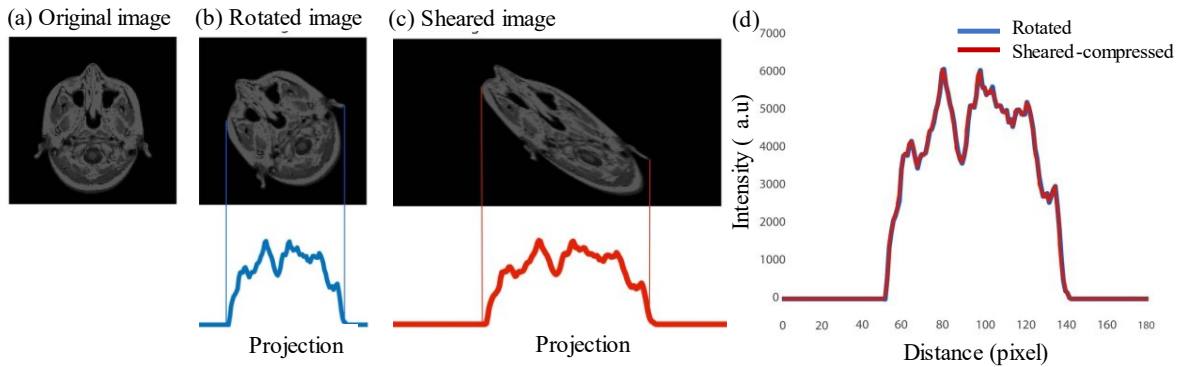


Figure 2.8 Equivalence of the scaled projections of rotated and sheared volumes demonstrated through numerical simulation. (a) The original 2D image (b) Rotation and sum-projection of ‘a’ along the vertical axis. In (c), image ‘a’ is sheared along the horizontal axis, and projected along the vertical axis. (d) Compressing the projection of the sheared volume gives an equivalent profile to the projection of the rotated image. Minor differences between the two profiles are attributed to numerical errors in the shearing and rotational transformation. Adapted and reproduced with permission from (Chang et al., 2021).

Unlike EDOF techniques, the projection method integrates slices imaged with a diffraction-limited detection PSF that has not been axially stretched, which means that for an image stack with n planes, the Strehl ratio is n -fold higher compared to EDOF (Chang et al., 2021). When combined with SPIM, each slice within the underlying volume has been blurred with a point spread function axially modulated by the light sheet profile.

In an optically sectioning microscope, the projection method can be used for improved sample navigation by simultaneous viewing of the whole projected volume, and real-time adjustment of the viewing angle. By using a beam splitter to relay part of the detected signal onto a second camera, multiple perspectives can be acquired simultaneously, enabling real-time stereoscopic rendering of the object. Additionally, combining information from projections taken at different viewing angles can be used to directly reconstruct 3D information in sparse objects. The lateral shearing can also be used to optically de-skew data acquired in a diagonal scan of the sample relative to the optical axis.

Acquiring the whole volume projection consisting of n images within a single frame offers n -fold speed improvements in cases where volume acquisition rate is limited by the frame rate of the camera. The authors demonstrated projection imaging using both the two-galvo-based shear unit, and a single galvo mirror in the Fourier plane, in commercial and custom-built spinning disc confocal and light-sheet systems, achieving up to 119 Hz acquisition rate, limited by the camera exposure time and sample brightness.

The method comes with trade-offs and limitations: the sum-intensity projection method is more suitable for low-background data since higher levels of background will eventually conceal low-contrast features of interest. Another potential drawback is the sensor size required to accommodate the sheared image, which limits the useable FOV in one of the lateral dimensions. Finally, sheared projection imaging at a single viewing angle results in loss of 3D information of the sample and is hence not compatible with quantitative 3D image analysis normally applicable to optically sectioned imaging.

2.2. System description

The optical set up of the inverted dual-objective flexible light-sheet fluorescence microscope is shown in **Figure 2.9**, with a photo of the system and a full list of parts is provided in **Figure A2.1** and **Table A2.1 (Appendix A2)** respectively. The original system was designed and constructed by Dr. Hugh Sparks and Prof. Chris Dunsby (Photonics Group, Dept of Physics). Modifications of the original configuration included introduction of dual-channel image splitter and implementing correction of Fluo-4 defocus (described in **Section 2.2.1**), and implementation of customized sample mounting for single cell, culture and tissue imaging. The system is mounted on a rotatable breadboard for easy conversion between vertical and horizontal configurations for optical alignment and compatibility with different types of samples. The microscope implements two complementary acquisition modes to achieve higher temporal and spatial resolution respectively. The first mode employs multi-directional selective plane illumination microscopy (mSPIM) (Huisken & Stainier, 2007), where light-sheet illumination is achieved using an angularly dithered Gaussian beam focused in one lateral direction. Combined with remote refocus of the detection plane, this mode is used for high-speed volumetric imaging. The second acquisition mode implements digitally-scanned light-sheet microscopy (DSLM)

(Keller et al., 2008) illumination with an axially scanned light-sheet waist (ASLM) (Dean & Fiolka, 2014; Gao, 2015) for higher axial resolution.

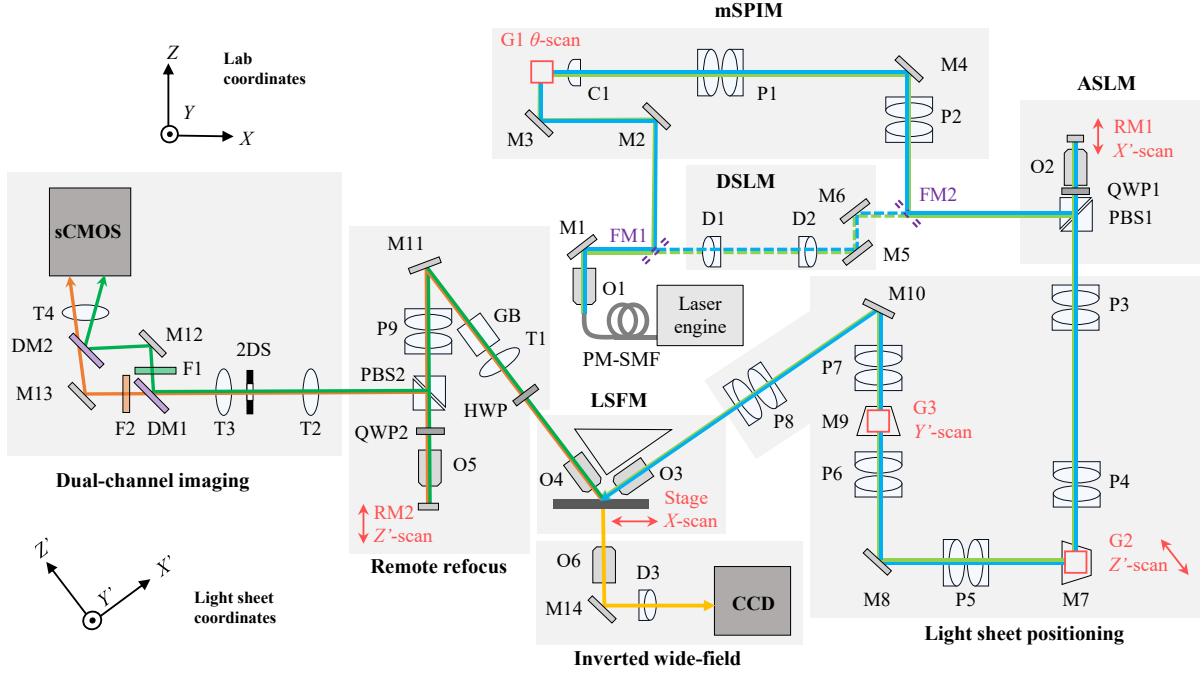


Figure 2.9 Optical system layout diagram. Key microscope element groups are identified with grey boxes: digitally-scanned light-sheet microscopy (DSLM), multi-directional single-plane illumination microscopy (mSPIM), axially swept light-sheet microscopy (ASLM), light-sheet positioning optics, light-sheet fluorescence microscopy (LSFM), remote refocus (RF), dual-channel imaging, and inverted widefield microscope. Other abbreviations denote: polarization maintaining fibre (PM-SMF), objectives (O1-6), broadband dielectric mirrors (M1-14), motorized flip mirrors (FM1-2), achromatic doublets (D1-3), cylindrical lens (C1), galvo-scanning mirrors (G1-3), Plössl doublets (P1-9), polarizing beam splitters (PBS1-2), quarter waveplates (QWP1-2), low-mass mirrors on translation stages (RM1-2), charge coupled device (CCD), half waveplate (HWP), tube lenses (T1-4), glass compensation block (GB), two-dimensional adjustable slit (2DS), dichroic beam splitters (DM1-2), emission filters (F1-F2), scientific complementary metal-oxide semiconductor camera (sCMOS). Cartesian coordinates X-Y-Z and X'-Y'-Z' are used for lab and light-sheet (microscope) coordinate frames respectively.

2.2.1. Optomechanical design

The primary water immersion excitation and detection objectives O3 and O4 are positioned such that their focal points coincide, and optical axes are orthogonal, with the right angle fixed using a custom made monolithic aluminium block. Precise adjustment of the axial position of these objectives is achieved using two micrometre stages attached to the block. The sample is mounted on a 3-axis translational stage arrangement, which itself is attached to a motorized linear translation stage for stage-scanned volumetric acquisition. The mechanical arrangement of the two objectives is such that the mutual focal point is in the horizontal sample plane and no mechanical interference during lateral stage translation is achieved for an angle of $\theta_{LS} \approx 37^\circ$ between the illumination axis and sample plane. A low-magnification wide-field microscope consisting of objective O6, mirror M14, doublet lens D3, and CCD are used for coarse sample positioning and orientation before high magnification imaging.

For image acquisition, the system implements scientific complementary metal-oxide semiconductor (sCMOS) detectors including Hamamatsu Orca Lightning and Hamamatsu Orca Fusion, with square pixel side dimensions of $5.5\ \mu\text{m}$ and $6.5\ \mu\text{m}$ respectively, and respective FOV of 4608×2592 pixels and 2048×2048 pixels. Hardware control and data acquisition is achieved using a HP Z840 Workstation with dual Intel® Xeon® Processors (3.40 GHz, 6 cores each), 128 GB RAM and a pair of 2 TB SSDs (SSD 960 PRO 2TB, Samsung) in software RAID0. The acquisition software used was written in LabVIEW by Dr. Hugh Sparks. Hardware synchronization and triggering (including laser modulation, angular positioning of galvo scanning mirrors, motorized sample stage, and remote refocus linear actuators in illumination and detection) was achieved using a digital acquisition (DAQ) box (USB-6363, NI). Image processing and analysis is carried out in MATLAB and FIJI (ImageJ).

Illumination path

Linearly polarized light from the laser engine is coupled into a polarization-maintaining single-mode fibre (PM-SMF). Objective lens O1 collimates the Gaussian beam output from the fibre. Motorized flip mirrors (FM1 and FM2) are used for remote switching between mSPIM and DSLM light-sheet illumination modes. The optical relays in the DSLM and mSPIM illumination paths are shown in **Figure 2.10**.

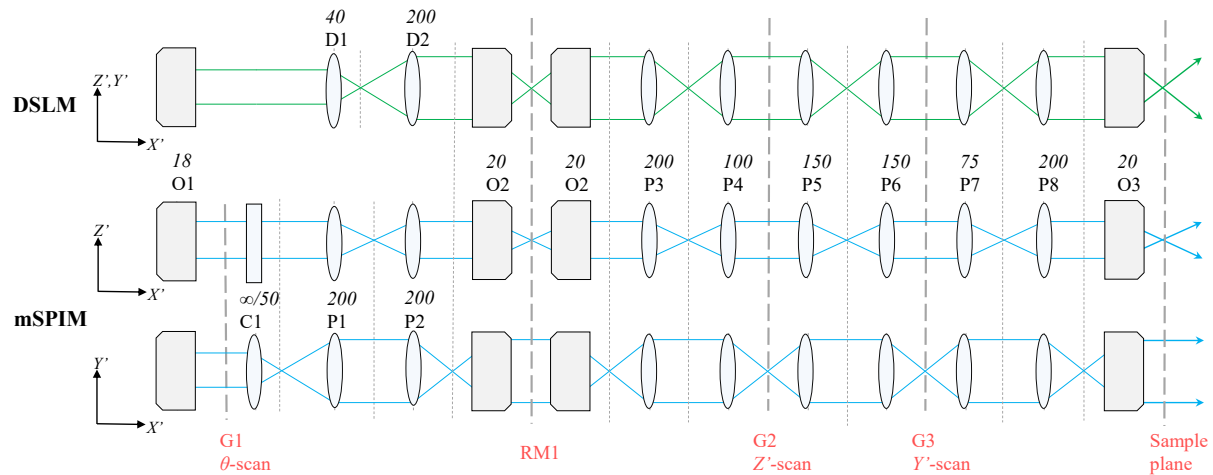


Figure 2.10 DSLM and mSPIM illumination path optical relays. Unfolded optical relays from collimating objective O1 to the sample plane for DSLM (green) and mSPIM (blue) illumination beam paths, which merge before remote refocusing objective O2. The focal lengths of respective optical elements and Plössl lens combinations are given in italic in mm. A beam expander (D1-D2) at the start of the DSLM beam path achieves a tightly focused beam waist in the sample plane. The cylindrical lens C1 in the mSPIM beam path is used to focus the Gaussian beam to a line along Z' in the back focal plane (BFP) of O3, hence achieving a Gaussian light-sheet in the $X' - Z'$ plane. Lateral scanning elements G2 and G3 are placed in the Fourier planes such that their rotation about an axis corresponds to a lateral translation of the light-sheet position in sample space. Meanwhile, the angular scanning element G1 is placed conjugate to the sample plane such that its rotation corresponds to angular dithering of the light sheet about its focus.

In the DSLM beam path, a beam expander consisting of two achromatic doublets (D1& D2) is used to achieve beam magnification by a factor of 5 to fill the back apertures of O2 and O3 for a tightly focused

beam waist in the sample plane. In the mSPIM beam path, the Gaussian beam is only focused in one lateral direction and less tightly than for the DSLM mode by underfilling the back aperture of excitation objective O3. Angular dithering (θ -scan) for removal of shadow artefacts due to sample refractive index (RI) irregularities is achieved using galvo scanning mirror G1, located conjugate to image planes of the ASLM remote refocus objective O2 and excitation objective O3. The beam is focused in one direction using cylindrical lens C1 positioned at its focal length from G1, and conjugate to the BFP of O2 and O3. A 4f relay consisting of Plössl lenses P1&2 with equal focal lengths are used to image the focal plane of C1 onto the BFP of remote refocusing objective O2 with unit magnification.

Folded remote refocusing within the ASLM unit is used to change the position of the beam waist along the illumination axis X' within the sample volume. This is achieved by axially translating the remote scanning mirror RM1, which is mounted on a linear voice-coil stage, away from the nominal focal plane of refocusing objective O2. Optical throughput in the folded remote refocus configuration is maximized by coupling the linearly polarized excitation light from either the mSPIM or DSLM illumination into the ASLM unit using a polarizing beam splitter PBS1. The light then passed through a quarter waveplate QWP1, which converts the linear polarization into circular. Upon reflection off RM1, the handedness is reversed, and after double pass through QWP1, the beam with reversed linear polarization is transmitted through PBS1.

Aberration-free remote refocusing (Botcherby et al., 2008; Botcherby et al., 2007), of the beam waist is achieved by having equal lateral and axial magnification from sample space to remote refocusing space such that $|m| = n_{sample}/n_{remote} = n_{water}/n_{air} = 1.33$. Lateral light-sheet positioning in Z' and Y' directions is achieved using a pair of galvo scanning mirrors G2 and G3 for Z' -scan and Y' -scan respectively. The back focal plane of O3 is demagnified onto G2 using a 4f relay consisting of Plössl lenses P3&4 and reimaged onto G3 at unit magnification by the P5&6 4f relay. Finally, G3 is reimaged onto the back focal plane of excitation objective O3 by the P7&8 4f relay at $2.67\times$ magnification.

Detection path

The detection path consists of a second folded remote refocusing system and an image-splitting arrangement for simultaneous dual spectral-channel imaging. The unfolded detection optical relay is shown in **Fig. 2.11**. The remote refocusing system consists of two separate microscope units: detection objective O4 and tube lens T1, designed to be used with a glass compensation block GB, form an intermediate image which is reimaged by a second microscope unit consisting of P9 & O5 onto remote refocusing mirror RM2 mounted on a piezoelectric actuator for fast axial scanning of the detection plane in the sample. For aberration-free remote refocus, similarly to the remote refocusing system in the ASLM unit of the illumination path, the focusing elements are selected such that the lateral and axial magnification from the sample to the focal plane of O5 are equal to $|m| = \frac{n_{sample}}{n_{remote}} = \frac{n_{water}}{n_{air}} = 1.33$.

Fluorescence is coupled into and out of the remote refocusing unit using a second quarter waveplate QWP2 and polarizing beam splitter PBS2. For linearly polarized excitation light in the Y' -direction, the emitted fluorescence will be preferentially polarized in the same direction. To maximize fluorescence transmission efficiency through the system, the emitted light collected by O4 is passed through a half wave plate (HWP) that is rotated to maximize light transmission by PBS2. The transmission efficiency variation with HWP angle will be most significant for fluorophores with high fluorescence anisotropy.

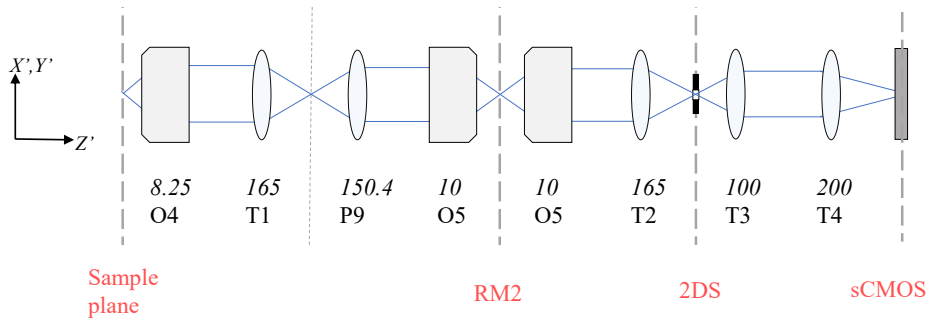


Figure 2.11 Detection path optical relay. Unfolded optical relay for the detection path from the detection objective O4 to the sCMOS detector. The focal lengths of respective optical elements and Plössl lens combinations are given in italic in millimeters. Axial translation of RM2 allows refocusing of the detection plane in the sample. The intermediate image formed at the two-dimensional slit is reimaged onto the sCMOS detector.

The refocused detection plane was imaged by refocusing objective O5 and tube lens T2 onto a two-dimensional adjustable slit (2DS), used to limit the FOV. The intermediate image in the plane of the slit is imaged onto the detector (sCMOS) using tube lenses T3-4 giving a final magnification from sample space to detector of $\sim 44\times$.

Dual-channel imaging

The biologically relevant fluorophores Fluo-4 AM and CellMask Orange (CMO) (ThermoFisher) were excited using the 488 nm and 561 nm laser lines. Simultaneous dual-channel imaging was achieved by separating the emission using two 560 nm edge long-pass dichroic beam splitters DM1&2 and emission filters F1&2 (ET525/50 and ET630/75 respectively). Mirrors M12 & 13 are used to direct the images corresponding to each spectral channel onto each half of the camera sensor. The relevant spectra for simultaneous dual colour imaging are shown in **Fig. 2.12**.

The filters were selected to maximize optical throughput and minimize cross talk between the emission from the two fluorophores. The contribution of CMO cross-excited by the 488 nm wavelength is used for joint excitation of both fluorophores in some of the later experiments (see **Section 5.2**). By temporally interleaving the laser excitation and detection of the two spectral channels, the background contribution from fluorophore cross-excitation could be removed, however, this would result in acquisition speed by approximately a factor of 2.

The co-registration parameters for two simultaneously acquired spectral channels were determined from a transmitted-light image of a USAF 1951 test target. The image containing the spatially separated spectral channels were overlaid by applying an affine transformation to one of the channels. The manually determined transformation parameters for best co-registration were then used for subsequent dual-channel image processing.

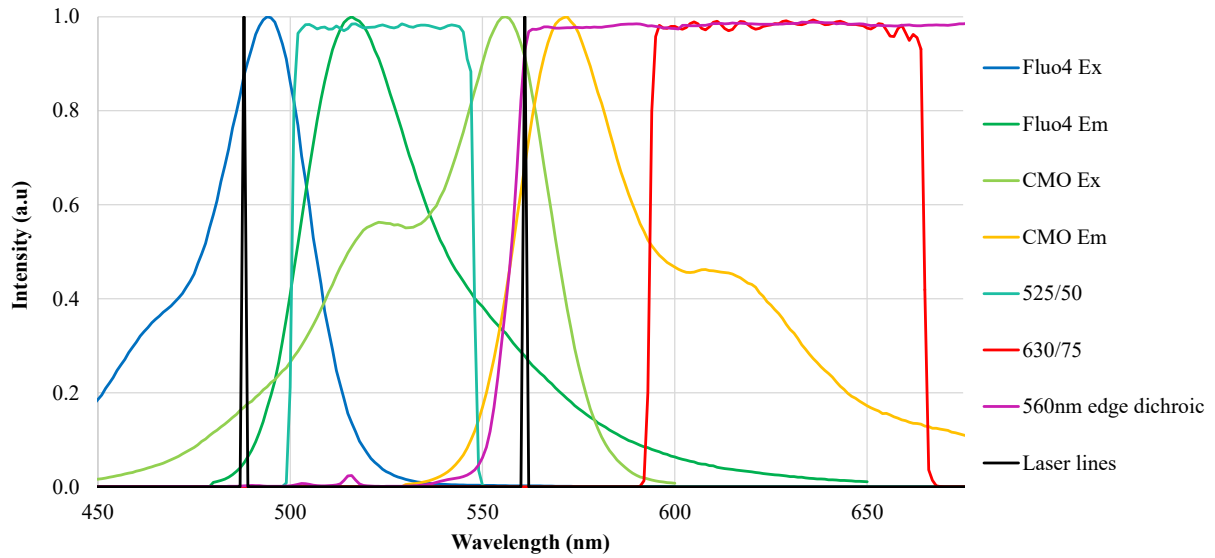


Figure 2.12 Relevant spectra for simultaneous dual-channel imaging. The 488 and 561 nm laser lines are used to excite Fluo-4 and CMO respectively (displayed excitation and emission spectra from Fluorescence SpectraViewer (ThermoFisher Scientific, 2022)). The separation of the emission spectra is achieved using 525/50 nm and 630/75 nm emission filters, as well as the 560 nm edge long pass dichroic. Filter and dichroic transmission spectra are from Chroma and Laser 2000 Photonics respectively (Chroma, 2021a; Chroma, 2021b; Laser 2000 Photonics). The Fusion camera had ~5% variation in responsivity across the spectral range of interest (data from manufacturer, not shown). All wavelengths are given in nm.

Correction of defocus in the fluo-4 spectral channel

The integration of the dual-channel image splitter assembly revealed defocus between the Fluo-4 and CMO channels. The initial separation between the best focus positions for the two spectral channels was estimated by imaging a chrome-on-glass alignment target (Optical Insights) in transillumination (**Fig. 2.13a**). Using the micrometer that adjusts the axial position of the remote refocusing mirror, the amount of axial translation required to go from the CMO channel being in focus, to the Fluo-4 channel in focus, was estimated to be around $\sim 5 \mu\text{m}$ in remote refocus space, in the direction towards the remote refocusing objective. In image space, accounting for the double pass through the remote refocusing assembly, this corresponds to $\sim 11 \text{ mm}$ of negative defocus (for $M_a = 1089$). This agreed with defocus estimates from direct axial translation of the detection objective.

Small amounts of defocus can be generated by introducing two lenses with near-equal but opposite magnification, separated by a small distance. Using the thin lens approximation, the total optical power $K_{12} = 1/f_{12}$ of two lenses with powers K_1 and K_2 is given by the Gullstrand equation (Hecht, 2002):

$$K_{12} = K_1 + K_2 - d_{12}K_1K_2 \quad (2.11)$$

Where d_{12} is the distance between the principal planes of the two lenses. As d_{12} increases, the effective power of the two lenses decreases. The combined power of the lens pair and the 200mm tube lens T4 in front of the detector is given by

$$K_{tot} = K_{12} + K_{TL} - d_{TL}K_{12}K_{TL} \quad (2.12)$$

Where $K_{TL} = 1/200 \text{ mm}$ is the optical power of the tube lens, and the distance from approximate combined principal plane of the lens pair to the principal plane of tube lens TL3 was estimated to be around $d_{TL} = 125 \text{ mm}$.

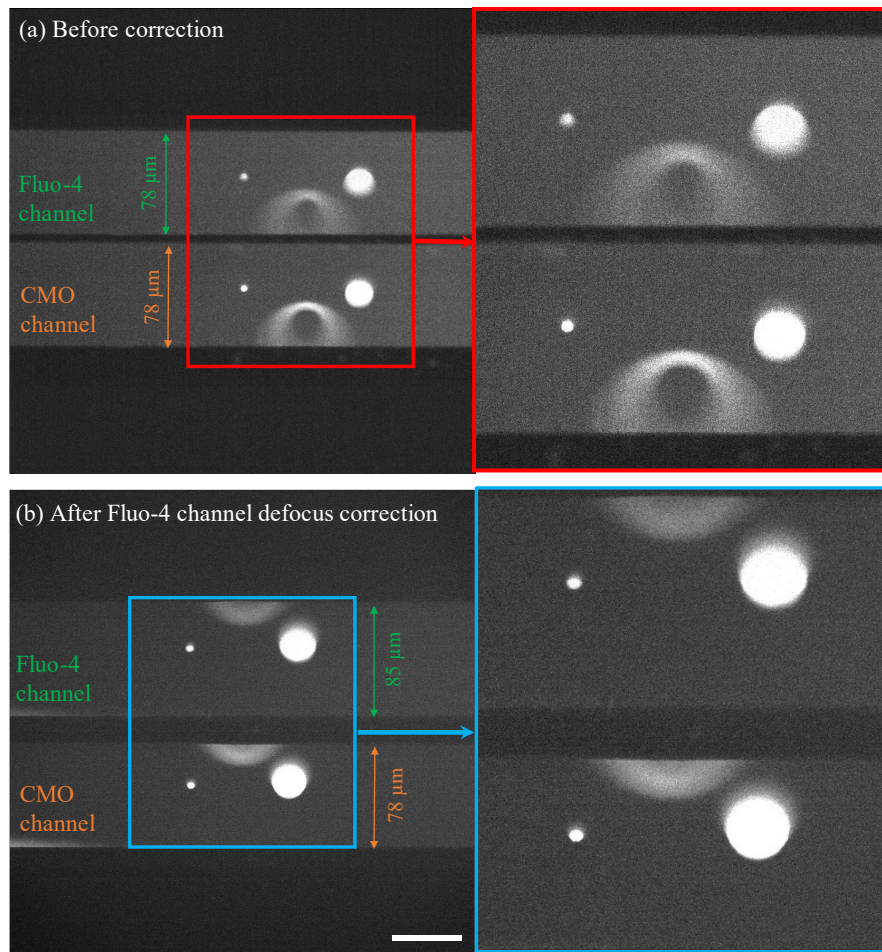


Figure 2.13 Image of test chart before and after Fluo-4 defocus correction. (a) Image of the test target prior to correction through the Fluo-4 (top) and CMO (bottom) emission paths, with the sample position adjusted such that the CMO channel is in focus. The features in the Fluo-4 channel appear blurrier (see inset panel on the right). (b) Image of a different area of the same target after the introduction of the positive and negative doublets in the Fluo-4 emission path. The feature sharpness is more consistent across the two channels; however, the Fluo-4 channel has been magnified by a factor of $\sim 1.1\times$, measured from the vertical range of the slit boundary. Scalebar: $50 \mu\text{m}$.

The defocus correction was achieved with two cemented doublet lenses L_+ and L_- with focal lengths of $f_1 = 160$ mm and $f_2 = -150$ mm respectively (**Fig. 2.14a**), introduced within the Fluo-4 beam path of the dichroic assembly, after emission filter F1 and before positioning mirror M12 (see **Fig. 2.9**). Lenses with equal and opposite focal lengths were considered, however, they did not give a sufficiently large defocus range without having to swap their order during alignment. To determine the optimal lens order and orientation, the lens sequence including the doublets L_+ and L_- and tube lens T4 was modelled in the optical design software Zemax OpticStudio for 525 nm wavelength, 4.5 mm beam diameter and up to 3 degrees field angle (**Fig. 2.14b**), using the manufacturer's Zemax lens data and black box data for the doublets and tube lens respectively. The principal planes in object and image space were determined from the cardinal point data summary after propagating a collimated beam through each element, with the aperture stop positioned at the first surface.

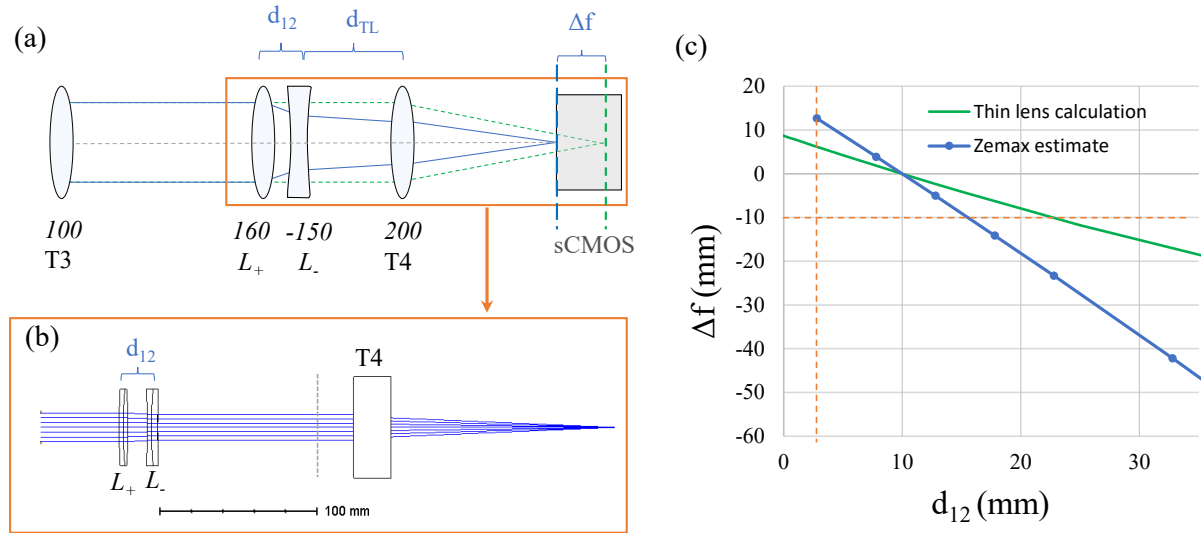


Figure 2.14 Fluo-4 channel defocus correction using a pair of lenses. (a) Diagram of the optical relay from tube lens T3 to the detector in the Fluo-4 emission path. The blue rays show how lenses L_+ and L_- with principal planes separated by $d_{12} \sim 15$ mm introduce a $\Delta f \sim 10$ mm negative defocus compared to the original ray path (green). (b) Zemax optical diagram for the L_+ and L_- lens pair and tube lens relay (orange rectangle in (a)). The dashed vertical line indicates the estimated location of the principal plane of T4. (c) Variation of the defocus Δf with L_+ and L_- principal plane separation d_{12} from thin lens calculation (green) and Zemax simulation (blue). The vertical orange dashed line indicates the minimal physical principal plane separation of 0.28 mm, and the horizontal dashed line shows the required defocus correction.

Several lens orientations and orders gave diffraction limited performance (Strehl ratio > 0.8) for the relevant field angles for a principal plane separation up to $d_{12} = 50$ mm. The chosen orientation, with the positive lens positioned first, had a minimum principal plane separation of $d_{12} = 2.79$ mm, and gave a nominal positive focus shift of $\Delta f = 12.8$ mm, which decreased with increasing lens separation.

The resultant defocus Δf for increasing lens separation d_{12} was sampled at 5 mm intervals in the Zemax model (**Fig. 2.14c**). The model gave a more rapid change in defocus compared to the thin lens calculation using equations (2.11) and (2.12) above. This is likely due to the incorrect estimate of the

principal plane location of tube lens T4. The Zemax model indicated that the required defocus correction of $\Delta f = -10$ mm is achieved at around $d_{12} = 15$ mm, which corresponds to a spacing of ~ 12 mm between the adjacent surfaces of the two lenses.

Figure 2.13b shows the test chart imaged after introducing the lens pair to correct for defocus in the Fluo-4 channel. The approximate spacing between the lens pair was ~ 1 cm, which agreed with the Zemax estimates. As a result, the focus for the Fluo-4 channel now coincided with that for the CMO channel, however, this introduced a magnification factor into the Fluo-4 channel. The resultant change in lateral magnification for the Fluo-4 channel was measured to be equal to $M = 1.08$ and was corrected for during the channel co-registration in post-processing. After the correction, the slit edges in the Fluo-4 channel were no longer as sharply in focus, which indicates that the defocus originates earlier in the optical path and is potentially a longitudinal chromatic aberration caused by the incorrect separation of the detection objective and tube lens T1 (see **Section 3.4**), or from the home-built tube lens T2.

2.2.2. Spatiotemporal imaging modes

mSPIM with Remote Refocus

High-speed volumetric imaging is achieved by galvo-scanning of the Gaussian light-sheet along the detection axis Z' synchronously with remote refocusing of the detection plane. The folded remote refocusing configuration allows for fast scanning of the detection plane without mechanical disturbance of the sample. To optimize the trade-off between optical sectioning and FOV, the BFP of the illumination objective is underfilled such that the resultant light-sheet length matches the diameter of the sample of interest, in this case a single cardiomyocyte cell with a length of ~ 100 μm . For remote refocus of the detection plane, the axial translation of RM2 was achieved using a piezoelectric actuator driven with an asymmetric saw tooth profile (**Fig. 2.15**), low-pass filtered to minimize unwanted high frequency motion generated by mechanical resonances. The actuator positions were recorded using a capacitive sensor. The acquisition window was limited to the initial window corresponding to 80% of the total cycle in order to avoid nonlinear regions of the sawtooth profile driving the piezo that translates RM2.

Synchronous scanning of the illumination and detection planes was calibrated by recording the actual position of RM2 for the given asymmetric saw-tooth motion profile prior to data acquisition. The RM2 position was sampled at 5 points over the linear region of the sawtooth profile range, with a 3rd degree polynomial fit used to provide the intermediate positions. The recorded mirror motion was then used to produce a matched voltage waveform used to drive the G2 Z' -scan galvo such that the light-sheet positioning along the detection axis matched the refocused detection focal plane.

Angular dithering of the lightsheet by G1 was driven by a sinusoidal waveform synchronized with the camera acquisition such that each frame was acquired during half of the dither period, with a constant phase offset. The sCMOS detector, lasers and camera were externally triggered using transistor-

transistor logic (TTL) pulses from the DAQ card. Reconstruction of remote-refocused image stacks involved axial resampling along the Z' -axis for uniform voxel dimensions, followed by rotation into lab frame coordinates by θ_{LS} about the Y -axis (**Fig. 2.16a**).

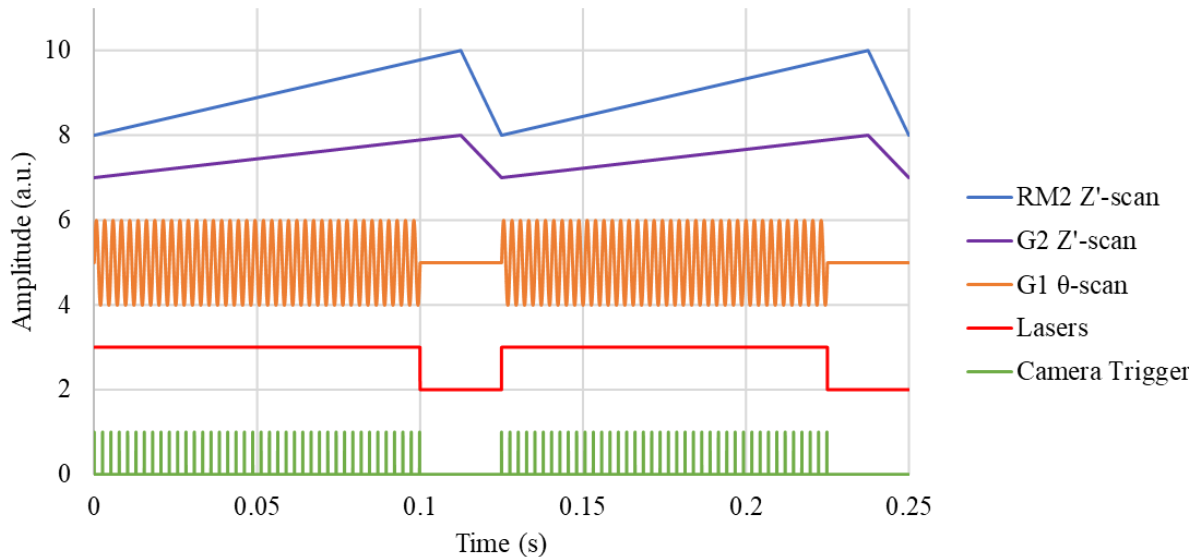


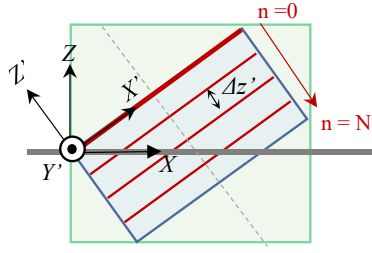
Figure 2.15 Hardware timing diagram for volumetric acquisition with remote refocus. The diagram shows the output signal generated in the LabVIEW acquisition software for two consecutive volumes, each containing 40 planes, acquired at 8 Hz (~ 400 fps). Through the DAQ card, the camera and lasers were triggered through TTL signals, and analog output signals were used to control the G1, G2 and RM2 positions. The amplitudes for each signal have been offset vertically for clearer visualization.

DSLM+ASLM with Stage Scan

Higher resolution imaging at slower acquisition speed was achieved using a digitally-scanned light-sheet illumination. The virtual light-sheet is produced through rapid scanning of a tightly focused Gaussian beam using G3 to produce a Y' -scan. It was driven with an asymmetric saw-tooth waveform profile synchronized to the camera frame rate.

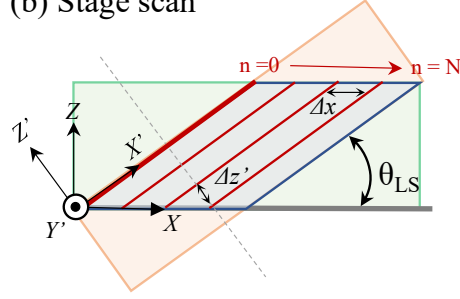
For improved optical sectioning and axial resolution, the beam was expanded to fill the BFP of excitation objective O3 to achieve a smaller beam waist in the focal plane. Axially swept light-sheet microscopy enables more uniform axial resolution across the FOV by scanning the beam waist along light-sheet propagation direction X' . The DSLM+ASLM illumination mode is combined with a continuous motorized stage scan of the sample along X' . The DAQ box was used to trigger the camera to acquire frames at $\Delta x = 0.1 \mu\text{m}$ intervals of stage travel. The data is desheared along the X' -direction, with the resultant spacing between adjacent planes equal to $\Delta z' = \Delta x \sin \theta_{LS}$, then resampled along the axial direction to obtain a uniform voxel size and rotated into lab coordinates about the Y' -axis by angle θ_{LS} . (**Fig. 2.16b**).

(a) Remote refocus



$$\begin{aligned} y &= y' \\ x &= x' \cos \theta_{LS} + z' \sin \theta_{LS} \\ z &= z' \cos \theta_{LS} - x' \sin \theta_{LS} \end{aligned}$$

(b) Stage scan



$$\begin{aligned} x'_n &= x' + \Delta x' n \cos \theta_{LS} \\ y &= y' \\ x &= x'_n \cos \theta_{LS} + z' \sin \theta_{LS} \\ z &= z' \cos \theta_{LS} - x'_n \sin \theta_{LS} \end{aligned}$$

Figure 2.16 Stage-scan and remote-refocus volumetric data acquisition modes. (a) For remote-refocused acquisition, the sample remains stationary, and the focus is swept along the Z' detection axis (dashed grey line), with consecutive images separated by distance $\Delta z'$ along the detection axis. (b) For stage-scanned acquisition, the sample is scanned through the focal plane along the X -axis, with images acquired at step-size Δx . Each frame in the acquired volume (blue) is shown in red, with the nominal focal plane indicated in bold. The green region indicates the bounding box of the reconstructed volume in lab coordinates.

For ASLM acquisition, multiple image volumes were acquired at each RM1 and corresponding beam waist position. The number of beam waist positions for each acquisition was determined by the ratio of the desired FOV along X' to the confocal parameter of the DSLM illumination beam. The spatial regions of the volumes containing each ASLM-scanned beam waist position were extracted and recombined in MATLAB postprocessing, producing a final volume with uniform optical sectioning across the FOV greater the confocal parameter of tightly focused beam without axial scanning.

Camera acquisition modes

Unlike CCD sensors, each pixel in an sCMOS sensor contains a photodiode which converts detected photons into electrical current, an amplifier which converts charge into voltage, and an analog-to-digital converter (ADC) on every row, with simultaneous readout for all pixels within that row. Compared to CCD sensors, sCMOS sensors have lower readout noise at around $1e^-$, higher acquisition speeds, larger FOV and are more power efficient. However, as a result of the individual pixel readout, sCMOS sensors have more temporal and fixed pattern noise.

The Hamamatsu Orca Fusion sCMOS camera implemented for most of the acquisitions in the LSFM system uses the rolling-shutter readout method, where exposure and readout are done line by line (Hamamatsu Photonics, 2019) The camera has two main readout modes: the normal area mode and the light-sheet readout mode. In the normal area mode, the image sensor is read out from the centre line to the top and to the bottom simultaneously. Meanwhile, for the light-sheet readout mode, designed to be synchronized with the illumination scan to reject scattered light and achieve higher SNR, the sensor is read out top to bottom or bottom to top. Both readout modes have three different operation modes: a

free running mode, an external trigger mode, and a start trigger mode. In the first mode, the exposure and readout timings are decided by an internal microprocessor. For the second mode, readout is initiated by an external trigger input, and for the last mode an external trigger input is used to start continuous imaging. Acquisition can be operated at three increasing scan speeds (at the trade-off of increased noise): ultra quiet scan (0.7 electrons r.m.s), standard scan (1.0 electrons (r.m.s)), and fast scan (1.4 electrons r.m.s).

For the normal area mode, using the fast scan combined with CoaXPress interface data transfer, and external trigger mode with synchronous readout trigger, the highest instantaneous frame rate is determined by the number of vertical pixel rows: image acquisition using the full sensor of $2304 \text{ px} \times 2304 \text{ px}$ can be achieved at 88.9 fps, while reducing the number of rows to 1024 pixels, 512 pixels and 256 pixels enables maximum frame rates of 199 fps, 397 fps and 787 fps respectively (Hamamatsu Photonics, 2019). For volumetric imaging with remote refocusing, since all frames are acquired during the rising edge of the sawtooth profile (**Fig. 2.15**), the average frame rate is lower than the frame rate during the sequence of exposures acquired for one volume.

The sensor FOV was decided based on considerations regarding the required acquisition speed, image dimensions, and resolution. For the 2D single cell timelapse experiments (**Chapter 4**), the detector FOV was set based on the dimensions of the two spatially separated images of a single cardiomyocyte (one for each spectral channel). Accounting for $44\times$ magnification from sample to image space, the required sensor FOV dimensions to fit a cardiomyocyte cell centered within the FOV of both spectral channels was selected to be at least $1152 \text{ px} \times 512 \text{ px}$ ($170.2 \text{ }\mu\text{m} \times 75.6 \text{ }\mu\text{m}$), with the shorter dimension along the vertical axis of the camera.

2.3. Variable-angle projection imaging

This section conceptually explores the potential to implement the multi-angle projection principle (described in **Section 2.1.4**) to the existing LSFM system, motivated by several potential benefits. In the current system, the default viewing angle of a single image or stack is at $\theta_{\text{LS}} = 37^\circ$ w.r.t. the normal to the X - Y horizontal surface, (**Fig.2.17a**). Having a top-down projection of the sample orthogonally to the coverslip would allow direct visualization of a wider area of the sample in comparison to the illuminated tilted orthoslice. This would enable real-time visualization without the need for computational rotation followed by projection of 3D datasets and could aid sample navigation during experiments. Implementing this modality would also enable projection-imaging of faster dynamics, as all planes within the sheared projection are acquired within a single camera exposure, as opposed to requiring multiple frames per volume.

2.3.1. Shear geometry

For n planes over an axial range of z' , the sheared projected image width in the direction of the shearing is given by $x'_{sh} = x' + \alpha z'$, where x' is the width of each image and α is the shear factor (**Fig. 2.17a**).

For the current system configuration, the Orca Fusion sensor has dimensions of 2304×2304 pixel, with an effective pixel side of $0.1477 \mu\text{m}$ in object space. For imaging at 397 fps, the FOV is restricted to the central 512 pixels in the vertical direction, with $x' = 38 \mu\text{m}$ (256 pixels), width per spectral channel (Fig. 2.17c). Hence, the maximum shear is $x'_{sh} = 170 \mu\text{m}$ (1152 px) for two spectral channels. An image stack depth of $z' = 50 \mu\text{m}$ would give a shear factor of $\alpha = (x'_{sh} - x')/z' = 2.64$, which corresponds to a maximum viewing angle of $\theta = -\arctan(\alpha) = -69^\circ$.

To achieve a flat-on viewing angle of the sample at $-\theta_{LS} = -37^\circ$ w.r.t to the current viewing angle, the required shear factor is $\alpha = -\tan(-\theta_{LS}) = 0.75$. This means that the required shear per spectral channel is $x'_{sh} = x' + \alpha z' = 75.5 \mu\text{m}$, (511px), which would fit within the central half (in the vertical direction) of the camera sensor (limiting the frame rate to a maximum of 199 fps). To account for the vertical scaling of the image in the shear direction, the image would need to be compressed, either optically, such as using a reversed cylindrical lens expander, or in post-processing, by a scaling factor equal to $1/\cos\theta$.

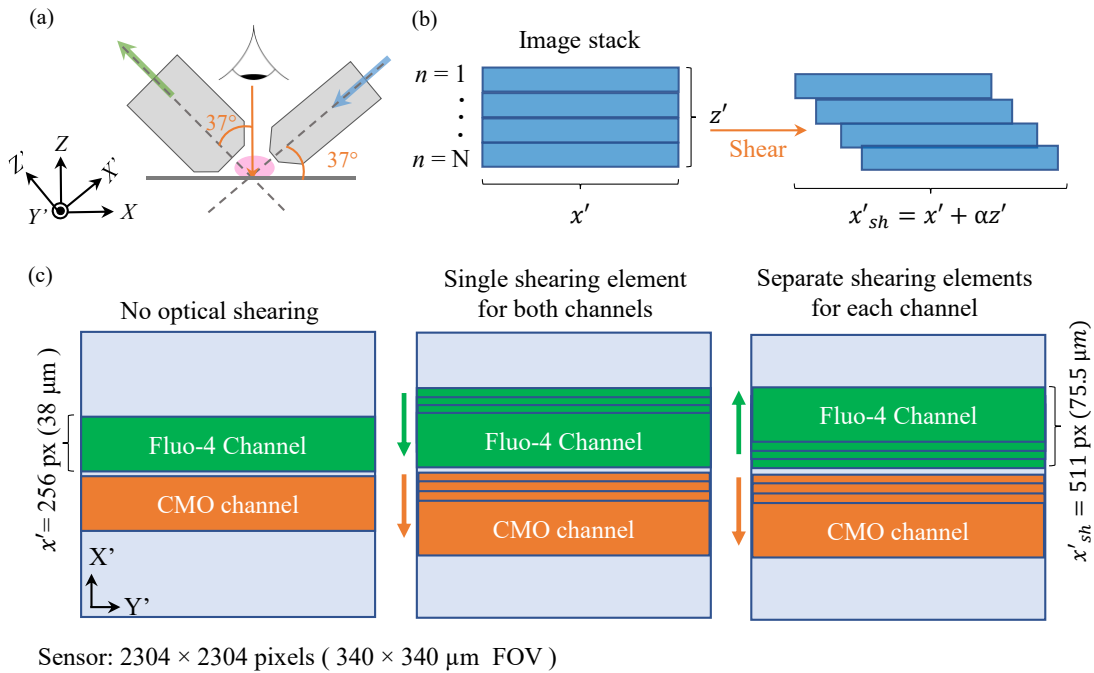


Figure 2.17 Multi-angle projection viewing through lateral shearing. (a) Dual-objective illumination-detection geometry in the existing LSFM system, indicating the desired top-down viewing angle of the sample. (b) Lateral shearing of the image stack prior to projection. (c) Fluo-4 and CMO spectral channel layout on the sCMOS camera sensor for no optical shearing (left), lateral shearing in the same direction using a single shearing element (middle) and lateral shearing in the same or opposite direction using separate shearing elements for each spectral channel (right). The green and orange arrows indicate the direction of the applied image shear.

2.3.2. Potential implementation

The shearing required for rotated projection viewing can be achieved using scanning galvos – this can be done in real space, for example with a two-mirror scan unit directly in front of the detector such as

the one in the original implementation by (Chang et al., 2021). Axial refocusing to build the sheared projection would be implemented using the existing folded aberration-free remote refocus. Lateral translation of the image can also be achieved using a single galvo mirror in Fourier space. In the current system, the galvo can be incorporated using a 4f relay after the remote refocusing unit and before tube lens T2 (see **Fig. 2.9**), providing a unidirectional shear to both spectral channels as shown in **Fig. 2.17c** (middle). However, the main challenge with this approach is the limited available space on the optical breadboard for additional optical elements and extension of the beam path.

The second method of achieving lateral shearing with scanning galvos in the Fourier plane is by replacing the non-scanning positioning mirrors M12 and M13 (located within the dual channel image splitter assembly). While this does not require any modification of the beam path, the key challenge here is the large beam size. The back focal plane diameter of the detection objective O4 (20×, 1 NA) is $BFP_d = 2NA \times f_{back} = 16.5 \text{ mm}$, where the back focal length of O4 is $f_{back} = f_{TL} \times M$, where $f_{TL} = 165 \text{ mm}$. For a fully filled pupil of detection objective O4, after tube lens T3, the detection beam diameter has been demagnified by 0.55, and is equal to 9.1 mm.

The galvos already in the system have a maximum beam diameter of 5 mm. While single axis galvo scanners for a 10 mm maximum beam diameter are commercially available (such as GVS411/M or QS10X-Y3 from Thorlabs), they would add to the total system expense. The beam size can be reduced by changing the combined magnification of tube lenses T2 and T3 by switching T2 to a lens with a longer focal length, and/or swapping T3 for one with a shorter focal length. For example, for T3 with a focal length of 50 mm, the beam size would be reduced to 4.5 mm, which would enable the use of galvo scanning mirrors with a maximum beam size of 5 mm. However, the reduced magnification would increase the effective pixel sampling size from $0.1477 \mu\text{m}$ to $\sim 0.295 \mu\text{m}$ in each lateral dimension in sample space, which would make the spatial resolution of the system pixel-limited (see **Chapter 3** for a detailed characterization of the systems resolution).

Acquisition speed

For high-speed volumetric imaging using remote-refocused acquisition, the speed limiting bottleneck is the camera frame rate for the selected FOV (up to a maximum frame rate of 397 fps for a vertical extent of 512 pixels, and up to 199 fps for 1024 pixels). For the smaller of the two FOV and an axial range of $50 \mu\text{m}$ sampled at $1 \mu\text{m}$ intervals, the maximum volumetric acquisition rate is 8 Hz. Galvanometric mirrors have a comparably high scan speed, with large beam diameter single axis scanning systems achieving up to 1 kHz scan rates for small angles and $>35 \text{ Hz}$ scan rate over full angular travel (and faster rates for smaller beam scanners) and are hence the fastest available option image stack shearing for rapid projection imaging.

The piezo actuator used to axially translate RM2 (with a mass of $\sim 13 \text{ g}$) is able to reach sweep speeds up to $3.3 \mu\text{m/ms}$, and hence for unidirectional axial scan over a range of $50 \mu\text{m}$ in sample space (which,

accounting for the double pass and magnification, corresponds to $33.3 \mu\text{m}$ scan range in remote refocus space), the upper limit for the acquisition rate is on the order of 100 Hz, with faster sweep rates potentially possible with smaller mirror masses. Hence, projected imaging could be achieved at rates limited by the remote refocusing speed, which corresponds to a $\sim 5\text{-}10\times$ speed improvement compared to frame-rate limited volumetric acquisition.

Sheared projection simulation with volumetric data.

To demonstrate the variable-angle sheared projection method for top-down sample viewing, the operation was demonstrated computationally on an image stack acquired through remote refocusing for a single time point. **Figure 2.18** compares three different renderings of the 40-frame stack, with each plane spaced by $d = 1 \mu\text{m}$: (a) a single raw $X'Y'$ slice halfway through the stack, (b) the image stack bilinearly interpolated axially along Z' for uniform voxel size, rotated by θ_{LS} about the Y -axis into the lab frame, with a maximum intensity projection (MIP) taken along the Z -axis. It can be seen that this perspective is equivalent to (c), where the original image stack was sheared along the X' -axis by total distance equal to $\alpha z'$ as described in **Section 2.3.1**, followed by a MIP along the Z -axis giving an XY projection. Minor intensity differences are attributed to artefacts from the different interpolations used in each method. The sample preparation and image acquisition conditions for this data are described in **Section 5.2** (see **Table 5.1**, lower sub-row of Exp. 2).

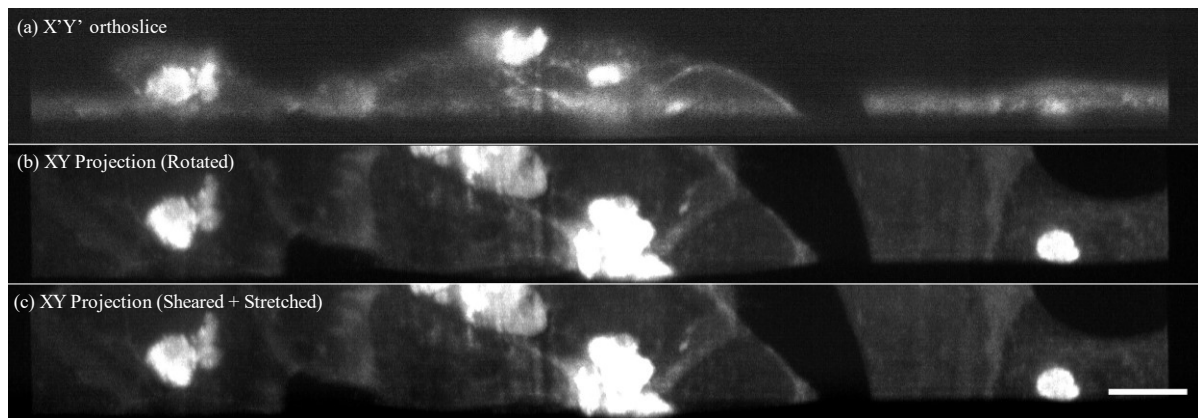


Figure 2.18 Demonstration of the equivalence of projected sheared image stack and a projected rotated image stack. (a) Single frame from the CMO channel for a remote refocused image stack of human induced pluripotent stem cell-derived cardiomyocytes (hiPSC-CM). In (b) the image stack has been bilinearly interpolated axially for a uniform voxel size and rotated into lab frame coordinates by θ_{LS} , and then a maximum intensity projection was taken along the z -axis. In (c) the image stack has been sheared along the x -axis by αz , projected along the z -axis and compressed by scaling factor of $1/\cos\theta_{LS}$. (b) and (c) give a top-down view of the sample, with minor differences attributed to various interpolation artefacts. Scalebar: $20 \mu\text{m}$.

It is worth noting that the shearing and projection operation used to generate image (c) is $> 6\times$ faster than the rotation and projection operation used for (b) (0.5 s compared to 3.2 s respectively for $256 \times 2048 \times 271$ matrix dimensions). The rotation was executed using the MATLAB *imrotate3* function, while the lateral shearing was implemented by applying a Fourier transform to each image

using *fftshift(fft2())* functions, multiplying the result with a phase ramp with a slope proportional to the shear factor α , and then applying an inverse Fourier transform *ifft2(ifftshift())*, followed by multiplication by the scaling factor $(1/\cos\theta_{LS})$. Doing the transformation through frequency space avoids the problem of lateral shifting of images by non-integer pixel intervals. For optically executed shearing, the acquired projection would be a sum of the sheared images, not a maximum intensity projection, and hence low background and high SNR are advantageous.

While there was no practical opportunity to implement this on the existing system, this concept has the potential of being a useful and simple modification, enabling faster projection-based imaging and visualization with variable viewing angles. As shown in the example above, the shear-warp transform is also useful for faster projected visualization of 3D data and can also be used to optically deshear the data acquired in a stage scan. Optically implemented shearing would be compatible with imaging fast dynamics in thin samples, where depth information is of less importance.

2.4. Summary

The aim of this chapter was to provide a background of existing approaches and alternatives to high-speed volumetric imaging, to explain the concept of aberration-free remote refocus and the benefits of using it for high-resolution volumetric imaging, and to provide a detailed description of the system design considerations and operation modes. The system was modified to integrate a spectral channel image splitter, and the axial defocus between the two colour channels was corrected through the introduction of a pair of doublets with near-equal but opposite focal lengths. The optical implementation of the shear warp transform for variable angle projection viewing was discussed and demonstrated computationally.

There is potential for further improvements that have not been implemented within the scope of this work: improved background rejection can be achieved by employing confocal slit detection using the rolling shutter acquisition mode on the sCMOS detector. Crosstalk between the two spectral channels can be minimized by temporally interleaving laser illumination, however, this would halve the acquisition rate. Faster imaging at the cost of decreased SNR can be achieved by reducing the detector FOV in the vertical direction by re-positioning the image of each spectral channel such that the rectangles bounded by the adjustable slit edges are adjacent on their short sides. In the future, higher 3D imaging rates and improved optical throughput can be achieved by using a deformable mirror for remote-refocusing, as in the implementation by (Wright et al., 2021). These developments may be part of future work on extending the performance and functionality of the system.

A key aspect in the volumetric image quality is the optical sectioning and axial resolution of the imaging system. The next chapter employs a detailed characterization of the systems resolution and compares the expected and modelled resolution with experimental PSF measurement.

3 Characterizing the spatial resolution

3.1 Introduction

Understanding the performance and limitations of an instrument is key both to its successful application and the interpretation of its measurements and results. The spatial resolution is a defining feature of an optical microscope and describes its ability to resolve fine detail in a specimen. In LSFM, the light-sheet illumination introduces optical sectioning, and can improve the axial resolution. However, for light sheets generated with a Gaussian beam, diffraction creates a trade-off between the light-sheet thickness and propagation length, limiting the lateral extent of the image over which good optical sectioning is maintained. The mSPIM and DSLM illumination modes in this system produce different light-sheet profiles, aimed at larger FOV and high-resolution imaging respectively.

The aim of this chapter is to evaluate the performance of the custom remote refocusing LSFM system by characterizing the spatial resolution and optical sectioning of the microscope. This chapter starts by defining spatial resolution in optical microscopy (**Section 3.1.1**) and reviews the mathematical description of image formation in incoherent imaging (**Section 3.1.2**). Next, **Section 3.1.3** briefly introduces the concept of resolution enhancement, including existing methods and limitations. This is followed by a review of approaches to characterizing optical sectioning (**Section 3.1.4**) and measuring the spatial resolution (**Section 3.1.5**). The following **Section 3.1.6** describes the resolution in a SPIM system for Gaussian light-sheet illumination.

Next, **Section 3.2** implements computational modelling of the spatially varying resolution of the LSFM system described in this work, initially for uniformly filled illumination pupils (**Section 3.2.1**), and subsequently by modelling the illumination path for the mSPIM and DSLM illumination modes to account for optical aberrations and aperture truncation effects on the light-sheet profile (**Section 3.2.2**). The theoretically-calculated and computationally-modelled resolutions are compared with experimental measurement of the system resolution, estimated by fitting Gaussian distributions to images of fluorescent beads (**Section 3.3**). Finally, **Section 3.4** identifies aspects in the optical configuration that can be modified for potential improvement in future system performance.

3.1.1. Resolution definition and criteria

In an optical microscope, the spatial resolution, or the ability of an imaging system to resolve the fine detail in an object, is fundamentally limited by diffraction, a physical property of light waves. For a perfect lens with a uniformly illuminated circular aperture, the best focused spot of light will form an Airy pattern consisting of a bright central region and concentric rings of decreasing brightness (Airy, 1835). For a diffraction-limited incoherent widefield system, the lateral (radial) and axial profiles respectively through the Airy pattern intensity distribution with a uniformly illuminated pupil can be expressed as (Born & Wolf, 1980):

$$I(v) = I_o \left(\frac{2J_1(v)}{v} \right)^2 \quad I(u) = I_o \left(\frac{\sin(u/4)}{u/4} \right)^2 \quad (3.1, 3.2)$$

Where $J_1(\dots)$ is a Bessel function of the first kind and I_o is the intensity at the maximum of the centre of the Airy pattern. Here we have introduced normalized optical coordinates v and u to represent the radial and axial distances respectively through:

$$v = knr \sin(\alpha) \quad u = 4knz \sin^2\left(\frac{\alpha}{2}\right) \quad (3.3, 3.4)$$

where $k = \frac{2\pi}{\lambda}$ represents spatial frequency, λ is the wavelength of light travelling through a medium with refractive index n at the maximum collection angle α w.r.t the optical axis of the system.

In the presence of optical aberrations, the resolution of an imaging system is degraded (Mahajan, 2001), and the diffraction pattern is modified, resulting in a redistribution of the intensity from the centre to the outer regions. This effect is often quantified by the Strehl ratio, defined as the ratio of the peak aberrated intensity in the image of a point source to the un-aberrated peak intensity in diffraction-limited system (Strehl, 1894). Accounting for aberrations, the response of real imaging system to a point source or object can be described by the more general three-dimensional intensity point spread function (PSF) (Born & Wolf, 1980).

Two-point resolution criteria define the ability of an optical system to resolve two points separated by a minimum distance by considering the total intensity distribution in the image produced by the sum of their respective diffraction intensity patterns. The Sparrow criterion considers two-point sources to be no longer resolved when the minimum in between the two peaks in the combined intensity distribution vanishes (Sparrow, 1916). According to the Rayleigh criterion, two points are just resolved when the maximum of the diffraction pattern intensity distribution of one of the sources is directly over the first minimum of the other (Rayleigh, 1879). Despite giving some measure of an optical system's ability of resolving fine features, these two-point resolution criteria do not provide a universal definition of the absolute limit of a system's optical resolution.

Point spread function-based resolution criteria consider the size and shape of the imaging system's PSF, typically described by its full-width-at-half-maximum (FWHM) in the axial and two lateral directions. For comparison of the three-dimensional resolving power of optical systems, the use of observation volume V_{obs} has been proposed (Hell & Stelzer, 1992a), defined as the ellipsoid volume enclosed by the iso-surface of the PSF (Lindek et al., 1994).

While the shape and size of the PSF and hence observation volume can be modified in digital post-processing using filters that give preference to high frequency content, fundamentally, no additional information content from the sample has been obtained (Schermele, Heintzmann &

Leonhardt, 2010). The information contained in an intensity distribution of an object can be expressed in terms of its spatial frequency components: fine details correspond to high frequencies, while slow varying features such as background have a low or zero spatial frequency. The system's imaging response in the frequency domain is described by the Fourier transform of the PSF – the optical transfer function (OTF) – which represents how well each spatial frequency is supported, or transferred, by the imaging system (Williams & Becklund, 2002). The OTF is a complex valued function with an absolute value, and complex argument: $OTF(v) = MTF(v)e^{iPhTF(v)}$. The absolute value of the OTF is known as the modulation transfer function (MTF), which represents how much of the objects contrast is transferred in the image as a function of spatial frequency v . The complex argument of the OTF, referred to as the phase transfer function PhTF, represents the pattern translation.

The fundamental limit on the optical resolution of an imaging system can be defined in terms of the system's ability to image the spatial frequency components of an object, which are related to the real-space intensity distribution through a Fourier transform. Ernst Abbe recognised that features of a periodic structure such as a diffraction grating will be resolved if the angle of first order of light diffracted by the structure is smaller than the acceptance angle of the imaging system (Abbe, 1873). Abbe's diffraction limit states that in an incoherent imaging system, the smallest resolvable feature size d with light of wavelength λ travelling at a maximum half-angle α to the optical axis of the system through a medium with refractive index n is

$$d_{min} = \frac{\lambda}{2n\sin\alpha} = \frac{\lambda}{2NA} \quad (3.5)$$

where $NA = n\sin\alpha$ is known as the numerical aperture of the system. Finer specimen detail will diffract light at angles too high to be collected by the objective lens. The spatial resolution limit corresponds to an OTF cut off frequency of

$$k_{max} = \frac{2NA}{\lambda} \quad (3.6)$$

The cut off frequency of the OTF gives a fundamental limit of the highest spatial frequency transmitted by the system: while enhancing high frequencies or attenuating low ones can help visualize the finer detail in an image, conventional imaging techniques are not able to extend the range of the support of the OTF beyond that limit.

3.1.2. Image formation in incoherent imaging

Under the scalar approximation, the amplitude distribution in image space can be expressed as a superposition of plane waves travelling at a range of angles, with higher angles corresponding to narrower minima-maxima intensity modulation and hence finer detail in image space. For monochromatic light, each angle accepted by the numerical aperture (NA) of the imaging system can be represented as a k-vector which lies on the Ewald sphere (Ewald, 1969), a spherical shell centered

on the origin in frequency space. This spherical cap of the Ewald sphere, bound by largest acceptance angle of the system's NA is known as McCutchen's generalized aperture (McCutchen, 1964) and its projection onto the k_{xy} plane represents the complex pupil function $\check{p}(\vec{k}_{xy})$. When generalized to three-dimensional space, the OTF is given by the autocorrelation of McCutchen's generalized aperture (Sheppard, 1989).

The inverse Fourier transform of the generalized aperture is the coherent amplitude PSF, which represents the image space electric field distribution for a point source in sample space origin. The absolute square of coherent amplitude point spread gives the intensity distribution recorded by the detector – the incoherent intensity PSF.

Fluorescence is generally modelled as an incoherent imaging process, which means that the light emitted from different positions in the sample does not interfere. Here $r = (x, y, z)$ is used to express coordinates in image or detector space, and $r' = (x', y', z')$ to define positions in object or sample space (scaled to account for magnification). The image intensity distribution in detector space $I(\vec{r})$, for a point in sample space can be described by a shifted version of the intensity PSF $h(\vec{r} - \vec{r}')$, scaled by the sample response for that point $S(\vec{r}')$. The total image intensity for all points in sample space can be expressed as an integral over the object volume, this is equivalent to a convolution of the sample intensity distribution with the intensity PSF:

$$I(\vec{r}) = \int S(\vec{r}')h(\vec{r} - \vec{r}')d^3r' = (S * h)(\vec{r}) \quad (3.7)$$

Taking the Fourier transform of the above equation expresses image formation in k-space:

$$\tilde{I}(\vec{k}) = \tilde{S}(\vec{k})\tilde{h}(\vec{k}) \quad (3.8)$$

Here, the sample frequency response $\tilde{S}(\vec{k})$ is multiplied by the Fourier transform of the PSF – the OTF, $\tilde{h}(\vec{k})$. The above equations assume homogenous sample illumination. However, for spatially varying object illumination $L(\vec{r}')$ the above equation becomes

$$I(\vec{r}) = \int L(\vec{r}')S(\vec{r}')h(\vec{r} - \vec{r}')d^3r' = ([LS] * h)(\vec{r}) \quad (3.9)$$

Taking the Fourier transform of the above gives

$$\tilde{I}(\vec{k}) = [\tilde{L} * \tilde{S}](\vec{k})\tilde{h}(\vec{k}) \quad (3.10)$$

The above equations assume a shift invariant PSF and linear fluorescence response of the sample (Gaskill, 1978). If the illumination intensity is high, fluorescence saturation effects can result in a nonlinear sample response to the illumination intensity $S(L)$.

3.1.3. Resolution enhancement

According to Abbe's diffraction limit (Abbe, 1873), under optimal conditions with minimal background, high signal-to-noise (SNR) and homogenous refractive index, the achievable spatial resolution for conventional wide field fluorescence microscopes is fundamentally limited by the visible wavelength and the NA of existing optical elements to around 200 nm laterally and 500 nm axially. Classical ways of enhancing resolution include using a shorter wavelength, maximizing the NA, and minimizing aberrations. Imaging techniques such as electron microscopy and x-ray-based imaging use waves with shorter wavelengths to resolve finer features, however, unlike optical microscopy, these modalities require sample preparation techniques that are not compatible with live cell imaging.

Deconvolution involves using prior knowledge about the imaging process to increase the SNR in computational post-processing. This process involves using an experimentally measured or computationally simulated PSF to reverse the distortion introduced by the imaging process through the reassignment of intensity to its estimated spatial origin. While this can improve image contrast and spatial resolution in three-dimensional fluorescence microscopy (Agard & Sedat, 1983), the resolution enhancement performance depends on the object imaged, and works better for sparse samples (Heintzmann, 2007).

The resolution enhancement of confocal microscopy can be understood by considering the effective system PSF. For uniform illumination, the light distribution at position \vec{r} in the image plane produced by a point source at position \vec{r}' in the object plane is given by $h_{em}(\vec{r} - \vec{r}')$. The pinhole function $p(\vec{r}')$ determines how much of this distribution is detected. For uneven, or structured, illumination, the resultant distribution in the image plane is scaled by the illumination intensity at the point source $h_{ill}(\vec{r})$. Hence the resultant confocal PSF corresponding to the total integrated intensity is:

$$h_{sys}(\vec{r}) = \int h_{ill}(\vec{r}) h_{em}(\vec{r} - \vec{r}') p(\vec{r}') d^3 r' \quad (3.11)$$

$$h_{sys}(\vec{r}) = h_{ill}(\vec{r}) \int h'_{em}(\vec{r} - \vec{r}') p(\vec{r}') d^3 r' \\ h_{sys}(\vec{r}) = h_{ill}(\vec{r}) (h'_{em} * p)(\vec{r}) \quad (3.12)$$

It can be seen that the detection PSF is a convolution of the mirrored emission PSF $h'_{em}(\vec{r}') = h'_{em}(-\vec{r})$ with the pinhole function:

$$h_{det}(\vec{r}') = \int h'_{em}(\vec{r} - \vec{r}') p(\vec{r}') d^3 r' \quad (3.13)$$

Hence the confocal PSF is equal to the product of the illumination and detection PSF (Wilson & Sheppard, 1984):

$$h_{sys}(\vec{r}) = h_{ill}(\vec{r}) h_{det}(\vec{r}) \quad (3.14)$$

The confocal OTF $\tilde{h}_{sys}(k)$ is given by

$$\tilde{h}_{sys}(k) = \tilde{h}_{ill}(\vec{k}) * (h'_{em}\tilde{p})(\vec{k}) \quad (3.15)$$

Which equivalently is equal to the convolution of the excitation and emission OTF:

$$\tilde{h}_{sys}(\vec{r}) = \tilde{h}_{ill}(\vec{r}) * \tilde{h}_{det}(\vec{r}) \quad (3.16)$$

Assuming that the excitation and emission wavelengths are approximately equal and that the same objectives are used to excite and collect the fluorescence, for an infinitely small pinhole, the detection PSF approaches the illumination PSF, meaning that the resultant confocal PSF is equal to the square of the conventional PSF, resulting in a $1/\sqrt{2}$ reduction in the PSF FWHM (Brakenhoff, Blom & Barends, 1979), and a doubling in OTF-cut off frequency (Sheppard & Choudhury, 1977). However, reducing the pinhole size results in decreased optical detection efficiency, requiring longer exposure times and increased exposure of the sample to the light.

Interferometric detection techniques combined with confocal microscopy further improve the axial (Sheppard & Gong, 1991) and lateral resolution (Wicker & Heintzmann, 2007). Axial resolution enhancement in 4Pi microscopy (Hell, 1990; Hell & Stelzer, 1992) is achieved using two opposing objectives with a common focus for coherent excitation and detection of fluorescence from either side of the sample, maximizing the collection angle. Constructive interference in illumination and/or detection results in modulation of the intensity distribution in the focus, while the increased numerical aperture leads to a reduction in the axial FWHM of the central peak (Hell, 1990). However, to fully exploit this enhancement, the effect of the excitation volume sidelobes needs to be considered, as it can produce ghost images (Hell & Stelzer, 1992b). Interferometric techniques with opposing objective lenses for illumination and detection in a widefield implementation such as I⁵M (Gustafsson, Agard & Sedat, 1999) achieve similar axial resolutions.

Confocal theta microscopy (Lindek & Stelzer, 1994) is a non-interferometric technique which achieves improved axial resolution by introducing an angle θ between the illumination and detection axes. When $\theta = 90^\circ$, the axial extent of the observation volume is substantially reduced, resulting in a near spherical shape of the system PSF. When combined with 4Pi-confocal microscopy, confocal theta microscopy makes the most of the resolution enhancement achieved in 4Pi techniques by suppressing the axial sidelobes (Lindek & Stelzer, 1994). The sidelobes produced by the interference pattern can further be suppressed using two-photon excitation, where the excitation PSF is equal to the square of the illumination intensity (Hell & Stelzer, 1992; Stelzer & Lindek, 1994).

While confocal theta microscopy provides enhancement of axial resolution, similarly to standard confocal microscopy, it remains a point-scanning technique. The widefield implementation of the confocal theta principle of decoupling the illumination and detection axes is realized in single plane illumination microscopy (SPIM) (Huisken et al., 2004). The resultant system PSF in SPIM has been modelled as the product of the illumination and detection PSFs, with consideration of the relative angle between the illumination and detection axes (Engelbrecht & Stelzer, 2006). Simulated PSFs indicate that the axial resolution in SPIM can be better than that in widefield and two-photon microscopy and, in some cases, is better than lower-NA confocal microscopy (Engelbrecht & Stelzer, 2006). **Section 3.1.6** further reviews the approaches to estimating the resolution in a SPIM system.

Other limitations on resolution

While the spatial resolution in an ideal optical system is limited by the NA and wavelength, in a real imaging system the resolution is limited by image contrast, which depends on the number of collected photons. Defining contrast as the difference between the lowest intensity and the peak intensity of the images of two objects, resolution can be expressed in terms of the minimal distance between two objects for a certain level of contrast. The relationship between contrast and distance is described by the contrast transfer function (CTF) for a periodic pattern consisting of black and white stripes of equal width. The smallest resolvable distance between two features – the contrast cut off distance – is the separation between two objects at which the contrast becomes zero (Stelzer, 1998).

Contrast and hence resolution can be degraded by multiple aspects of the imaging process, including aberrations, noise and discrete sampling effects. Noise, or the signal variation over repeated measurements, introduces an uncertainty in the optical measurement, reducing contrast and hence resolution. In fluorescence microscopy, where the number of photons is limited, Poisson noise dominates (Stelzer, 1998). Additionally, resolution is degraded by pixelation: since each pixel provides the total optical system response over a finite area, it will decrease the values of maxima, and increase the values of minima, reducing the contrast (Stelzer, 1998). Undersampling below the Nyquist minimum sampling rate can result in pixel-limited resolution and aliasing (Nyquist, 1928).

For fluorescence microscopy, the emitted light is not solely single wavelength, but can be represented by a spectrum, which results in a broadening of the detection PSF (Hell & Stelzer, 1992), which can be described as the incoherent sum of individual single-wavelength PSFs weighted by the emission spectrum (Becker & Heintzmann, 2019). Using a weighted-average effective emission wavelength will give more accurate estimates of the detection PSF width. The broadening effect can be minimized by restricting the detected spectrum using narrowband emission filters, however, this comes at the cost of fewer collected photons or a longer observation periods required to maintain the SNR.

Super-resolution

In the resolution enhancement techniques discussed above, the illumination and detection remain diffraction-limited. Circumventing Abbe's diffraction limit requires violating one or several of the assumptions made when defining the resolution criterion. Collectively, these techniques are referred to as super-resolution microscopy, or nanoscopy. Near-field techniques such as total internal reflection fluorescence microscopy (TIRFM) (Ambrose, 1956; Axelrod, 1981), and near-field scanning optical microscopy (SNOM, NSOM) (Dürig, Pohl & Rohner, 1986; Oshikane et al., 2007) use evanescent fields to collect information beyond the diffraction limit. However, the exponential decay of evanescent waves limits the application of near field techniques to surface structures (Betzig & Trautman, 1992). Single molecule localization microscopy techniques such as PALM (Betzig et al., 2006) and STORM (Rust, Bates & Zhuang, 2006) achieve sub-diffraction resolution using prior knowledge through consecutive localization of individual point fluorophores at a higher precision than the diffraction-limited intensity distribution produced by a point source.

Structured illumination microscopy (SIM) is a far-field super-resolution technique using inhomogeneous illumination (Gustafsson, 2000; Heintzmann & Cremer, 1999). While both the illumination and detection intensity patterns are diffraction limited, structured high frequency illumination is used to down modulate high spatial frequencies in the sample to lower frequencies supported by the microscope optics. Through computational up-modulation of this information in Fourier space, the OTF region of support is extended, with up to two-fold resolution enhancement given by the combination of the highest spatial frequencies of illumination and detection.

This two-fold enhancement limit is general to techniques which combine spatially varying illumination with a linear sample excitation response (including confocal microscopy) (Scherelleh, Heintzmann & Leonhardt, 2010). Using spatially-varying illumination to circumvent Abbe's limit would require a nonlinear sample response: this principle is used in nonlinear saturated structured illumination microscopy (SSIM) (Gustafsson, 2005; Heintzmann, Jovin & Cremer, 2002) and stimulated emission depletion (STED) (Hell & Wichmann, 1994). The latter is a scanning technique implementing nonlinear saturation for de-excitation using donut shaped depletion beam to shape the PSF beyond the diffraction limit, such that the effective observation volume is reduced.

3.1.4. Characterizing optical sectioning

In a non-optically sectioning system such as a conventional widefield microscope, out-of-focus light reduces contrast of in-focus features. In the three-dimensional optical transfer function, this lack of optical sectioning is represented by the "missing cone" through the centre of the OTF. Optical sectioning can be defined more concretely by considering the attenuation of spatial frequencies with defocus. In a conventional microscope, as defocus is introduced, non-zero spatial frequencies are attenuated, while the spatially uniform background is not. In a confocal microscope, however, all spatial

frequencies, including the uniform background fluorescence, are attenuated with defocus. This results in efficient imaging of detail only from the in-focus plane of the objective, known as optical sectioning (Wilson, 2011).

The fluorescence distribution in a sample can be represented by the superposition of spatial frequencies, plus a constant term corresponding to background. Considering an object with fluorophore distribution $f(x) = m \cos(kx) + 1$, where m is the modulation depth, k is a spatial frequency, and the second term represents a constant background, the image intensity distribution can be expressed as (Wilson, 1989):

$$I(x) = C(0, u) + mC(k, u)\cos(kx) \quad (3.17)$$

Where the $C(k, u)$ transfer function varies with spatial frequency k and normalized optical axial coordinate u that represents defocus (defined in Eq. 3.4). The above equation can be rewritten as

$$I(x) = C(0, u)[1 + m\Gamma(k, u) \cos(kx)] \quad (3.18)$$

Where effective contrast function $\Gamma(k, u)$ is given by

$$\Gamma(k, u) = \frac{C(k, u)}{C(k = 0, u)} \quad (3.19)$$

For conventional widefield microscopy, $C(k = 0, u) = 1$, hence the contrast function is equal to the optical transfer function $\Gamma(k, u) = C(k, u)$. In the limit of large defocus, the image intensity distribution approaches a uniform background $I(x) \approx C(k = 0, u) = 1$.

For an optically sectioning microscope, because the zero-order spatial frequency is attenuated slower than other frequencies, the effective contrast function narrows with increasing defocus. Considering a sample distribution consisting of multiple frequencies, $C(k = 0, u)$ represents an envelope function for the intensity distribution with defocus and is hence a direct measure of optical sectioning strength. In real space, the optical sectioning strength can be expressed in terms of the decay of total energy in an image slice as a function of defocus u (Sheppard & Wilson, 1978):

$$I_{int}(u) = \iint_0^\infty I(x, y, u) dx dy \quad (3.20)$$

For a system without optical sectioning, from intensity flux conservation, the power in any plane must be the same, and hence the laterally integrated axial intensity profile of a fluorescent point source is constant with defocus. This metric has previously been used to quantify optical sectioning in a two-photon microscope (Dong, Koenig & So, 2003).

The normalized laterally-integrated axial intensity profile for a point source is equivalent to the intensity decay of a uniformly fluorescent thin planar object (Wilson, 1989). The axial response to a thin fluorescent sheet can be measured by axial translation of the sheet along the detection axis and has been used as a method for quantifying optical sectioning in a range of imaging systems including structured illumination LSFM (Landry et al., 2019) dual-line scanning (Jin et al., 2021) line-illumination modulation microscopy (Zhong et al., 2021) and OPM (Maioli, 2016).

Alternatively, for a homogeneously-fluorescent thick object, optical sectioning can be evaluated from the response to an infinitely steep edge (Hell & Stelzer, 1992), and has been used to determine light-sheet thickness in OPM (Dunsby, 2008). The intensity decay with defocus when imaging the surface of a perfect reflector was used as one of the first metrics of depth discrimination in non-fluorescent confocal microscopy (Wilson, 1989).

While the terms axial resolution and optical sectioning have occasionally been used interchangeably, it is important to distinguish between the two. In the context of light-sheet fluorescence microscopy, differentiating between the two concepts is particularly useful when comparing the performance of different illumination beams. For example, the axial resolution, defined in terms of the width of the intensity profile of the system PSF along the detection axis is dominated by the smaller of the detection microscope objective axial PSF, or the illumination sheet thickness, whereas the optical sectioning is dominated by the thickness of the light sheet.

3.1.5. Measuring spatial resolution

Measuring the spatial resolution of an optical system is fundamental to assessing its performance, limitations and evaluating whether it is appropriate for a specific application. The two main experimental approaches for quantifying the spatial resolution are based on measurements of the imaging system's response in Fourier and real space. The former is typically done by imaging test targets consisting of repeated bar patterns with varying separations and sizes, with the resolution limit determined by the smallest resolvable set of bars. The MTF can be measured by considering the modulation depth in an image with sinusoidal intensity patterns with varying frequencies (Leung & Donnelly, 2017) and can be computed along one dimension by taking the Fourier transform of the image of an edge-spread intensity distribution such as a knife-edge target (Tatian, 1965). The phase transfer function PhTF is related to wavefront aberrations, and is hence important in adaptive optics, and can be measured interferometrically (Chu et al., 2008).

In real space, the resolution can be characterized by the shape and size of the PSF, with the OTF recovered by taking a 3D Fourier transform. Point-spread function simulation frequently requires rigorous theoretical modelling, and for high-NA, nonparaxial effects and the vector nature of light fields need to be considered (Sheppard & Matthews, 1987), particularly to describe the axial intensity variation (Richards, 1956). Experimentally determined PSFs are often preferable both for system

characterization and deconvolution as they account for any physical deviations from the ideal model and can be used for microscope calibration and troubleshooting. The system response to a point source can be experimentally measured by imaging sub-resolution fluorescent beads (Cole, Jinadasa & Brown, 2011; Gibson & Lanni, 1991), or, alternatively other “point” sources such as quantum dots (Courty et al., 2006; Heidbreder et al., 2010; Li et al., 2018) however aggregate formation makes sample preparation with the latter difficult (Choi et al., 2010).

Experimental PSF measurement using fluorescent beads comes with three main challenges: bead size selection, pixel sampling and SNR considerations. The finite size of the imaged small fluorescent microspheres blurs the PSF, and while smaller point sources provide a more accurate measure of the PSF, larger beads typically offer a brighter signal and enhanced SNR: doubling the microsphere diameter increases the signal by a factor of 8 (Gibson & Lanni, 1991). An upper bound of around 30% of the diameter of the first dark ring of the in-focus 2D PSF was found to be the tolerable bead size for deconvolution reconstructions (Preza et al., 1992). For sufficient pixel sampling of the finer details of the experimentally measured PSF, high resolution detectors or higher magnification lenses are required, however, doubling the magnification or halving the pixel dimensions results in a pixel photon count reduction by a factor of 4 (Gibson & Lanni, 1991). For a system with a space invariant PSF, in the case of insufficient signal for PSF determination, multiple bead images can be coaligned and averaged to increase the SNR.

Quantifying the resolution from images of point sources can be time-consuming and tedious. Image restoration software such as Huygens offers tools such as the PSF Distiller (Scientific Volume Imaging, B. V., 2022) to extract the experimentally measured PSF from 3D bead images for deconvolution. Similarly to how the original object or sample can be restored by deconvolving the image using the known PSF, the PSF can be distilled using known dimensions of the bead/microsphere using an inverse deconvolution algorithm (Van der Voort & Strasters, 1995). Other existing software such as PSFj (Patrick Theer, Cyril Mongis & Michael Knop, 2014) allows rapid automated quantification of the spatially varying PSF across the full FOV by estimating the spatial extent of images of sub-resolution beads (bead spread functions, BSF) through 1D axial and 2D lateral Gaussian fits. The PSF FWHM is extracted by applying correction factors to account for the known bead size. This approach is implemented in PyCalibrate (Corbett, 2021), which calculates the FWHM of the images of the fluorescent features in PSF check slides (Corbett et al., 2018).

The experimental PSF measurement approach in this chapter extends the principle of fitting single- and multi-dimensional Gaussians to intensity profiles of bead images for custom automated characterization of the spatially varying resolution across a volume acquired with a light-sheet fluorescence microscope. The method is also used to determine the sectioning ability across the FOV by considering the laterally

integrated intensity variation with defocus. The resolution and optical sectioning are compared to the theoretically expected system performance.

3.1.6. Resolution in SPIM

Approaches to modelling SPIM resolution

The improvement in axial resolution and optical sectioning in a system with light-sheet illumination over a conventional widefield microscope is due the fluorescence excitation and emission being confined to a thin slice of the sample. One of the earliest approaches for modelling the resolution enhancement in orthogonal illumination-detection LSFM geometry (Engelbrecht & Stelzer, 2006), assumes a space invariant SPIM PSF, modelled as the elementwise product of the illumination and detection PSFs, with the detection PSF calculated for a uniformly illuminated circular aperture, and the illumination PSF calculated for Gaussian illumination of a slit aperture. Experimental PSF estimation is done by fitting Gaussian-like functions to lateral and axial intensity distributions through images of sub resolution fluorescent beads ($n = 5$). After accounting for bead size by convolving the modelled system PSF with a spherical object of the corresponding diameter, and pixelation effects by shifting the detection PSF position by ± 0.5 pixels, the predicted and experimental resolution agree. However, for the low NA illumination, the spatially varying light-sheet thickness is not taken into account.

Becker and others also implement elementwise multiplication to define a theoretical “system PSF” for a LSFM system for the purpose of deconvolution, arguing that insufficiently high pixel sampling during experimental PSF measurements at low magnification limits the accuracy (Becker et al., 2019). Wu et al. similarly used the approach of considering the system PSF as an elementwise product, however, of the detection PSF with the Gaussian illumination profile, rather than the illumination PSF (Wu et al., 2016).

While the lateral resolution with respect to the detection axis is approximately uniform across the FOV, the axial resolution will be modulated by the light-sheet beam width, which varies along the illumination axis. Considering the spatial variation of the system PSF is particularly important in deconvolution, and for assessing the limitations on useable FOV, with the use of spatially varying PSF’s for deconvolution demonstrated in (Kim & Naemura, 2015; Ogier, Dorval & Genovesio, 2008). The above-mentioned work by Becker et al. (2019) found some limited improvement when considering the light-sheet variation in thickness along the direction of propagation but assumed a uniform light-sheet for computational speed and simplicity. Chen et al. used sparse fluorescent bead measurements to estimate a spatially varying PSF for image restoration (Chen et al., 2018). In the approach by Toader et al., spatially varying deconvolution of LSFM data is implemented by combining the image formation model with spatial variation of the effective system PSF (Toader et al., 2021). The model also incorporated optical aberrations represented as Zernike polynomials and took into account mixed Gaussian and Poisson noise in the reconstruction, overall outperforming deconvolution with a spatially invariant PSF.

In this chapter, we begin by treating the resolution in a LSFM system from the perspective of image formation, followed by a series of approximations to reduce the complexity of the problem. Considering a light-sheet fluorescence microscope with decoupled illumination orthogonal to the detection axis z , image formation with spatially varying illumination can be described similarly to that in **Section 3.1.2-3.1.3**. In this case, the image is acquired by scanning the object along detection axis z through a static light-sheet aligned with the detection focal plane x - y (or, equivalently, synchronous translation of the detection plane and light-sheet through the sample). Rewriting Eq. 3.9 in Cartesian coordinates, the recorded image intensity distribution I for a sample fluorophore distribution S and light-sheet profile L scanned along z can be written as:

$$I(x, y, z) = \iiint L(x', y', z - z') S(x', y', z') h(x - x', y - y', z - z') dx' dy' dz' \quad (3.21)$$

Where h is the PSF of the detection system. For an “ideal” light-sheet with an intensity distribution invariant in x' and y' , the above equation can be simplified to

$$I(x, y, z) = \iiint L(z - z') S(x', y', z') h(x - x', y - y', z - z') dx' dy' dz' \quad (3.22)$$

And hence the image formation process can be described in terms of an “effective PSF” $h' = hL$, similarly to the confocal case:

$$I(x, y, z) = \iiint S(x', y', z') h'(x - x', y - y', z - z') dx' dy' dz' \quad (3.23)$$

In reality, diffraction prevents light-sheets from maintaining a uniform thickness over its entire extent, and hence, neglecting any intensity modulation along the light-sheet propagation direction, the “system” PSF will vary spatially with the position along the light-sheet propagation x' , with its axial profile equal to the detection PSF axially modulated by the light-sheet thickness at that point in the sample: $h'(x') = h \times L(x')$. In the rest of this chapter, we will evaluate the spatial resolution in a LSFM system by considering a spatially varying system PSF defined as the product of the detection PSF and illumination profile at that point along the light-sheet propagation axis. The next sections treat the detection PSF, the Gaussian light-sheet profile and the system PSF in more detail.

Detection and illumination PSF for uniformly filled pupils

For a diffraction-limited optical system with a uniformly filled pupil, we can describe the spatial resolution in terms of the lateral and axial FWHM of the central lobe of the Airy pattern intensity distribution (see Eq. 3.1 and 3.2) (Wilson, 2011):

$$\Delta r_{FWHM}^{det} = \frac{0.51 \lambda_{em}}{NA_{det}} \quad \Delta z_{FWHM}^{det} = \frac{1.77 n \lambda_{em}}{NA_{det}^2} \quad (3.24, 3.25)$$

where λ_{em} is the wavelength of emitted fluorescence, NA_{det} is the numerical aperture (NA) of the detection objective, and n is the RI of the surrounding medium. Similarly, the lateral and axial FWHM of the diffraction-limited illumination PSF for a uniformly filled pupil can be expressed as:

$$\Delta r_{FWHM}^{ill} = \frac{0.51\lambda_{ex}}{NA_{ill}} \quad \Delta z_{FWHM}^{ill} = \frac{1.77n\lambda_{ex}}{NA_{ill}^2} \quad (3.26, 3.27)$$

Here, λ_{ex} is the excitation wavelength and NA_{ill} is the NA of the illumination objective.

Gaussian illumination beam

For an objective pupil illuminated with a Gaussian beam, using the coordinate system defined in **Figure 3.1**, under the paraxial ($w_0 \gg \lambda/n$) scalar approximation, the lateral (r') and axial (x') intensity, distribution for a focused 3D Gaussian beam propagating along the X' -axis can be expressed as (Siegman, 1986; Svelto, 2010):

$$I(r', x') = I_0 \left(\frac{w_0}{w(x')} \right)^2 \exp \left(\frac{-2r'^2}{w^2(x')} \right) \quad (3.28)$$

Where I_0 is the on-axis intensity at its beam waist $w_0 = w(x' = 0)$, here defined as the radial distance from the beam axis at it focus to the point where the beam intensity falls to $1/e^2$ of its maximum. At different points along the beam axis, the beam radius will vary as

$$w(x') = w_0 \sqrt{1 + \left(\frac{x'}{x_R} \right)^2} \quad (3.29)$$

Here, x_R is the Rayleigh range, the distance from the beam waist until where the beam cross section is doubled and $w(x' = x_R) = \sqrt{2}w_0$.

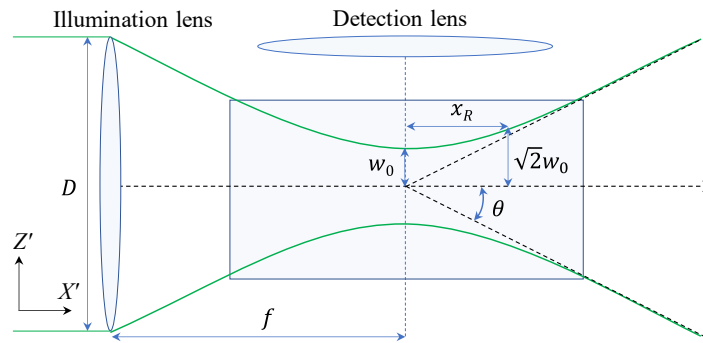


Figure 3.1 Gaussian illumination beam focused by lens with focal length f and diameter D propagating along the X' -axis, perpendicular to the detection axis Z' . The beam waist radius is denoted by w_0 , θ is the divergence half-angle, and x_R is the Rayleigh range – the distance from the beam waist until the point where the beam radius is equal to $\sqrt{2}w_0$.

The transverse beam profile $I(r')$ at any point along the beam axis is Gaussian:

$$I(r') \propto \exp\left(\frac{-2r'^2}{w(x')^2}\right) \quad (3.30)$$

while the axial intensity profile $I(x')$ for $r' = 0$ follows a Lorentz distribution centered on $x'=0$:

$$I(r' = 0, x') = I_0 \left(\frac{w_0}{w(x')} \right)^2 = \frac{I_0}{1 + \frac{x'^2}{x_R^2}}. \quad (3.31)$$

In the paraxial case, for a Gaussian beam of wavelength λ_{ex} focused by a lens with focal length f and diameter $D = 2w$, ignoring aperture truncation effects, the beam waist radius measured at $1/e^2$ of the on-axis intensity can be expressed as (Svelto, 2010):

$$w_0 = \frac{\lambda_{ex}}{n\pi\theta} \approx \frac{\lambda_{ex}}{\pi NA_{ill}} \approx \frac{2\lambda_{ex}f}{n\pi D} \quad (3.32)$$

Where n is the refractive index of the immersion media, θ is the beam divergence half angle and $NA_{ill} = n\sin\theta$ is the numerical aperture of the beam measured at $1/e^2$ of the on-axis intensity, which for small divergence angles can be approximated as $NA_{ill} \approx n\theta \approx \frac{nD}{2f}$. For a Gaussian beam focused by a physical lens, the waist will be larger due to lens truncation of the tails of the Gaussian profile. Along the beam propagation axis, the confocal parameter C_P , used to characterize the depth of field (DOF) of a focused Gaussian beam is defined as twice the Rayleigh range, and can be expressed as:

$$C_P = 2x_R = \frac{2\pi n w_0^2}{\lambda_{ex}} = \frac{2n\lambda_{ex}}{\pi NA_{ill}^2} \quad (3.33)$$

The FWHM of the radial intensity distribution $I(r')$ at different points along the illumination beam axis x' can be expressed as:

$$\text{FWHM}_{ill}^{lat}(x') = w(x') \times \sqrt{2\ln 2} \quad (3.34)$$

Which at the beam waist is equal to:

$$\text{FWHM}_{ill}^{lat}(x' = 0) = w_0 \times \sqrt{2\ln 2} = \frac{\lambda_{ex}}{\pi NA_{ill}} \times \sqrt{2\ln 2} \quad (3.35)$$

For a radially symmetric focused Gaussian beam, from the axial intensity distribution expression $I(r' = 0, x')$ in Eq. 3.31, it can be seen that at the Rayleigh distance away from the focus, the intensity falls to half of the peak:

$$I(r' = 0, x' = x_R) = \frac{I_0}{2} \quad (3.36)$$

Hence, along the beam propagation axis, the FWHM of the intensity distribution can be defined as twice the Rayleigh range:

$$\text{FWHM}_{ill}^{ax} = 2x_R = \frac{2n\lambda_{ex}}{\pi NA_{ill}^2} \quad (3.37)$$

Gaussian 2D light-sheet

However, a Gaussian light-sheet generated by focusing a Gaussian beam in solely one lateral dimension is different to the well-known intensity distribution of a focused radially-symmetric beam. Using the same definitions for Rayleigh range x_R and beam width $w(x')$ as above, the Gaussian beam propagating along the X' -axis and focused only along the Z' dimension will have the following intensity distribution (Du, Zhao & Zhao, 2019; Verdeyen, 2000):

$$I_{2D}(z', x') \propto \frac{1}{w(x')} \exp\left(\frac{-2z'^2}{w^2(x')}\right) \quad (3.38)$$

Hence, while the transverse intensity profile $I_{2D}(z')$ at any point along the beam axis also follows a Gaussian distribution, similarly to the expression for $I(r')$ in Eq. 3.30, the axial intensity profile will vary inversely with the beam width:

$$I_{2D}(z' = 0, x') \propto \frac{1}{w(x')}. \quad (3.39)$$

From Eq. 3.29, it can be seen that the on-axis intensity in Eq. 3.39 drops to half of its maximum at a distance of $x' = \sqrt{3}x_R$ away from the waist, when the beam radius has doubled: $w(x' = \sqrt{3}x_R) = 2w_0$. At $x' = x_R$, the on axis intensity will drop by $\sqrt{2}$ compared to the intensity at the waist. Hence, while the FWHM_{ill}^{lat} for a 2D Gaussian light-sheet is identical to the equivalent expression for a focused 3D Gaussian beam, the FWHM of the intensity profile along the beam propagation axis is modified to:

$$\text{FWHM}_{ill}^{ax} = 2 \times \sqrt{3}x_R = \frac{2\sqrt{3}\pi n w_0^2}{\lambda_{ex}} = \frac{2\sqrt{3}n\lambda_{ex}}{\pi NA_{ill}^2} \quad (3.40)$$

Hence, the propagation length of a 2D static light-sheet, when defined in terms of the axial intensity profile, is a factor of $\sqrt{3}$ larger than that for a digitally-scanned light-sheet with the same beam waist. Intuitively, the longer propagation length defined in terms of the on-axis intensity can be understood by considering that the energy density will solely decay in one lateral dimension with increased distance along the beam propagation axis away from the waist.

System PSF

As explained earlier in this section, due to the spatially varying light sheet profile, the image formation model from **Section 3.1.2** does not simplify to object convolution with a space-invariant system PSF. Considering a light-sheet fluorescence microscope where the detection axis z' is perpendicular to the illumination axis x' (as shown in **Fig. 3.1**), the system PSF at the light-sheet beam waist can be modelled as the elementwise product of the Gaussian beam illumination profile and the detection PSF:

$$h_{sys}(x', y', z') = h_{det}(x', y', z') \times h_{ill}(x', y', z') \quad (3.41)$$

Considering each of the three dimensions independently, the axial (z') and lateral (x' and y') profiles of the system PSF can be expressed as:

$$h_{sys}^{x'} = h_{det}^{lat} \times h_{ill}^{x'} \quad (3.42)$$

$$h_{sys}^{y'} = h_{det}^{lat} \times h_{ill}^{y'} \quad (3.43)$$

$$h_{sys}^{z'} = h_{det}^{ax} \times h_{ill}^{z'} \quad (3.44)$$

For a static or digitally-scanned light-sheet in the geometry defined above, the illumination profile is assumed to be constant along y' , and hence the system PSF along that dimension is given by $h_{sys}^{y'} = h_{det}^{lat}$ and hence $FWHM_{sys}^{y'} = FWHM_{det}^{lat}$.

Along the detection axis, the system PSF can be expressed as the product of the axial profile of the detection PSF, and the transverse profile of the illumination. The central lobe of the lateral and axial intensity profiles of the detection PSF, given by the Airy pattern for a uniformly filled pupil, can be approximated by a Gaussian (Zhang, Zerubia & Olivo-Marin, 2007). As shown earlier in this section, the transverse profile of a radially symmetric 3D Gaussian beam and a 2D Gaussian light-sheet is Gaussian at any point along the propagation axis. As can be seen from the following relationship, the product of two Gaussians gives another Gaussian (Bromiley, 2003):

$$e\left(-\frac{x^2}{a^2}\right) \times e\left(-\frac{x^2}{b^2}\right) = e\left(-x^2\left(\frac{a^2+b^2}{a^2b^2}\right)\right) \quad (3.45)$$

The FWHM of the product of the two Gaussians with $FWHM_1$ and $FWHM_2$, can be expressed as

$$FWHM_{12} = \frac{FWHM_1 \times FWHM_2}{\sqrt{FWHM_1^2 + FWHM_2^2}} \quad (3.46)$$

Hence the FWHM of the axial system PSF can be approximated as

$$FWHM_{sys}^{z'} = \frac{FWHM_{det}^{ax} \times FWHM_{ill}^{z'}}{\sqrt{FWHM_{det}^{ax}^2 + FWHM_{ill}^{z'}^2}} \quad (3.47)$$

Where $FWHM_{det}^{ax}$ is the axial detection PSF FWHM and $FWHM_{ill}^{z'}$ is the FWHM of the transverse illumination profile, which is proportional to the beam width varying along the beam propagation axis:

$$FWHM_{ill}^{z'} = w(x') \times \sqrt{2 \ln 2} \quad (3.48)$$

Along the illumination axis x' , the peak irradiance of a focused 3D Gaussian beam has a Lorentzian profile, while a 2D Gaussian light-sheet on-axis intensity varies inversely with the beam width (see Eq. 3.31 and 3.39). However, for an overfilled excitation objective, the central lobe of the axial intensity profile will tend to a Gaussian, and hence the lateral PSF FWHM along the illumination beam axis x' can similarly written as

$$FWHM_{sys}^{x'} = \frac{FWHM_{det}^{lat} \times FWHM_{ill}^{x'}}{\sqrt{FWHM_{det}^{lat^2} + FWHM_{ill}^{x'^2}}} \quad (3.49)$$

However, as typically $FWHM_{ill}^{x'} \gg FWHM_{det}^{lat}$, we have $FWHM_{sys}^{x'} \approx FWHM_{det}^{lat}$ and hence we expect only minor modulation of the system PSF along the direction of the light-sheet propagation at the beam waist.

In the next section, the spatially varying resolution in the light-sheet system used in this thesis is considered through MATLAB simulation and Zemax modelling of the illumination path.

3.2. Modelling the system resolution

3.2.1. System PSF for uniformly filled illumination and detection pupils

The aim of this section is to compare 3 models for MATLAB-simulation of the spatially varying axial resolution of a LSFM system along the illumination axis for orthogonal illumination-detection geometry. The models are referred to as the following: the physical *image formation (IF)* model, *space-invariant (SI)* multiplication model and *spatially-varying (SV)* multiplication model.

Illumination and detection PSF

As a starting point, we consider the illumination and detection PSFs for uniformly filled pupils of the illumination and detection objectives respectively. For a diffraction-limited widefield detection system, the lateral and axial resolutions can be expressed in terms of the FWHM of the detection PSF (Section 3.1.6, Eq. 3.24 - 3.27). Hence for objective O4 with numerical aperture of $NA = 1$, peak emission wavelength $\lambda_{em} = 525$ nm, and RI of immersion media of $n = 1.33$, the diffraction limited lateral and axial FWHM for the detection PSF are given by

$$\Delta r_{FWHM}^{det} = \frac{0.51\lambda_{em}}{NA_{det}} = 0.268 \mu m, \quad \Delta z_{FWHM}^{det} = \frac{1.77n\lambda_{em}}{NA_{det}^2} = 1.236 \mu m$$

Similarly to the detection PSF, for a uniformly filled excitation objective O3 with a $NA_{ill} = 0.3$, excitation wavelength $\lambda_{ex} = 488$ nm, and immersion media RI of $n = 1.33$, the lateral and axial FWHM for the illumination PSF are equal to $\Delta r_{FWHM}^{ill} = 0.830 \mu m$ and $\Delta z_{FWHM}^{ill} = 12.76 \mu m$ respectively.

The detection and illumination PSF three-dimensional intensity distributions were simulated using the Java-based “PSF generator” application (Kirshner et al., 2013) using the Born & Wolf scalar-based diffraction model (Born & Wolf, 1980). The PSFs were generated using the wavelength, NA and RI input parameters listed above for a uniformly filled pupil. To compromise between adequate spatial sampling of the high-NA objective focus and computational time in the following analysis, the PSFs were simulated across a $201 \times 201 \times 201$ pixel matrix corresponding to a $20 \times 20 \times 20 \mu m$ volume with isotropic voxels size of 100 nm in each direction. The light-sheet is simulated through lateral scanning of the illumination PSF perpendicular to the detection axis. The central region of the X-Z orthoslice through the centre of the detection and illumination PSFs is shown in **Fig 3.2a&b**.

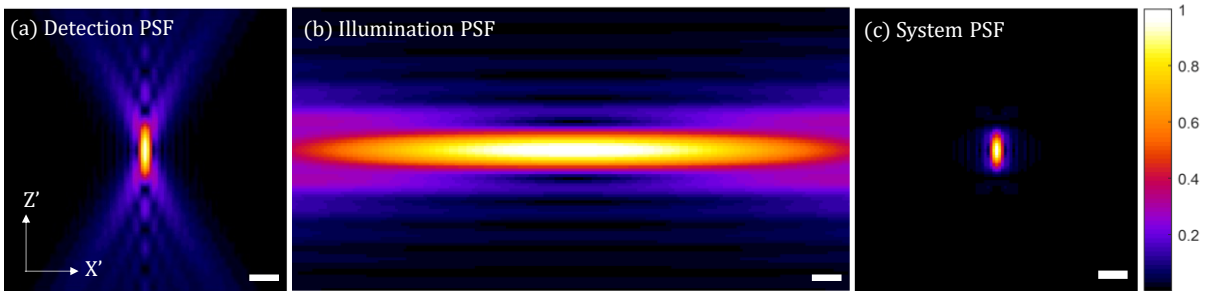


Figure 3.2 Simulated detection (a), illumination (b) and system PSF (c) modelled for uniformly filled pupils. Scalebar is 1 μm . Gamma correction of 0.5 was applied to all three plots to visualize weaker features.

Image formation

For direct comparison with experimental PSF measurement (described in **Section 3.3**), the object is modelled as an array of (pixelated) uniformly fluorescent spheres with 200 nm diameter (**Fig. 3.3a**), with the centres distributed at 2 μm intervals along the illumination axis within a 3D matrix of equal size and spacing as those of the modelled PSFs.

The image formation process for the *IF model* is simulated the following steps: a volume is acquired by the synchronous translation of the detection plane and light-sheet relative to the sample along the detection axis z' using the *circshift* function. At each z -scan position, the object undergoes elementwise multiplication with the illumination profile, followed by 3D convolution with the space-invariant detection PSF using the *convn* function. The image recorded by the detector is found by selecting the plane in the resulting volume corresponding to the position of the illumination sheet. As the illumination is scanned through the sample, a z -stack of images is built up.

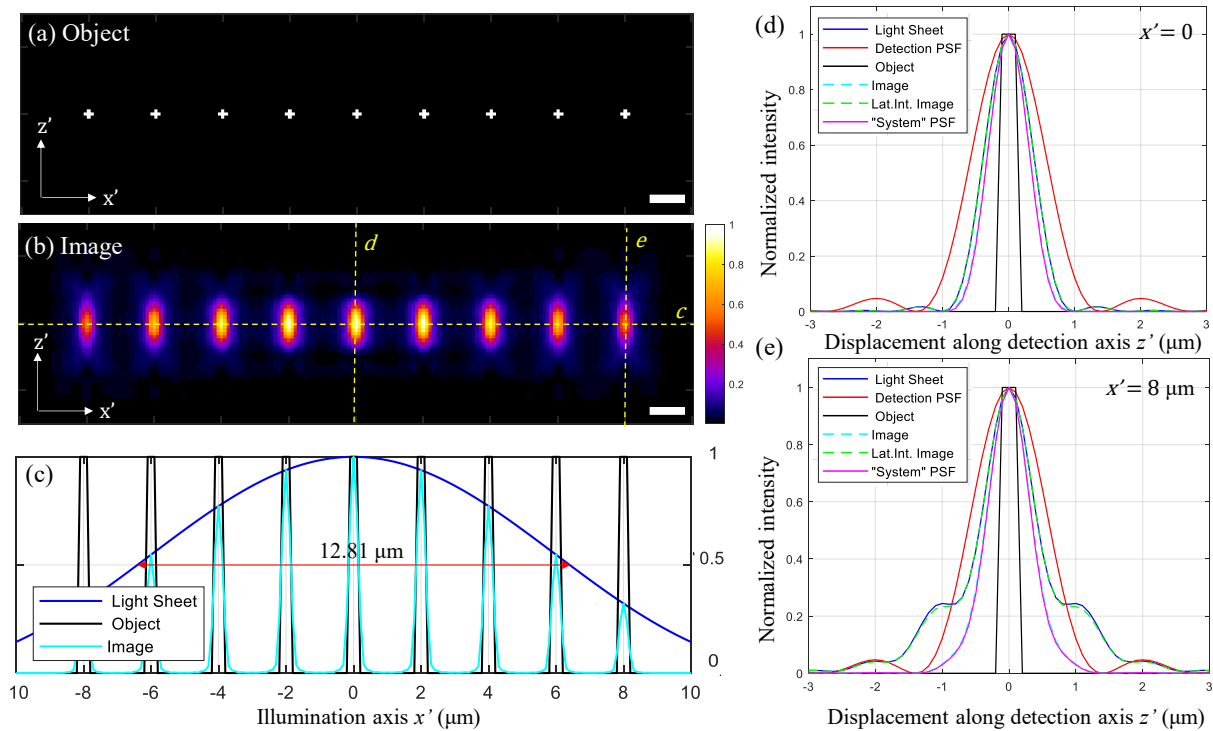


Figure 3.3 Spatially varying axial resolution in LSFM simulated using image formation. (a) XZ-orthoslice through a simulated object consisting of an array of identical (pixelated) spheres spaced 2 μm apart, over a $\pm 8 \mu\text{m}$ range from the centre. (b) XZ-orthoslice through the image of the object shown in (a), generated using the *image formation* model. (c) Normalized intensity profile along the illumination axis x' , illustrating the intensity modulation of the bead images (cyan) at increasing distance away from the beam waist. The confocal parameter and axial FWHM of the illumination beam (blue) is 12.81 μm . (d-e) Line profile along the detection axis z' through the intensity distributions for the 200 nm bead object (black line), detection PSF (red), illumination profile (blue), effective system PSF (magenta), image (dashed cyan) and laterally integrated image for object at (d) the beam waist ($z'=0$) of the illumination profile and (e) at $z'=8 \mu\text{m}$ displacement along the light-sheet. The voxel size for the simulation was $100 \mu\text{m} \times 100 \mu\text{m} \times 100 \mu\text{m}$.

In the *space-invariant* multiplication model, the image is generated by using the MATLAB *convn* function to convolve the 3D object matrix with the spatially invariant “system PSF” (**Figure 3.2c**), defined as the elementwise product of the simulated detection PSF and light-sheet intensity profiles.

For the *spatially-varying* multiplication model, the spatially-varying (along the x' -axis only) system PSF is computed by modulating the detection PSF only in the axial direction through multiplication with the axial profile through the illumination at each x' -position along the light-sheet. To generate the image at that point along the illumination axis, the object is convolved with the system PSF for that x' -position using the *convn* function. The process is repeated for each of the positions along the x' -axis to build up the full image. Here, the process was modelled for a sparse object, and hence the spatially-varying system PSF was sampled at discrete points corresponding to the centre of each bead.

XZ-slices through the object and image generated using the *image formation* model are shown in **Figure 3.3a&b**. **Figure 3.3c** shows the intensity profile along the illumination axis (line “c” in **Fig. 3.3b**) for the object, image and light-sheet. The illumination modulates the intensity distribution along the x' -axis and results in degraded axial resolution away from the waist. The axial profiles for a bead object at the centre of the light-sheet (line d) and at 8 μm displacement away from the illumination beam waist (line “e”) is shown in **Figures 3.3d&e** respectively. The wider beam width away from the waist results in axial broadening of the image profile. The axial profile of the laterally integrated image intensity closely follows the illumination curve indicating the optical sectioning introduced by the illumination.

A summary of the FWHM, estimated from the linearly interpolated positions through the linear intensity profiles in the axial and lateral directions for the three different computational models (*SI*, *SV*, and *IF*) is given in **Table 3.1**. We can see that at the beam waist ($x' = 0$), the estimated axial PSF, image and laterally integrated image FWHM is identical across all three models: 0.706 μm , 0.718 μm and 0.838 μm respectively. However, unlike the other two, the *SI* model does not show the expected degradation of the axial resolution with increasing displacement from the waist along the light-sheet propagation direction. The lateral system PSF and image FWHM doesn’t show measurable increase with increasing distance from the waist, as expected for the minimally varying lateral resolution over the FOV in a LSFM system is minimal (see **Section 3.1.6**).

For computational speed and simplicity, the axial resolution variation along the illumination axis can be closely approximated using the *SV* model, where the detection PSF is modulated along detection axis only, and the modulation varies with the thickness of the light-sheet along the illumination axis. Since the spatially-varying PSF only needs to be calculated for each position along the illumination axis, this offers a speed advantage to the full *image formation* approach, or ones that consider a system PSF spatially-varying along all three dimensions. These results are in agreement with the simplification that the spatially-varying axial resolution in LSFM can be approximated using a “system PSF” that varies only along the illumination axis.

				Displacement along x' (μm)				
				0	2	4	6	8
	FWHM (μm)	X'	Y'	Z'				
Detection PSF		0.276		1.241				
Illumination PSF		12.806	∞	0.838	0.840	0.845	0.859	0.892
System PSF	<i>SI Model</i>	0.276		0.706				
	<i>SV Model</i>			0.706	0.706	0.708	0.713	0.732
Image	<i>SI Model</i>	0.301		0.718				
	<i>SV Model</i>			0.718	0.719	0.721	0.727	0.738
	<i>IF Model</i>							
Lat. Integrated Image	<i>SI Model</i>	-		0.838				
	<i>SV Model</i>			0.838	0.839	0.845	0.859	0.894
	<i>IF Model</i>							

Table 3.1 Comparison of resolution simulations from the *space-invariant (SI) multiplication model*, *spatially varying (SV) multiplication model* and the *image formation (IF) model*. Axial full-width half-maximum (FWHM), calculated from linearly interpolated positions through one-dimensional linear profiles through the intensity distributions for the simulated detection, illumination and system PSF, as well as the axial profile and laterally integrated axial profiles through images of the 200 nm bead objects at various positions along the illumination axis.

So far, the light-sheet profile has been modelled as the digitally scanned illumination PSF profile for a uniformly filled pupil. However, the system implements two different illumination modes: mSPIM and DSLM, designed to achieve different light-sheet profiles, with a larger confocal parameter for the former, and a tighter beam waist for the latter. The optical components in each beam path magnify the illumination beam to underfill and overfill the excitation objective for the two modes respectively. The following section uses computational modelling of the illumination path to consider the effects of beam truncation due to aperture clipping and optical aberrations introduced by the lenses on the final beam waist and confocal parameter of the focused illumination beam in the sample plane.

3.2.2. Modelling the illumination path in Zemax

The optical components on the excitation path affect the size and quality of the illumination beam. The influence of these components was analysed by modelling the two illumination paths in Zemax OpticStudio 16.5 (lens data provided in **Figure A3.1** and **A3.2 (Appendix A3)**) using the Physical Optics Propagation (POP) tool (Zemax, 2016), which models the propagation of the beam wavefront through an optical system. The beam is represented using an array of discretely sampled points of a user-defined beam profile, such as a Gaussian of a specified beam width. The POP tool uses vector representation of the electrical field with a first approximation made to neglect the axial component, and considers the effect of finite lens apertures to model the expected beam profile after propagation through a series of known optical components by computing a transfer function. Automatic sampling was chosen to compromise between computational time and calculation accuracy.

The illumination path was modelled for a 488 nm wavelength collimated Gaussian input beam profile with the $1/e^2$ beam waist half-width (HW) set to 1.262 mm to match the experimentally measured profile after the collimating objective O1. The cylindrical lens in the mSPIM path, achromatic doublets in the DSLM path, and Plossl lenses were modelled using the Zemax lens files provided by the manufacturer. As the Zemax lens for the used objectives are not available, the refocusing objective O2 and excitation objective O4 were modelled as paraxial lenses (ideal thin lens surfaces) with defined back focal lengths and clear semi-diameters to account for the effect of aperture clipping of the Gaussian beam.

The back focal plane diameter of an objective is given by $BFP_d = 2NA \times f_{back}$, where the back focal length is equal to $f_{back} = f_{TL}/m$, where f_{TL} is the focal length of the tube lens designed by the manufacturers to be used with that objective, and m is the magnification stated on the objective (Stelzer, 2006). To ensure a 4f relay arrangement, the lenses were separated by the sum of the distances from the lens surface to plane of best focus. All lens separations were optimized by determining the distance-to-focus by propagating a collimated Gaussian beam with the required beam diameter.

Beam waist

Figure 3.4 shows linear profiles through the centre of the 2D irradiance distribution in the image plane, calculated using POP for beam propagation through the two illumination paths. For the beam waist formed by the DSLM illumination path (**Figure 3.4a**), overfilling of the excitation objective results in beam truncation and sidelobes, hence the beam waist (FWHM and $1/e^2$ HW) respectively were determined from lateral coordinates calculated through linear interpolation between the two data points directly above and below the relevant intensity. The lateral intensity distribution for the radially symmetric DSLM illumination beam resulted in a beam waist of 0.876 μm FWHM. For the Gaussian light-sheet generated by the mSPIM illumination path with an underfilled excitation objective and a beam focused preferentially in the z' -direction, the beam waists, calculated by fitting 1D Gaussian

distributions (**Figure 3.4b**), were estimated as 2.18 μm and 450 μm FWHM respectively for the fast and slow lateral axes.

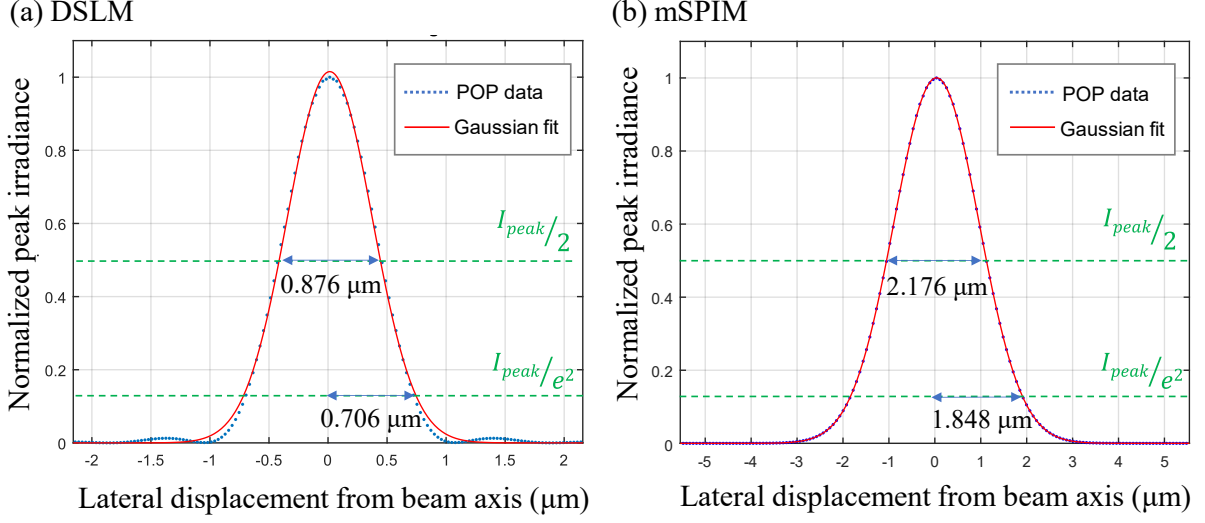


Figure 3.4 POP simulation of beam waist at focus for the DSLM and mSPIM illumination modes. One-dimensional lateral irradiance profiles (blue dotted line) and Gaussian fits (red line) through the irradiance in the focal plane of the (a) DSLM and (b) mSPIM illumination paths (fast Z' -axis). The FWHM of the intensity distributions are given by 0.876 μm and 2.176 μm respectively, corresponding to a $1/e^2$ half-width (HW) of 0.706 μm and 1.848 μm for the two illumination modes respectively.

Axial illumination profile

Figure 3.5 shows the variation of the peak irradiance with defocus along the illumination axis, measured by shifting the image plane and sampling the peak irradiance provided by the POP report. For a radially symmetric Gaussian beam, at the Rayleigh distance x'_R away from the beam waist, the beam radius $w(x' = x'_R) = w_0\sqrt{2}$ and hence $I(0, x' = x'_R) = I_0/2$. For the DSLM beam path, the confocal parameter can directly be estimated from the range along the beam axis where peak irradiance is higher than half of the peak intensity at the beam focus (**Figure 3.5a**).

The on-axis intensity for the tightly focused beam did not follow the expected Lorentzian profile, and was well described by a Gaussian distribution, which is consistent with an overfilled excitation objective. The FWHM of the Gaussian fit to the intensity profile was found to be 12.17 μm , which is slightly shorter than the expected FWHM for a uniformly filled pupil ($\Delta z_{FWHM}^{ul} = 12.76 \mu\text{m}$, see **Section 3.2.1**), and larger than the confocal parameter for a focused radially symmetric Gaussian beam $C_P = 2x_R = 2n\pi w_0^2/\lambda_{ex} = 8.54 \mu\text{m}$, calculated for the beam waist radius $w_0 = 0.706 \mu\text{m}$ estimated using the POP tool, indicating beam truncation and a profile resembling a flat top beam more than that of a Gaussian. The POP results demonstrate some axial asymmetry is present with positive and negative defocus, with the intensity dropping to half the peak at $x'_R = -5.626 \mu\text{m}$ and $+6.547 \mu\text{m}$ respectively, suggesting the presence of positive spherical aberration. For the mSPIM beam path where the beam is solely focused in one direction, the peak irradiance with defocus along the beam axis varies inversely

with the beam width, giving a confocal parameter of $C_P = 2x_R = 58.3 \mu\text{m}$, dropping to half the peak intensity at $x' = \sqrt{3}x_R = 50.5 \mu\text{m}$ (**Figure 3.5b**).

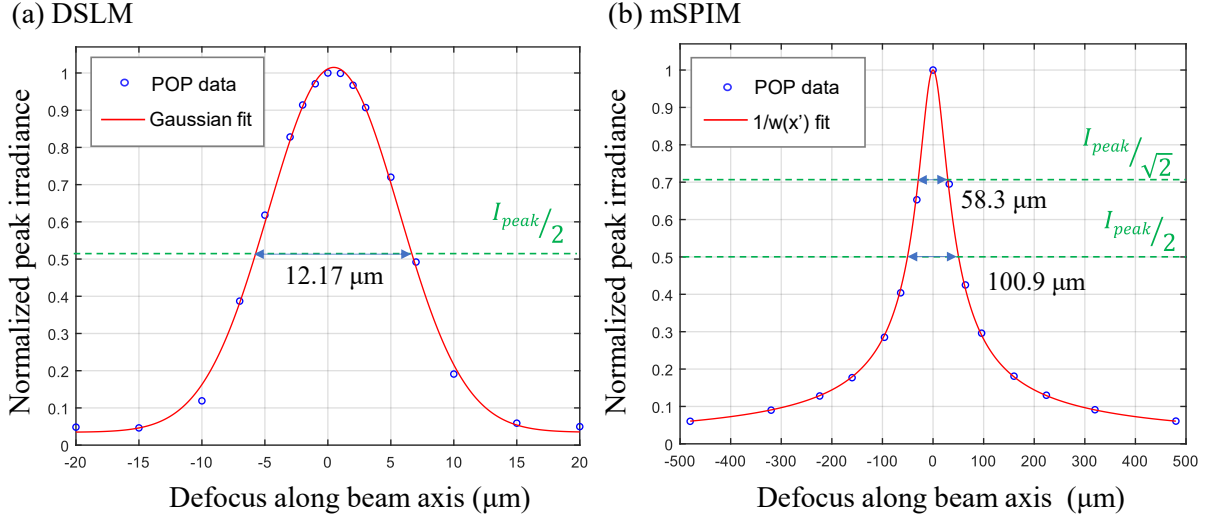


Figure 3.5 POP simulation of on-axis intensity with defocus for DSLM and mSPIM illumination modes. One-dimensional normalized peak irradiance profiles along the beam propagation direction for the DSLM +ASLM (a) and mSPIM (b) illumination paths sampled by axial translation of the image plane of the illumination path. The intensity distributions (blue circles) were fitted with a Gaussian plus offset fit, and $1/w(x')$ for (a) and (b) respectively (red curves).

The confocal parameter can also be estimated by considering the beam width variation with defocus along the beam axis. This was implemented by fitting 1D Gaussian distributions to the lateral irradiance, sampled at various defocus increments along the beam axis (**Figure 3.6**). For the DSLM illumination beam path (**Figure 3.6a**), the beam width variation with defocus is flattened in the $x' = \pm 5 \mu\text{m}$ region, indicating extended DOF of the illumination due to spherical aberration. The confocal parameter, sampled by linear interpolation of the horizontal axis coordinate between the two data points closest to $w(x' = x'_R) = w_0\sqrt{2}$ is equal to $C_P = 2x_R = 12.08 \mu\text{m}$, within interpolation error of the confocal parameter estimated from the on-axis irradiance (12.17 μm).

For the beam width variation for the mSPIM illumination path (**Figure 3.6b**), the beam diverged slower than for a 3D radially symmetric Gaussian beam of the same waist. Fitting the distribution with a function for $w(x')$ with the decoupled beam parameters w_0 and x'_R yielded a beam waist of 1.848 μm and a confocal parameter of 58.3 μm , in agreement with the value derived from the on-axis irradiance profile in **Figure 3.5b** and those calculated from the beam waist. This demonstrates that for a 2D light-sheet, defining the Rayleigh range as the point where the beam width increases by $\sqrt{2}$ compared to the waist is equivalent to the range over which the axial intensity is greater than $1/\sqrt{2}$ of the peak on-axis intensity. The calculated and measured beam waists and confocal parameters for the two modes are summarized in **Table 3.2** below.

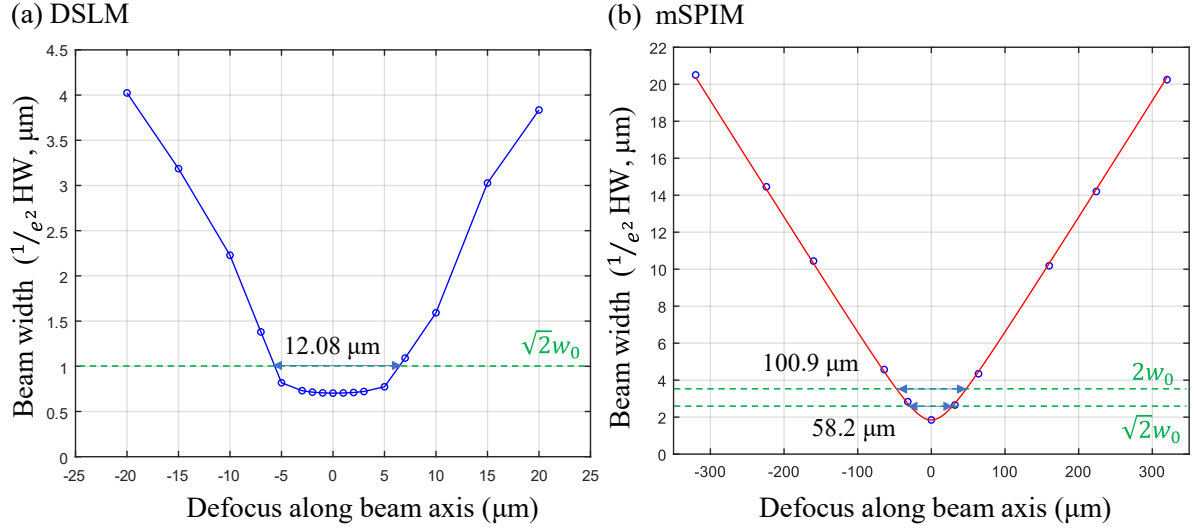


Figure 3.6 Calculated beam width variation with defocus for the DSLM and mSPIM illumination modes. Beam width ($1/e^2$ HW) calculated by fitting one dimensional Gaussians to the lateral irradiance sampled using POP tool at different positions along the (a) DSLM and (b) mSPIM illumination beam axes. The confocal parameters are estimated as 12.08 μm and 58.2 μm for the two illumination modes respectively. The measured beam width datapoints are (a) connected with an eye-guide (blue line) and (b) fitted with the expression for $w(x')$ with uncoupled variables x_R and w_0 (red curve)

Illumination mode		Beam waist (μm)		Rayleigh Range (μm)			Confocal Parameter, $2 x_R $ (μm)		
		$1/e^2$ HW	FWHM	Calculated from waist	Measured (POP)		Calculated from waist	Measured (POP)	
					$-x_R$	$+x_R$			
DSLM	DL	0.705	0.830	4.255	N/A		8.511	N/A	
	POP	0.706	0.876	4.267	-5.626	6.547	8.534	12.17	
mSPIM (fast axis)		POP	1.848	2.176	29.24	-29.10	29.10	58.48	58.20

Table 3.2 Beam waists, Rayleigh ranges x_R and confocal parameters $C_P = 2|x_R|$ estimated for the DSLM and mSPIM illumination modes, measured by considering the lateral irradiance profile and axial peak irradiance calculated using the POP tool, along with the diffraction limited (DL) values for a uniformly filled excitation pupil.

Axial resolution at the beam waist

Using the elementwise multiplication approach for the effective system PSF outlined in **Section 3.1.6**, by approximating the lateral and axial one-dimensional intensity profiles through the detection PSF and light-sheet illumination profile as Gaussians, we can estimate the expected lateral and axial FWHM of the system PSF at the light-sheet beam waist. The variation of the axial system PSF FWHM with illumination and detection NA is shown in **Figure 3.7a**. **Figure 3.7b** shows the equivalent for the PSF FWHM along the detection axis for the corresponding range of illumination and detection PSF FWHM along the detection axis z' . As the lateral PSF FWHM scales inversely with the NA, while the axial FWHM scales inversely with NA^2 , a decrease in the illumination NA has more effect than the equivalent reduction in the detection NA. At higher detection NA, the illumination NA gives less

improvement in axial resolution than at lower detection NA – in other words, the axial FWHM at high detection NA is dominated by the detection PSF.

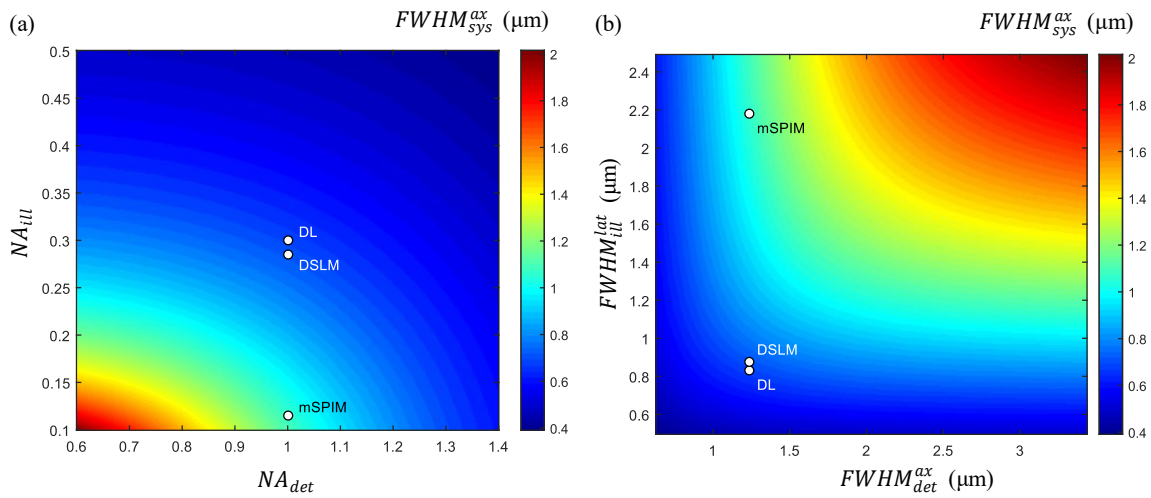


Figure 3.7 Theoretical axial system PSF FWHM dependence on illumination and detection NA. Variation of the theoretical system axial PSF FWHM for (a) a range of numerical apertures for illumination and detection and (b) the corresponding axial detection PSF FWHM and lateral illumination PSF FWHM in an LSFM configuration with orthogonal illumination and detection axes. Here, the FWHM is calculated for the PSF for a uniformly filled circular aperture. The labelled points correspond to the diffraction limited (DL) axial PSF FWHM for the current system, and the theoretical prediction for DSLM and mSPIM illumination profiles from the Zemax model.

The estimated PSF FWHM are summarized in **Table 3.3**. Since the confocal parameter of both illumination modes is much larger than the lateral detection PSF FWHM, the lateral system PSF, equal to $0.267 \mu\text{m}$ in both the X' and Y' lateral directions is predominantly determined by the detection PSF, and hence uniform across the FOV. The axial system PSF is modulated by the illumination beam width, and smaller than the detection PSF of $1.23 \mu\text{m}$ FWHM. The experimentally measured PSF FWHM will be further degraded by stage motion, sampling interval and the bead dimensions. The effect of these contributions is further estimated in **Section 3.3.2** and compared to the measured FWHM of the images of fluorescent beads.

	Lateral FWHM (μm)						Axial FWHM (μm)		
	DSLML (DL)		DSLML		mSPIM		DSLML (DL)	DSLML	mSPIM
	X'	Y'	X'	Y'	X'	Y'	Z'		
Detection (DL)	0.267						1.23		
Illumination	8.511		12.17		100.9	∞	0.830	0.876	2.176
System (Ideal)	0.267						0.688	0.714	1.071

Table 3.3 Modelled system resolution at the beam waist, calculated using elementwise multiplication of the diffraction-limited (DL) detection PSF and the illumination profile by approximating the distributions as Gaussian.

Axial resolution variation along the illumination axis

The axial system PSF FWHM, will be modulated by the spatially varying illumination beam width. The modelled axial system PSF FWHM variation along X' for the DSLM and mSPIM illumination modes is shown in purple in **Figure 3.8**. The illumination profiles are modelled using the expression for $w(x')$ with decoupled parameters x'_R and w_0 taken from POP beam waist and confocal parameter estimates (see **Table 3.2**). The detection PSF FWHM (red) is constant along the illumination beam axis.

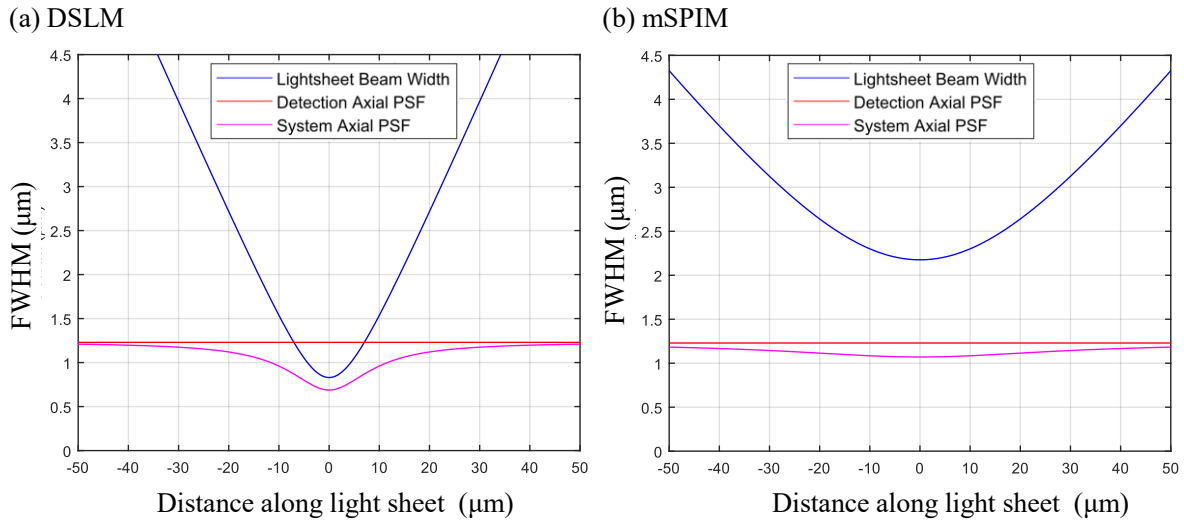


Figure 3.8 Modulation of the axial resolution at different positions along the illumination beam. The modelled system axial PSF FWHM (purple) along the illumination axis for the (a) DSLM (a) and (b) mSPIM illumination modes, calculated by considering the product of two Gaussian distributions, with a homogenous detection PSF across the FOV.

For the highly divergent beam with a tight waist used in the DSLM illumination mode (**Figure 3.8a**, blue), the resultant axial FWHM of the PSF is modulated along the detection axis, remaining below 1 μm within $x' = \pm 11$ μm of the illumination focus, where the light-sheet beam width (FWHM) is just over 1.5 μm. These considerations can be useful in determining the range along the illumination axis over which a certain axial resolution is maintained, and hence defining the scanning intervals of the illumination beam waist (ASLM) for uniform axial resolution across the FOV.

For the slower diverging beam with a bigger waist used in the mSPIM illumination mode (**Figure 3.8b**, blue), the axial system PSF FWHM is reduced less at the waist and approaches the axial detection PSF FWHM away from the beam waist. The improvement in axial resolution is minimal when the light-sheet is much bigger than the axial detection PSF. However, despite minimal resolution enhancement from an illumination beam of this width, it still maintains its second key function of providing optical sectioning.

Next, the experimentally measured PSF is evaluated and compared with the results of the model.

3.3. Experimental resolution measurement

The 3D spatial resolution and optical sectioning of the system was characterized through experimental measurement of the system PSF by imaging 200 nm diameter fluorescent beads. The sample preparation, volume acquisition and image processing steps are described in **Section 3.3.1**, and the PSF characterization results are presented in **Section 3.3.2** below. Parts of the data and figures presented in this section have been published in our work (Sparks et al., 2020).

3.3.1. Method

An overview of the method for experimental PSF characterization is presented in **Figure 3.9**.

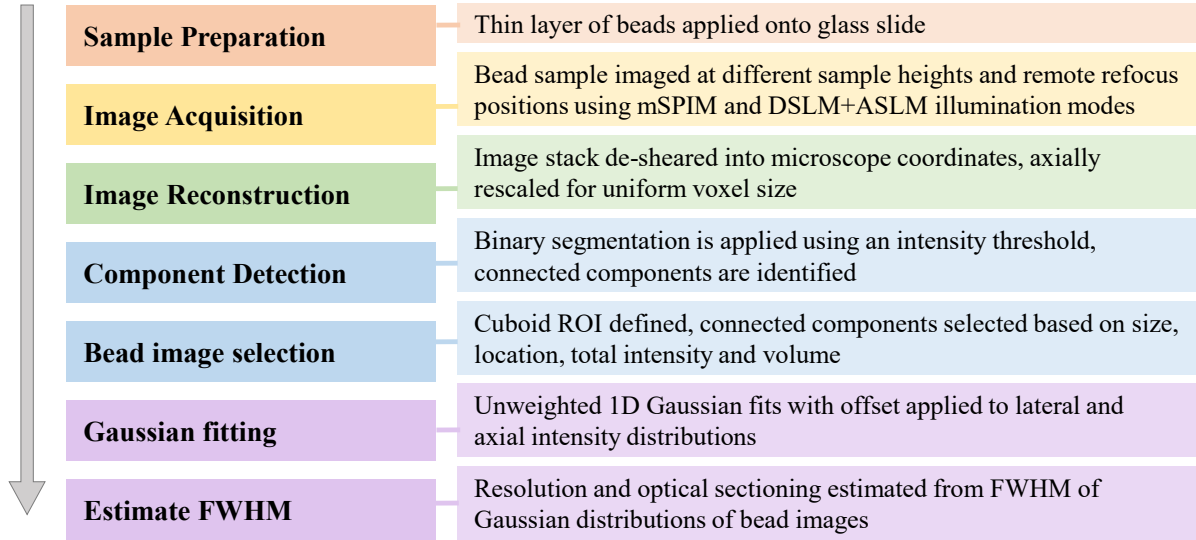


Figure 3.9 Experimental PSF characterization workflow. Overview of the method used to characterize the 3D spatial resolution and optical sectioning of a light-sheet system through Gaussian fitting of the intensity distribution of sub-resolution fluorescent bead images.

The bead sample was prepared as a thin layer on a glass slide, rather than a volume suspended in agarose, to avoid any aberrations from the refractive index interface between the water immersion and the agarose. The sample was imaged at three different sample heights in the Z -direction using both the mSPIM and DSLM+ASLM illumination modes. For the mSPIM illumination mode, designed to be combined with remote refocus (RF) for high-speed volumetric imaging, the sample was also imaged at three different RF positions. Acquired image stacks were de-sheared into microscope coordinate frame, and axially rescaled to achieve uniform voxel spacing. The acquired volume was segmented through binarization using an intensity threshold. Connected components were detected, analysed and selected based on their physical properties including location, size and intensity. Within a cuboid region of interest (ROI) about the weighted centroid of each selected bead image, 1D unweighted Gaussian fits in each of the three dimensions (X' , Y' , Z') as well as an axial fit for the laterally integrated axial intensity profile (Z^{*}) were used to estimate the X' -, Y' -, Z' - and Z^{*} -FWHM for each bead image, and

used to characterize the lateral and axial resolution, as well as optical sectioning of the system. The detailed method is described below.

Preparation of a thin layer of fluorescent beads on glass

The sample containing a layer of sparsely distributed fluorescent beads on a glass slide was prepared by first coating a clean glass microscope slide in 1mL 1% poly-L-Lysine dissolved in MilliQ (MQ) and leaving it on for 10 minutes. In the meantime, a stock solution of 200 nm fluorescent microspheres (T7280, TetraSpeck™, Thermofisher Scientific) was agitated for 10 seconds on an Eppendorf vortex, and then diluted in MQ by 500:1. The remaining excess poly-L-Lysine solution was removed from the glass slide by aspirating the liquid with a pipette, with the rest washed away by pipetting MQ against the surface. A volume of 250 μ L of the bead solution was spread across the slide and left for 10 minutes. Remaining liquid was removed by gently pouring MQ against the glass surface. Prior to imaging, the sample was stored dry in the fridge, and protected from light.

Bead volume acquisition

Bead fluorescence was excited using the 488 nm laser line at 400 μ W power (measured in the back focal plane of O3) and detected through the ET525/50 emission filter. The image stacks were recorded using the stage scanning acquisition mode, with the sample continuously horizontally translated by $\Delta x = 100$ nm in-between each frame, parallel to the optical bench. The mSPIM bead datasets were acquired with 2 μ m/s stage scan velocity, corresponding to 20 fps, with the exposure limited to half of the step duration (10 ms). The DSLM+ASLM data was acquired at 5 μ m/s stage scan velocity, corresponding to 50 fps, and 25 ms exposure time. In both stage scanning modes, this resulted in 0.05 μ m motion blur along the stage scanning direction X . The mSPIM and DSLM+ASLM datasets were acquired on the Hamamatsu Orca Lightning and Fusion detectors respectively, with image dimensions of 1152 \times 1152 pixels. The mSPIM dataset consisted of 1000 images, while the ASLM+DSLM dataset was concatenated from six volumes with 500 frames each (3000 in total), acquired at six stepped axial beam waist positions, such that the useable FOV is extended beyond the confocal parameter of the tightly focused beam. Regions within the confocal parameter of the beam waist were selected from each volume and stitched together to form a 500-frame image stack. The DSLM + ASLM dataset acquisition and concatenation was carried out by Hugh Sparks.

For the mSPIM illumination mode, the bead sample was imaged at three different refocus positions (**Figure 3.10a**). The remote refocusing mirror RM2 was manually axially translated by 30 μ m in each direction from the nominal focal plane of refocusing objective O5. Accounting for the double pass geometry and 1.33 magnification from refocus space to sample space, the detection plane was refocused by ~ 45 μ m along Z' in the opposite direction from the nominal focal plane of the emission objective O4. The illumination light-sheet plane is adjusted to match the refocused detection plane using the Z' galvo-scanning mirror G2.

For both the mSPIM and DSLM+ASLM illumination modes, image volumes were acquired at different sample heights (**Figure 3.10b**), with the sample vertically displaced along Z by $\pm 15 \mu\text{m}$ and $\pm 35 \mu\text{m}$ for datasets imaged with the mSPIM and DSLM+ASLM illumination modes respectively. Accounting for the tilt between the sample plane and detection axis, this corresponds to a displacement of $\sim \pm 25 \mu\text{m}$ and $\sim \pm 58 \mu\text{m}$ respectively across the FOV along illumination axis X' .

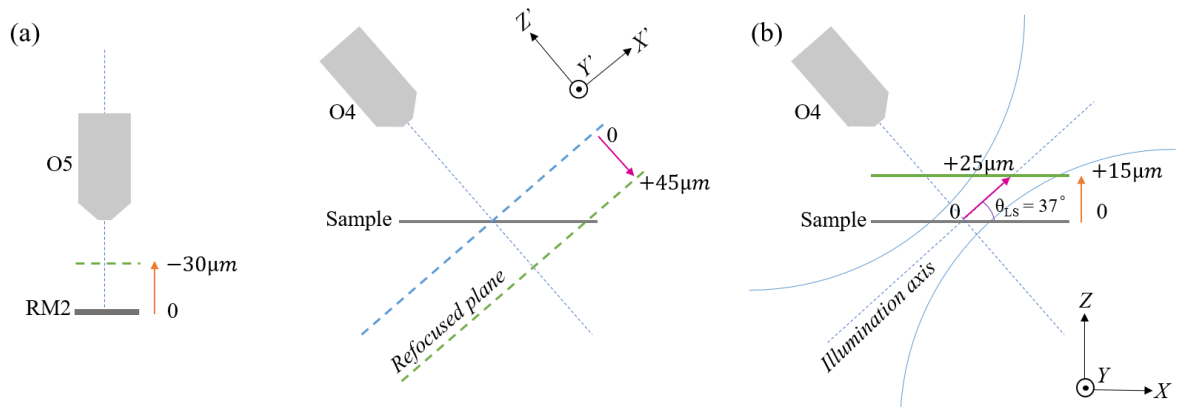


Figure 3.10 Data acquisition for varying amounts of remote refocus and positions along the light-sheet. (a) Remote refocus of the detection plane in sample space by axial translation of the refocus mirror RM2, with the implemented displacement accounting for the double pass geometry and 1.33x magnification from sample space to RF space. (b) Vertical displacement of the sample results in bead images appearing displaced in X' , against the light-sheet propagation direction, hence sampling a different beam width of the light-sheet.

De-shearing and axial resampling

The image stacks were de-sheared in MATLAB into the microscope reference frame, subtracting an averaged background dataset acquired with the laser off. The de-sheared mSPIM dataset had new dimensions of 1791×1152 pixels, with the resultant axial spacing in between two adjacent planes equal to $\Delta z' = \Delta x \times \cos(90 - \theta_{LS}) \approx 60 \text{ nm}$. Applying axial rescaling through bilinear interpolation to achieve a uniform sample space voxel size of 125 nm in all three dimensions gave final volume dimensions of $1791 \times 1152 \times 481$ pixels. Equivalently, for the DSLM+ASLM dataset, the resultant de-sheared and axially resampled volume had a uniform sample-space voxel size with each side equal to 147.7 nm , and final volume dimensions of $1423 \times 1152 \times 203$ pixels. **Figure 3.11** shows sum intensity projections (SIP) through a de-sheared and axially resampled bead image stack acquired using the mSPIM illumination mode at zero RF and nominal sample height, such that the light-sheet beam waist, sample plane and detection focal plane intersect in one line.

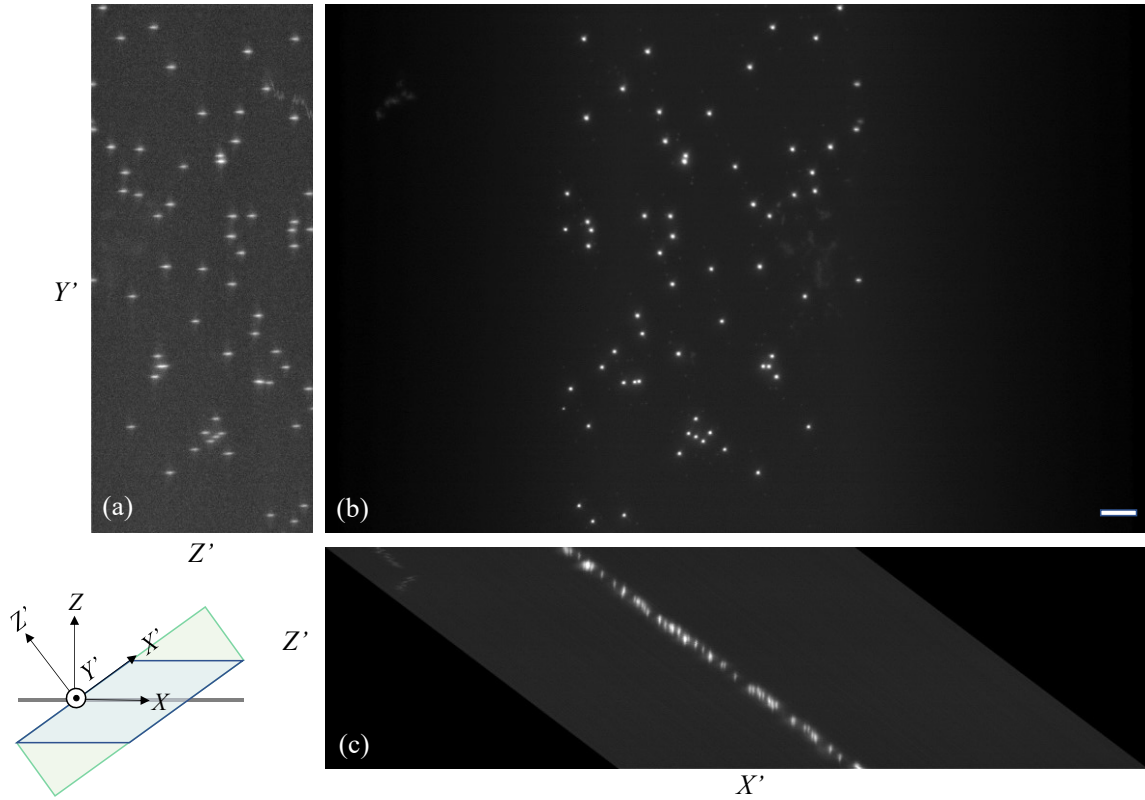


Figure 3.11 Sum intensity projections along (a) X' , (b) Z' , and (c) Y' of the de-sheared bead sample image stack in microscope coordinates, acquired using the mSPIM illumination mode at zero RF and nominal sample height. The X' , Y' , Z' dimensions are $1791 \times 1152 \times 481$ pixels. The diagram on the bottom left shows the geometry of the de-sheared volume (green) for a sample consisting of beads on glass (shown in grey) stage-scanned along X . Regions outside the blue parallelogram are padded with zeros to complete the cuboid volume (green) in light-sheet coordinates. Scalebar: $10 \mu\text{m}$

Detection and selection of bead images

To identify the individual bead images, the volume was segmented by applying a binary mask using an intensity threshold, with the individual connected components identified using MATLAB's *bwconncomp* function. To include as many bead images as possible for analysis, the lowest intensity threshold above noise levels is desirable, however a threshold too close to the noise levels can result in false positive detection of connected components not corresponding to real images of beads. The threshold intensity value was selected through iterative threshold increases performed until the decreasing number of detected connected components reached a plateau. When accounting for the predicted PSF size, bead and pixel dimensions, the expected lateral bead image FWHM dimensions are approximately 3 pixels. Hence, given that the typical threshold applied is approximately 10% of the peak bead image intensity (well below the half-maximum), to reduce computational load during the following analysis, binarized bead image components extending less than 3 pixels in any of the three dimensions were directly excluded at this stage.

Cuboid regions of interest (ROI) were selected about the weighted centroids of each connected component. The lateral extent of the cuboid region was set to a multiple of $5\times$ the initial lateral FWHM

guess of 0.5 μm , rounded up to the nearest pixel. For the DSLM illumination mode data, the axial extent of the cuboid ROI was defined as $2.5\times$ the lateral extent, where the scaling factor was obtained from the ratio of the expected axial and lateral diffraction limited system PSF FWHM from **Section 3.2.2**. For the mSPIM mode, the axial dimensions of the ROI were scaled by a further $1.5\times$ to accommodate for the broader axial profile due to the thicker lightsheet. Components were excluded from further analysis if their surrounding ROI overlapped with the edge of the imaged bead volume or another component's ROI. Additionally, to remove large and bright components corresponding to clumps of multiple beads, and smaller bright regions created by hot pixels on the sCMOS detector, connected components were excluded if their total intensity or total volume fell outside the main peak in that parameter's distribution across all connected components; this is explained more in the following text.

The total volume and total intensity enclosed in the connected component was calculated from outputs of the *regionprops3* MATLAB function. Those components with total volumes or total intensities less than $0.3\times$ or more than $2\times$ the median of the distribution for that property were excluded. For the DSLM+ASLM dataset, the upper threshold was changed to a factor of $3\times$ above the median to provide a bigger margin to account for a sparse bead volume and hence a noisier parameter distribution. **Figure 3.12** shows a subsection of the sum intensity projections along X' for the dataset presented in **Fig. 3.11**, corresponding to the raw image, binary mask and adjusted binary mask showing the connected components selected for analysis.

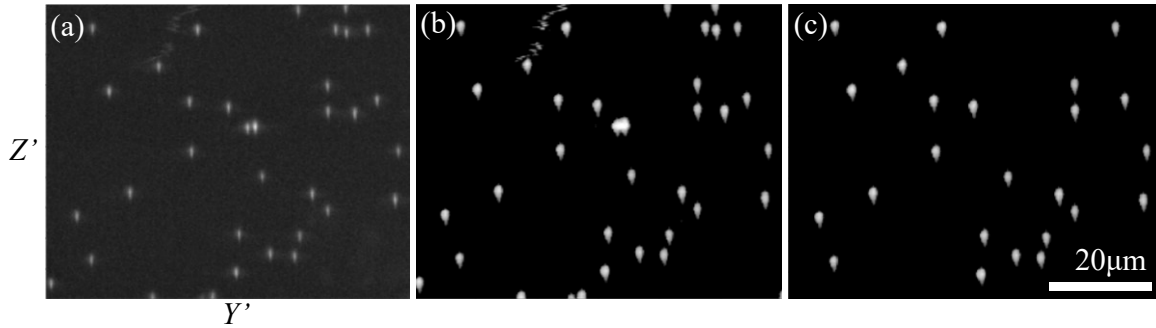


Figure 3.12 Subsection of the sum intensity projections (SIP) along X' of bead images corresponding to the example dataset presented in **Fig. 3.11**. (a) Raw intensity distribution (b) Binary mask with connected components (d) Binary mask with connected components selected for Gaussian fitting.

Gaussian fitting

A multistep unweighted Gaussian fitting procedure was used to estimate the lateral and axial FWHM of the bead images. First, a 3D Gaussian distribution with offset c was applied to each ROI using the nonlinear least squares fitting method.

$$G_{3D}(x', y', z') = A \times \exp \left[- \left(\frac{(x' - \mu_{x'})^2}{2\sigma_{x'}^2} + \frac{(y' - \mu_{y'})^2}{2\sigma_{y'}^2} + \frac{(z' - \mu_{z'})^2}{2\sigma_{z'}^2} \right) \right] + c \quad (3.50)$$

Starting points for the fit were provided by initial guesses for each of the 8 fit parameters: peak intensity A was taken as the median of the maximum intensity parameter distribution across the selected connected components, the centre coordinates of the weighted centroid of each connected component were used as initial guesses for the central positions μ_x' , μ_y' , μ_z' , and starting points for the widths σ_x' , σ_y' , σ_z' were expressed in terms of user-specified FWHM guesses. The starting point for the offset c was given by the estimated background for the analyzed dataset. Next, a 1D Gaussian fit was applied axially (along Z') through the laterally integrated intensity to identify the axial position of the intensity peak and determine the sectioning strength $Z_{FWHM}'^*$:

$$G_{1D}(z') = A \times \exp \left[-\frac{(z' - \mu_z'^*)^2}{2\sigma_{z'}^2} \right] + c \quad (3.51)$$

The fit was applied twice: initially without offset or any starting points to establish estimates for the peak, centre and standard deviations, then with an offset, with other parameter guesses provided by those estimated in the first round. The offset guess was given by the estimated offset from the 3D Gaussian fit, multiplied by the lateral $X'Y'$ area of the ROI to account for the laterally integrated intensity.

In the next step, 1D Gaussian distributions with offset $G_{1D}(x')$ and $G_{1D}(y')$ were fitted laterally in X' and Y' directions through the axial peak position μ_z' calculated in the laterally integrated intensity fit $G_{1D}(z')$ and through the through peak intensity positions μ_x' and μ_y' determined from the 3D Gaussian fit (Eq. 3.50), allowing X'_{FWHM} and Y'_{FWHM} to be determined.

$$G_{1D}(x') = A \times \exp \left[-\frac{(x' - \mu_x')^2}{2\sigma_{x'}^2} \right] + c, \quad (3.52)$$

$$G_{1D}(y') = A \times \exp \left[-\frac{(y' - \mu_y')^2}{2\sigma_{y'}^2} \right] + c \quad (3.53)$$

Finally, 1D Gaussian fits with offset were applied axially through the centres found from the two lateral 1D fits, and were used to measure the Z'_{FWHM} .

$$G_{1D}(z') = A \times \exp \left[-\frac{(z' - \mu_z')^2}{2\sigma_{z'}^2} \right] + c \quad (3.54)$$

3.3.2. Results

Exemplar lateral, axial, and laterally integrated bead image intensity profiles and corresponding unweighted 1D Gaussian fits for representative bead images acquired using the mSPIM and DSLM+ASLM illumination modes for zero remote refocus and nominal sample height are shown in **Fig 3.13**. It was found that unweighted 1D Gaussian fits provided the best fit quality to both the peak and offset of the intensity distributions.

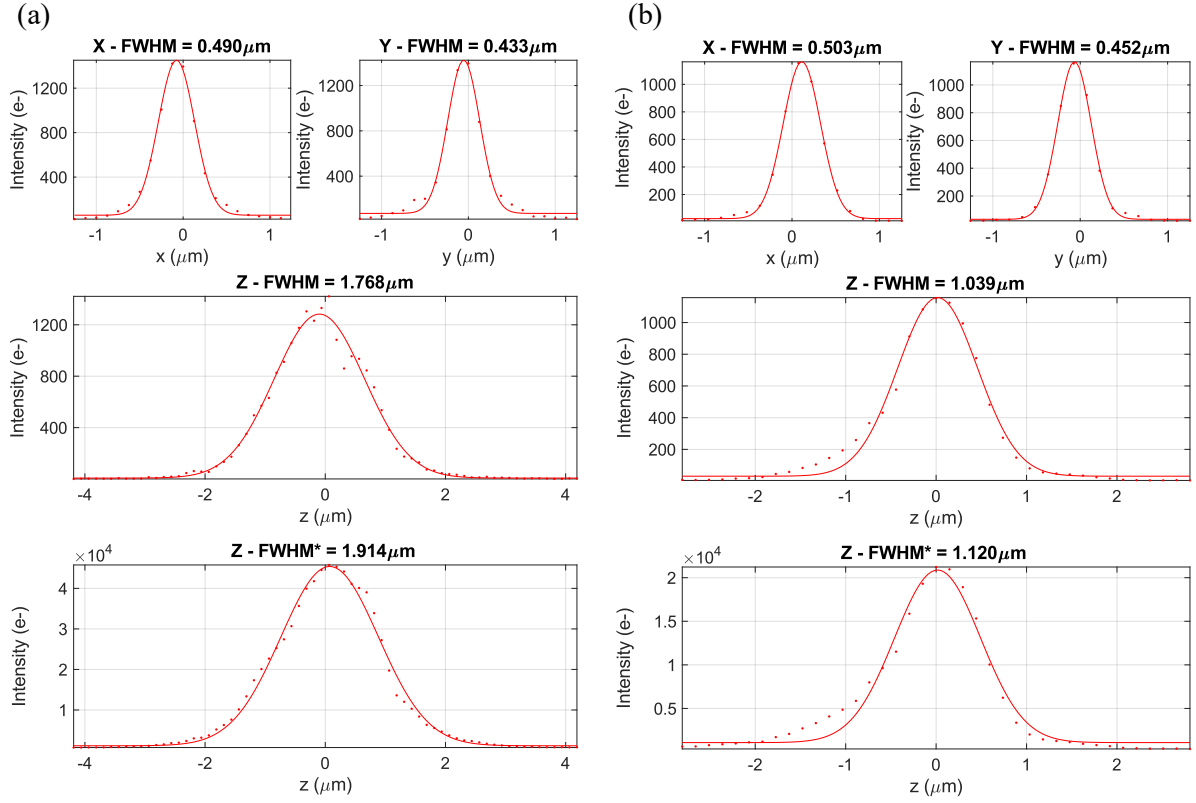


Figure 3.13 1D intensity profiles with corresponding 1D unweighted Gaussian nonlinear least squares fits through representative bead images from the FOV centre at zero remote refocus for datasets acquired using (a) mSPIM and (b) DSLM+ASLM illumination modes. Intensity values are given in photoelectrons, converted from the digital number (DN) detector output using the manufacturer's stated conversion factor. Figure published in (Sparks et al., 2020), reproduced with format modifications under CC BY 4.0 License.

Excluding failed fits by considering the confidence intervals on each estimated parameter and applying an error threshold, the final estimated FWHM are summarized in a histogram (**Figure 3.14**).

Orthoslices through representative bead images at different positions across the FOV are shown in **Fig. 3.15**. The corresponding X' -, Y' -, Z' - and Z'^* -FWHM, expressed as the mean \pm standard deviation across all analyzed bead images in the dataset are presented in **Table 3.4**. For the mSPIM dataset, (**Fig. 3.15a**), the measurements were also carried out at three different RF positions: $z' = -45, 0, 45 \mu\text{m}$.

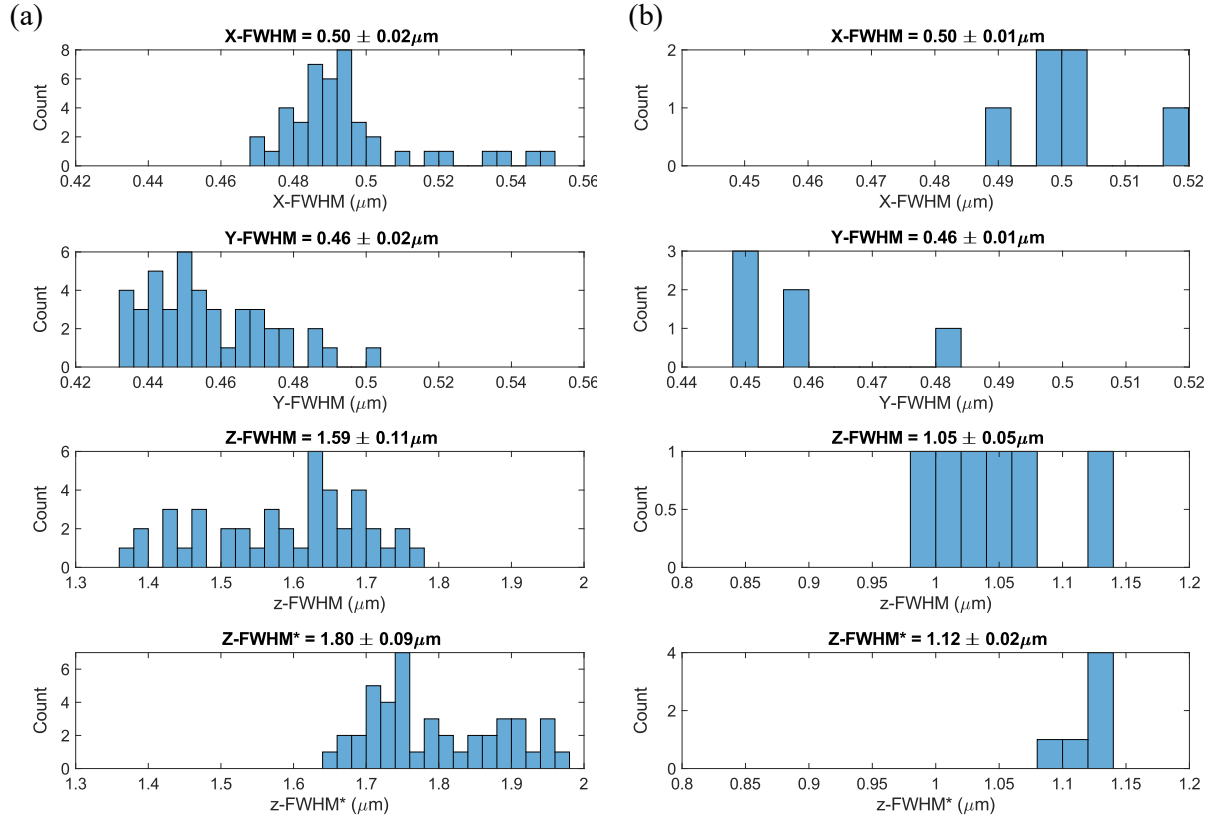


Figure 3.14 Histograms of measured bead image X' -, Y' -, Z' -, and Z'^* -FWHM at the centre of the FOV and at zero remote refocus from datasets acquired using (a) mSPIM and (b) DSLM + ASLM illumination modes. The title on top of each plot indicates the mean \pm SD. The small number of analyzed bead images for the DSLM+ASLM dataset is due to few beads present in the prepared sample. Published in (Sparks et al., 2020), reproduced with format modifications under CC BY 4.0 License.

Table 3.5 summarizes the lateral and axial system PSF FWHM for each illumination mode by considering (1) the ideal case of diffraction limited detection PSF and the illumination profile estimated using a Zemax model, (2) modelled case for the expected experimentally measured PSF and (3) experimentally measured system PSF FWHM from Gaussian fitting of bead images. For (2) the effects of stage motion blur, bead size and the lateral and axial sampling were taken into account by convolving the system PSF with Gaussian approximations to the spatial distribution of the beads ($0.2 \mu\text{m}$ diameter), stage motion blur ($0.05 \mu\text{m}$ stage motion along X decomposed into its components along X' and Z' , giving $0.04 \mu\text{m}$ and $0.03 \mu\text{m}$ in the respective directions), and lateral and axial sampling ($0.148 \mu\text{m}$ and $0.125 \mu\text{m}$ pixel dimensions and $0.06 \mu\text{m}$ axial separation of the acquired frames), modelled as Gaussian distributions with the standard deviations added in quadrature.

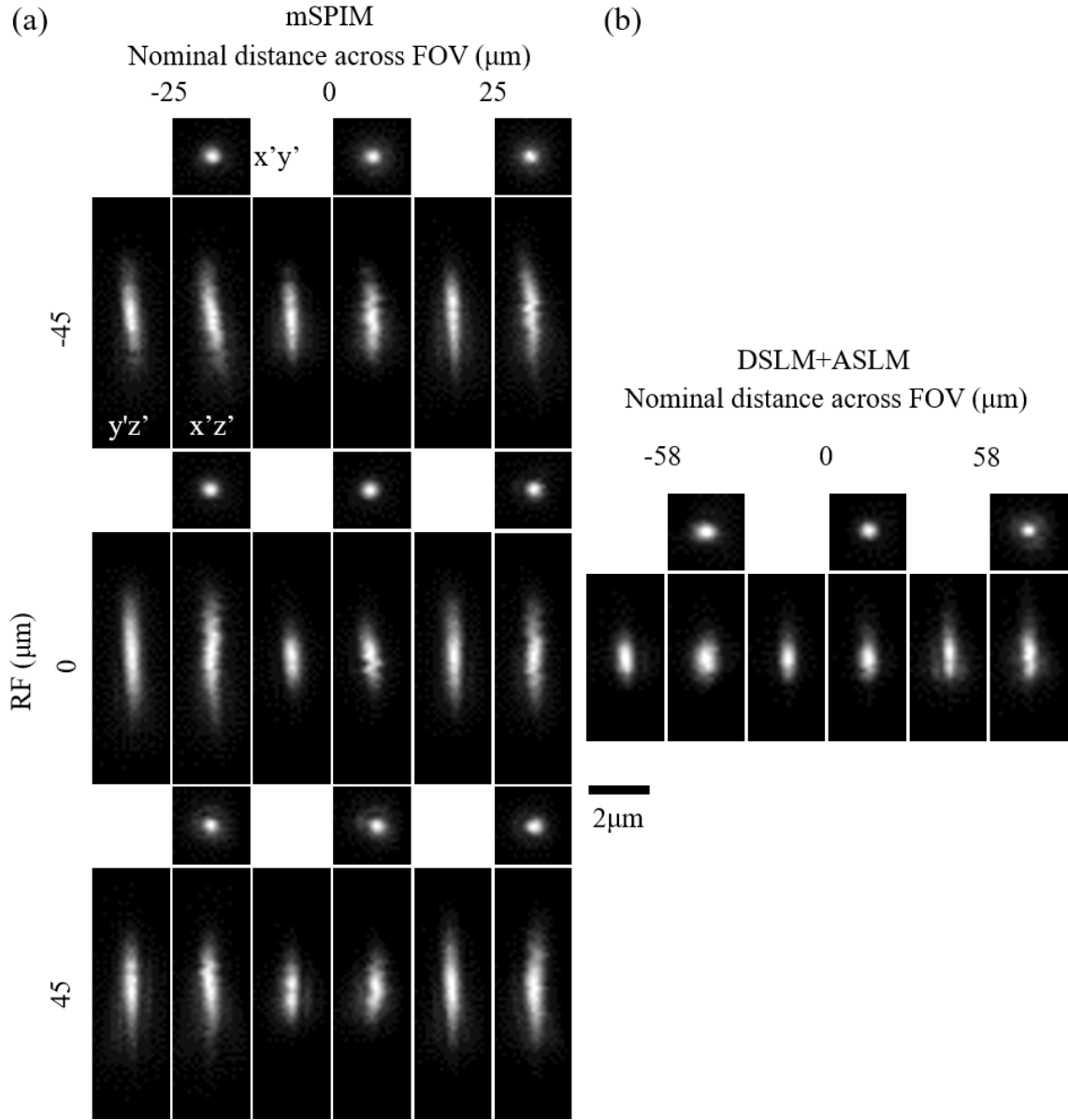


Figure 3.15 Three-way orthoslices through representative bead images at three different positions across the FOV along the light-sheet propagation direction from datasets acquired using (a) mSPIM and (b) DSLM + ASLM illumination modes. For the mSPIM mode, the figure also displays orthoslices at positive and negative remote refocus (RF), measured away from O4. Figure published in (Sparks et al., 2020), reproduced with format modifications under CC BY 4.0 License.

		Nominal distance across FOV (μm)			
	RF(μm)		-25	0	25
mSPIM	-45	X'	0.55 ± 0.03	0.52 ± 0.03	0.51 ± 0.03
		Y'	0.48 ± 0.03	0.46 ± 0.02	0.46 ± 0.02
		Z'	2.28 ± 0.17	1.76 ± 0.13	2.14 ± 0.16
		Z'*	3.55 ± 0.15	1.95 ± 0.12	2.99 ± 0.13
		n	52	52	42
	0	X'	0.49 ± 0.02	0.50 ± 0.02	0.49 ± 0.01
		Y'	0.45 ± 0.02	0.46 ± 0.02	0.46 ± 0.02
		Z'	2.75 ± 0.15	1.59 ± 0.11	2.19 ± 0.12
		Z'*	4.35 ± 0.24	1.80 ± 0.09	2.90 ± 0.11
		n	41	43	48
	+45	X'	0.51 ± 0.03	0.52 ± 0.03	0.54 ± 0.02
		Y'	0.47 ± 0.03	0.48 ± 0.02	0.47 ± 0.03
		Z'	2.38 ± 0.15	1.58 ± 0.10	2.33± 0.12
		Z'*	3.37 ± 0.17	1.63 ± 0.11	2.78 ± 0.13
		n	52	56	54
		Nominal distance across FOV (μm)			
			-58	0	58
DSLM+ ASLM	0	X'	0.50 ± 0.03	0.50 ± 0.01	0.57 ± 0.03
		Y'	0.42 ± 0.02	0.46 ± 0.01	0.47 ± 0.05
		Z'	1.34 ± 0.07	1.05 ± 0.05	1.05 ± 0.04
		Z'*	1.43 ± 0.06	1.12 ± 0.02	1.08 ± 0.03
		n	13	6	9

Table 3.4 Measured FWHM of the lateral (X' and Y'), axial (Z') and laterally integrated axial (Z'*) bead image intensity distributions at positive, zero and negative remote refocus (RF) and different positions across the FOV along the light-sheet propagation direction X'. The quoted FWHM correspond to the mean \pm SD of the estimated FWHM for n individual bead images. Figure published in (Sparks et al., 2020), reproduced under CC BY 4.0 License.

System PSF FWHM	Lateral FWHM (μm)				Axial FWHM (μm)	
	DSLM		mSPIM		DSLM	mSPIM
	X'	Y'	X'	Y'	Z'	
(1) DL-detection	0.267				0.714	1.071
<i>Sampling interval</i>	0.147		0.125		0.06	
<i>Stage motion blur</i>	0.04	-	0.04	-	0.03	
(2) Modelled	0.367	0.365	0.359	0.356	0.744	1.091
(3) Measured	0.50 ± 0.01	0.46 ± 0.01	0.50 ± 0.02	0.46 ± 0.02	1.05 ± 0.05	1.59 ± 0.11

Table 3.5 Estimated system lateral and axial PSF FWHM for the DSLM and mSPIM illumination modes for the (1) diffraction-limited (DL) detection, (2) modelled with the pixel and axial sampling, stage motion blur and bead image size ($0.2 \mu\text{m}$) taken into account, and (3) experimentally measured from bead images for zero remote refocus. The values are for the system PSF at the centre of the FOV.

DSLM+ASLM mode

The average measured lateral bead image FWHM for the DSLM + ASLM illumination was $0.52 \pm 0.03 \mu\text{m}$ and $0.45 \pm 0.02 \mu\text{m}$ in the X' - and Y' - directions respectively. Axially, the estimated bead Z' - and Z^{*} - FWHM, averaged over the three distances across the FOV were $1.15 \pm 0.14 \mu\text{m}$ and $1.21 \pm 0.16 \mu\text{m}$ respectively, and were both lower and more uniform across the FOV in comparison that those measured for the mSPIM acquisition mode, due to scanning of the beam waist along the illumination axis using remote refocused ASLM. The Z' - and Z^{*} - FWHM were larger for negative ASLM refocus of the illumination beam from the centre of the FOV (by 28% for both). The bead image FWHM was larger than the theoretically expected value even when accounting for blurring effects from pixelation, bead size and estimated stage motion blur, suggesting that the estimated effective detection PSF may be larger than expected due to aberrations introduced in the detection path. However, the tightly focused beam resulted in improved axial resolution compared to the diffraction limited detection PSF, and the effective PSF with the mSPIM illumination mode.

mSPIM + remote refocusing mode

The average measured lateral bead image FWHM for the mSPIM illumination was equal to $0.51 \pm 0.02 \mu\text{m}$ and $0.47 \pm 0.01 \mu\text{m}$ in the X' - and Y' - directions respectively. The lateral FWHM in each direction had $< 0.06 \mu\text{m}$ variation across the FOV, and up to 12% increase with remote refocus. The consistently larger value in the X' - direction can be attributed to the motion blur produced by the stage scan during the detector exposure time, as well as effect of mechanical vibrations of the translation stage, visible in the zig-zag-like shape of the $X'Z'$ profile (**Fig. 3.15a**). Similarly to the resolution measured for the DSLM+ASLM illumination mode, the lateral and axial PSF FWHM were higher than expected from the theoretical predictions using elementwise multiplication of the detection PSF and illumination profile, with the effects of pixelation, stage motion blur and bead size taken into account, indicating that the detection PSF is likely worse than expected. The estimated axial bead Z' - FWHM averaged across the three RF positions at the centre of the FOV was $1.64 \pm 0.08 \mu\text{m}$. The estimated laterally integrated axial bead Z^{*} - FWHM, averaged across the three RF positions was $1.79 \pm 0.13 \mu\text{m}$. At all RF positions, both Z' and Z^{*} - FWHM increased away from the centre of the FOV.

Figure 3.16a. shows the measured mSPIM axial PSF FWHM (black symbols) at different positions along the light-sheet for three different RF positions, along with detection PSF axial FWHM (red), the light-sheet illumination profile (blue) and the modelled system axial PSF FWHM (purple), with the effects of bead size, stage motion blur and axial sampling incorporated into the model. We can see that the measured axial PSF FWHM is larger and exhibits more spatial variation along the direction of the light-sheet than predicted by the modelled system axial PSF.

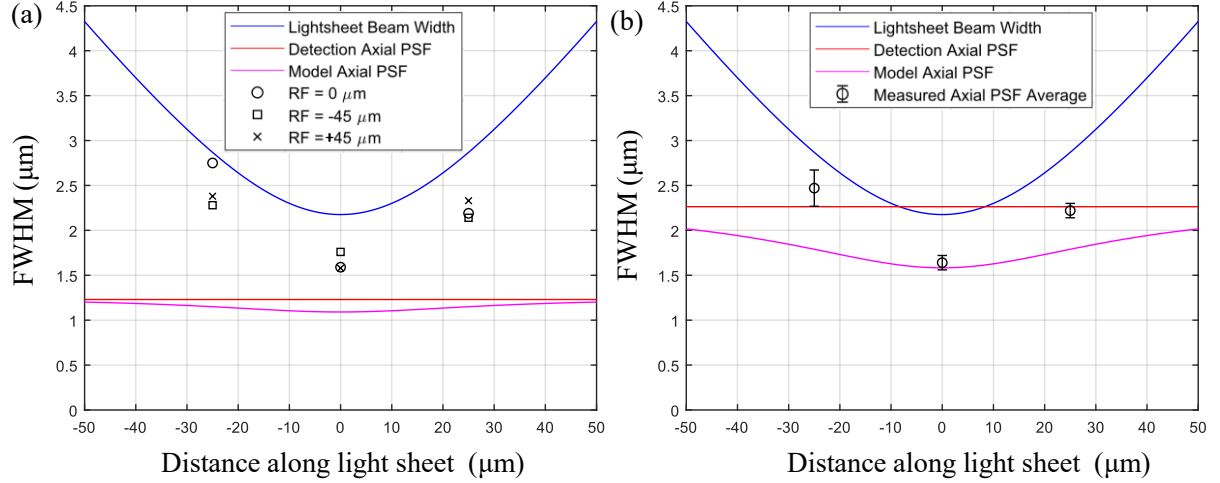


Figure 3.16 Comparison of modelled and measured axial FWHM variation along illumination axis. Variation of the modelled axial system FWHM along the illumination axis (purple) for the mSPIM illumination mode, with the space-invariant detection PSF axial FWHM shown in red and illumination beam FWHM shown in blue. (a) The measured axial bead image FWHM at three different remote refocus (RF) positions with the diffraction-limited model for the system axial FWHM. (b) Mean axial bead image FWHM for the three RF positions. The detection and model axial system FWHM were calculated using an increase in the axial detection PSF FWHM by a factor of 1.84 based on expected and actual measurements for the lateral resolution, see main text for further explanation.

Since the measured lateral resolution was also worse than expected for the given bead size, motion blur and pixel dimensions, it is possible that this is due to actual detection PSF being larger than in the model. On average, for the mSPIM mode, the measured lateral PSF FWHM is larger than the modelled values by $1.36\times$. While the lateral detection resolution is inversely proportional to the detection NA, the axial detection PSF FWHM will vary with NA^{-2} and will hence be degraded by a factor of $1.36^2 = 1.84$. We can crudely adjust the model by increasing the axial detection PSF FWHM by that factor, resulting in increased modulation of the axial system PSF FWHM (**Figure 3.16b**) and recovering the measured bead image axial FWHM at the beam waist. However, it does not account for the measured variation in the axial system PSF FWHM away from the waist along X' . One possible reason is that optical aberrations in the system result in the axial detection PSF FWHM varying more than the lateral detection PSF FWHM across the FOV. Also, the light-sheet may differ from the modelled beam profile due to higher level of filling of the excitation objective – this would cause the beam to have a tighter waist and diverge faster, giving more spatial variation of the axial FWHM.

The measured axial FWHM and laterally integrated axial FWHM of the bead image at $x' = -25 \mu\text{m}$ displacement (towards the excitation objective) at 0 RF was higher than at the same displacement in the opposite direction along the light-sheet propagation direction for both positive and negative RF. It is possible that this is due to spherical aberration in the detection path, or misaligned bead sample positioning during the acquisition of the dataset, resulting in sampling of the light-sheet further away from the beam waist than estimated, giving a higher axial PSF FWHM. It would also be useful to sample

the axial resolution at positions further away from the waist to see whether the shape of the axial PSF FWHM variation along the illumination axis follows the model predictions.

3.4. Discussion and conclusion

The aim of this chapter has been to characterize the spatial resolution of a light-sheet fluorescence microscope system. The first section (**Section 3.1**) introduced the concept of resolution and optical sectioning in a microscope imaging system and outlined the main approaches to modelling and measuring spatial resolution. An effective system PSF at the beam waist was approximated by modulating the axial detection PSF profile by the light-sheet width and simplifying the calculation by approximating the illumination and detection PSF profiles along the detection axis as Gaussian.

Section 3.2 modelled the LSFM resolution, initially for uniformly filled illumination and detection pupils, and demonstrated that the spatial variation of the axial resolution along the light-sheet propagation direction can be modelled using an effective system PSF that only varies along the illumination axis. This was done by MATLAB-simulation of the image formation process for bead-like objects at different positions along the light-sheet propagation axis. Next, for a more accurate description of the light-sheet profiles of the two illumination modes, the optical relays of the DSLM and mSPIM illumination paths were modelled in Zemax. The Physical Optics Propagation tool was used to model the influence of initial Gaussian beam size, aperture truncation and lens aberrations along the optical relay on the final shape, size and quality of the focused illumination beam in the sample plane. The resultant transverse and longitudinal beam intensity profiles through the focal plane were found to qualitatively agree with the theoretical descriptions provided in **Section 3.1.6**, particularly with the described differences of the axial irradiance profile for a focused 3D radially symmetric beam and a 2D light-sheet, the latter having a longer confocal parameter. The sampled axial and lateral illumination profiles quantified in terms of the beam waist and confocal parameter were used to calculate the expected spatial resolution for each illumination mode.

Finally, **Section 3.3** presented an experimental measurement of the system PSF through automated image processing of bead image datasets, allowing a comparison of the modelled and measured system resolution. A detailed characterization of the system resolution confirmed the functionality of some key design features of the microscope. The Gaussian light-sheet provided optical sectioning and improved the axial resolution of the system. The DSLM illumination mode generated a tightly focused light beam, while the mSPIM illumination mode produced a light-sheet with a longer confocal parameter for imaging of a larger FOV without axial scanning of the beam waist.

Positive and negative remote refocus of the detection plane did not introduce significant degradation in lateral or axial resolution, indicating a successful application of the principle and design requirements for aberration-free remote refocus. However, the measured lateral and axial resolution were found to be worse than expected from the model. One possible reason for the discrepancy are potential aberrations

in the detection path due to incorrect spacing between optical elements in the first microscope relay. The detection objective O4 is designed to work with tube lens T1 followed by an 80 mm thick NBK-7 glass compensation block for optimal aberration correction. In the system, the objective and tube lens were set up approximately in a 4f configuration, with the mounting shoulder of the objective and the tube lens separated by ~ 87 mm. However, the designed separations are 132 mm between adjacent surfaces of O4 and T1, and 55 mm between adjacent surfaces of T1 and the glass compensation block (Wartmann, 2007). This incorrect separation of O4 and T1 is likely to be the reason for the lateral and axial resolution being worse than the theoretically predicted values, and, along with the home-built tube lens T2, may also contribute to the longitudinal chromatic aberration resulting in the spatial separation of the foci of the two spectral channels along the optical axis i.e. the Fluo-4 defocus corrected in **Section 2.2.1**. Hence, reviewing the axial positions of these components may improve the system resolution.

The variation of the axial resolution along the illumination axis was found to be greater than predicted by the spatially varying system PSF, modelled as the detection PSF axially modulated by the spatially varying light-sheet thickness. The possible reasons for this include a degraded detection PSF, as well as a more tightly focused beam waist than modelled (due to more filling of the excitation objective BFP, and spherical aberration in illumination. Experimentally verifying whether the system PSF model provides an accurate description of the variation of the axial resolution along the illumination axis would require more measurements at larger distances away from the light-sheet beam waist. Besides optimization of the current optical setup to reduce the influence of aberrations, further resolution improvement can be achieved by combining the DSLM illumination with rolling shutter confocal slit scanning and light-sheet engineering to achieve better optical sectioning and axial resolution over a larger FOV.

4 High-speed 2D imaging of calcium dynamics in ventricular cardiomyocytes

4.1 Introduction

4.1.1 Calcium regulation of excitation contraction coupling

Calcium ion dynamics play a key role in the regulation of excitation-contraction coupling in cardiomyocytes. When an action potential depolarizes the cell, the voltage change activates dihydropyridine receptors (DHPR), also termed L-type calcium channels, located mainly in the transverse-axial tubular system (t-tubules), which are inward extensions of the sarcolemma (the plasma membrane of cardiomyocytes) that penetrate deep into the cardiomyocyte centre (**Fig. 4.1**).

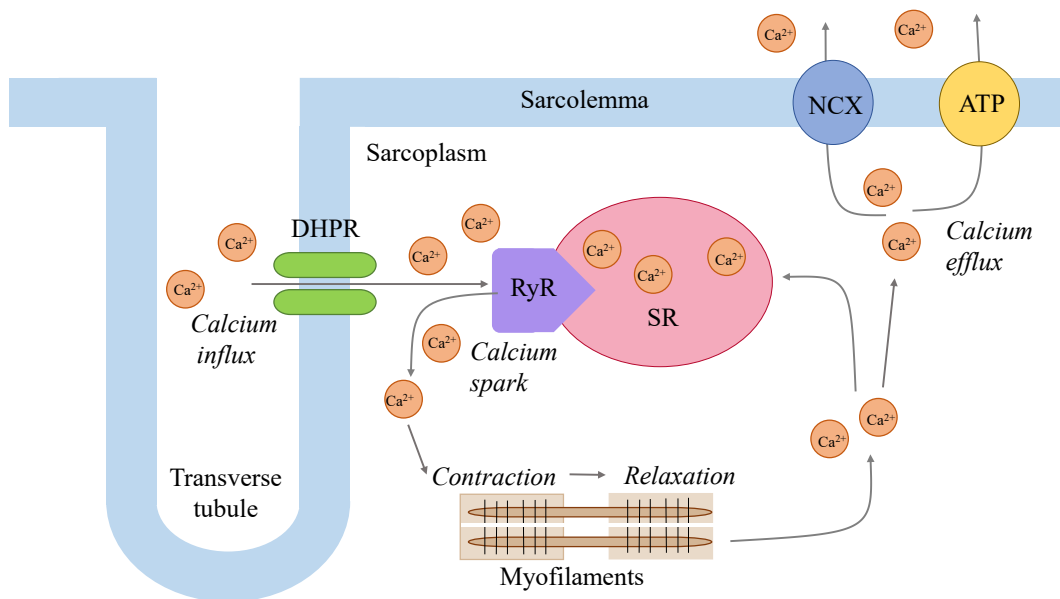


Figure 4.1 Simplified illustration of calcium regulation during excitation-contraction coupling in cardiomyocytes. Diagram adapted from (Bers, 2002).

In close proximity to DHPRs are areas of the sarcoplasmic reticulum (SR) membrane. Depolarization of the t-tubule system is thought to simultaneously activate DHPRs in all parts of the cell, which results in the channels opening, and an influx of calcium ions into the cell. The increase of the local calcium concentration just below the membrane surface activates nearby type-2 ryanodine receptors (RyR), which are calcium release channels on the SR, grouped in clusters of up to ~20 channels. Activation results in RyR opening, which enables rapid release of Ca²⁺ from internal SR stores into the cytoplasm – a process known as calcium-induced calcium release (CICR) (Fabiato, 1983).

It is thought that one L-type Ca channel controls the activation of a cluster of RyRs, and hence calcium release from the SR occurs in the form of localized release events known as *calcium sparks* (Cheng, Lederer & Cannell, 1993). While sparks have widely been considered the elementary unit of calcium release, evidence suggests that these are made up of even smaller sub-micron fundamental building

blocks known as *calcium quarks*, which correspond to the opening of a single Ca^{2+} channel (Brochet et al., 2011; Niggli, 1999; Niggli & Egger, 2002).

When large numbers of DHPRs are activated, the cumulative effect of these individual events result in a global increase of calcium concentration across the cell, known as a *calcium transient*. The calcium ions bind to troponin, a protein complex bound to actin myofilaments, initiating cell contraction. The increased calcium concentration in the cell also leads to more cytoplasmic Ca^{2+} binding to DHPR, resulting in channel closure (Ca-dependant deactivation), hence preventing further calcium ions from entering the cell. Cardiac relaxation is achieved by deactivation of troponin due to Ca being removed from the cytosol. This is achieved by ion transport out of the cell by the sarcolemmal sodium-calcium exchanger (NCX) and sarcolemmal Ca^{2+} ATPase, as well as the uptake of calcium ions back into the SR by active transport against its concentration gradient by the sarcoplasmic reticulum Ca^{2+} ATP-ase (SERCA) (Bers, 2002).

4.1.2 Desynchronization of calcium dynamics

Under stable conditions the cyclical contraction and relaxation of healthy ventricular cardiomyocytes is regulated by calcium flux in and out of the cytosol. However, in the failing heart, many of the mechanisms described above in **Section 4.1.1** break down, reducing contractility. These effects include (Bers, 2006): (1) reduced function of SERCA causing slower and decreased Ca reuptake into the SR, (2) functional modifications to RyR resulting in more Ca leak from the SR, (3) increased expression of the NCX, which results in a change in the balance of Ca uptake into the SR and Ca efflux from the cell, and (4) structural changes in the organisation and density of the t-tubule network (Lyon et al., 2009).

This loss of t-tubule structure results in some RyRs not being closely associated with DHPRs – these have been termed “orphaned” ryanodine receptors (Song et al., 2006) and cannot be directly activated by surface Ca channels, but can instead be activated by Ca released from neighbouring clusters. The result of this delayed activation of orphaned RyR is reduced synchrony in Ca^{2+} release (Louch et al., 2006), leading to slower and smaller calcium transients and weaker contraction. These alterations to cellular Ca control can provoke arrhythmias (Heinzel et al., 2011; Ibrahim et al., 2011).

Øyehaug et al. combined confocal line scan data with computational modelling to study the desynchronization of calcium dynamics as a result of heart failure in mice and showed that reduced SR Ca^{2+} content desynchronized the Ca^{2+} transient (Øyehaug et al., 2013). The computational model predicted greater dyssynchrony of calcium release due to t-tubule disorganization than what was measured experimentally. The discrepancy was attributed to increased RyR sensitivity, indicating that the dyssynchrony of calcium release in cardiomyocytes could be the result of complex interplay between RyR sensitization and SR calcium content. More recent computational modelling by Marchena and Echebarria showed that detubulation reduced transient amplitude and synchronization, leaving the SR load unaffected (Marchena & Echebarria, 2020).

Desynchronized calcium release across the cell can lead to formation and propagation of spontaneous *calcium waves* through the cell. These calcium events differ from the homogenous and regular oscillations in Ca^{2+} concentration that occur in synchronized and electrically stimulated calcium transients. Calcium waves have been observed in both isolated cardiomyocytes and entire cardiac organs (Kaneko et al., 2000), indicating that irregular calcium dynamics within individual cardiomyocytes may lead to arrhythmia at the tissue level.

4.1.3 Differences in left and right ventricle cardiomyocytes

The left and right ventricle function at different pressures: the right ventricle (RV) is responsible for providing output to the low-pressure pulmonary circulation, while the contraction of the left ventricle (LV) provides cardiac output to the high-pressure systemic circulation. These pressure differences account for variation in their shape, with the left ventricle having a longer ellipsoidal shape, thicker walls and different pressure-volume loops (Redington et al., 1988). The differences have also been partially attributed to the distinct embryological origins of the two ventricles (Boukens et al., 2009).

The cardiac structural and functional heterogeneity is fundamental to the heart's function, and on a cellular level, left and right ventricle cardiomyocytes may have differences in EC-coupling and hence calcium dynamics and contraction both at baseline and in pathology. However, reports of differences are inconsistent in studies on different animal models (Molina, Heijman & Dobrev, 2016): for example, Kondo et al. measured weaker shortening in RV myocytes in mice, accompanied by lower transient amplitude (Kondo et al., 2006), however Sathish et al. showed no difference in transient amplitude in rats (Sathish et al., 2006).

More recent work by Medvedev et al compared differences in cellular microstructure and calcium handling between LV and RV cardiomyocytes from healthy and pathological samples (Medvedev, 2020). Control RV CMs were found to be of similar length but thinner than LV CM, with differences in tubular network organization: LV CMs had shorter axial tubules but longer transverse tubules. Cardiomyocytes from the two ventricles also had differences in contraction and calcium transients, with RV cardiomyocytes having slower shortening and relaxation, and increased transient dyssynchrony, but similar rise and decay times. Calcium sparks in RV myocytes were found to have lower amplitude, smaller FWHM and mass (see **Section 4.3.3** for definition). Some differences in physiological properties of RV myocytes have been attributed to a modified calcium sensitivity due to lower expression of calcium-binding protein which regulate the activity of myofilaments (Jeon et al., 2019).

Certain differences only manifested in disease models: under pulmonary hypertension (PH), a condition where blood pressure in lung arteries is increased (Chesler et al., 2009), confocal line scan measurements by Medvedev showed increased spark frequency, spark duration and transient time-to-peak in RV myocytes. Other differences between calcium dynamics in control LV and RV myocytes were amplified in PH models compared to control myocytes: RV under PH had further

increased transient dyssynchrony in comparison to PH LV. Finally, certain differences between LV and RV calcium dynamics present in healthy samples were reversed in PH models, with PH RV myocytes having larger spark amplitude and mass compared to PH LV myocytes (Medvedev et al., 2021).

4.1.4 Multidimensional imaging of calcium dynamics: approaches and challenges

Understanding the relationship between structural changes and the spatial variation and dyssynchrony in calcium release requires correlative imaging of calcium dynamics and cell architecture, which in turn needs optical techniques capable of fast imaging with high resolution over a sufficiently large FOV to adequately sample the spatial features and events of interest within the whole cell. Calcium sparks are highly localized both in space and time: the events are confined to a 2 μm diameter and happen on a time scale on the order of tens of ms, reaching the peak in ~ 10 ms and decaying to half intensity in 20 ms (Cheng & Lederer, 2008). Ventricular cardiomyocytes isolated from rats, have an elongated cylindrical shape, with an average length and width of 115 μm and 25 μm respectively (Sorenson et al., 1985). The average diameter of t-tubules in cardiomyocytes, measured from deconvolved two photon fluorescence imaging, was estimated to be 250 nm, with 1.8 - 2 μm periodicity along the long axis of the cell (Soeller & Cannell, 1999). Hence, correlative imaging of these dynamics with the cell microstructure requires millisecond acquisition rates, and sub-micron spatial resolution.

The standard method for imaging calcium dynamics in myocytes at subcellular resolution has been with a laser scanning confocal microscope in line-scanning mode, building up a one-dimensional x-t image at 1-2 ms temporal resolution (Louch et al., 2006; Song et al., 2006). Line-scan confocal has previously been used to demonstrate that most sparks occur within 0.5 μm proximity of a t-tubule (Shacklock, Wier & Balke, 1995). However, the limited spatial information is insufficient for full characterization of calcium dynamics in physiologically anisotropic cardiomyocytes. Additionally, the variable distances of calcium release events from the scan line introduces a significant bias in measurements of spark morphology (Cheng et al., 1999).

Significant effort has been invested into progressing from line-scanning to increasing spatial dimensionality while maintaining a sufficiently high signal-to-noise ratio (SNR) and temporal resolution. Acousto-optical deflector (AOD) scanning enabled two-dimensional confocal line-scanning at up to 240 fps allowing visualization of a 2 μm periodic striation pattern in calcium indicator fluorescence at the start of the stimulated calcium transients (Cleemann, Wang & Morad, 1998). High-speed (240 Hz) two-dimensional confocal imaging of the midsection of rat atrial cardiomyocytes by (Woo, Cleemann & Morad, 2002), demonstrated earlier transient onset at the periphery of the cell, compared with its centre. This phenomenon was previously observed in atrial myocytes at lower spatiotemporal resolution (Hüser, Lipsius & Blatter, 1996; Kockskämper et al., 2001; Mackenzie et al., 2001). Line-scan confocal imaging demonstrated more synchronous calcium release in rat ventricular cardiomyocytes, which was attributed to the more developed tubular network in comparison to atrial

cardiomyocytes (Berlin, 1995). Since then, high-speed slit-scanning confocal microscopes have achieved up to 667 fps over a 512×30 -pixel frame (Iribe et al., 2009), while spinning disc confocal microscopy has been used for imaging of neural calcium dynamics at up to 2000 fps (Takahashi et al., 2010).

Multiphoton fluorescence microscopy offers an alternative optically-sectioned imaging technique with less out of plane photobleaching than confocal microscopy and has been used for in vivo imaging of cardiomyocytes in the beating mouse heart (Jones, Small & Nishimura, 2018). However, multiphoton imaging requires high power laser excitation, which can lead to photobleaching and phototoxicity in the confined focal spot (Patterson & Piston, 2000). While single-molecule localization microscopy (SMLM) has been useful for resolving sub-diffraction structural biological elements, the stochastic image reconstruction is often the bottleneck in imaging dynamic biological processes. However, recent work by Hurley et al. implemented correlative imaging of calcium dynamics with cellular microstructure by combining diffraction-limited optically-sectioning total internal reflection fluorescence (TIRF) of Ca^{2+} sparks with super resolution DNA-PAINT (Jungmann et al., 2014) imaging of ryanodine receptor calcium channels (Hurley et al., 2021).

The challenges of achieving optically-sectioned imaging with reduced phototoxicity and fast imaging speed are addressed by the fundamental principles of light-sheet fluorescence microscopy, where illumination is confined to the imaged plane, also enabling parallelized acquisition of the fluorescence across the whole illuminated slice. The earliest application of oblique plane microscopy (OPM) (Dunsby, 2008), a single objective light-sheet fluorescence microscopy technique, for proof-of-concept high-speed live cell imaging of calcium dynamics in cardiomyocytes achieved optically sectioned imaging at over 900 fps (Kumar et al., 2011). In work by Sikkel et al. (2016) dual-channel 3D OPM imaging of calcium dynamics in correlation with the sarcolemma and t-tubule network revealed that Ca^{2+} waves in HF rat cardiomyocytes originate in regions of high t-tubule organization (Sikkel et al., 2016). Two-dimensional imaging of calcium sparks at 667 fps demonstrated increased spark frequency in tubulated regions, with higher spark rates on tubules, as opposed to between them. The correlative imaging approach combining high spatial and temporal resolution also allowed direct comparison of spark morphology in relation to its spatial origin with respect to the tubular structure.

4.1.5 Experimental objectives

The key objective for the work in this chapter is to target the challenges of quantitative imaging of dynamics calcium events in ventricular cardiomyocytes for insight into their electrophysiology and function, as a key step towards understanding the changes that occur with disease. While HF is known to contribute to desynchronization of calcium release (**Section 4.1.2**), some spatial dyssynchrony within normal healthy cells may be expected due to the directionality of myocyte shortening, with increased displacement and stress measured at the ends of the cell by traction force microscopy

(McCain et al., 2014), as well as the spatial distribution of the t-tubule network and RyR clusters, and any selective cluster activation within each transient period. Additionally, previous work has suggested that calcium spark frequency and the transient rising phase correlates on the proximity of calcium release sites to the t-tubule network (Dries et al., 2013; Sikkel et al., 2016), indicating differences between release events from “coupled” and orphaned RyR clusters. However, motion artefacts from contraction and limited spatio-temporal resolution of employed imaging techniques have prevented the multi-dimensional characterization of calcium transient development and correlation of calcium release with cell structure. Finally, while left and right ventricle myocytes are known to have differences in structure and membrane organization, there are limited and conflicting measurements of differences in calcium handling and release in healthy cells (**Section 4.1.3**).

Application of the new dual-objective flexible light-sheet fluorescence system described in the previous chapter and in (Sparks et al., 2020) targets the optical and instrumental limitations of the OPM system implemented in the work described above (Sikkel et al., 2016). The Gaussian light-sheet thickness is reduced from 3.8 μm to 2.2 μm (FWHM), resulting in improved contrast and fewer artifacts from out of focus calcium dynamics and structural features. In OPM, reimaging the tilted plane of observation within the intermediate image results in loss of nearly half of the light due to partial overlap of the collection cones of the primary and refocusing objectives. The dual-objective geometry in the new custom system circumvents the reduced collection efficiency, allowing the use of a lower photodose with minimal decrease in SNR, while avoiding the loss of spatial resolution in OPM from the smaller effective detection NA of 0.64. The improved spatial resolution is accompanied by higher pixel sampling, with an effective pixel size of 0.15 μm compared to 0.24 μm in the OPM system. Additionally, the larger sensor size and higher frame rate of the employed camera allow high-speed imaging over a larger field of view (FOV) (the PCO.edge camera implemented in the OPM system imaged a 234 x 49 μm area) and can be multiplexed for several spectral channels.

The work described in the rest of this chapter addresses the challenges of correlative high-speed imaging of calcium dynamics and cellular microstructure in cardiomyocytes using the custom dual-objective light-sheet fluorescence microscope to image calcium sparks and transients in 2D. The novel microscopy approach requires optimization of sample preparation and imaging protocols, development of a custom image analysis pipeline for automated analysis of tens of cells, and subsequent interpretation of the collected data. Automated analysis of sparks and transients is used to resolve the spatial dyssynchrony in calcium release in healthy ventricular cardiomyocytes, correlating this with the t-tubule network. Finally, the analysis is used to compare LV and RV cardiomyocytes for insight into physiological differences at the macro scale. Hence, the aims of the work done in this chapter are the following:

1. To apply high-speed dual-channel 2D imaging of calcium dynamics and microstructure in ventricular cardiomyocytes.
2. To establish an image analysis pipeline for automated detection and characterization of calcium sparks and transients in correlation with the detected t-tubule microstructure.
3. To investigate the spatial dyssynchrony of transient development across the cell.
4. To compare the spatiotemporal properties of calcium sparks and transient development based on their correlation to the t-tubule structure.
5. To investigate the differences in calcium spark and transient dynamics in left and right ventricle cardiomyocytes.

As part of aims 3-5, the following hypotheses are tested:

1. Transient development is not fully synchronized across all regions of the cell.
2. Characteristics of calcium spark and transient dynamics correlate with the t-tubule structure.
3. LV and RV cardiomyocytes have differences in calcium spark and transient dynamics.

4.2 Experimental methods

All studies were carried out with the approval of the local Imperial College ethical review board and the Home Office, UK and in accordance with the United Kingdom Home Office Guide on the Operation of the Animals (Scientific Procedures) Act 1986, which conforms to the Guide for the Care and Use of Laboratory Animals published by the U.S. National Institutes of Health under assurance number A5634-01. Single left and right ventricular male rat cardiomyocytes were enzymatically isolated by Peter O’Gara at the Imperial Centre for Translational and Experimental Medicine (ICTEM) following the method outlined in (Sato et al., 2005) and then suspended in a low Ca^{2+} enzyme solution (mM): NaCl (120), KCl (5), MgSO_4 (5), Na pyruvate (5), glucose (5), taurine (20), HEPES (10), CaCl_2 (0.2), pH 7.4 adjusted with 1M NaOH. The cells were transported to Blackett Laboratory, stored at room temperature and imaged within 8 hours of isolation.

Left and right ventricular cardiomyocytes from $N = 7$ male rat hearts were imaged on separate days within similar time frames. Cells from each ventricle were labelled as “A” and “B” when received, and all image acquisition and analysis was done blinded with respect to ventricle type. The imaging was done following two separate dye loading procedures, with each procedure containing an aliquot from each ventricle, imaged consecutively: cells from “A” then cells from “B”, or vice versa. For the second loading, the order of imaging was reversed.

Sample preparation for imaging

The live-cell dual-labelling preparation protocol was based on that used by (Sikkel et al., 2016) for OPM-based imaging of live cardiomyocytes, and on that used for our proof-of-concept live cell imaging with the new dual objective system (described in (Sparks et al., 2020)). For simultaneous monitoring of

the calcium dynamics and intracellular tubular microstructure, the live isolated adult rat cardiomyocytes were dual-labelled with cell-permeant calcium indicator Fluo-4 AM (ThermoFisher Scientific) and CellMask Orange (CMO) plasma membrane stain (ThermoFisher Scientific). For each labelling procedure, 1 mL of the myocyte suspension from each ventricle was incubated with 0.16% Pluronic acid, a dispersive agent that facilitates dye solubility, and 5 μ M Fluo4-AM (dissolved in dimethyl sulfoxide, DMSO) for 15 minutes at 37°C, followed by the addition of 5 μ g ml⁻¹ CMO, and incubated for another 5 minutes. Throughout the incubation period, the cells, suspended in a 10 mL Falcon tube, were placed on a rotary mixer set to low speed to ensure homogenous dye distribution and protected from light by wrapping in aluminium foil.

After the incubation time, the cells were centrifuged at low speed (21 RCF (relative centrifugal force, or G-force)) at 20°C for 1 minute to form a pellet. The supernatant was removed and the pellet was resuspended in the “working solution” composed of a 1:1 mixture of Dulbecco's modified Eagle's medium (DMEM) (Gibco BRL, Life Technologies Ltd., UK) solution containing 1.8 mM Ca²⁺ and 0.2 mM Ca²⁺ enzyme solution and left in the dark at room temperature for 30 minutes for de-esterification. For imaging, the cells were attached to the imaging chamber using 1.5 μ L mouse laminin (Gibco) and immersed in Normal Tyrode containing (in mM): NaCl (140), KCl (6), Glucose (10), HEPES (10), MgCl₂ (1), CaCl₂ (1), pH adjusted to 7.4 with NaOH. For correlative mapping of calcium dynamics with cell structure, and to avoid motion artefacts from cell contraction, para-Nitroblebbistatin (NBleb) (Axol Bioscience), a non-phototoxic low-fluorescence derivative of the myosin inhibitor blebbistatin (Képiró et al., 2014) was used to decouple cell contraction from the calcium dynamics. The decoupler was added to the working solution and Normal Tyrode at 25 μ M concentration, ensuring thorough solution mixing.

Single cell imaging chamber

The imaging chamber for single cell adult cardiomyocytes consisted of a glass slide, with a 2 mm high silicone strip around the perimeter to contain the immersion liquid (**Fig. 4.2**). Electric field stimulation at a frequency of 0.5 Hz and 2 ms pulse duration was delivered by 0.8 mm diameter platinum electrodes separated by 5 mm at 1.5 \times the threshold voltage for contraction, found to be approximately 20 V.

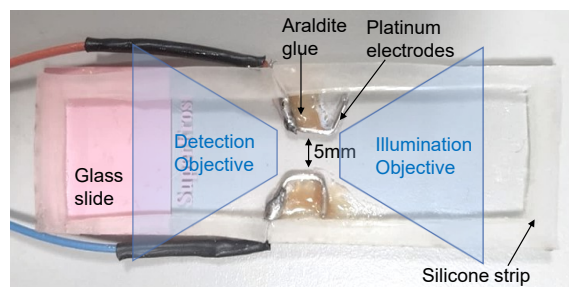


Figure 4.2 Top view of the pacing chamber prototype. The arrangement consists of two platinum 0.8 mm diameter electrodes separated by approximately 5 mm, attached to a glass slide using Araldite glue. A silicone strip around the perimeter of the slide contains the cell media. Objective positioning is illustrated in blue.

2D LSFM data acquisition

Fluo-4 and CMO were excited simultaneously by the 488 nm and 561 nm laser lines at 25 μ W and up to 35 μ W power respectively, measured in the back focal plane of the excitation objective. Fluorescence emission was acquired in the form of two-dimensional dual-channel time-lapse data using a Hamamatsu Orca Fusion sCMOS camera with a $6.5 \times 6.5 \mu\text{m}$ pixel size. The camera was operated in normal area external trigger mode, with synchronous readout trigger, with angular dithering, at 395 fps for a 1152×512 pixel ROI, which corresponds to a $170.2 \times 75.6 \mu\text{m}$ FOV in sample space at $44\times$ magnification and $0.1477 \mu\text{m}$ pixel size. The horizontal extent of the camera ROI was chosen to fit the length of a cardiomyocyte image, and the height was set to fit the extent of the two vertically displaced spectral channels, each large enough to fit the width of a cardiomyocyte image. Sample navigation was carried out using the widefield low-NA objective mounted below the sample stage in transillumination, allowing selection of cells which had their long axis approximately perpendicular to the light-sheet propagation direction to fit within the rectangular FOV.

The acquisition duration ranged between 12,000-18,000 frames (~ 30 -45 s). The cells were electrically stimulated starting 1 minute before each acquisition, with the electrical stimulation maintained for the first half of each acquisition. The synchronization monitor signal from the electric field stimulation unit was recorded as a digital input to the DAQ card.

Statistical analysis

A standard approach to statistical hypothesis t-testing is the Student's t-test (Student, 1908), which is used to determine whether the means of two datasets are significantly different. The t-test operates under the assumption that the underlying compared distributions are normal (Gaussian), and that the variances of the compared populations are equal. Unpaired t-tests compare independent samples, while paired t-tests consider the difference between matched pairs from two datasets. Hence, each pair acts as its own control, and this additional information about the sample can be used to increase the statistical power, reducing the probability of type II errors, or false negatives.

The analyzed parameters of calcium dynamics from single cells have a hierarchical structure, with multiple cardiomyocytes isolated from the same rat heart (Sikkel, 2015). Individual physiological differences between the animals from which the cells originate, as well as minor variation in the isolation process or experimental conditions mean that cells from the same heart may be more similar. Ignoring this dependence can lead to over-estimation of significance through type-I errors (false positives). In this chapter, we apply three statistical approaches to evaluate whether differences between categories are significant: (1) unpaired (disaggregated) testing, where hierarchy is ignored and each measurement on cellular level is considered independent, (2) paired testing, where quantified parameters of calcium dynamics within the same cell are treated as dependant, and (3) aggregated-

paired testing, which compares the differences between each cell, averaged across all cells from a single heart/animal.

The D'Agostino-Pearson normality test (D'Agostino & Pearson, 1973) was used to test for normal (Gaussian) distribution, and, if the dataset did not pass the normality test, for lognormal distribution, to evaluate whether parametric testing should be applied. For normal and log-transformed lognormal distributions, the paired and unpaired t-tests (PT and UT respectively) were used to determine statistical significance. When applying two-sample t-tests, the F-test of equality of variances was used to test for homoscedasticity, or the homogeneity of variance across the datasets. When the variances of two datasets were significantly different, the unpaired t-test was applied with Welch's correction (UTWC) (Welch, 1947). For datasets which did not follow a normal or log-normal distribution, the unpaired Mann-Whitney test (MW) (Mann & Whitney, 1947) and paired Wilcoxon signed rank test (WSRT) (Wilcoxon, 1992) were used. Statistical analysis of significance was carried out in GraphPad Prism 9.1.1 software. P-values < 0.05 were considered statistically significant.

4.3 Image analysis

4.3.1 Data pre-processing

All acquisitions were previewed in ImageJ/FIJI software, with intensity time traces taken through rectangular ROIs placed manually within the cells to provide an overview of the calcium dynamics in the cell. Each acquisition was screened based on the following four criteria to determine whether it would be included for subsequent analysis: (1) cell health, (2) successful decoupling, (3) transient presence and amplitude, and (4) acquisition quality. Cells were considered healthy if they had an elongated brick-like (not curled or rounded) shape, predominantly intact t-tubule structure, no spontaneous contractions or calcium waves during observation, and no irreversible change in shape or basal fluorescence during acquisition – the acquisition was excluded if the total variation in baseline fluorescence over the whole acquisition exceeded the transient amplitude. Cells that exhibited mechanical contraction during stimulation were also excluded. Additionally, only cells with transient amplitude of at least 5 digital numbers (DN) above baseline (with an amplitude of approximately $\Delta F/F_0 \geq 1$) were selected, as this was found to correspond to the required SNR for robust automated transient characterization. Finally, each analyzed acquisition was required to have the central part of the cell in focus and no sample drift in any direction.

Before undergoing analysis of the calcium dynamics in correlation with the cell microstructure, the acquired x-y-t data underwent a series of pre-processing steps implemented using MATLAB, including spectral channel co-registration, background subtraction, and segmentation. In the next few sections, the pre-processing and analysis will be demonstrated on a representative *Cell X*. First, fixed pattern noise estimated from an average of 1000 frames acquired with the laser shutter closed was subtracted from each raw frame in the dataset (**Fig 4.3a**). Next, the two spectral channels are split and co-registered

using an affine transformation (i.e., one that preserves co-linearity) consisting of rotation, two-dimensional scaling, and translation. As the Fluo-4 detection path has additional magnification introduced by the two lenses used to correct for Fluo-4 channel defocus (see **Section 2.2.1**), the Fluo-4 images were demagnified by ~ 0.9 in each lateral dimension as part of the co-registration process (**Fig. 4.3b**). The exact parameters for the transformation were manually determined by achieving best visible overlap for a dual-channel dataset obtained by imaging 200 nm diameter fluorescent beads (T7280, TetraSpeck™, Thermofisher Scientific) embedded in agarose. The co-registered and merged channel time-lapse acquisition for Cell X is demonstrated in **Video 4.3**.

For the Fluo-4 channel, the background is determined by estimating the average signal across a rectangular area manually selected from outside the cell area using the *imrect* MATLAB function. The background is subtracted as a constant offset from each image. Finally, the cell segmentation is achieved through intensity thresholding of the mean image across 3,160 frames from the Fluo-4 channel, and a series of subsequent modifications of the resultant mask, which are described in the next paragraph. The binarization was achieved through global image thresholding using Otsu's method (Otsu, 1979) implemented in MATLAB's *graythresh* and *imbinarize* functions.

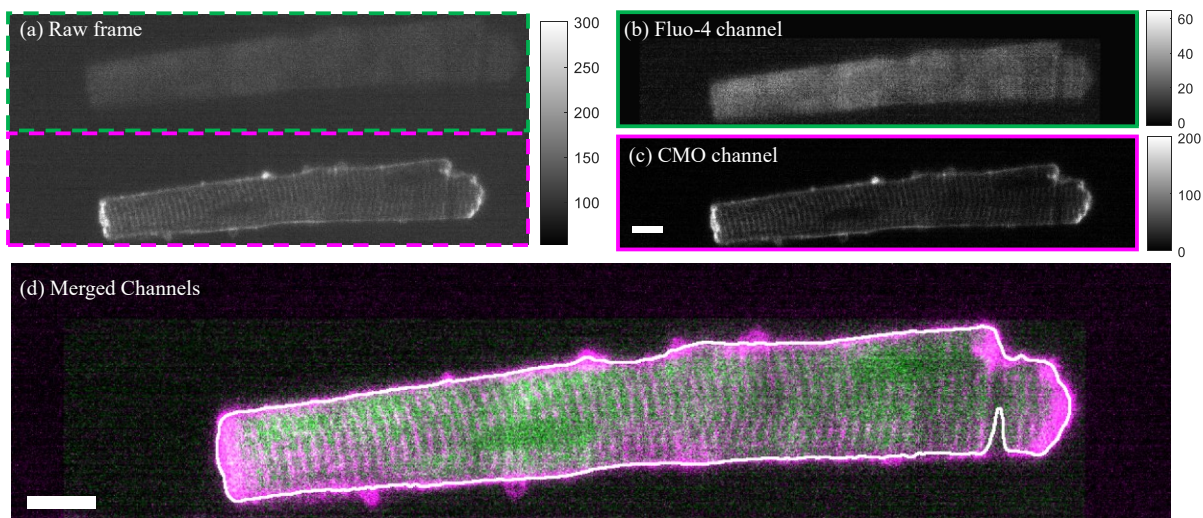


Figure 4.3 Pre-processing of the dual-channel data demonstrated for a single frame from a 12,000-frame acquisition of a representative Cell X at 395 fps at the peak of the first transient. (a) Raw single frame with green and magenta dashed rectangles indicating the ROI used for the Fluo-4 and CMO channels respectively. (b) Separated and co-registered spectral channels with subtracted fixed pattern noise. (c) The Fluo-4 (green) and CMO (magenta) spectral channels overlaid with the segmentation mask outlined in white. Intensities are in digital numbers. Scalebar: 10 μm .

To exclude any unwanted particles or parts of other cells appearing within the imaged FOV, connected components containing fewer than 30,000 pixels (corresponding to a cell area of $\sim 650 \mu\text{m}^2$) are removed, and the thresholding step is repeated with that region masked out. Any holes within the masked region are filled using the *imfill* function. The remaining cell mask is smoothed by convolution

with a $5 \times 5 \times 5$ pixel x-y-t kernel using the *convn* function. The resultant mask (shown as a white outline in the merged channel image in **Fig 4.3d**) is used to define the cell area for the next steps of the analysis.

4.3.2 T-tubule detection and nuclear segmentation

Correlation of calcium dynamics with the tubular microstructure requires a method of extracting the structural features from the imaged cell. Existing methods make use of the t-tubule periodicity and extract the spatial frequency peaks from the two-dimensional Fourier transform of the image. AutoTT (Guo & Song, 2014), a MATLAB automated analysis program, uses morphological feature extraction from a skeletonized tubular network to identify transversely and longitudinally oriented t-tubules, and uses peak extraction from the 2D FFT image to characterize the density and regularity of the transverse elements, but requires image alignment such that the cell is parallel to the horizontal axis. The ImageJ/Fiji plugin TTorg (Pasqualin et al., 2015) also uses peak extraction in the spectral domain to identify periodic structure and accommodates any cell orientation without need for rotation. In the approach by Sikkel et al., the tubule mask was calculated within the well-tubulated region of the cell based on extracted orders in the 2D FFT of the CMO image (Sikkel et al., 2016). These approaches use the frequency domain to only treat the transverse elements of the tubular structure, and do not consider structural elements that have a different rotational orientation to the main longitudinal axis of the cell.

In the approach used in this analysis the structural features were extracted without any prior assumptions of their orientation or organization level, and the analysis was carried out directly in image space. The tubule microstructure was extracted from the fluorescence of the CMO membrane stain using an intensity threshold. As the cell is immobilized and there are minimal motion artefacts during acquisition, an average across 12,000 frames in the CMO-channel was taken to maximize the SNR (**Fig. 4.4a**). To account for local background spatially varying across the cell, the average image was blurred by a 15×15 -pixel median filter, with the resultant image subtracted from the original (**Fig. 4.4a&b**). In order to calibrate for the CMO intensity variation across individual cells, a single global threshold, manually selected for the whole dataset, was multiplied by a scaling factor determined from the cell membrane intensity for each individual cell. The cell membrane intensity was calculated by taking a vertical maximum intensity projection (MIP) of the CMO image and calculating the average in the horizontal direction across the central third of the FOV (**Fig. 4.4d**), which allowed exclusion of the peaks in the vertical MIP at the ends of the cells. The scaled intensity threshold was used to produce a binary mask and connected components with areas less than 20 pixels were excluded, as they were predominantly found to be due to noise artefacts. The tubule mask was multiplied by the cell segmentation mask to exclude any regions outside of the cell and smoothed by a 3×3 px median filter (**Fig. 4.4f**).

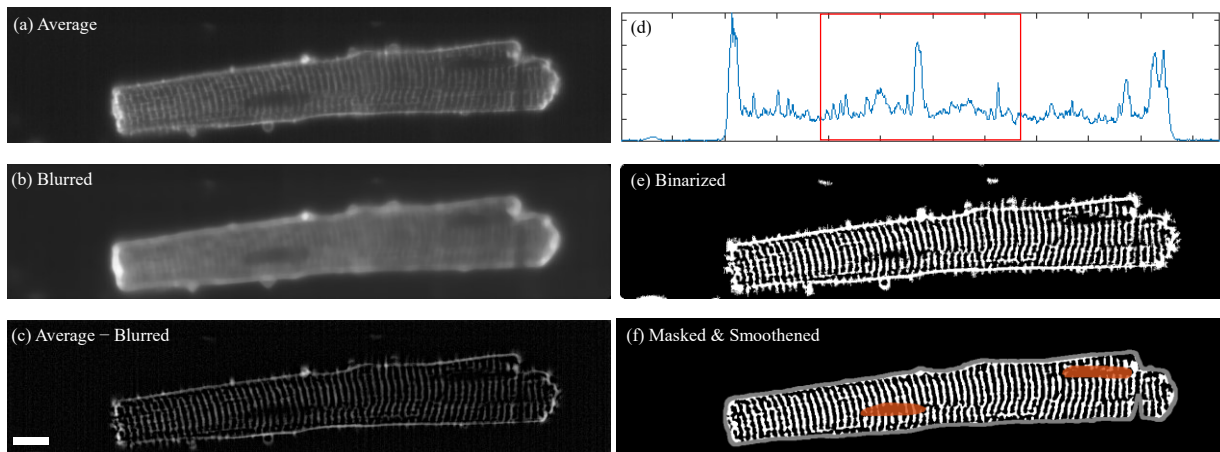


Figure 4.4 Extraction of tubular microstructure from the CMO-channel fluorescence, demonstrated on Cell X. (a) CMO channel image stack average. (b) Average image blurred by a 15×15 px median filter. (c) Image 'b' subtracted from image 'a'. (d) Maximum intensity projection of image 'a' taken along the vertical axis, with intensity (a.u.) on the vertical axis and horizontal position (in pixels) on the horizontal axis. The cell membrane intensity is estimated by taking an average within the central third of the horizontal axis (red rectangle outline). (e) Binarized version of image 'c' using a global manually determined intensity threshold scaled by the cell membrane intensity for this individual cell. (f) Smoothed t-tubule map multiplied by the cell segmentation mask with cell membrane outline shown in grey and the manually identified nuclei in orange. Gamma correction of 0.5 has been applied to the non-binary images a-c to aid visualisation. Scalebar: 10 μm .

Nuclei are manually segmented by visual inspection of the stained cell membrane in the CMO-channel averaged over the full acquisition. The nuclear envelope was outlined manually using the *drawassisted* MATLAB tool to create a ROI. Certain cells did not have an identifiable nucleus in the imaged plane, while others had up to two visible nuclei, and this was reflected in the manual nuclei segmentation. The selected ROI were combined to create a binary mask, within which connected components were identified and characterized using the *bwconncomp* and *regionprops* MATLAB tools.

For Cell X shown in **Fig. 4.4**, 43% of the cell area is covered by t-tubules, which, despite the presence of two nuclei within the imaged plane, is still at the higher end in comparison to the $39 \pm 4\%$ (mean \pm standard deviation (SD)) cell area average across the $n = 60$ cells analyzed. The t-tubule period, measured from line profiles through a tubulated region, was estimated to be 2 μm (or 14 pixels, to the precision of one pixel), in agreement with previous measurements in other studies (Soeller & Cannell, 1999). A selection of t-tubule maps with masked nuclei from 8 ventricular cardiomyocytes is shown in **Fig. 4.5**, with the full set of maps for all analyzed cells ($n = 60$) presented in **Fig. A4.1 (Appendix A4)**. In total, 48 nuclei were labelled, with nuclei identified within the imaged plane in 40 out of the 60 cells analyzed.

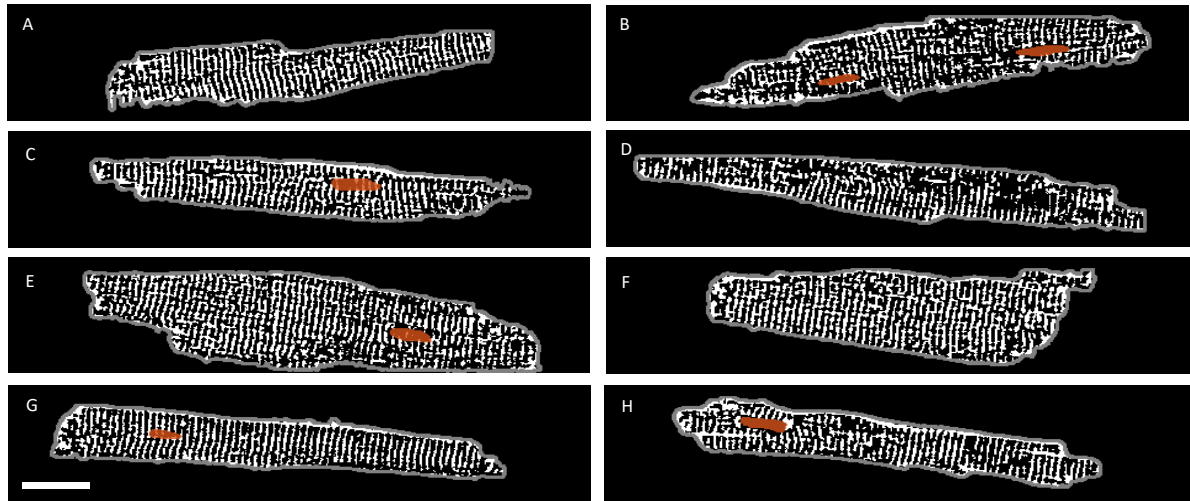


Figure 4.5 T-tubule maps (white) with the cell membrane outline (grey) and identified nuclei (orange) across a selection of 8 different cells (A-H). Scalebar: 20 μm .

Distance to nearest tubule

For non-binary correlation of calcium dynamics with the cell structure, we want to assess the distance of the calcium release events to the closest part of the tubular network. This is done by calculating the “distance to the nearest tubule” (DNT) map by taking the Euclidian distance transform (Maurer, Qi & Raghavan, 2003) of the tubule binary mask using the MATLAB *bwdist* function. In **Fig. 4.6**, this is demonstrated on cell D, which has less than the average tubule coverage of the cell area (34% in comparison to the $39 \pm 4\%$ (mean \pm SD across $n = 60$ cells)). The DNT metric is used to distinguish between tubules (DNT = 0), tubulated ($0 < \text{DNT} \leq 5\text{px}$) and detubulated ($\text{DNT} > 5\text{px}$) regions of the cell (**Fig 4.6b-d**). For this cell, the fraction of the area classified as detubulated was higher than average (8% of the cell compared with $2.9 \pm 4.9\%$ (mean \pm SD) across $n = 60$ cells). The 5-pixel ($0.74\text{ }\mu\text{m}$) threshold used to distinguish tubulated and detubulated areas was determined by taking line profiles through DNT maps in visually identified areas of well-organized tubules within cells and considering the upper limiting DNT value within those areas.

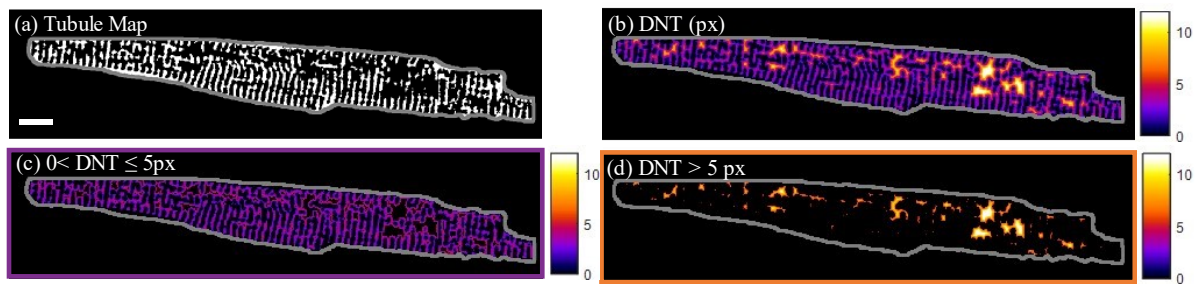


Figure 4.6 T-tubule and distance to nearest tubule maps. (a) Binary tubule map of cell D with the cell outline shown in grey. (b) Pixel distance to nearest tubule (DNT) map of cell D. (c) Tubulated regions of cell D with $0 < \text{DNT} \leq 5\text{px}$. (d) De-tubulated regions of cell D with $\text{DNT} > 5\text{px}$. Scalebar: 10 μm .

4.3.3 Spark analysis

The automatic detection and quantification of calcium sparks in time-lapse data is crucial for large-scale unbiased analysis of spark dynamics. The standard method involves identifying sparks based on how much their intensity deviates from the background noise level. However, in presence of noise, a single spark risks being detected as multiple events due to several intensity peaks exceeding the threshold. To avoid this, Cheng et al. implemented a two-fold thresholding method to identify sparks in distance-time confocal line-scan data (Cheng et al., 1999). This method defines sparks as connected areas above a lower threshold, with parts of the area exceeding a higher threshold, and has been adapted into ImageJ-based software such as *SparkMaster* (Picht et al., 2007) and *IOC BIO* (Laasmaa et al., 2019). Building on previously described approaches, Bray and others implemented a robust algorithm for spark detection in two-dimensional confocal time-lapse data, incorporating a sophisticated method to account for the temporally varying background fluorescence for each pixel (Bray, Geisse & Parker, 2007). More recent work by Illaste et al. (Illaste et al., 2019) optimized the method by Tian and others, which utilizes pixel-wise fitting of calcium events in frame-scan data (Tian, Kaestner & Lipp, 2012). However, both are designed for and limited up to 150 Hz frame rates. Software adaptations of automatic spark detection in x-y image stacks include the ImageJ based plugin *xySpark* (Steele & Steele, 2014), and MATLAB/ImageJ based *iSpark* (Tian et al., 2015; Tian et al., 2019).

To accommodate the temporal sampling used in the light-sheet 2D time-lapse data, and to allow integration of the spark analysis into an automated spark, transient, structure and correlation analysis pipeline, spark detection and characterization was performed using a custom MATLAB code adapted from an earlier version implemented by Vincent Maioli for detection and characterization of sparks in OPM 2D time-lapse data (Maioli, 2016; Sikkel et al., 2016). Compared to the aforementioned analysis method, the key modifications include implementation of the Otsu method (Otsu, 1979) for thresholding in cell segmentation, calculation of *spark mass*, exclusion of sparks which start before the analyzed time series range, and adjustment of thresholds and parameters to optimize for the SNR and spatiotemporal sampling of the imaging system and settings used.

Spark detection

Calcium spark analysis was carried out on the last 5,000 frames (12.7 s) of each acquisition during which the electrical stimulation was switched off. The spark detection and quantification algorithm was implemented through the following steps. Spatio-temporal smoothing was applied by convolving the x-y-t data with a $5 \times 5 \times 3$ kernel using the *convn* function. Next, to account for any temporal variation in cell background intensity, the 5,000-frame dataset was divided into 5 intervals, each consisting of 1,000 frames, over which the background is assumed to be constant with time. To normalize for background and varying labelling levels in between individual cells, the spark detection algorithm was implemented on data divided by the mean intensity map, calculated for each pixel across each 1000-frame interval.

The initial detected sparks were defined as connected components with intensities above the lower threshold T_L , with at least one point above a higher threshold T_H . The selected thresholds were defined as $T_L = \mu + 2.9\sigma$ and $T_H = \mu + 5.4\sigma$, where μ is the mean and σ is the standard deviation in $\Delta F/F_0$ for each pixel across each data interval, where $\Delta F = F - F_0$ and F_0 is the baseline cell fluorescence. Any sparks present during each interval will influence the estimates of cell baseline fluorescence, and hence to improve the spark detection accuracy, the algorithm was run two times. After the first iteration, the detected preliminary sparks were masked out, and the baseline fluorescence F_0 was recalculated across the first 100 frames of each analyzed data segment. The spark detection algorithm was repeated with the recalculated mean and standard deviation x-y maps with the preliminary sparks excluded. Sparks were identified as connected components in x-y-t with a minimum 6-pixel connectivity.

Spark characterization

The x-y-t spark mask is collapsed along the time axis to give a 2D spark mask which includes any pixel that reaches intensity values above threshold T_L during the spark duration. The *spark area* is calculated as the total number of pixels within the 2D x-y spark mask. Next, the two-dimensional spark mask is projected along the time axis and the temporal intensity profile is found by averaging over the spark area in x-y. The *spark amplitude* ($\Delta F/F_0$) is calculated as the difference between peak and baseline intensity divided by the latter, and the *spark full-duration half-maximum (FDHM)* is defined as the time between the first and last time points that the spark is above half of its peak intensity above baseline (F_{50}). The *centre of mass (COM)* coordinates in x and y are calculated by taking the weighted average of the spark projections profiles in the two spatial directions and define the spark location within the cell. Additionally, the *spark FWHM* in x and y directions are calculated by taking line profiles through the spark peak in time and centre of mass coordinate and counting the number of pixels with intensities at or above F_{50} .

Another parameter used to characterize and quantitatively compare individual calcium sparks is *signal mass*, introduced in (Sun et al., 1998), which for an in-focus spark is expected to be proportional to the volume integral of the fluorescence change ($\Delta F/F_0$) of the calcium indicator (Hollingworth et al., 2001). The calculation of spark mass has been simplified through a series of approximations: assuming that the three-dimensional calcium release can be approximated as the product of three isotropic Gaussians, the spark mass can be approximated as $\text{Mass} = \Delta F/F_0 \times 1.206 \times \text{FWHM}^3$, where $\Delta F/F_0$ is the spark amplitude and FWHM of the spark is in the direction of the line scan (Chandler, Hollingworth & Baylor, 2003; Hollingworth et al., 2001). In other work (Kolstad et al., 2018), the spark mass is defined as the product of the spark amplitude, FWHM and FDHM: $\text{Mass} = \Delta F/F_0 \times \text{FWHM} \times \text{FDHM}$. This definition is further used in the comparison of spark mass in left and right cardiomyocytes in (Medvedev, 2020). In this analysis, for direct comparison with the results presented by Medvedev et al., the latter definition of spark mass is used (the product of the spark amplitude, FWHM and FDHM) with the FWHM calculated as the average of the respective FWHM in x and y directions.

Finally, the identified sparks are filtered by area and duration to exclude those too small or too short and may have been a consequence of noise. Sparks with areas below 50 pixels ($<1 \mu\text{m}^2$) and durations (here defined as time the spark is “on” or above the lower threshold T_L) below 4 frames (10 ms) are rejected. Additionally, sparks which don’t fall below F_{50} within the analyzed time series are considered “unfinished” and are also excluded. The centre-of-mass coordinates of the 139 detected sparks overlaid with the extracted t-tubule structure for the example cell X are shown in **Fig. 4.7**, with panels b-e illustrating the rise and decay of one of the sparks in x-y-t dimensions.

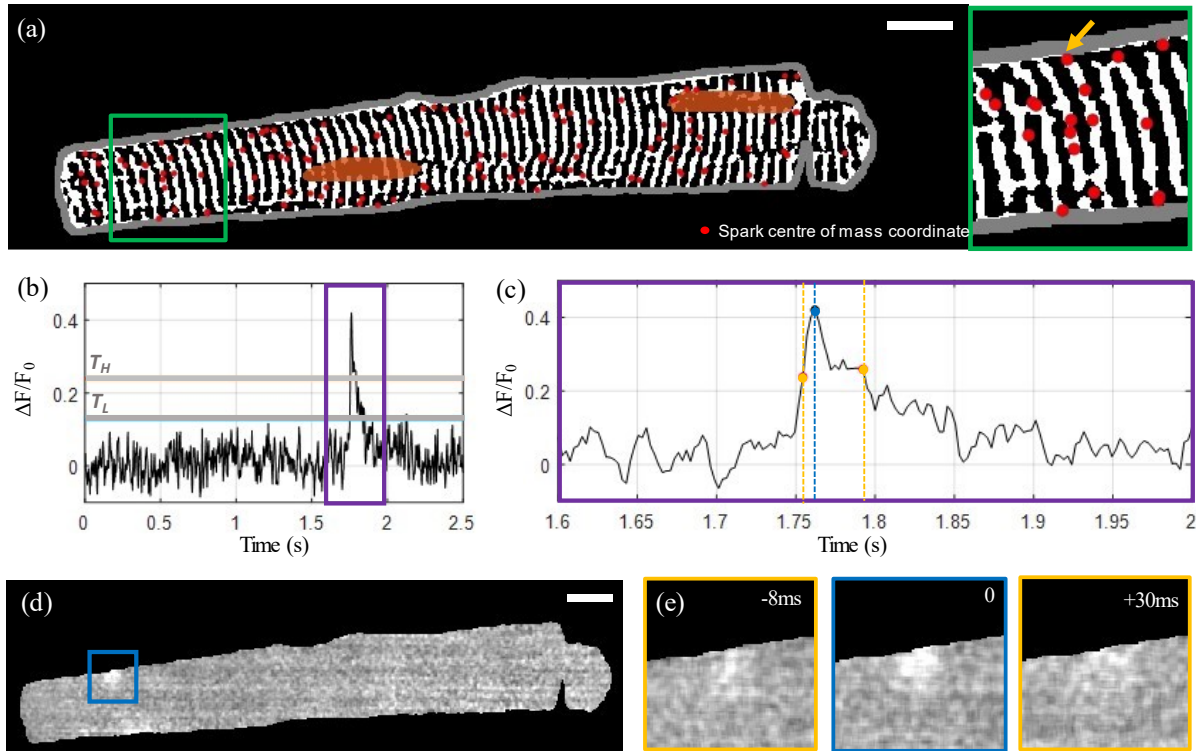


Figure 4.7 Calcium spark detection and correlation with cell structure (a) Centre of mass coordinates (red marker) for a total of 139 detected sparks overlaid on the extracted tubular microstructure of the example Cell X. The cell membrane outline is shown in grey and the manually segmented nuclei are shown in orange. (b) Intensity time profile through the 1,000-frame sequence for the spark indicated by the yellow arrow in the inset of ‘a’. The upper and lower intensity thresholds are indicated by T_H and T_L respectively (grey lines). (c) A zoom-in on the time region indicated by the purple rectangle in ‘b’. The detected peak is indicated by the blue marker, and the first and last frames above F_{50} are indicated with yellow. (d) Normalized fluorescence intensity at the time point corresponding to the selected spark’s peak intensity. (e) The 100 by 100 pixel region centred on the spark centroid indicated by the blue square in panel ‘d’ at peak intensity (middle) with the intensity distributions at the timepoints corresponding to F_{50} before and after the peak shown on the left and right respectively. Scalebar: $10 \mu\text{m}$

4.3.4 Transient analysis

Similarly to high-throughput analysis of spark dynamics, there is a need for multidimensional automated analysis of the spatial dyssynchrony of transient development. Some previous studies (Amanfu, Muller & Saucerman, 2011; Mukamel, Nimmerjahn & Schnitzer, 2009) implement automated analysis of transient dynamics by averaging the intensity time trace across the entire cell. CalTrack, a recently developed open-source MATLAB-based tool (Psaras et al., 2021) integrates

single- or multi-cell segmentation with extraction of a range of temporal parameters, including determination of the time-to-peak by linear interpolation of the rising edge, and decay time by fitting an exponential decay curve to the decreasing part of the fluorescence intensity time-trace. However, similarly to previous approaches, the fluorescent time trace is averaged across all pixels within the cell, and hence does not offer any insight into the spatial variation of transient development within the cell.

Various approaches for quantifying the variation of transient development on a pixel-wise basis were considered. One of these approaches involved cross-correlation of each pixel's transient intensity time-trace with the cell average for quantifying the time delay in transient onset. However, it was found that the rising edges of the transient differed more significantly in slope, rather than horizontal offset corresponding to the delay from the electrical stimulation to transient start. Transient fitting with two types of functions was also explored: the first one with an equation consisting of the sum of weighted exponentials with variable rise and decay constants and weighting factors (referred to as "Vial's type" equation (Li et al., 2016)). Analogously to the fitting of fluorescence lifetime data, the cell average transient shape could be fit by an exponential decay convolved by a Gaussian response, however, extending the fitting process to individual pixels proved to be slow and frequently inaccurate due to varying transient shapes. Secondly, a phasor-based approach used for fluorescence lifetime analysis (Digman et al., 2008) was also considered. However, since the aim was to compare the transient onset and rise in calcium rather than the calcium decay after the peak, instead, the T50 – the time point corresponding to half of the transient amplitude (F50) – was determined. A similar approach was previously attempted on 2D OPM data, however, cell contraction and low SNR limited its applicability (Maioli, 2016). Here, the T50 time point was determined by calculating the peak and baseline levels for each pixel, and linearly interpolating the time point corresponding to F50. The method is outlined in detail below.

Pixel-wise determination of transient time-to half-maximum (T50)

The transient analysis was performed on an 8 second (3,160 frame) sequence from the paced part (first half) of each acquisition, corresponding to 4 pacing periods, starting 2 pacing periods (4 s / 790 frames) in. The x-y-t data set was smoothed spatially using a 5×5 px median filter and temporally using a moving average over a 3-frame window using MATLAB's *movmean* function. The segmented cell mask (see **Section 4.3.1**) was applied to the transient data to define the cell area. The global cell transient peaks along the time dimension were identified using the *findpeaks* function, with the minimal peak separation time set to 95% of a single pacing period.

A total of three consecutive transients were selected for analysis, with each individual transient cropped to a 525 frame (1.3 s) window centred on the peak (**Fig 4.8a**). The electrical pacing trace was cropped to the same time window as the transient, and the rising edge of the top-hat shaped pulse, determined using MATLAB's *edge* function, was used as the excitation trigger point and a consistent point of

reference for the transient onset and rise. The time-to-half-maximum (T50) is defined as the time from the start of the pacing signal until the transient reaches half of its peak amplitude (F50) for that pixel, where F50 is defined as half of the difference between the peak and baseline intensity for that pixel. The baseline intensity (**Fig. 4.8b**) is calculated as the average intensity across a 50-frame window (126 ms) up until the start of the pacing signal. The peak intensity (**Fig. 4.8c**) for each pixel is calculated as an average across 20 frames starting from the cell average peak intensity time point. The $\Delta F/F_0$ signal is calculated as the pixel-wise difference between the signal and the baseline, divided by the baseline, with the corresponding map at the transient peak shown in **Fig. 4.8d**. After calculating the half-max intensity, the corresponding time point is identified by linearly interpolating between the last frame before and first frame after F50 (**Fig. 4.8e&f**). The time-to-half-maximum is then calculated as the duration from the electrical excitation reference time point until the time point of F50. The T50 maps for the three consecutive transients are shown in **Fig. 4.8g**, with some repeated features, corresponding to spatial domains with earlier transient T50 compared to the rest of the cell, consistent across the three transients (indicated by white arrows). The average and standard deviations of the T50 maps for three consecutive transients are shown in **Fig. 4.8h&i** respectively.

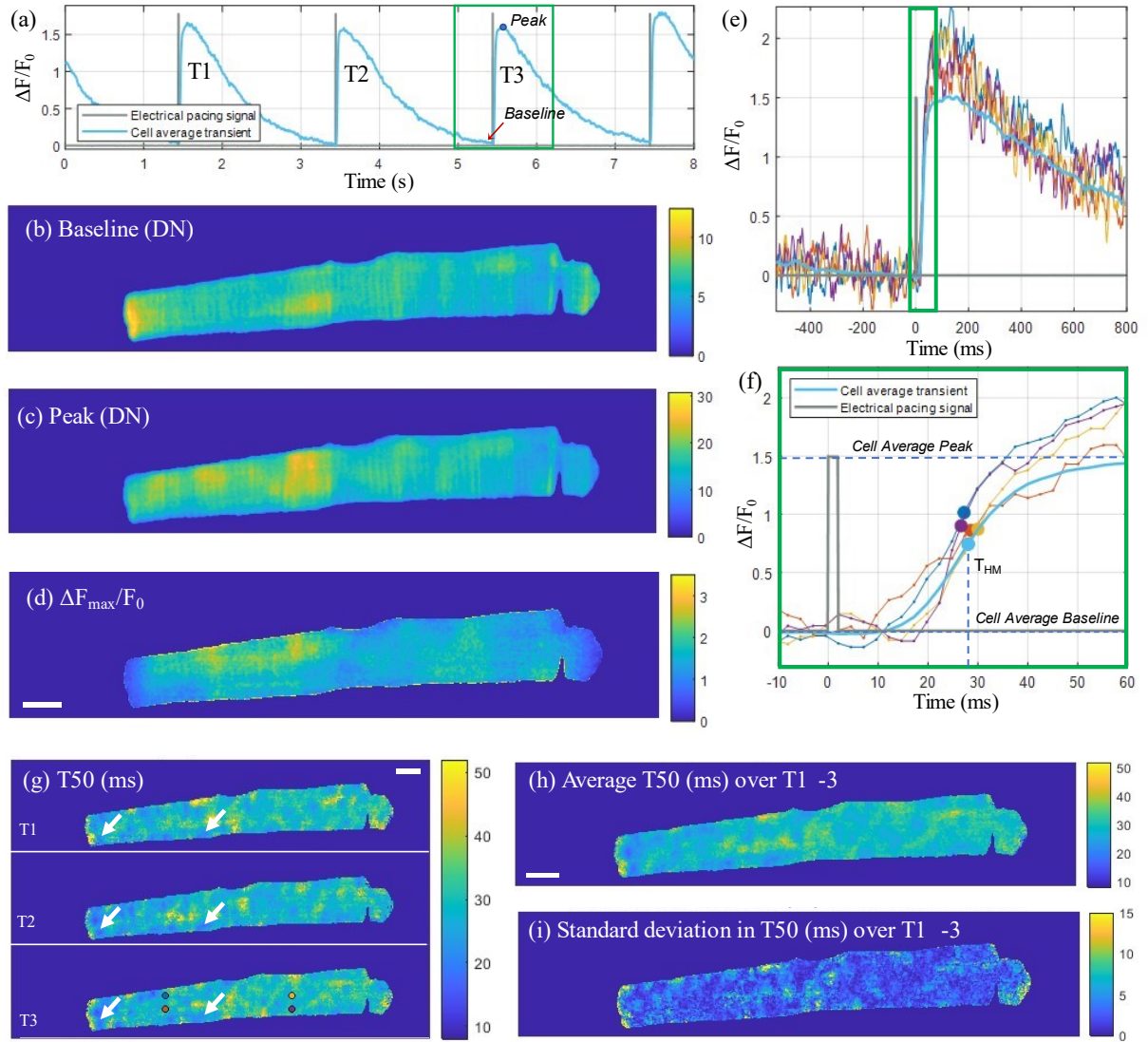


Figure 4.8 Pixel-wise determination of transient T_{50} . (a) Cell average transient ($\Delta F/F_0$) for the example cell X as a function of time across the sampled time-sequence including three consecutive transients (T1, T2, T3). The recorded pacing signal at 0.5 Hz is shown in grey. For the third transient T3, two-dimensional maps for the baseline fluorescence (in digital numbers), peak intensity (in digital numbers) and $\Delta F_{\max}/F_0$ are shown in (b), (c) and (d) respectively. (e) Intensity time traces through individual pixels indicated with circular markers in panel 'g' for T3, and the cell-average time trace for T3. (f) Zoom-in on the rising edge of the transient (indicated by the green rectangle in 'e') with the T_{HM} time points for the selected pixel traces indicated with markers. (g) T_{50} (ms) maps for the three consecutive transients, with some exemplar repeating features, corresponding to areas of early T_{50} , indicated by white arrows. (d) Average T_{50} map (ms) and (e) standard deviation in T_{50} (ms) of the three transients. Scalebar: 10 μm .

For the cell displayed in **Fig. 4.8**, the median \pm inter-quartile range (IQR) time-to-half-maximum for the map representing the cell average across three transients was 28.9 ± 4.6 ms. The automated analysis was applied to all $n = 60$ cells, with a selection of T_{50} maps for 8 of the cells shown in **Fig 4.9**, with the rest of the resultant T_{50} maps shown in **Fig. A4.2 (Appendix A4)**. The time-to-half-maximum across all analyzed cells, calculated as an average over the medians for each T_{50} distribution for each cell, is equal to 29.35 ± 4.62 ms (mean \pm SD), with a standard error of $SE = SD/\sqrt{n} = 0.60$ ms.

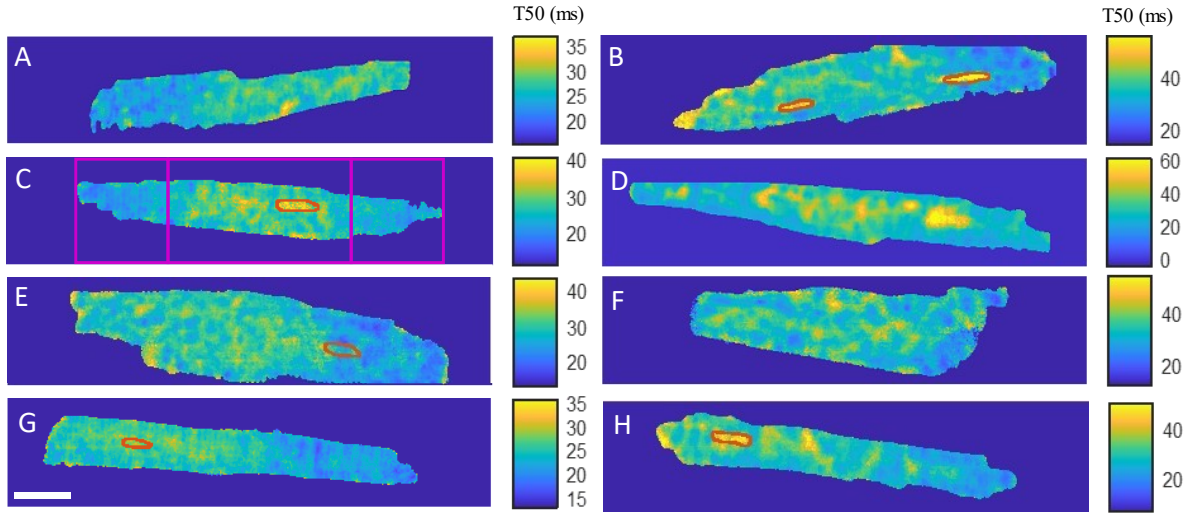


Figure 4.9 Time-to-half-maximum maps (ms) averaged over three consecutive transients for a selection of cells A-H, with the colormap autoscaled between the median \pm ($3 \times \text{IQR}$) T50 range, and identified nuclei outlined in orange. The purple rectangles in cell C indicate the centre and edge ROI of the cell. Scalebar: 20 μm

Spatial variation of T50 across the cell

Upon inspection of the T50 maps, a range of features can be observed. Firstly, the T50 distribution is spatially non-homogenous across a (healthy) cell, with a “patchy” pattern visible. The ends of multiple cells (A, B, C, E, G) have visibly lower T50 values, indicating earlier transient rise. We can also observe delayed T50 in nuclear regions (cells B, C, G, H), and a transverse striped pattern resemblant of the t-tubule network visible in certain regions (cells A, B, C, G). To evaluate the dyssynchrony in calcium transients across the cell, these features are investigated quantitatively by comparing the T50 for the outer and central areas of the cell, as well as T50 in nuclear regions compared to the rest of the cell, and correlating the T50 spatial variation with the cell structure.

Previous studies on nuclear calcium handling have shown that while the nuclear transient is dependent on the cytoplasmic calcium concentration due to passive ion diffusion through the nuclear envelope, the nuclear $[\text{Ca}^{2+}]$ is partially directly regulated by calcium release from its own perinuclear stores (Ljubojevic & Bers, 2015). Calcium transients in the nucleus undergo a slower and delayed rise, have a lower peak amplitude and slower decay compared with the dynamics in the cytosol (Ljubojević et al., 2011; Sutanto et al., 2020). This prolonged nuclear transient has previously been demonstrated in 2D using Nipkow disc confocal imaging at 30 fps (Kockskämper et al., 2001) and 120 fps (Kockskämper et al., 2008) and at over 500 fps using OPM (Kumar et al., 2011).

The nuclear and exonuclear T50 are calculated as the median time-to-half-maximum across all pixels within the masked nuclear and non-masked exonuclear pixels respectively. To compare the time-to-half-maximum at the ends of the cell to the middle, assuming approximate alignment of the cell with the horizontal axis of the FOV, the cell is divided into rectangular regions along its length. The two ends of the cell are identified from the first and last horizontal pixel coordinates corresponding to

a non-zero value within the (masked) T50 map. Next, the cell is divided into three regions (indicated by the magenta rectangles in **Fig 4.9**, cell C): a central ROI with the longer side corresponding to half of the cell length, and two ROI at each end of the cell with the horizontal dimensions of both ROI equal to a quarter of the cell's length. The outer ROI are grouped together, and the area corresponding to the segmented nuclei is excluded.

4.4 Results

4.4.1 Calcium spark morphology and correlation with t-tubule structure

After excluding cells with less than 15 detected sparks ($n = 5$) to achieve sufficient statistical power for each cell, a total of $n = 60$ acquisitions of unique cells were analyzed from 7 different male rat hearts. A total of 5,785 sparks were detected across the 60 cells, with an average of 96 ± 66 sparks (mean \pm SD) per analyzed 12.7 s sequence per cell. The calculated spark amplitude, area, duration, and mass distributions across all sparks are summarized in histograms presented in **Fig. 4.10**. The modal distribution of the spark amplitude agrees with previous findings of a preferred amplitude for in-focus sparks from x-y-z-t data acquired with fast-scanning confocal (Shkryl, Blatter & Rios, 2012) rather than the monotonically decaying amplitude distribution observed through confocal line scan imaging (Cheng et al., 1999).

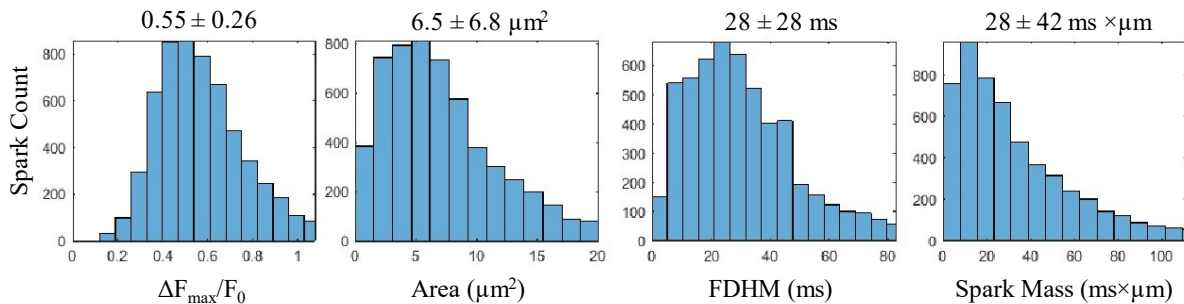


Figure 4.10 Spark count histograms for a selection of calculated parameters (with mean \pm SD quoted above) for the total 5,785 sparks detected across $n = 60$ cells. The horizontal axis range is limited up until the median value plus $2 \times \text{IQR}$ offset.

The average distance from a random pixel to the nearest detected tubule was 1.5 ± 0.5 pixels (mean \pm SD, standard error $\text{SE} = \text{SD}/\sqrt{n} = 0.06$), while the average spark centre of mass (COM) distance to nearest tubule (DNT) was equal to 0.85 ± 0.5 pixels (mean \pm SD, $\text{SE} = 0.07$), indicating that the spark COM are significantly ($p < 0.0001$, MW and WSRT test) more likely to be located on a t-tubule than a random pixel in the cell. **Table 4.1** summarizes the total number of sparks (average per cell), grouped in three different spatial categories based on their DNT: epitubular ($\text{DNT} = 0$), paratubular ($0 < \text{DNT} \leq 5\text{px}$) and sparks from detubulated regions ($\text{DNT} > 5\text{px}$). On average across all cells, 63% of sparks per cell have a COM co-localized with the tubules. A further 30% sparks per cell are within 3 pixels ($0.44 \mu\text{m}$) of tubules, and a further 5% are within 5 pixels ($0.74 \mu\text{m}$). Only 1.6% of sparks per cell are found to be more than 5 pixels ($0.74 \mu\text{m}$) away from the nearest tubule.

		DNT = 0	0 < DNT ≤ 5	DNT > 5
Percentage of total cell area		38.3%	54.6%	2.9%
Mean	96.42	61.2	33.1	1.58
SD	66.73	44.4	24.17	3.22
SE	8.62	5.7	3.12	0.42

Table 4.1 Total spark number per cell in each distance to nearest tubule (DNT) category, calculated as a mean (with corresponding standard deviation SD and standard error SE = SD/√N) across the total number of sparks in each category for each of the n = 60 cells. The percentage of total cell area (on average across all analyzed cells) in each DNT category is indicated. The remaining fraction of the cell area (4.2 %) corresponds to nuclear regions.

Only 6 out of 60 cells had more than 3 sparks in detubulated regions, and hence detubulated sparks could not be statistically compared with sparks from other spatial categories. **Table 4.2** and **Fig. 4.11** compare the calculated spark parameters for epitubular and paratubular sparks.

	Epitubular (DNT = 0)			Paratubular (0 < DNT ≤ 5)			Unpaired		Paired		Heart averages
	Mean	SD	SE	Mean	SD	SE	P-value	Test	P-value	Test	P-value
Spark Rate (100μm ² s ⁻¹)	0.74	0.56	0.07	0.29	0.23	0.03	<0.0001	UT	<0.0001	PT	0.0009
ΔF _{max} /F ₀	0.61	0.14	0.02	0.62	0.17	0.02	0.970	UT	0.918	PT	0.425
FDHM (ms)	28.0	6.1	0.8	25.5	11.1	1.4	0.144	UTWC	0.016	PT	0.458
Area (μm ²)	6.70	1.91	0.25	5.51	2.34	0.30	0.006	MW	<0.0001	WSRT	0.149
Spark Mass (ms μm)	28.1	9.2	1.2	24.3	13.6	1.8	0.005	UTWC	0.0002	PT	0.100

Table 4.2 Spark parameter comparison for epitubular (DNT = 0) and paratubular (0 < DNT ≤ 5) sparks with respective standard deviation (SD) and standard errors (SE = SD/√n, n = 60 cells) calculated from the medians of the spark populations for each cell. Based on considerations outlined in Section 4.2, the p-values are calculated using two-sample unpaired t-test (UT), unpaired t-test with Welch's correction (UTWC), unpaired Mann-Whitney (MW), paired t-test (PT), the paired Wilcoxon signed rank test (WSRT), and one-sample t-test with cell-by-cell differences averaged by heart. P-values <0.05 are highlighted in green, with only the spark rate difference between epitubular and paratubular sparks maintaining statistical significance across all used testing approaches.

Comparing the average across the means calculated for all sparks within each DNT category for each cell using paired testing, epitubular sparks were found to have 8% longer FDHM (28.0 ± 6.1 ms vs 25.5 ± 11.1 ms, p = 0.016, PT), 18% larger area (6.70 ± 1.91 μm² vs 5.51 ± 2.34 μm², p < 0.0001, WSRT), and 13 % larger spark mass (28.1 ± 1.2 ms μm vs 24.3 ± 13.6 ms μm, p = 0.0002, PT) than paratubular sparks. Accounting for the area of the cell belonging in each spatial DNT category, the spark rate, (number of sparks per 100 μm² per second) in paratubular regions was ~60% lower than in

epitubular regions ($p < 0.0001$). The difference in spark amplitude in epitubular and paratubular sparks was not significant (0.61 ± 0.14 vs 0.62 ± 0.17 , $p = 0.92$, PT).

Figure 4.11b shows the spark parameters for epitubular and paratubular spark populations in each cell, averaged over all cells from each isolation. One of the $n = 7$ isolations, from which only one cell was included in the final analysis, was excluded from the heart averages presented in all following results. For the remaining heart isolations, the number of cells analyzed varied between 6 and 14. When applying one sample t-test to the differences for spark parameters in each cell, averaged for all cells from each heart, only the spark rate was significantly different between paratubular and epitubular spark populations.

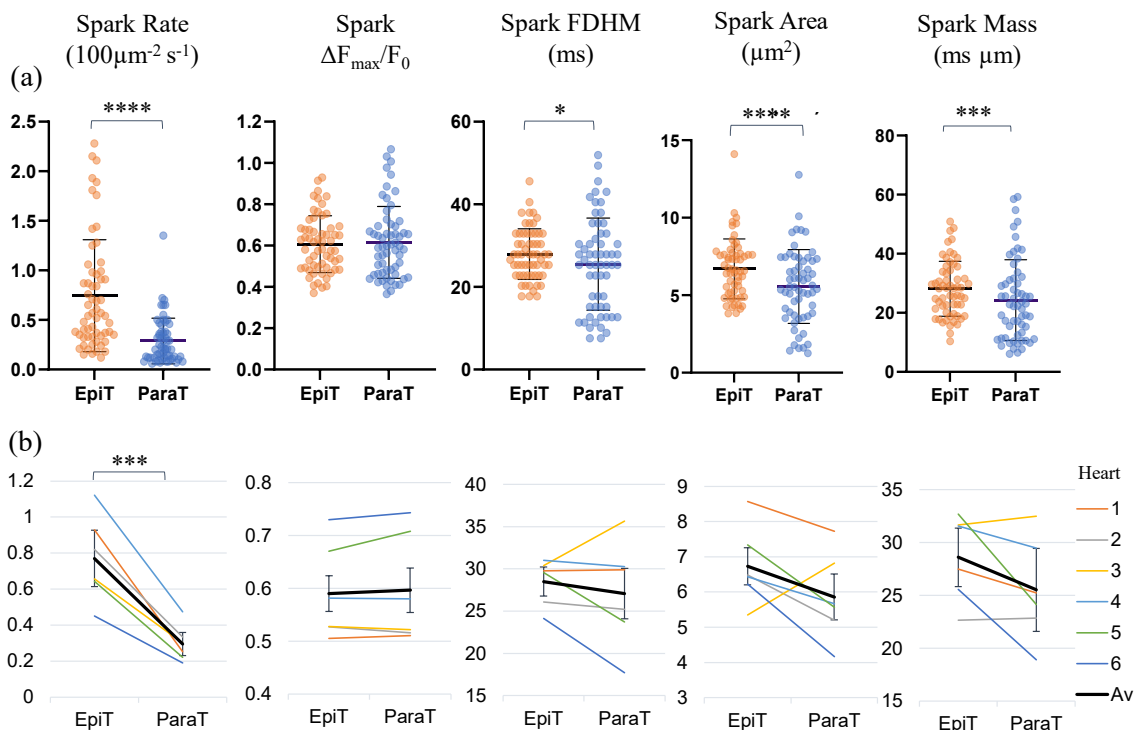


Figure 4.11 Spark parameters compared for epitubular (EpiT, DNT=0) and paratubular (ParaT, $0 < \text{DNT} \leq 5$) regions. (a) Spark parameter distributions, with each datapoint corresponding to the median across epitubular (orange) and paratubular (blue) spark populations within each cell. The horizontal lines indicate the mean \pm SD over all cells ($n = 60$). The levels of significance illustrated in the form of stars are based on paired testing (see **Table 4.2**). (b) Median spark parameter for epitubular and paratubular spark populations in each cell, averaged for each heart (1-6, see legend). The overall average (“Av”) across the 6 hearts is shown in black. The error bars represent the standard errors (SE = SD/ \sqrt{n}) across the heart averages. When comparing cell-by-cell differences, averaged for each heart using a one-sample t-test, only the spark rate is significantly different between epitubular and paratubular populations.

The co-localization of sparks and tubules is in agreement with previous findings (Cleemann, Wang & Morad, 1998; Shacklock, Wier & Balke, 1995; Sikkel et al., 2016b). However, unlike the findings by Sikkel et al. (2016), using paired testing, epitubular sparks were found to have larger spark area than paratubular sparks. Additionally, unlike the findings from the aforementioned study, paratubular sparks did not have longer FDHM, with epitubular sparks being slower and having larger spark mass. One

possible reason for the discrepancy could be due to the minor difference in the spark category definitions: the masked tubules in this work are broader than those generated by Sikkel et al., and hence more sparks are likely to be categorized as epitubular, skewing the comparison of the differences between the two populations. Additionally, more than two thirds of the analyzed sparks in the mentioned study were from rats with HF, a condition that may influence spark morphology of the two categories. Finally, the fact that epitubular sparks, despite having a larger area, duration and signal mass, had no difference in amplitude compared to paratubular sparks, gives confidence that the measured morphology of sparks was minimally skewed by out of focus events, and larger area for epitubular sparks may be a consequence of the epitubular spark involving joint activation of larger or several RyR clusters colocalized with the t-tubules.

4.4.2 Calcium transient dyssynchrony and correlation with t-tubule structure

The T50 values for different regions of the cell, across all analyzed cells are presented in **Table 4.3** and **Figure 4.12**. The nuclei were found to reach F50 later than the rest of the cell by $\Delta = 3.47$ ms on average ($p < 0.0001$, WSRT, for $n = 40$ cells with detected nuclei,) compared to the rest of the cell. The longer nuclear transient rise time in comparison to the rest of the cell is in qualitative agreement with previous findings in studies mentioned in **Section 4.3.4**.

	T50 (ms)			Δ (ms)	Unpaired		Paired		Heart averages
	Mean	SD	SE		P-value	Test	P-value	Test	P-value
Cell	29.30	4.63	0.73	-3.47	0.0009	MW	<0.0001	WSRT	0.00627
Nucleus	32.77	7.39	1.17						
Central	30.07	4.54	0.59	1.97	0.0018	MW	<0.0001	WSRT	<0.0001
Outer	28.10	4.87	0.63						

Table 4.3 Comparison of average time-to-half-maximum (T50) for different regions of the cell: the cell (excluding the nucleus), the nucleus, the central IQR and the outer quarters. The mean, standard deviation (SD) and standard errors ($SE = SD/\sqrt{n}$) calculated across the medians for each T50 distribution for each of the $n = 40$ cells with identified nuclei for the first category, and all $n = 60$ cells for the second category. The Δ column indicates the difference between the T50 for each region, averaged over all cells. Based on statistical considerations outlined in Section 4.2, the p-values are calculated using the unpaired Mann-Whitney (MW), the paired Wilcoxon signed rank test (WSRT), and one-sample nested t-test with cell-by-cell differences averaged for each heart. For all three statistical analyses (unpaired, paired by cell, and averaged for each heart) the nuclei and central regions of the cell had a significantly (p -values < 0.05 are highlighted in green) longer time-to half than the rest of the cell and the central region respectively.

By dividing the cell into a central and outer region as described in **Section 4.3.4**, on average, the outer regions of the cells reached F50 by $\Delta = 1.97$ ms earlier than the cell middle ($p = 0.0018$, WSRT, for $n = 60$ cells). These results confirm the spatial dyssynchrony of calcium transients across the cell, supporting the first hypothesis (**Section 4.1.5**). Further investigation with and without mechanical decoupling would be required to determine whether this spatial variation along the long axis of the cell,

with earlier transient onset at the edges of the cell, is related to the anisotropy of longitudinal cell shortening during contraction.

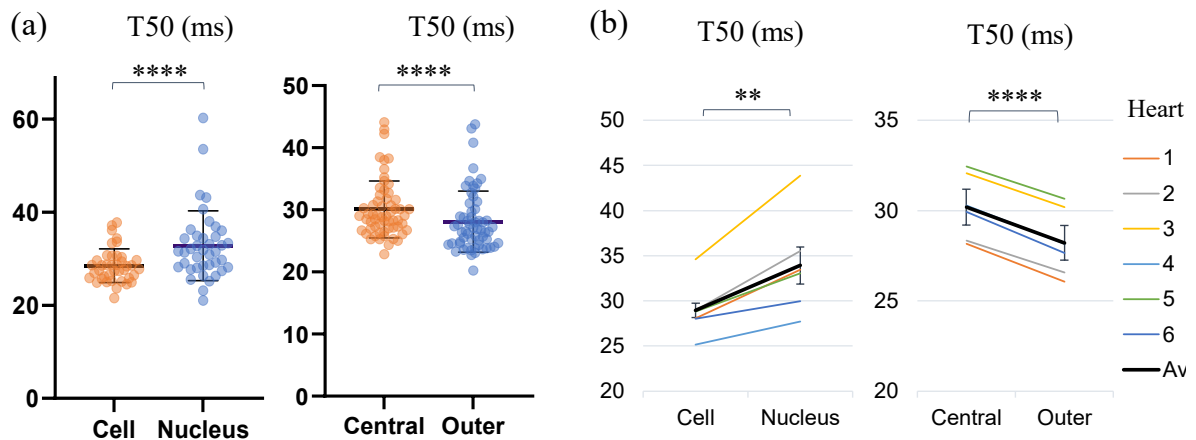


Figure 4.12 Comparison of average time-to-half-maximum (T50) for different regions of the cell: the cell (excluding the nucleus), the nucleus, the central IQR and the outer quarters. (a) Transient T50 distributions, with each datapoint corresponding to the median across all pixels within a region of a cell. The horizontal lines indicate the mean \pm SD over all cells ($n = 40$ for cells with identified nuclei for the first category, and all $n = 60$ cells for the second category). Levels of significance illustrated with stars are based on paired testing (see **Table 4.3**). (b) Transient T50 in different regions of each cell, averaged over the cells from each heart (1-6, see legend). The overall average (“Av”) across the 6 hearts is shown in black. The error bars represent the standard errors ($SE = SD/\sqrt{n}$) across the heart averages. When comparing cell-by-cell differences, averaged for each heart using a one-sample t-test, both region comparisons maintained statistical significance, with the nuclei and central regions of the cell having a significantly longer time-to half than the rest of the cell and the central region respectively.

Overlaying the T50 map with the tubule structure for cell D (previously shown in **Fig. 4.5** and **Fig. 4.6a**) shows how some cell regions with delayed transient rise (with larger T50 values) coincide with cell areas that lack regular tubule structure (**Fig. 4.13a**). This is quantified in terms of the slope of the linear fit to the correlation scatterplots of T50 and DNT values for each pixel in the cell (**Fig. 4.13b**). For the example cell D, the slopes are 0.99 ms/px, (95% CI: [0.94, 1.04]) and 1.99 ms/px (95% CI: [1.89, 2.08]) for tubulated and detubulated regions respectively, indicating positive correlation of T50 with DNT, with a stronger correlation in detubulated regions. Taking a horizontal line profile through the T50 and DNT maps through a tubulated region in cell C (**Fig 4.13c-d**) indicates delayed transient development in between the tubules.

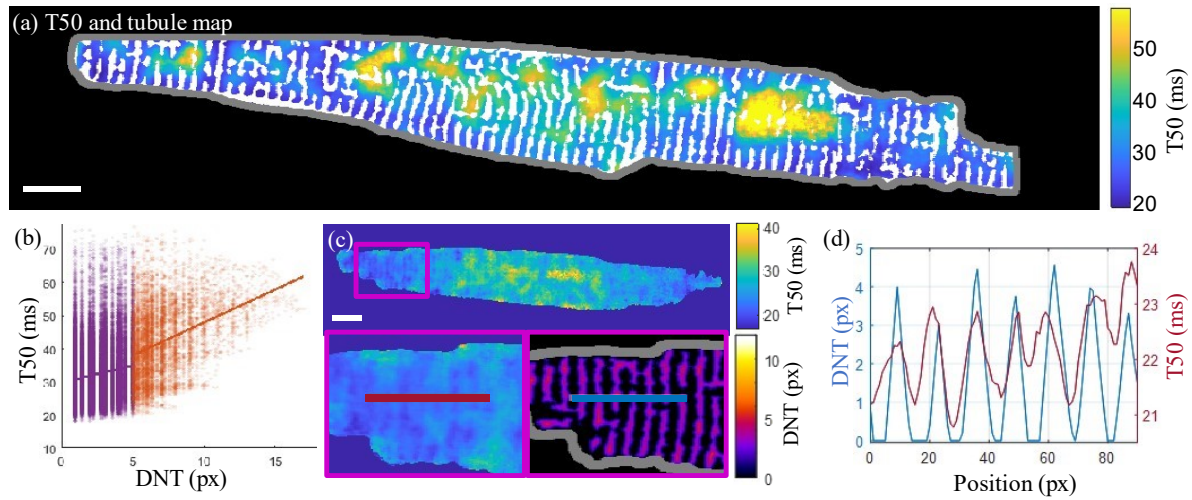


Figure 4.13 Correlation of the t-tubule structure with transient time-to-half-maximum (a) Time-to-half-maximum (T50, in ms) map for the T50 average over three consecutive transients of cell D with binary t-tubules overlaid in white. (b) T50 correlation with DNT across all pixels in cell D. Linear fits to tubulated (purple) and detubulated (orange) regions have slopes of 0.99 ms/px, (95% CI: [0.94, 1.04]) and 1.99 ms/px (95% CI: [1.89, 2.08]) indicating increased positive correlation of T50 with DNT in detubulated regions. (c) Horizontal line profiles (averaged vertically over a 5-pixel width) taken through the T50 (left and top) and DNT (bottom right) maps of cell C. (d) The line profiles through T50 and DNT maps shown in panel 'c' are overlaid, indicating earlier transient rise in areas closer to tubules. Scalebar: 10 μ m.

When considering the median T50 values within each DNT category averaged across all cells, there was no significant difference between the time-to-half-maximum within epitubular (DNT = 0), paratubular ($0 < \text{DNT} \leq 5$) or detubulated (DNT > 5) regions (**Table 4.4, Fig. 4.14**). The T50 in epitubular regions was on average 0.04 ms earlier than the T50 in ParaT regions on cell-by-cell basis, but the difference was not statistically significant for any of the statistical methods applied. The $\Delta = 0.09$ ms difference between T50 in paratubular and detubulated regions was also not statistically significant.

	T50 (ms)			Δ (ms)		Unpaired		Paired		Heart averages	
	Mean	SD	SE			P-value	Test	P-value	Test	P-value	
EpiT	29.25	4.76	0.61	-0.04	0.09	0.85	MW	0.29	WSRT	0.92	0.63
ParaT	29.29	4.54	0.59								
DeT	29.20	5.38	0.69								

Table 4.4 Transient T50 variation with DNT: Comparison of T50 values (ms) within epitubular (DNT = 0), paratubular ($0 < \text{DNT} \leq 5$) or detubulated (DNT > 5) regions, calculated as an average across the medians for each cell. Positive Δ value indicates that the T50 in the first DNT category is larger than that in the second. The p-values are calculated using the unpaired Mann-Whitney (MW), the paired Wilcoxon signed rank test (WSRT), and one-sample nested t-test with cell-by-cell differences averaged for each heart. For all three statistical analyses (unpaired, paired by cell, and averaged for each heart) the transient T50 was not significantly different between the DNT categories.

The average slope of the linear fits to the transient T50 and DNT correlation scatterplots in each cell was 0.03 ± 0.20 ms/px (mean \pm SD) ([0.00 0.06] 95% C.I.) and 0.14 ± 0.93 ms/px (mean \pm SD) ([-0.11 0.38] 95% C.I.) (**Fig. 4.14, Table 4.5**). While the T50/DNT slope for detubulated regions was, on average, higher than for tubulated regions, the difference between the two slopes was not statistically significant, and hence the second part of the second hypothesis, which states that the characteristics of transient dynamics correlate with the t-tubule structure (**Section 4.1.5**) is not supported within the statistical power provided by the results presented here. Transient rise time correlating positively with distance from t-tubule would be expected from previous studies involving correlative measurements of transient dyssynchrony in correlation with t-tubule structure (**Section 4.1.2**), due to the colocalization of calcium release units with the tubules. However, this study used cardiomyocytes from healthy samples, with a regular t-tubule structure set as one of criteria for inclusion of cell in the analysis, and hence in the future, further insight into transient dyssynchrony in detubulated cells could be obtained by looking at cells with loss of t-tubules such as those in HF animal models.

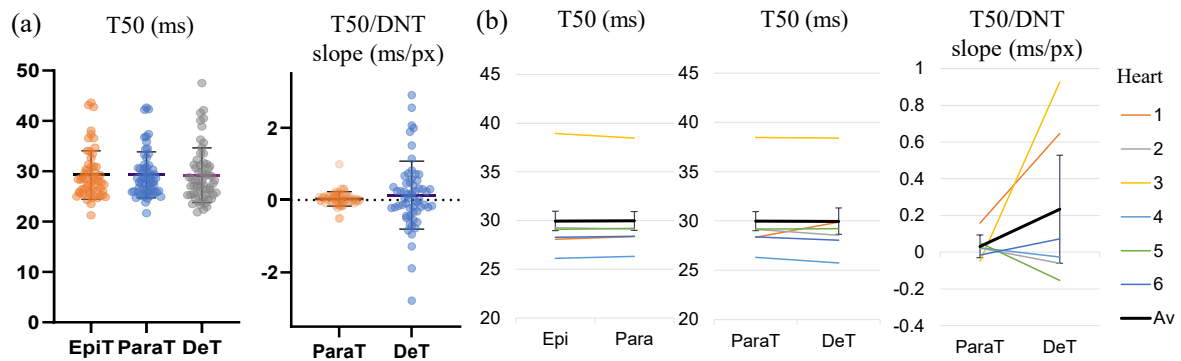


Figure 4.14 Transient T50 and T50/DNT slope for different DNT regions. (a) Transient T50 distributions, with each datapoint corresponding to the median T50 (ms) across all pixels within epitubular (EpiT, DNT = 0), paratubular (ParaT, $0 < \text{DNT} \leq 5$) or detubulated (DeT, $\text{DNT} > 5$) regions. The horizontal lines indicate the mean \pm SD over all cells ($n = 60$). None of the differences were statistically significant. (b) Transient T50/DNT slope in different regions of each cell, averaged over the cells from each heart (1-6, see legend). The overall average (“Av”) across the 6 hearts is shown in black. The error bars represent the standard errors ($\text{SE} = \text{SD}/\sqrt{n}$) across the heart averages. When comparing cell-by-cell differences, averaged for each heart using a one-sample t-test, there was no significant difference in T50 and T50/DNT slopes in parts of the cell corresponding to the various DNT categories.

	$\Delta\text{T50}/\Delta\text{DNT}$ (ms/px)				Unpaired		Paired		Heart Averages
	Mean	95% C.I.	SD	SE	P-value	Test	P-value	Test	P-value
ParaT (DNT ≤ 5)	0.03	[0.00 0.06]	0.20	0.03	0.75	MW	0.5162	WSRT	0.32058
DeT (DNT > 5)	0.14	[-0.11 0.38]	0.93	0.12					

Table 4.5 Comparison of correlation slopes ($\Delta\text{T50}/\Delta\text{DNT}$) in tubulated (DNT < 5) and detubulated (DNT > 5) cell areas, calculated as an average across the slopes for each cell. The p-values are calculated using the unpaired Mann-Whitney (MW), the paired Wilcoxon signed rank test (WSRT), and one-sample nested t-test with cell-by-cell differences nested by heart. For all three statistical analyses (unpaired, paired by cell, and nested by heart) the T50/DNT slope was not significantly different between the two DNT categories.

4.4.3 Comparison for left and right ventricle cardiomyocytes

All image acquisition, data selection, processing and image analysis was done blinded with respect to ventricle. However, upon unblinding, it was revealed that the labelling of the received batches of cells for each ventricle (“A” and “B”) had not been randomized on each acquisition day. While the ventricle imaging order for the two loads on each acquisition day had been alternated, it was also not randomized, and this resulted in more RV CM imaged first in the sequential acquisition process. The calculated parameters for the full dataset are presented in **Table. 4.6** – with no significant differences found between myocytes from the two ventricles.

	LV (n = 32 Cells)			RV (n = 28 Cells)			Δ (%)	p-value	T-test
	Mean	SD	SE	Mean	SD	SE			
Spark Rate ($100 \mu\text{m}^{-2} \text{s}^{-1}$)	0.48	0.33	0.04	0.41	0.24	0.05	14	0.94	UT
Spark $\Delta F_{\text{max}}/F_0$	0.64	0.15	0.03	0.59	0.14	0.03	7	0.23	UT
Spark FDHM (ms)	26.8	8.0	1.4	27.5	6.4	1.2	-3	0.75	UT
Spark Area (μm^2)	6.12	1.68	0.28	6.39	2.15	0.41	-4	0.76	UT
Spark Mass ($\text{ms} \times \mu\text{m}$)	27.0	10.1	1.8	26.3	9.0	1.7	3	0.79	UT
Transient T50 (ms)	28.4	4.2	0.7	30.3	4.9	0.9	-6.7	0.09	MW
Transient DI (ms)	5.42	2.29	0.40	6.19	2.37	0.45	-14	0.21	MW

Table 4.6 Comparison of the spark and transient parameters calculated for LV and RV CM the full n = 60 dataset quoted as the mean, standard deviation (SD) and standard errors ($\text{SE} = \text{SD}/\sqrt{n}$) calculated from the medians of the cell parameters in each of the two cell populations. The differences (Δ) are calculated as the difference between corresponding parameters in left and right ventricles, divided by the former value, and converted to a percentage. The p-values are calculated using the unpaired t-test (UT) and the unpaired Mann-Whitney (MW). For the full n = 60 dataset there were no significant differences across any of the spark parameters.

To evaluate the possibility of systematic bias from imaging order due to un-randomized blinding of the two ventricles, the correlation of each parameter with the imaging time point (relative to the first imaged cell in that batch) was considered. Correlation was assessed by linear fits to the data for cells from each ventricle and considering the coefficient of determination R^2 . The slopes (Δ), vertical axis intercepts (Y_0) and R^2 coefficients for the linear fits are summarized in **Table 4.7**. A weak correlation with the time of imaging was found for some spark and transient parameters ($R^2 = 0.12\text{-}0.49$), with a positive time correlation for spark rate and FDHM in both ventricles and LV respectively, and a negative time correlation for spark amplitude and transient dyssynchrony for LV CM and RV CM respectively.

	LV (n = 32 Cells)			RV (n = 28 Cells)			Combined		
	Δ	Y0	R^2	Δ	Y0	R^2	Δ	Y0	R^2
Spark Rate ($100 \mu\text{m}^{-2} \text{s}^{-1}$)	0.005	0.05	0.15	0.004	0.27	0.13	0.003	0.24	0.12
Spark $\Delta F_{\text{max}}/F_0$	-0.003	0.94	0.49	5×10^{-5}	0.59	<0.001	-0.001	0.67	0.05
Spark FDHM (ms)	0.090	18.7	0.13	0.03	26.2	0.014	0.03	24.9	0.03
Spark Areas (μm^2)	0.001	5.16	0.046	-0.003	6.49	<0.001	0.001	6.17	<0.001
Spark Mass ($\text{ms} \times \mu\text{m}$)	0.013	25.8	0.002	0.010	26.0	0.001	0.013	25.9	0.003
Transient T50 (ms)	-0.018	30.0	0.02	-0.036	31.7	0.033	-0.03	31.3	0.06
Transient DI (ms)	-0.002	5.60	<0.001	0.034	4.83	0.12	-0.001	5.83	<0.001

Table 4.7 Correlation of the calculated spark and transient parameters with relative imaging time point. The slope (Δ), y-axis intercept (Y0) and the coefficient of determination (R^2) are given above, with $R^2 > 0.1$ highlighted in yellow and $R^2 > 0.3$ in green. The spark rate of LV, RV and combined cardiomyocytes may have weak positive correlation with imaging time. The transient dyssynchrony index of RV cardiomyocytes also exhibits weak positive correlation with imaging time. Spark amplitude of left ventricle CM had stronger positive correlation with imaging time ($R^2 = 0.49$).

The scatterplots for parameters with a weak correlation ($R^2 > 0.1$) present are shown in **Figure 4.15**. Two of the selected left ventricle acquisitions had a significantly earlier relative imaging time point compared to the rest (0 and 7 min respectively). To evaluate the influence of these outliers on the time correlation of spark amplitude, the linear correlation was calculated for the dataset excluding those two points (**Fig. 4.16**). As a result, the slope and intercept of the new linear correlation fit remained nearly unchanged ($\Delta = -0.003$, $Y0 = 0.93$), while the coefficient of determination decreased from $R^2 = 0.49$ to $R^2 = 0.31$, indicating a lower negative correlation level, but with a similar time dependence.

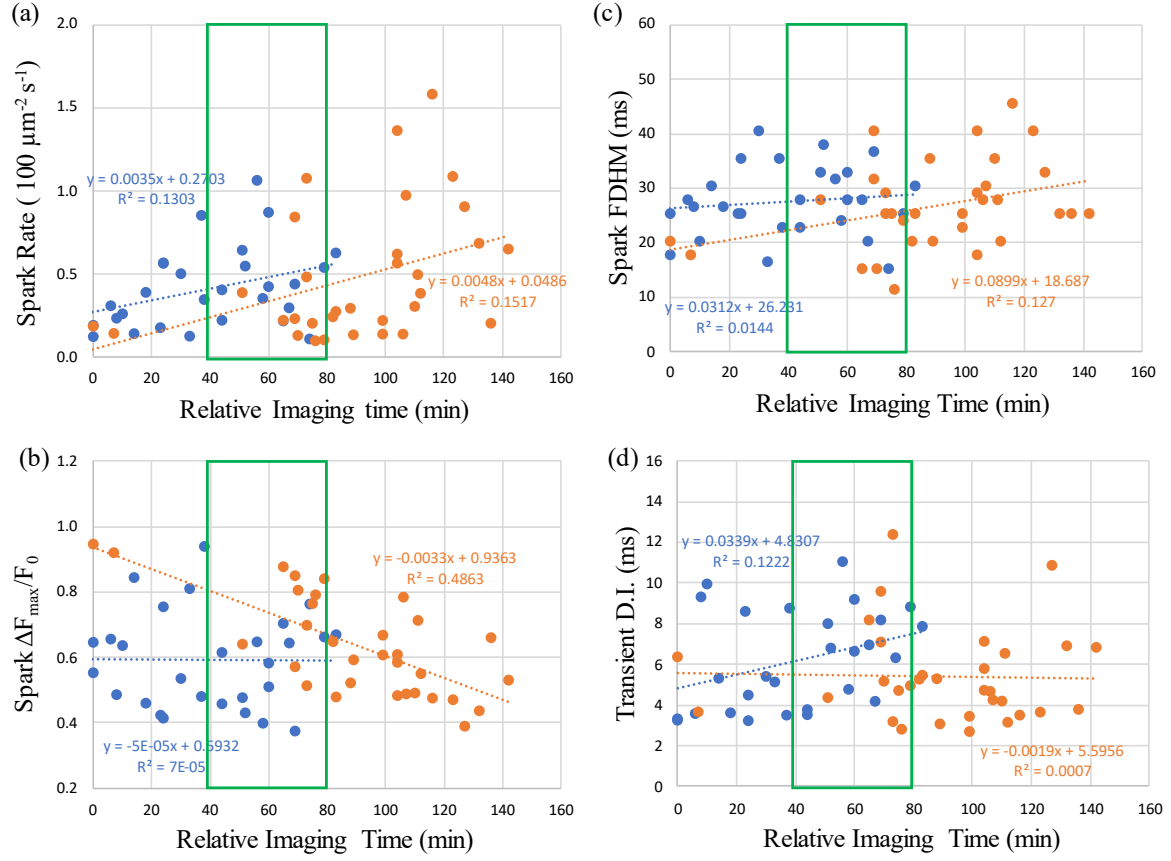


Figure 4.15 Correlation of selected spark and transient parameters medians for each cell ($n = 60$) with the relative time of imaging for left (orange) and right (blue) ventricle cardiomyocytes. The equation and R-squared (R^2) coefficients of determination for the linear fits are provided next to the datapoints. The green rectangles indicate the time window selected for the reduced dataset ($n = 24$, $n_{\text{LV}}=10$, $n_{\text{RV}}=14$ cells).

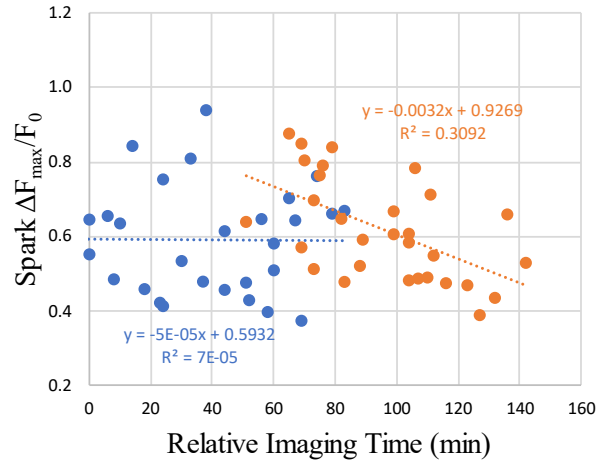


Figure 4.16 Correlation of spark amplitude with the relative time of imaging for LV (orange) and RV (blue) CM, with two earliest LV CM datapoints excluded. The equation and R-squared (R^2) coefficients of determination for the linear fits are provided next to the datapoints.

Restricting the LV RV dataset to fixed imaging time window

To reduce the possibility of systematic bias due to imaging time point on differences in the parameter comparison between the two ventricles, the comparison reported below was performed on a sub dataset that only included cells imaged within a shorter 40-minute time window (indicated by the green rectangle in **Fig. 4.15**). The window was selected manually by considering scatterplot distribution and aiming to maximize imaging time overlap for the two ventricles and the sample size for the reduced dataset. This resulted in a sample size reduction to $n = 24$ cells.

The comparisons for spark rate, amplitude, duration, area and mass as well as transient time-to-half-maximum and dyssynchrony index (defined as the IQR about the median T50 for each cell) are shown in **Fig. 4.17** and **Table 4.8**. For the comparison of spark and transient parameters between left and right ventricle cardiomyocyte, only the unpaired t-test was used, as the parameters were calculated across different cardiomyocyte populations from the two ventricles.

Left ventricle cardiomyocyte sparks had a 25% larger amplitude than those in right ventricle cells (0.73 ± 0.12 vs 0.55 ± 0.12 , $p = 0.0016$), which supports the third hypothesis (**Section 4.1.5**), while differences in other parameters were not statistically significant. The data exclusion from earlier and later imaging time points resulted in the previously not statistically significant larger spark amplitude for left ventricle being significant, indicating that there may be a gradual change in the cell physiology or environment with time that may decrease the spark brightness.

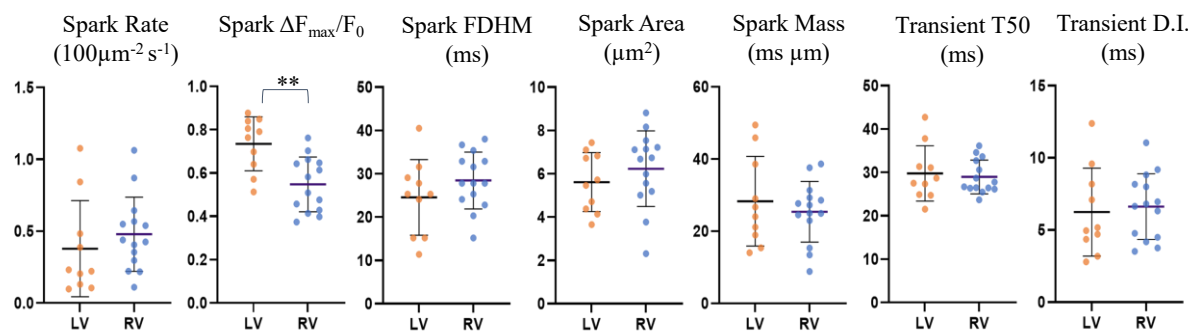


Figure 4.17 Comparison of spark and transient parameters for LV and RV cardiomyocytes for the restricted $n = 24$ dataset. The horizontal lines represent the averages across the medians for each cell within each ventricle population ($n_{\text{LV}} = 10$, $n_{\text{RV}} = 14$). The error bars correspond to the standard deviation. The average spark amplitude in left ventricle cardiomyocytes was found to be 25% larger than those in right ventricle cardiomyocytes ($p = 0.0016$, UT).

	All (N= 24 cells)			LV (N=10 cells)			RV (N=14 cells)			Δ (%)	p-value
	Mean	SD	SE	Mean	SD	SE	Mean	SD	SE		
Spark Rate ($100\mu\text{m}^{-2}\text{s}^{-1}$)	0.44	0.28	0.06	0.38	0.32	0.10	0.48	0.25	0.07	-27	0.415
Spark $\Delta F_{\text{max}}/F_0$	0.63	0.15	0.03	0.73	0.12	0.04	0.55	0.12	0.03	25	0.0016
Spark FDHM (ms)	26.9	7.5	1.5	24.6	8.3	2.6	28.5	6.3	1.7	-16	0.22
Spark Area (μm^2)	5.98	1.56	0.32	5.62	1.29	0.41	6.23	1.68	0.45	-11	0.36
Spark Mass ($\text{ms}\times\mu\text{m}$)	26.6	9.9	2.0	28.3	11.8	3.7	25.4	8.1	2.2	10	0.50
Transient T50 (ms)	29.3	4.9	1.0	29.8	6.0	1.9	29.0	3.7	1.0	2.7	0.70
Transient DI (ms)	6.46	2.51	0.51	6.24	2.88	0.91	6.62	2.19	0.59	-6.1	0.73

Table 4.8 Comparison of the spark parameters and transient T50 calculated for left and right ventricle cardiomyocyte populations from a sub-dataset within a restricted time window ($n = 24$ cells), quoted as the mean, standard deviation (SD) and standard errors ($\text{SE} = \text{SD}/\sqrt{n}$) calculated from the medians of the cells in each of the two populations. The differences (Δ) are calculated as the average for each parameter for LV myocytes minus the average for RV myocytes, divided by the former value, and converted to a percentage. Positive Δ indicates larger value for LV myocytes. All datasets were normally distributed, and each dataset pair passed the F-test for equal variance, and hence p-values were calculated using two sided, two sample, homoscedastic unpaired t-test (UT). For the calculated parameters, only the spark amplitude was significantly different between the two ventricles, with LV CM having 25% larger spark amplitude ($p = 0.0016$).

The reduced spark amplitude in RV myocytes agrees with findings by Medvedev made using confocal line-scan measurements (Medvedev, 2020). Other differences between LV and RV identified in Medvedev's study such as smaller spark mass and higher dyssynchrony index in control RV cells are qualitatively consistent with the results in this work, however, were not found to be statistically significant in this case. This can be due to the smaller sample size and differing methodologies, and future research is needed to verify the results with more certainty.

4.5 Discussion & conclusion

This chapter described the application of a custom dual-objective light-sheet fluorescence microscope for correlative dual-channel 2D time-lapse imaging of calcium dynamics and cellular microstructure in ventricular cardiomyocytes from rats. The sample preparation, data acquisition, image processing, data analysis, as well as the biological findings, context and implications are outlined. Left and right ventricle cardiomyocytes labelled with a membrane stain and loaded with a calcium indicator were imaged with electrical stimulation and decoupled contraction (**Section 4.2**). Compared to previous approaches, a simpler method involving filtering and thresholding allowed automated and orientation-independent detection of t-tubules (**Section 4.3.2**). The spatiotemporal resolution and optimized balance between SNR and photodose allowed detection and characterization of calcium sparks, as well as the determination of transient time-to-half-maximum across the cell. By correlating the spark centres with the detected tubule structure, morphological parameters for epitubular and paratubular sparks were compared (**Section 4.4.1**). Correlating the transient time-to-half-maximum with the tubular structure

allowed comparison of transient development dependence on tubule proximity in tubulated and detubulated areas (**Section 4.4.2**). Finally, spark parameters and transient dyssynchrony in left and right ventricle cardiomyocytes were compared (**Section 4.4.3**).

By immobilizing the cell using para-Nitroblebbistatin, a non-phototoxic, lower-fluorescence alternative to the default decoupler blebbistatin, and implementing an automated pixel-level analysis of calcium indicator fluorescence time traces during pacing, it was possible to map the transient development in 2D without the accompanying motion artefacts from contraction. In line with qualitative findings from previous work (Ljubojević et al., 2011; Sutanto et al., 2020), the nuclear regions within each cell were found to have a significantly longer time-to-half-maximum than the rest of the cell by 3.47 ms ($p < 0.0001$, WSRT). Comparing the T50 in the central part of the cell to the two ends revealed a time-to-half-maximum that was on average 1.97 ms earlier ($p < 0.0001$, WSRT) at the cell ends. The statistical significance was maintained when considering the cell-by-cell differences, averaged for each heart, providing strong support for the dyssynchronous nature of transient development across the cell, in agreement with the first hypothesis (**Section 4.1.5**).

Correlating the T50 maps with the DNT maps derived from the detected tubules, detubulated regions had higher levels of positive correlation of transient T50 with the distance away from tubules 0.14 ± 0.93 ms/px (mean \pm SD) ($[-0.11 \ 0.38]$ 95% C.I.) vs 0.03 ± 0.20 ms/px (mean \pm SD) ($[0.00 \ 0.06]$ 95% C.I.) however, the difference was not significant, and hence the second hypothesis (**Section 4.1.5**) is not supported by the results, within statistical power of the data. It is possible that correlation of transient dyssynchrony with distance from the nearest t-tubule is predominant in detubulated cells, of which there was not enough of in the samples from healthy control animals.

In agreement with previous work (Shacklock, Wier & Balke, 1995; Sikkel et al., 2016), spark centre of mass distribution demonstrated high colocalization with t-tubules, with an average of 63% of sparks per cell centered on tubules. Besides higher spark rate, using paired statistical tests where parameters are compared for the same cell, epitubular sparks were found to, on average, have significantly longer FDHM (28.0 ± 6.1 ms vs 25.5 ± 11.1 ms, $p = 0.016$, PT), larger area (6.70 ± 1.91 μm^2 vs 5.51 ± 2.34 μm^2 , $p < 0.0001$, WSRT), and larger spark mass (28.1 ± 1.2 ms μm vs 24.3 ± 13.6 ms μm , $p = 0.0002$, PT) than paratubular sparks, while no significant difference in amplitude between the two spark categories was found.

When considering the paired cell differences in spark parameters, averaged for each animal, only the difference in spark rate remained significant. While this level of testing accounts for potential cardiac heterogeneity, and for the dependence of individual data points on cellular and animal level, the statistical power of this analysis is reduced, and hence it is possible that the other spark parameter differences were not statistically resolved due to the sample size being too small. These challenges can

be addressed with higher throughput technology, and more complex multilevel statistical models such as that used in (Sikkel, 2015) to account for the dependence of measurements on cell and animal level.

Comparison of left and right ventricle cardiomyocytes after restricting the dataset to a narrower imaging time window, revealed that left ventricle cells had significantly brighter sparks (0.73 ± 0.12 and 0.55 ± 0.12 , $p = 0.0016$, UT, $n = 24$), hence supporting the third hypothesis (**Section 4.1.5**). However, the differences in spark rate, duration, area, mass and transient time-to-half-maximum and dyssynchrony were not statistically significant.

Overall, the findings indicate that certain spatiotemporal properties of calcium dynamics in cardiomyocytes may spatially correlate with the t-tubule network coverage of the cell, which supports the idea that disruption of the tubular network would introduce changes in spatial dyssynchrony of calcium dynamics across the cell, which could have implications on the contractile strength and uniformity, and hence overall cardiac function. The earlier transient onset at the cell periphery could be due to higher levels of contraction at the cell ends, and hence comparison with non-immobilized cells would be of interest. Further research is required to address the limitations of the work described in this chapter and further investigate the findings. Potential future directions include correlative imaging of transient development and labelled RyR channels to evaluate their role in the spatial dyssynchrony of calcium transients across the cell. More insight into transient desynchronization with detubulation using the novel high-speed 2D imaging modality can be achieved by imaging HF cells with more disrupted t-tubule structure.

More fundamentally, biological complexity is best navigated with full spatiotemporal dimensionality. A more complete picture of the morphology of calcium dynamics and its interplay with cell microstructure is achieved through time-lapse imaging in 3D. Approaches to high-speed volumetric imaging and the application of the system to studying calcium dynamics in multicell and tissue samples are discussed in the next chapter.

5 High-speed 3D imaging of calcium dynamics in stem-cell derived and adult cardiomyocytes.

5.1 Introduction

5.1.1 Stem cell regenerative therapy and hiPSC-CM

During the last two decades, research into stem cell regenerative therapy has shown potential as a treatment for cardiovascular diseases. Pluripotent stem cells can be differentiated into any cell within the body, enabling their application in drug screening, disease modelling, cell replacement therapy and tissue engineering. Successful electromechanical coupling in the form of synchronized regular calcium transients and the formation of electromechanical junctions between native cardiac tissue and grafted embryonic stem cell (ESC)-derived cardiomyocytes has been demonstrated in non-human primate models (Chong et al., 2014). While the pluripotency of ESCs has facilitated their use for regenerative purposes, their harvest requires manipulation or destruction of pre-implantation embryos (Klimanskaya et al., 2006), which has raised controversy regarding the ethics of their use. Unlike ESCs, induced pluripotent stem cells (iPSCs) are derived directly from somatic cells in adult tissue (Takahashi & Yamanaka, 2006), avoiding the need for embryos (Kimbrel & Lanza, 2016). Additionally, iPSC can be derived in a patient-matched manner, with lower risk of immune rejection of transplanted autologous cells (Morizane et al., 2013).

Advances in iPS-cell cardiac tissue engineering have provided an alternative tool for cardiac rejuvenation. Work by Chow et al. demonstrated that injection of an iPSC-CM-encapsulating bioactive hydrogel improved rat heart function following myocardial infarction (MI) (Chow et al., 2017). The development of hiPSC-CM containing engineered heart tissue (EHT), where stem cells are embedded in a three-dimensional scaffold which imitates the natural cardiac environment, has offered an alternative to the limitations of previous stem cell transplantation techniques (Tiburcy et al., 2017; Weinberger, Mannhardt & Eschenhagen, 2017). EHT-based approaches have shown promise in small animal models such as rats (Zimmermann et al., 2006), and have been cleared for human trials (Mitchell, 2019). As an intermediate scale model, recent work by Jabbour et al. tested the efficacy of a larger-scale EHT patch containing up to 20 million hiPSC-CM embedded in hydrogel in an in-vivo 4-week rabbit myocardial infarction model (Jabbour et al., 2021). For infarcted hearts that received EHTs, the study demonstrated improved function, reduced infarct scar size, and improved contraction and calcium transients within the hiPSC-CMs over 28 days, without increased arrhythmia. However, in this study no electrical coupling was observed between the EHT and the host heart.

5.1.2 Excitation-contraction coupling in hiPSC-CM

Assessing the full potential of regenerative stem cell therapy using hiPSC-CM requires an accurate understanding of the excitation-contraction (EC) coupling, the mechanism responsible for converting

the electrical stimulation received by cardiomyocytes into a mechanical force. EC coupling in adult ventricular cardiomyocytes is outlined in **Section 4.1.1** in the previous chapter. The limited maturity of iPSC-CM's in comparison to adult-CM is manifested in structural and calcium handling differences. However, while the cell lines and differentiation protocols are well controlled (Kane, Couch & Terracciano, 2015), there is still significant variation in the resulting hiPSC-CM physiology due to different culture conditions, particularly cell density (Du et al., 2015).

A defining feature of hiPSC-CM and an indicator of their successful differentiation is spontaneous beating, which also involves a global calcium release. The automaticity originates from an internal "Ca²⁺ clock" mechanism which involves calcium cycling through the sarcoplasmic reticulum (SR). Spontaneous SR release generates a depolarizing current through the Na⁺-Ca²⁺ exchanger (NCX), created from the electrogenic stoichiometry derived from the inward movement of 3Na⁺ ions in exchange for the expulsion for each Ca²⁺ ion. This creates sufficient current to depolarize a cell to a threshold that allows the generation of action potentials (Kim et al., 2015). The rate of spontaneous calcium correlates positively with external Ca²⁺ concentrations, suggesting that greater SR Ca²⁺ loads produced by increasing external Ca²⁺ concentration increased the frequency of spontaneous calcium release from the SR, which in turn increased automaticity (Kim et al., 2015).

The functionality of hiPSC-CM is thought to be at least partially limited by structural immaturity (Kane, Couch & Terracciano, 2015). While hiPSC-CM have similar levels of expression of L-type Ca²⁺ channels to the adult human heart (Rao et al., 2013), unlike adult cardiomyocytes, hiPSC-CM lack t-tubules (Gherghiceanu et al., 2011) and have functional but fewer ryanodine receptors (RyR) (Rao et al., 2013), sparsely spatially distributed in the cytosol, and denser clustering in perinuclear (Itzhaki et al., 2011) and sub-sarcolemmal regions (Zhang et al., 2013b). The inhomogeneous clustering of RyR contributes to the inward propagating Ca²⁺ transients and overall less efficient calcium-induced calcium release (CIRC), with uncoupled RyRs activated by the global rise in Ca²⁺ concentration rather than direct activation by local Ca²⁺ channels (Lee et al., 2011; Zhang et al., 2013a).

The calcium transients in hiPSC-CM are of lower amplitude and have a significantly slower rise and decline compared to those observed in adult cardiomyocytes (Hwang et al., 2015; Lee et al., 2011; Zhang et al., 2013). The slower decline of calcium transients in hiPSC-CM is attributed to less effective Ca²⁺ uptake by the SR and reduced Ca²⁺ efflux from the cell by the NCX. Spark characteristics in hiPSC-CM were found to be comparable with those in adult-CM, with multiple occurrences at the same location (Kane, Couch & Terracciano, 2015), and differences in morphology between those at the centre and edge of the cell, also indicating inhomogeneous ryanodine receptor distribution (Zhang et al., 2013).

The natural beating frequency of iPSC-CM is influenced by environmental factors including temperature and time: experiments by Laurila et al. showed a beat frequency peak at ~80 beats per minute (BPM) at 42°C, which dropped to < 20 BPM by 31°C (Laurila et al., 2016). At a constant

temperature of 37°C, the beating frequency recorded in the aforementioned study decreased with time, dropping to nearly half of the initial rate within an hour, indicating potential sensitivity to other environmental/culture parameters such as changes in pH or O₂/CO₂ concentration. As for stimulated transients, unlike adult cardiomyocytes in most species (including humans), hiPSC-CM exhibit a negative force-frequency response (FFR) (Germanguz et al., 2011), meaning that the contraction force decreases with increasing stimulation rate, indicating reduced ability in using internal Ca²⁺ stores.

5.1.3 Electromechanical coupling of hiPSC-CM and adult-CM

Synchronized contraction of cardiac tissue is supported by intercalated discs, which are complex structures that connect adjacent cardiomyocytes and contain three types of cell-to-cell junctions: gap junctions, desmosomes and fascia adherens (Zhao et al., 2019). Gap junctions provide an electrical connection between the cytoplasm of adjacent cells, enabling the transfer of ions, allowing depolarization and propagation of cardiac action potentials. Desmosomes bind intermediate filaments, cytoskeletal components within the cells, maintaining structure. Fascia adherens junctions connect actin, the cytoskeletal microfilaments, reinforcing cell-cell contact.

Hence, the synchronized contraction between cardiomyocytes is enabled by the efficient transmission of both electrical signals and mechanical forces. Previously, the limited improvement of cardiac function following grafting has been attributed to lack of electrical coupling between donor and host cells (Passier, van Laake & Mummery, 2008). However, work by Aratyn-Schaus et al. (2016) has considered the role of mechanotransduction on the integration of host and graft cardiomyocytes (Aratyn-Schaus et al., 2016). The study implemented an in-vitro muscle-on-chip-model to characterize heterogenous cardiomyocyte coupling by measuring intra-cellular force transmission between embryonic- and iPSC-derived cardiomyocytes at different levels of maturity. The model found that stem-cell derived cardiomyocytes of different origin and intrinsic contractile and calcium handling properties were able to couple both electrically with the formation of gap junctions and mechanically with synchronized contraction. However, the coupling of cardiomyocytes with differing contractile properties resulted in formation of more focal adhesion structures which resulted in decreased force transmission between cells.

Other co-culture models have been used to study the interaction and integration of heterogenous cardiac cells. Chu et al. demonstrated that co-culture of iPSC with a population of iPSC-derived cardiomyocytes is sufficient to promote their differentiation (Chu et al., 2020). Work by Beauchamp et al. implemented co-culture of hiPSC-CM and cardiac fibroblasts, demonstrating that 3D culture more closely resembled native myocardium than 2D culture (Beauchamp et al., 2020).

5.1.4 Living myocardial slices

Both 2D and 3D in-vitro culture are simplified models of the in-vivo biological system and do not provide insight into cell physiology within complex tissue architecture, and this is manifested in the

behaviour and phenotype of cultured cells (Banyasz et al., 2008). On the other end of the spectrum, while whole-organ and larger-scale tissue models maintain more of the native in-vivo environment, the limited throughput constrains their use in disease model studies. Living myocardial slices (LMS) provide a multicellular model of intermediate complexity for simulating the cardiac physiological environment, allowing the interaction of adult myocytes with endogenously applied cells to be studied (Watson, Terracciano & Perbellini, 2019).

The ultrathin (~300 µm, approximately 11-13 layers of CM) slices are prepared using a high precision vibratome which retains the tissue structure, while allowing sufficient oxygen diffusion for maintaining viability (Watson et al., 2020). The damage to individual cells from transection by the blade is minimized by identifying fiber orientation within the tissue, allowing careful detachment of neighbouring cardiomyocytes during slicing, resulting in 40-60% cell viability of CM on the LMS surface (Watson et al., 2017; Watson, Terracciano & Perbellini, 2019). Live myocardial slices offer a medium-throughput model, with around 6-8 LMS generated from rat LV, and up to 30 LMS from larger mammals (Watson et al., 2020).

At optimal preparation, the slices only contract under electrical stimulation, with spontaneous activity signifying potential tissue damage (Watson et al., 2020). Non-ratiometric dyes such as Fluo-4 have been used for widefield optical mapping of Ca^{2+} dynamics in LMS, with motion artefacts reduced through the use of myosin inhibitor Blebbistatin or EC uncoupler 2,3-butanedione monoxime (BDM) (Wang et al., 2015; Watson et al., 2020). The highly optically scattering structure of cardiomyocytes limits the imaging depth (20-30 µm for confocal and 50-80 µm and two-photon microscopy) making deep 3D imaging of cardiac tissue slices challenging (Scherschel & Rubart, 2008). While optical clearing can enable high resolution volumetric imaging of the LMS structural organization (Perbellini et al., 2018), existing methods are not compatible with live cell imaging (Costantini et al., 2019).

5.1.5 Experimental objectives

Evaluation of the integration level of iPSC-derived cardiomyocytes and hence their potential for regenerative therapy requires observation and characterization of the electrophysiological dynamics and electromechanical coupling between graft and host tissues. Light-sheet fluorescence microscopy offers the possibility of resolving fast calcium dynamics in multi-layer co-culture through gentle optically sectioning imaging compatible with live cells. Using the novel LSFM imaging platform described in this thesis for high-speed volumetric imaging at subcellular resolution, it is possible to study the interaction of stem cells and adult cardiomyocytes in culture and tissue in 3D.

The aims of the work done in this chapter are the following:

1. To develop a basic protocol for hiPSC-CM culture, co-culture with adult-CM, and sample preparation compatible with live cell 3D LSFM with electrical stimulation.

2. To apply high-speed 2D and 3D LSFM to imaging calcium dynamics in hiPSC-CM and their short-term co-culture with ventricular adult CM.
3. To investigate the early-stage electromechanical coupling of co-cultured adult-CM and hiPSC-CM, and the influence of co-culture duration and decoupling with a myosin inhibitor.
4. To develop a basic protocol for high-speed 3D LSFM imaging of calcium dynamics in LMS as a step towards a higher-complexity model of hiPSC-CM and LMS co-culture microscopy experiments.

As part of aims 2 and 3, the following hypotheses are tested:

1. Electromechanical coupling between hiPSC-CM and adult-CM in the form of synchronized transients and contraction will increase with co-culture duration.
2. Mechanical uncoupling with para-Nitroblebbistatin will inhibit coupling and stop transient synchronization in the co-culture.

Section 5.2 provides an outline of the imaging experiments and methods for sample preparation of LMS, hiPSC-CM culture and co-culture with adult-CM, data acquisition and processing. **Section 5.3** outlines the main observations and results from the imaging experiments, and **Section 5.4** discusses the findings, and presents conclusions and an outlook for the future.

5.2 Experiment outline and methods

This section provides an overview of the experiments and details of the methods (sample preparation, image acquisition and data processing) used for dual-channel 2D and 3D LSFM imaging of LMS, hiPSC-CM and their coculture with isolated adult rat ventricular cardiomyocytes (adult-CM). **Table 5.1** presents an outline of the main experiments and the key acquisition parameters.

Initial experiments (Exp. 1-2) were aimed at establishing a working imaging and sample preparation protocol and exploring the nature of existing dynamics in hiPSC-CM (Aims 1-2). Experiments 3-4 focused on investigating the influence of two variables on cell coupling and dynamics: co-culture time and mechanical decoupling (Aims 2-3). hiPSC-CM and adult-CM were co-cultured for different durations (0 – 2 days) prior to imaging in order to investigate the change in their coupling with co-culture time. The cells were imaged with and without electrical pacing, and with and without mechanical decoupling using NBleb. In addition to high-speed volumetric imaging using light-sheet fluorescence microscopy, low-NA fluorescence and transillumination widefield microscopy recordings were acquired to provide a larger FOV overview of the cell contraction and calcium dynamics. Finally, Exp. 5 involves preliminary application of 3D LSFM to imaging LMS (Aim 4). Existing sample preparation protocols used for widefield optical mapping including decoupling with 2,3-butanedione monoxime (BDM) were adapted to be compatible with imaging on the LSFM system.

Exp.	Sample	Mode	FOV (x-y-z, μm)	FPS	VPS	Duration (s)	Pacing Period (s)	Co-culture duration (days)	Decoupl.
1	hiPSC-CM	2D	170×38	175	N/A	57	–/2/4/6	N/A	–
2	hiPSC-CM	3D	302×76×40	195	4	15	–/2	N/A	–
			302×38×40	390	8	15			
3	Co-culture	3D	302×38×40	390	8	15	–/2	0, 1, 2	–/NBleb
4	Co-culture	3D	302×76×40	195	4	15	–/2	0, 1	–/NBleb
5	LMS	3D	302×76×40	195	4	15	2	N/A	BDM

Table 5.1 Overview of the main time-lapse experiments with hiPSC-CM cells and their co-culture with adult LV CM, and the key parameters and acquisition settings: the sample type, acquisition mode (2D or 3D), FOV dimensions (per spectral channel), frame and volume acquisition rate in frames per second (FPS) and volumes per second (VPS) respectively, total duration of each acquisition, presence and period of the electrical pacing, co-culture duration and presence of motion decoupler (NBleb). Lack of pacing or decoupler is denoted by “–”.

hiPSC-CM differentiation and culture

The hiPSC-CM cells were differentiated from the human lung fibroblast IMR-90 (iPS(IMR90)-4, WiCell) by Thusharika Kodagoda (Prof. Sian Harding’s group) in ICTEM according to the protocol outlined in (Jabbour et al., 2021). From day 15 onwards after start of differentiation, the hiPSC-CM

were maintained by Liliana Brito (Prof. Sian Harding's group) in hiPSC-CM *maintenance media* containing RPMI 1640 (Thermo Fisher Scientific) with added 1× B27 (Thermo Fisher Scientific) and 1% AA (Antibiotic-Antimycotic, Thermo Fisher Scientific). The replating was conducted by Liliana Brito on day 23 after start of differentiation using the following process. First, cell detachment was attained using a Cell Dissociation Solution (at 2:2:1 ratio, Cell Dissociation Buffer (Thermo Fisher Scientific) : RPMI 1640 : 0.05% Trypsin-EDTA (Thermo Fisher Scientific) for 15 min at 37°C. Next, trypsin de-activation was achieved using the hiPSC-CM maintenance media supplemented with 10% FBS (Fetal Bovine Serum, Thermo Fisher Scientific), and cells were pelleted by centrifugation at 200 g for 5 minutes and counted with the Vi-CELL XR cell counter. Finally, the cells were replated at 150k/cm² cell density onto plastic coverslips (Nunc Thermanox 150067, Thermo Fisher Scientific), which had been previously cut to fit within the 1 cm² area chambers in a µ-Slide 8-Well Glass-Bottom Chamber (Ibidi), with the replating media containing 10% FBS and 10 µM Rock inhibitor Y-27632 (Strattech) added to the the hiPSC-CM maintenance media. The coverslips were coated beforehand with fibronectin from bovine plasma (F11410-1 mg, Sigma Aldrich), diluted in 1:100 in 1× PBS for 1 h at 37°C. The plating was not done directly onto the chamber bottom in order to enable easy sample transfer from the dish to the chamber used for the imaging experiments.

One day after replating, the media was replaced by the hiPSC-CM maintenance media. The replated hiPSC-CM were transported between campus locations in a heated chamber which maintained a temperature of 37°C, and then maintained at 5% CO₂, 37°C, until at least 4 weeks past start of differentiation prior to use in experiments, with media change every 3 days. Prior to any further use, cell quality was controlled by observing a regular spontaneous beating activity with a period of <10s upon direct observation after removal from incubator.

hiPSC-CM co-culture with adult-CM

The hiPSC-CM were co-cultured with male rat left-ventricle cardiomyocytes freshly isolated by Peter O'Gara following the method outlined in (Sato et al., 2005) and suspended in low Ca²⁺ enzyme solution (mM), containing (in mM) NaCl (120), KCl (5), MgSO₄ (5), Na pyruvate (5), glucose (5), taurine (20), HEPES (10), CaCl₂ (0.2), pH 7.4 adjusted with 1M NaOH. The cells were re-suspended at 1:10 dilution in M199+ adult culture medium containing (per 500 ml M199): 5 mL P/S, 1g BSA (A7906-100G, Sigma), 0.33 g Creatinine (C3630-100G, Sigma), 0.33 g Taurine (T8691-100G, Sigma), 0.0088 g Ascorbate (A5960-25G), 0.161 g Carnitine (C9500-100G), provided by Dr. Laura Fedele and Dr. Jose Sanchez Alonso Mardones. To make the co-culture, the RPMI cell media was aspirated almost completely from the hiPSC-CM culture and quickly replaced with the same amount of adult-CM culture medium. Next, isolated adult-CM were added on top of the cultured stem cells through gentle dropping using a Pasteur pipette to achieve a scattered isolated adult-CM distribution on top of the hiPSC-CM cells such as that shown in **Fig. 5.1a**. The cells were then placed back into the incubator and cultured

for varying durations (4 hours, 1 day, 2 days) up until the point of imaging, with adult-CM culture medium change every 1-2 days.

hiPSC-CM and co-culture preparation for calcium imaging

During sample preparation for fluorescence imaging, the plastic coverslips were carefully transferred using tweezers into a larger chamber and resuspended in 1 mL M199 Adult-CM culture medium. Similarly to the procedure used for labelling isolated rat ventricle cardiomyocytes, described in **Section 4.2**, the co-cultures were incubated with 0.16% pluronic acid and 5 μ M Fluo4-AM in DMSO for 15 minutes at 37°C, followed by the addition of 5 μ g ml⁻¹ CellMask Orange (CMO) for another 5 minutes. Throughout the incubation period, the chamber containing the coverslip-seeded cells was placed on a rotary mixer (at the lowest speed setting) to ensure homogenous dye distribution and protected from light by wrapping the dish in foil. After the total 20 minutes of incubation, the sample was resuspended in the adult-CM culture medium, that was pre-heated to 37°C. After allowing ~20 minutes for de-esterification, the coverslip was gently transferred to the imaging chamber using tweezers, and placed between the two electrodes, taking care to not flip the coverslip upside down. The coverslip sample and front lenses of the two objectives were immersed in 1 mM Ca²⁺ Normal Tyrode solution, which was also pre-heated to 37°C. One of the experimental variables, mechanical length changes (shortening and re-lengthening) was prevented by decoupling the excitation from contraction using the non-phototoxic low fluorescence myosin inhibitor para-Nitroblebbistatin (NBleb, Axol Bioscience) (see **Section 4.2**), which was added to the M199 and NT at 25 μ M concentration, with thorough mixing of the solution.

hiPSC-CM and co-culture pacing chamber

A new version of the pacing chamber (shown in **Fig 5.1b**) was designed and used for all imaging experiments with hiPSC-CM. The chamber consisted of a glass slide cut to a rectangle with dimensions of ~6 × 5 cm, with the pacing delivered using two parallel 4 cm-long electrodes made out of 0.8 mm diameter platinum wire (Goodfellow). The electrodes were attached to the glass slide using Araldite glue, separated by ~1 cm and parallel over a distance of ~2 cm, and bent away from each other at two of the ends to minimize the risk of scratching the objectives. This chamber prototype did not use a silicon strip to contain the liquid, and instead relied on surface tension to maintain the liquid immersion of the objectives and sample – the silicon strip used with this wire configuration did not function well due to leakage at contact points with the wire.

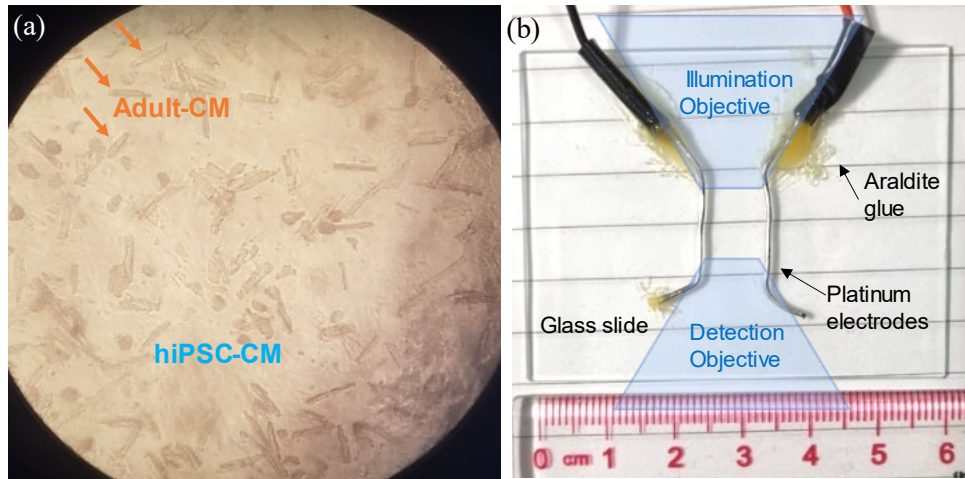


Figure 5.1 hiPSC-CM and adult CM co-culture and pacing chamber. (a) Representative distribution of adult-CM on top of a weakly scattering layer of hiPSC-CM, as seen ~4 hours after start of co-culture. Image recorded through the eyepiece of an inverted transillumination widefield microscope through the glass bottom of the well and the plastic coverslip using a 4× air objective. (b) Top view of the chamber used for imaging and electrical stimulation of hiPSC-CM and their co-culture with adult-CM. Approximate objective positioning is illustrated in blue.

Live myocardium slices sample preparation

The $\sim 9 \times 8$ mm ventricular LMS were prepared by Dr Raquel Nunez Toldra (Prof. Cesare Terraciano's group) and Dr. Thomas Owen (Prof. Sian Harding's group) from freshly isolated rat hearts following the protocol outlined in (Watson et al., 2017) with slicing done using a high precision vibratome. Custom-made holders made from biocompatible polyethylene terephthalate (Taulman3D T-glase) were attached to each side of the LMS with surgical glue (HistoAcryl; Braun) to allow stretching of the tissue along the fibre direction. Custom-made stainless-steel stretchers made by Prof. Cesare Terraciano's group were used to stretch the slices by $\sim 20\%$ to a sarcomere length of $2.2 \mu\text{m}$ (Watson et al., 2019).

The protocol used for preparing the LMS for imaging was adapted from that used for widefield optical mapping in (Dries et al., 2021; Watson et al., 2017) and the sample preparation protocol used for dual channel imaging of single cells and culture. The slices were transported in between campus locations (from ICTEM to Blackett Laboratory) stretched, on ice, in Normal Tyrode “slicing” solution containing (in mM) NaCl (140), KCl (6), Glucose (10.32), HEPES (10), MgCl_2 (1), CaCl_2 (1), 2,3-butanedione monoxime (BDM,30) – an excitation-contraction uncoupling agent used to suppress motion artefacts from contraction. The slices were imaged within 2-3 hours of preparation. Dye loading and imaging was performed in a Normal Tyrode “recording” solution identical to the “slicing” solution, except for a lower potassium concentration (4.5 mM KCl) and a higher calcium concentration (1.8 mM CaCl_2). The slices were incubated unstretched (**Fig. 5.2a**) with 0.16% Pluronic acid and $5 \mu\text{M}$ Fluo4-AM in DMSO for 15 minutes at 37°C , followed by the addition of $5 \mu\text{g ml}^{-1}$ CellMask Orange (CMO) for another 5 minutes. The tissue sample was then placed back onto the stainless-steel stretcher positioned in the centre of a 5.5 cm diameter and 1.2 cm depth petri dish. The pacing and imaging chamber prototype

used platinum electrodes at opposite ends of the dish used to deliver electric field stimulation (**Fig. 5.2b**). The stretched sample was oriented such that cardiomyocyte long axis is perpendicular to the light-sheet direction (**Fig. 5.2c**). The sample was then immersed in the recording solution, pre-heated to 37°C, and left for 10 minutes of de-esterification prior to imaging.

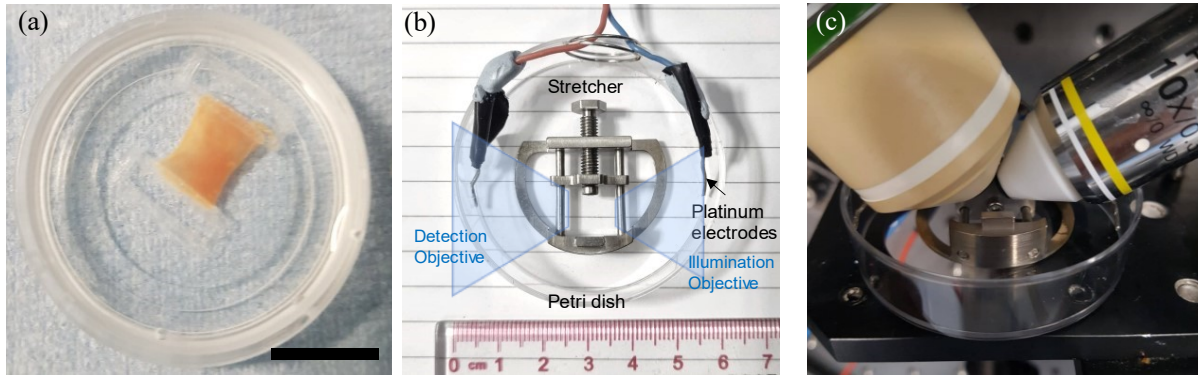


Figure 5.2 LMS sample mounting for imaging (a) Unstretched LMS with attached holders immediately prior to staining. Scalebar: 1 cm. (b) Top view of the chamber used for imaging and electrical stimulation of hiPSC-CM and their co-culture with adult-CM. Approximate objective positioning is illustrated in blue (c) LMS pacing and imaging chamber positioning under the detection and illumination objectives (right and left respectively).

Widefield fluorescence and transillumination imaging

For imaging over a larger FOV than achievable with the LSFM system, brightfield transillumination and epi-fluorescence 2D-timelapse of the hiPSC-CM and adult-CM co-culture carried out on an inverted widefield microscope (IX73, Olympus) equipped with LED illumination (CoolLED pE300) and a B/W CCD digital camera (Hamamatsu C4742-95-12ER). Detection and epi-fluorescence illumination was achieved using infinity corrected air objectives: UplanFL 4×/0.13 NA (1-U2B522, Olympus) and CPlan FL N 10× 0.30 NA PhC (1-U2C543, Olympus). Each acquisition consisted of an image sequence of between 100-200 frames covering durations of 40-60s, each one with image dimensions of 1344×1024 pixels. This corresponds to physical image dimensions of $867 \times 661 \mu\text{m}$ and $2167 \times 1651 \mu\text{m}$ for the 10× and 4× objectives respectively. Data was acquired at either 2 fps or 5 fps, and exposure times varied between 5 and 200 ms between the different magnifications and illumination modes. For imaging of calcium dynamics, Fluo-4 was excited using the blue LED (peak at 450nm) and a $472 \pm 30 \text{ nm}$ (centre and FWHM) excitation filter. Fluorescence was collected through a GFP-3035C-000 filter with a detection range of $520 \pm 35 \text{ nm}$. A 495 nm long-pass dichroic mirror was used to separate the excitation and emission.

2D and 3D LSFM imaging

For 2D LSFM stem cell imaging, the laser power was kept at the same level as that used for single-cell cardiomyocyte imaging (**Section 4.2**). For 3D LSFM imaging, the fluorescence of both CMO and Fluo-4 was excited using only the 488 nm excitation line with an excitation power of 312 μW (measured in the BFP of the excitation objective). For co-culture imaging, sample navigation and pre-find was done

in transillumination, with individual adult cardiomyocytes distinguished from the underlying stem cell layer due to their stronger scattering (**Fig. 5.3**). Individual adult-CM were centred within the FOV and any pre-visualization of the sample fluorescence was performed using a lower laser power ($<100 \mu\text{W}$) to minimize photodose. Each FOV containing an adult cardiomyocyte was imaged first without electrical pacing. Then, after pre-pacing the sample for 1 min prior to the acquisition, imaging was repeated with electrical stimulation applied, using the same pacing parameters as previously (2 ms pulse duration, 20 V and 0.5 Hz frequency, unless stated otherwise). LMS were paced at 20 ms pulse duration, 40 V and 0.5 Hz frequency. The synchronization monitor signal from the electric field stimulation unit was recorded as a digital input to the DAQ card. Co-culture and LMS 3D time-lapse acquisitions were 15 s long and consisted of either 120 volumes at 390 fps (8 vps) or 60 volumes at 195 fps (4 vps).

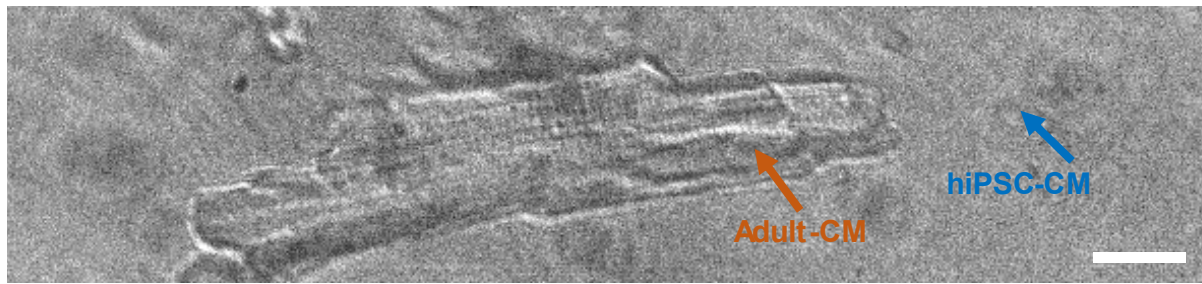


Figure 5.3 Adult-CM on top of weakly-scattering hiPSC-CM, as seen in transillumination on the light sheet fluorescence microscope. Scalebar: 20 μm .

Data processing, reconstruction and analysis.

Co-registration of the two spectral channels for 2D and 3D stem-cell, co-culture and LMS data was carried out in MATLAB following the approach outlined in **Section 4.3**. Pre-processing included subtraction of fixed pattern noise and an affine transformation of the Fluo-4 channel, with transformation parameters determined from a dual-channel 200 nm bead image dataset acquired prior to each set of experiments and after any adjustment of the positioning mirrors within the dichroic assembly in the detection path.

For visualization of the 3D-time-lapse data (x-y-z-t), the XY image stack, recorded as a sequence of N XY frames, where $N = Z \times T$, was re-ordered into a XY-z-t image hyperstack in ImageJ. Each XY image in the data stack was cropped to the FOV of the light transmitted through the CMO channel to exclude the dark frame around the part of the image transmitted through the slit, and axially re-scaled to attain a uniform voxel size extending 0.1477 μm in each dimension. Next, the dataset was re-sliced horizontally to achieve an XZ view of the sample and rotated by 37° about the y-axis to transform the volume into lab coordinates. Next, the XZ view was resliced top to bottom and rotated by 90° to achieve top down XY view of the sample in lab coordinates. For the side view YZ, the end view XZ was resliced left to right, and rotated by 90 degrees. The resliced orthogonal cuts of the volume were rendered as MIP's or orthogonal slices and the two spectral channels were combined for multicolour visualization.

Statistical analysis of significance was carried out in GraphPad Prism 9.1.1 software, with p-values calculated using Chi-square tests, with $p < 0.05$ considered statistically significant.

5.3 Results

5.3.1 Exp. 1-2: Imaging calcium dynamics in hiPSC-CM in 2D and 3D.

This section summarizes the main findings and observations from imaging live hiPSC-CM culture using 2D- and 3D-timelapse LSFM with and without electrical pacing, with example acquisitions illustrating key features. **Table 5.2** summarizes the acquisitions from $n = 3$ different hiPSC-CM culture samples imaged on separate occasions (all on day 30 past start of differentiation) using 2D-timelapse LSFM imaging. A total of 19 unique imaged FOVs (N_{FOV}) within the cultures had calcium transients, out of which 11 acquisitions were electrically stimulated at three different periods: $T = 2$ s, 4 s and 6 s, with the cells pre-paced for 30 s prior to each acquisition. Each time-lapse dataset was visually screened to check for mechanical contraction (beating) of the cells.

hiPSC-CM culture	N_{FOV} with transients	Paced N_{FOV}	Pacing Period (s)	N_{FOV} with contraction
I	6	0	—	6
II	4	3	—/2	2
III	9	8	—/2/4/6	6
Combined	19	11	—/2/4/6	14

Table 5.2 Summary of 2D timelapse acquisitions of unpaced and paced hiPSC-CM culture, imaged on three different occasions. All acquisitions consisted of 10,000 frames at 175 fps (57 s duration), over a 1152×512 px FOV, imaged with and without electrical pacing.

Calcium transient $\Delta F/F_0$ vs time traces were analyzed by manually defining square regions of interest (ROI) within the Fluo-4 channel. **Figure 5.4** illustrates the range of calcium dynamics present in a selection of unpaced and paced acquisitions from the three hiPSC-CM cultures listed in **Table 5.2**. The CMO channel (purple) allowed visualization of the cell membrane and hence boundaries between adjacent cells. In comparison to adult ventricular cardiomyocytes imaged in single cell experiments (**Chapter 4**), hiPSC-CM cells were smaller, with up to ~ 20 cells partially visible within a 2D image for the same FOV, and had no t-tubule network visible within the cells. Depending on the confluence level of the culture, certain parts of the culture surface had no cells, and cell layers ranged from a single cell to localized centres with a thickness of >10 cells. Most acquisitions were limited to imaging areas which had a culture layer up to ~ 5 cells thick.

Overall, the cells were observed to have spontaneous transients (without any external stimulation), which occurred both with and without accompanying contraction. Unpaced transient periods ranged between 4-14s. In **Fig. 5.4a**, unpaced hiPSC-CM have spontaneous transients at a period of $T = 12.5$ s. It was also possible to electrically stimulate the calcium transients, with the stimulated transients occurring both with and without contraction. In **Fig. 5.4b**, the cells are electrically stimulated at 0.5 Hz

(2 s period), and the cells have transients at the stimulated frequency. It can be seen that the signal amplitude does not plateau at a baseline, and is lower than that in the slower spontaneous dynamics in (a). For 2 of the N_{FOV} acquisitions paced at $T = 0.5$ Hz, paired transients, separated by a longer delay from consecutive pairs, were observed, with an example demonstrated in **Fig 5.4c**. It was also possible to pace the cells at slower frequencies, with stimulated transients demonstrated at a period of $T = 4$ s and 6 s (**Fig 5.4d&e** respectively).

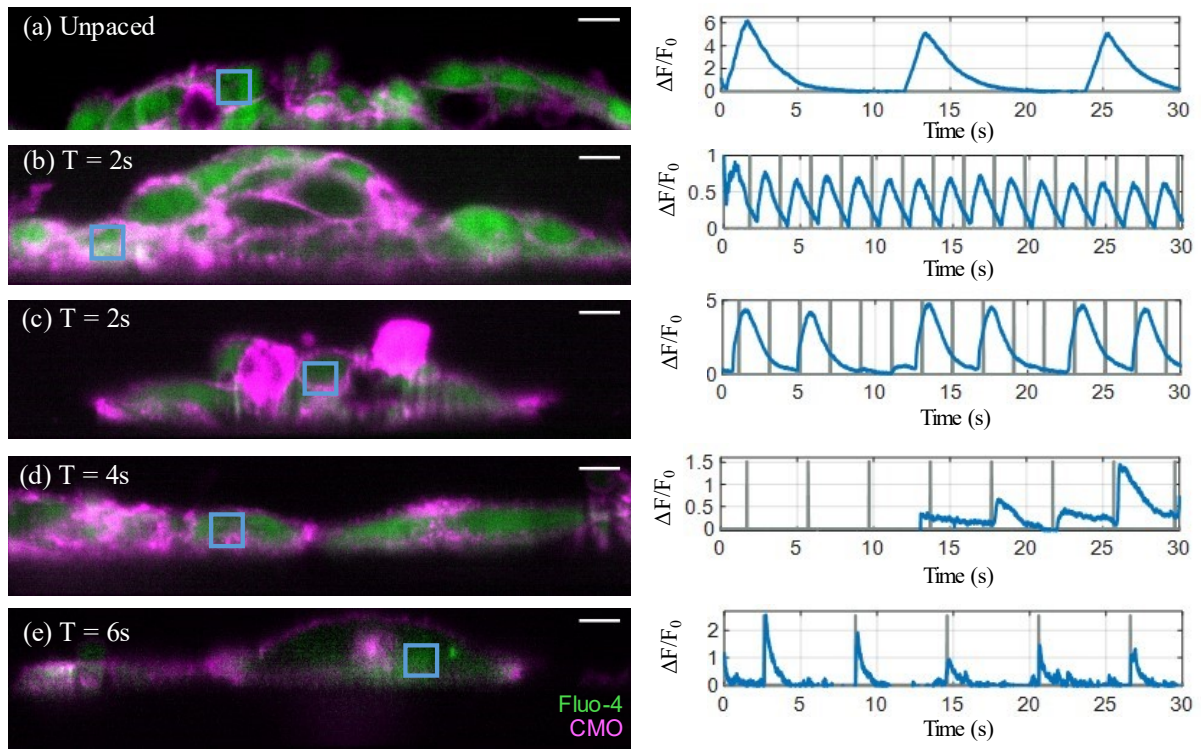


Figure 5.4 2D imaging of spontaneous and stimulated calcium transients in hiPSC-CM. Left column: merged Fluo-4 (green) and CMO (magenta) channels of a single frame at the peak of the first transient from a 10,000 frame (57 s) 2D time-lapse dataset imaged at 175 fps. Right column: corresponding Fluo-4 $\Delta F/F_0$ time-traces (blue) taken through the 50×50 2D ROI indicated by the blue square outlines in the left column. The panels show cells unpaced (a) and paced at a period of (b) $T = 2$ s, (c) $T = 2$ s, (d) $T = 4$ s, and (e) $T = 6$ s, with a pulse duration of 2 ms. The pacing timing is shown in grey. The dynamics were synchronized within most cells in the FOV. The first part of acquisition (d) lacks signal due to an unintentionally unopened laser shutter. Scalebar: 10 μm .

Figure 5.5 shows Fluo-4 (a), CMO (b) and merged channel (c) orthogonal cuts through hiPSC-CM culture imaged in 3D, with the corresponding timelapse presented in **Video 5.5**. The dataset was axially rescaled for isotropic voxel size and rotated into lab coordinates for horizontal alignment of the coverslip-cell boundary. This particular FOV contains a monolayer of cells, with the reconstructed top-down XY-view allowing more comprehensive visualization of the culture morphology. The same FOV was imaged in two consecutive acquisitions, first unpaced, then with electrical pacing at 0.5 Hz. The unpaced acquisition demonstrated spontaneous transients beginning 6.25 s apart, while the paced

hiPSC-CM culture had stimulated transients at the paced frequency, however, with a lower relative change in intensity.

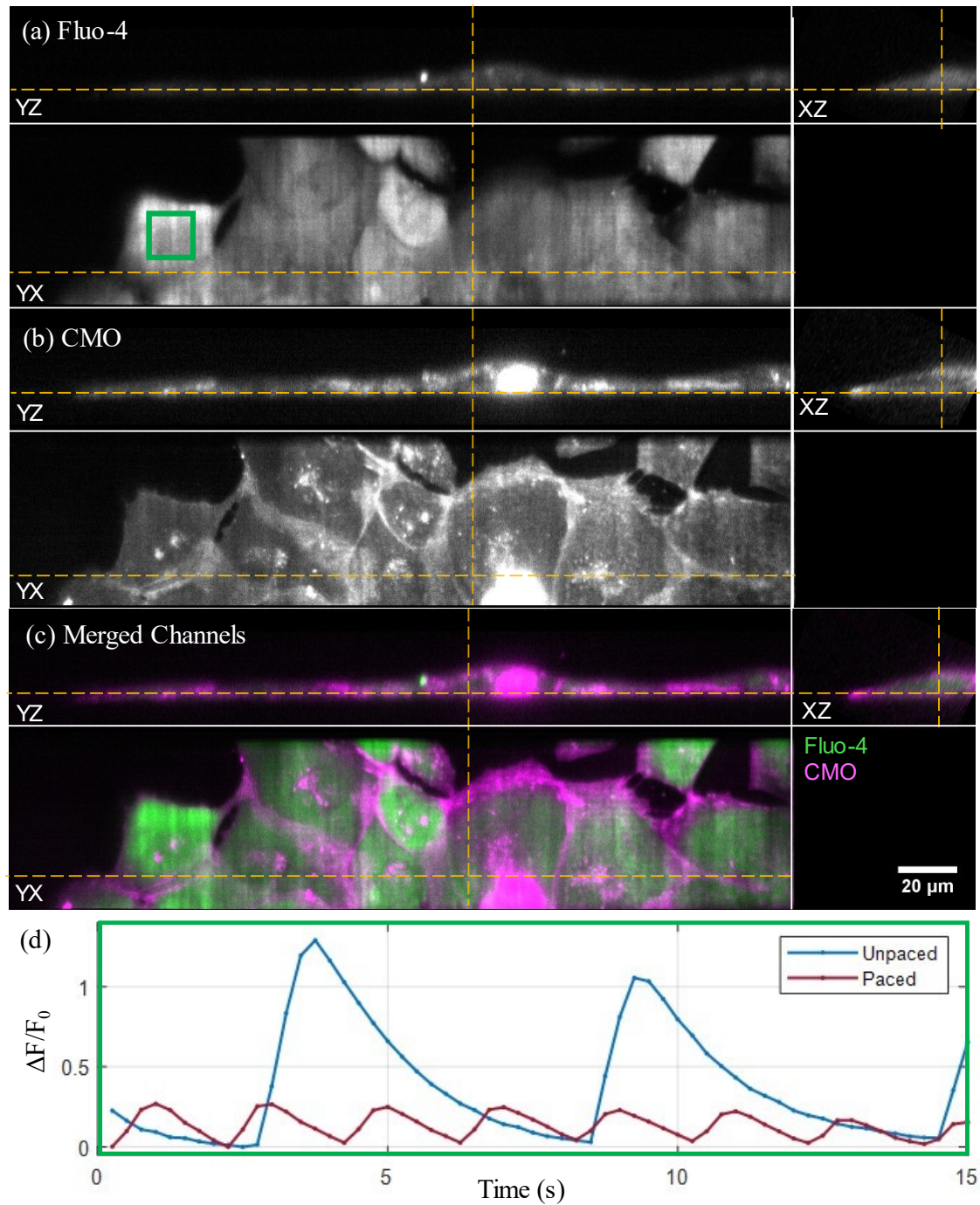


Figure 5.5 3D LSFM imaging of spontaneous and stimulated calcium transients in hiPSC-CM. Orthogonal cuts through the (a) Fluo-4, (b) CMO and (c) merged channels of hiPSC-CM culture imaged in 3D at 4 vps, 195 fps, displayed at the peak of the first spontaneous transient ($t = 3.75$ s) during an unpaced acquisition – the corresponding timelapse is shown in **Video 5.5**. The yellow dashed lines indicate the intersecting planes of the displayed orthoslices. (d) Calcium transient $\Delta F/F_0$ time traces calculated over the three-dimensional $100 \times 100 \times 1$ -voxel ROI (green rectangle in (a)) in consecutive unpaced and paced (at 0.5 Hz) acquisitions of the same FOV. The dynamics were synchronized between most cells in the FOV.

5.3.2 Exp. 3: Imaging coupling of hiPSC-CM and adult-CM

The original aim of co-culturing hiPSC-CM and adult-CM was to examine the nature of calcium signal propagation between the two cell types. Upon observing the co-culture 1 day after its start under a regular transillumination microscope, it was discovered that the added adult-CM and the underlying hiPSC-CM culture exhibited **spontaneous contraction, synchronized** both to other adult-CM, and the beating of the underlying hiPSC-CM layer, without any external electrical pacing. This synchronization of transients and/or contraction between individual adult-CM and hiPSC-CM cells is referred to as *coupling* within this chapter. This phenomenon was further investigated using widefield transillumination and fluorescence microscopy, and high-speed volumetric LSM.

For Experiment 3 (see **Table 5.1**), two co-cultures A & B were created on day 29 and day 34 respectively after start of hiPSC-CM differentiation. For each co-culture, a total of three samples were prepared (A_{I-III} & B_{I-III}). One of the three samples for each co-culture (A_I & B_I) was prepared with stem cells plated directly on the glass bottom of the well, instead of onto the removeable plastic coverslip. This was done to enable higher image quality imaging on the widefield microscope, without having to image through both the glass bottom and the plastic coverslip. The co-culture development was observed on days 0, 1 and 2 after the start of the co-culture, with 3D volumetric LSM imaging done on the plastic coverslip-plated samples A_{II} , B_{II} and B_{III} on days 1&2.

Widefield imaging of unpaced synchronized transients and contraction

Example transillumination images of samples co-cultured for 0-2 days are shown in **Fig. 5.6**, with the corresponding timelapse presented in **Video 5.6**. In the day 0 sample (left), the adult-CM can be distinguished from the underlying layer of hiPSC-CM by their rectangular shape and stronger scattering. By 24 hours of co-culture (middle), the adult-CM become more rounded, and by day 2 of co-culture (right), most have a circular shape. Unpaced synchronized contractions between spatially separated adult-CM were observed as early as 4 hours after co-culture (left), with the cells exhibiting shortening along their long axis at the same time. Simultaneous beating of the underlying hiPSC-CM layer can also be observed, indicating that the synchronization is occurring between the two cell types. Contracting cells can be identified from the brighter regions in the standard deviation maps for the widefield transillumination channel, shown in **Fig. 5.6** (bottom row).

Figure 5.7 shows examples from widefield epifluorescence recordings acquired on day 0, 1 and 2 of co-culture (left, middle and right columns respectively), with the corresponding timelapse presented in **Video 5.7**. The fluorescence intensity distribution at baseline and at the peak of the first calcium transient is shown in the top and middle rows respectively, with the third row displaying the standard deviation in intensity across the acquisition duration. On day 0, some of the adult-CM (distinguishable from the underlying hiPSC-CM layer by their shape and difference in baseline intensity) undergo synchronized transients with the stem cells (examples are indicated by orange arrows in **Fig. 5.7**), while

others do not. By day 1 and day 2 of co-culture the majority of adult-CM have simultaneous transients with the hiPSC-CM. Examples of synchronized transients within individual adult-CM and areas of hiPSC-CM are shown through the $\Delta F/F_0$ time traces shown in the bottom row of **Fig. 5.7** (panels k-m). Within the time-resolution of the acquisition (2 fps and 5 fps), the two cell types appear to have simultaneous transient start.

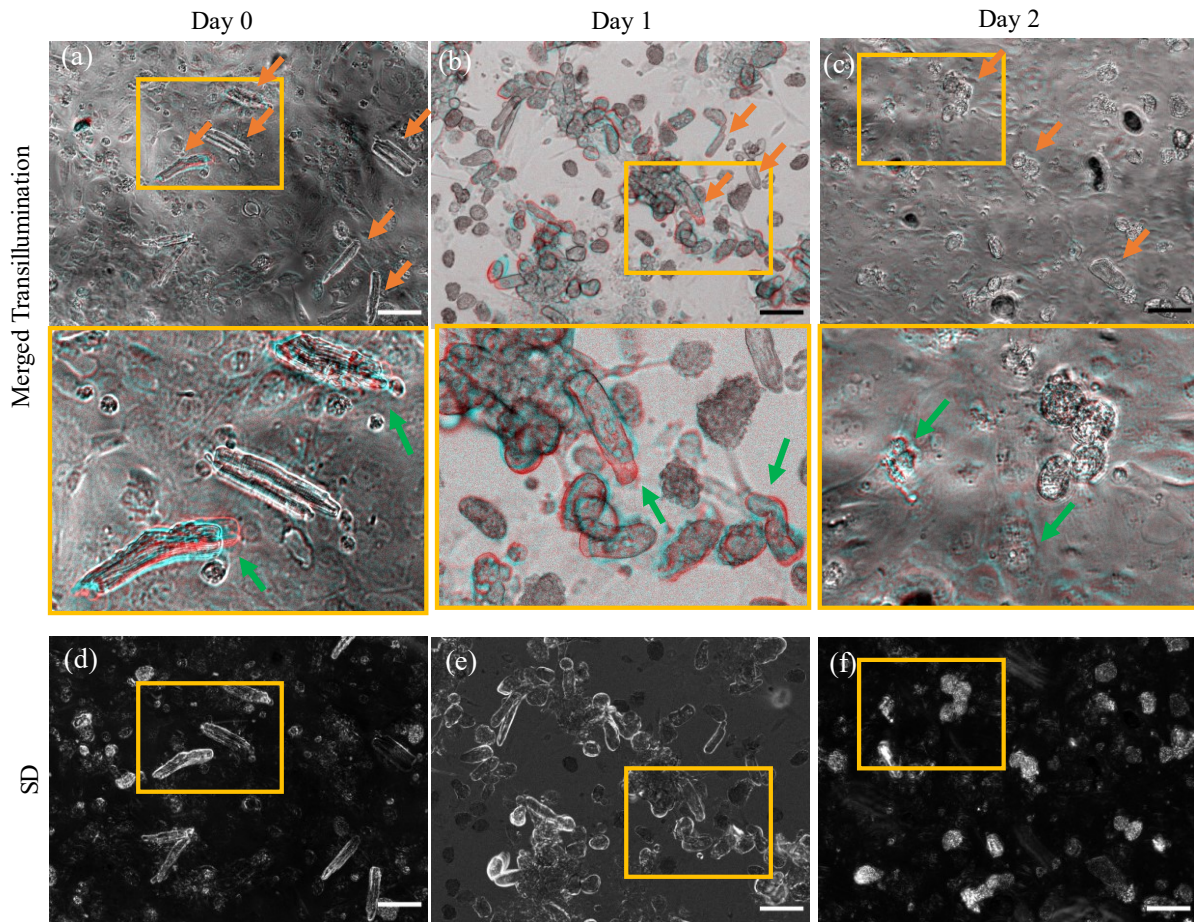


Figure 5.6 Synchronized contraction in day 0, 1, 2 co-culture imaged under widefield transillumination. Top row demonstrates two merged frames: at peak of contraction (cyan), and at baseline (red), taken $t = 2.5$ s apart for samples at day 0 (a), day 1 (b) and day 2 (c) of co-culture. Orange arrows indicate some of the adult cardiomyocytes on top of the layer of hiPSC-CM co-culture. The middle row shows zoomed in ROI indicated by the yellow rectangle in top and bottom rows, with green arrows pointing out some of the contraction movement between the merged frames (see **Video 5.6** for 50 s timelapse). Bottom row images are calculated as the standard deviation across the whole acquisition, indicating movement during acquisition. Scalebar: 100 μm .

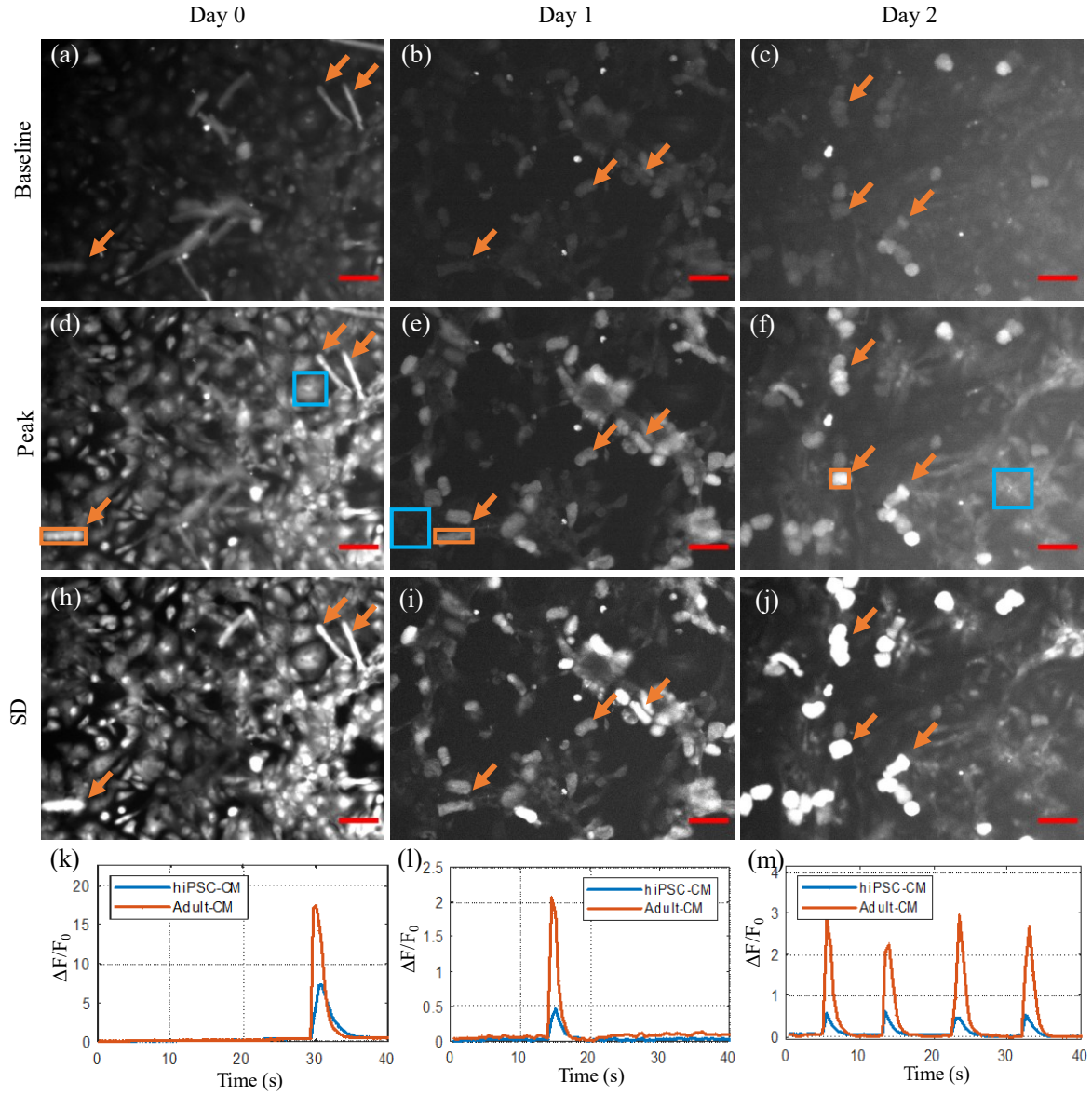


Figure 5.7 Widefield fluorescence imaging of calcium transients in adult-CM and hiPSC-CM co-culture on day 0 (left), day 1 (middle) and day 2 (right). Single frames at baseline (a-c) and peak of first transient (h-j), with frames from the same sample displayed on the same intensity scale. (h-j) Standard deviation calculated across the whole acquisition. Orange arrows indicate examples of coupled adult-CM. (k-m) Fluorescence intensity variation through hiPSC-CM (blue square ROI in middle row) and adult-CM (orange square ROI in middle row) indicating synchronized calcium transients. Scalebar: 100 μ m. The corresponding timelapse is shown in **Video 5.7**.

Table 5.3 summarizes the dynamics observed in day 0, 1 and 2 samples from two co-cultures with contraction and transient synchronicity observed in all samples except for one, which did not appear to have any visible dynamics – potentially due to poor sample health.

Co-culture	Age (Days)	Sample	Widefield Imaging Observations			
			Transillum. – sync. contraction		Fluoresc. – sync. transients	
			hiPSC-CM	Adult-CM	hiPSC-CM	Adult-CM
A	1	A _I	+	+	+	+
		A _{II}	+	+	N/A	
		A _{III}	+	+	–	–
	2	A _{II}	+	+	+	+
B	0	B _I	+	+/-	+	+/-
	1	B _{II}	+	+	N/A	
		B _{III}	+	+	+/-	+/-
	2	B _{II}	+/-	+/-	+	+/-

Table 5.3 Summary of dynamics identified from widefield transillumination and fluorescence imaging of the hiPSC-CM and adult-CM co-cultures A & B after 0, 1 and 2 days of co-culture. Presence of synchronized contraction and transients of 5+ cells is denoted as “+”, while the presence in <5 less is denoted as “+/-“, and samples without identified synchronized transients or contraction are labelled as “-“. Samples A_{II} and B_{II} were not labelled or imaged in fluorescence mode on day 1 and are labelled as N/A.

3D LSM imaging of synchronized transients and contraction

Three of the samples from co-cultures A & B prepared on transferable plastic coverslips (A_{II}, B_{II} and B_{III}) were successfully imaged in 3D on days 1 and 2 days of co-culture. For each of the 3 samples, ≥ 5 co-culture FOVs (N_{FOV}) containing unique cardiomyocytes were imaged. Acquisitions were acquired both with and without electrical pacing at 0.5 Hz. For manual visualization of the full sample and identification of present dynamics, a maximum intensity projection (MIP) along the detection axis was taken for each FOV. The optically sectioned 3D data allowed manual selection of ROI within each cell, hence allowing analysis of changes in fluorescence emission within that region, with minimal contribution from out-of-focus fluorescence.

Figure 5.8 and **Video 5.8** demonstrate an example 3D time-lapse acquired at 8 Hz through a FOV within an unpaced day 1 co-culture of hiPSC-CM and adult-CM. Data pre-processing and reconstruction was carried out as described in **Section 5.1**, and involved subtraction of fixed pattern noise, co-registration of the two spectral channels, axial re-scaling for uniform voxel size, and volume rotation into lab-coordinates. The adult-CM has retained some of the elongated shape, with some loss of rectangularity. By considering $\Delta F/F_0$ variation with time through square ROIs within orthogonal planes of the volume, it is possible to observe the transient synchronicity, with lower transient amplitude and slower decay in hiPSC-CM.

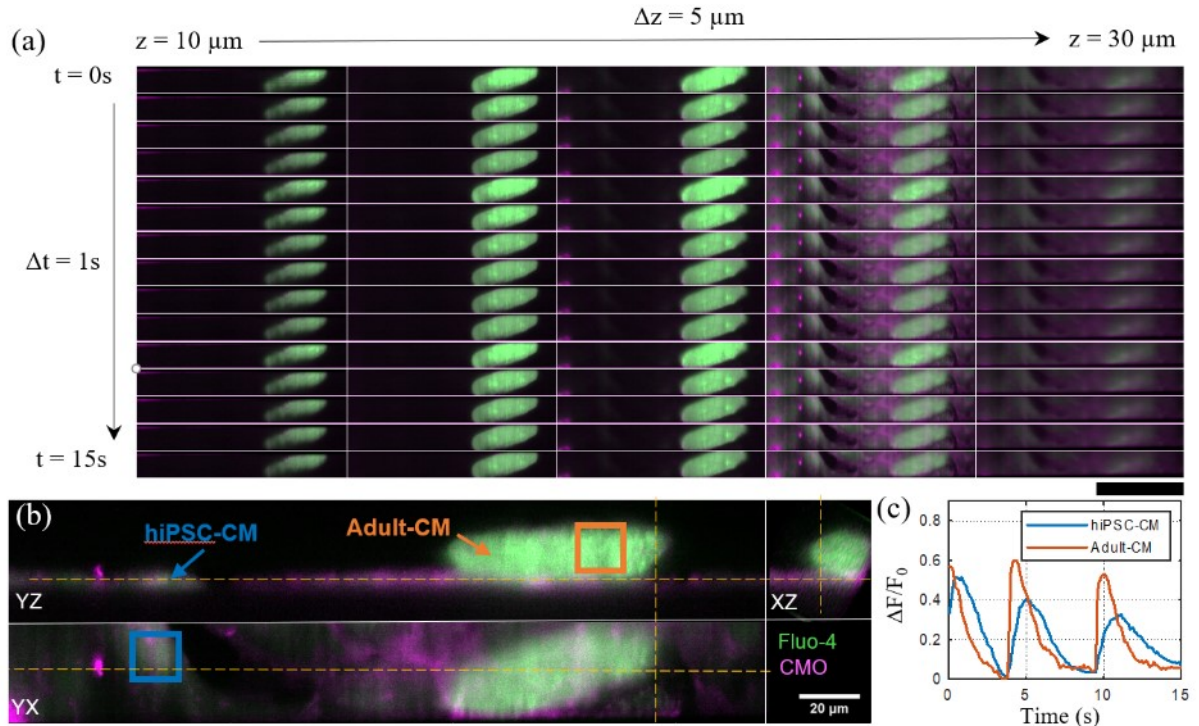


Figure 5.8 Synchronized spontaneous transients in adult-CM and hiPSC-CM co-cultured for 24 hours. (a) Montage showing merged Fluo-4 (green) and CMO (purple) 3D time-lapse for a single unpaced 15s acquisition at 8 vps (390 fps), see **Video 5.8**. Each column represents XY-planes spaced 5 μm apart axially within the central third of z-range (depth into sample, increasing towards the coverslip) of the volume. Each row represents timepoints 1 s apart. Scalebar: 100 μm . (b) Orthogonal cuts through the merged channels displayed at the peak of the second transient ($t = 4.6$ s). Yellow lines indicated the intersecting planes of the displayed orthoslices. (c) Calcium transient $\Delta F/F_0$ time traces calculated over the three-dimensional $100 \times 100 \times 1$ -pixel ROI within hiPSC-CM and adult-CM cells, indicated by the blue and orange rectangles respectively in (b).

The results over a total of $N_{\text{FOV}} = 21$ unique FOV, each containing a different adult-CM, from 3 different samples of two unique co-cultures (A & B) are summarized in **Table 5.4**. For the Day 1 co-culture, 6 out of 10 imaged adult-CM had coupled dynamics with hiPSC-CM. For the Day 2 co-culture samples, the imaged FOVs did not contain any coupled events, however, there were fewer paced and unpaced calcium transients in general, with slower dynamics, indicating that potential environmental factors or reduced sample health were preventing frequent regular transients. Additionally, by day 2 of co-culture, healthy adult-CM were more difficult to identify during sample pre-find with transillumination due to their loss of elongated shape and regular t-tubule structure (compared to freshly isolated day 0 cardiomyocytes), and hence it is possible that the lack of transients from some of the imaged adult-CM from Day 2 samples was due to selection of unwell cells.

Co-culture	Age (days)	Sample	N_{FOV}	Unpaced Transients				Stimulated Transients				Coupled CM
				N_{UnP}	hiPSC-CM	Adult-CM	Coupled Events	N_P	hiPSC-CM	Adult-CM	Coupled Events	
A	2	A _{II}	6	3	2	0	0	5	5	3	0	0
B	1	B _{III}	10	10	4	1	1	10	9	9	6	6
	2	B _{II}	5	5	0	0	0	5	1	1	0	0
Total	Age (days)	1	10	10	4	1	1	10	9	9	6	6
		2	11	8	3	0	0	11	6	1	0	0

Table 5.4 Summary of the 3D LSFM imaging of day 1 and day 2 co-cultures of hiPSC-CM and adult-CM A and B. The number of unique FOVs containing adult-CM imaged within each co-culture sample is indicated by N_{FOV} . N_{UnP} and N_P indicate the number of unpaced and paced acquisitions respectively. The number of acquisitions containing transients in unpaced and paced acquisitions were counted in both hiPSC-CM and adult-CM were counted. the last column indicates how many out of the N_{FOV} for each co-culture sample contained adult-CM that were considered coupled according to the criteria discussed above.

The limited FOV in the y' -direction (perpendicular to the propagation of the light sheet) made location of adult-CM within the co-culture challenging, with many elongated adult-CM from the day 1 sample not being aligned with the long axis of the rectangular FOV. In order to address this limitation, the FOV extent along the x' - direction was doubled for Experiment 4, which is described in the following section. Co-culture duration was limited to days 0-1 to simplify identification of adult-CM and allow more detailed investigation of the early-stage coupling of the two cell types. Finally, to evaluate whether it is the mechanical contraction of hiPSC-CM that drives the coupling of the two cell types, the following experiment investigated samples with and without mechanical decoupling with para-Nitroblebbistatin.

5.3.3 Exp. 4: Influence of co-culture duration and decoupling with NBleb

Experiment 4 (see **Table 5.1** in **Section 5**) investigated the coupling of adult-CM and hiPSC-CM for variable co-culture duration, and presence of the mechanical decoupler para-Nitroblebbistatin (NBleb). A total of two co-cultures (referred to as co-culture *A* and co-culture *B*) of hiPSC-CM and LV myocytes from two unique adult male rats were created on day 34 and day 40 respectively past the start of hiPSC-CM differentiation. For each of the two co-cultures A & B, a total of 4 samples were prepared, each consisting of adult-CM suspended in M199 medium, added drop-wise on top of cultured hiPSC-CM growing on cut plastic coverslips within a larger glass bottom chamber (as described in **Section 5.1**). For both co-cultures, the first two samples were labelled and imaged using 3D LSFM on the same day after ~3-4 hr of co-culture, while the remaining two were imaged the following day, ~24 hours after start of co-culture. Within each pair, the second coverslip sample was prepared and imaged with mechanical decoupling using NBleb, while the first was prepared and imaged without. Additionally, the four samples prepared for co-culture B were imaged on a widefield fluorescence microscope immediately prior to LSFM imaging, in order to assess adult-CM contraction and presence of transients on Day 0 & 1 of co-culture, and with and without NBleb.

Widefield imaging of transients and contraction

Each of the four samples from co-culture B was imaged in two consecutive 40 s, 200 frame acquisitions, first in transillumination mode, then in fluorescence mode, focused on the adult-CM, with the hiPSC-CM layer slightly out-of-focus. The total number of adult-CM (N_{CM}) was counted from the image averaged over all frames from the transillumination acquisition (**Figure 5.9a**). Contracting adult-CM (N_{contr}) were identified from the standard deviation of the transillumination acquisition, divided by the average (**Figure 5.9b**), as those with bright outlines of the cell ends. Adult-CM with transients (N_{Tr}) were identified from the image calculated as the standard deviation of all frames from the fluorescence channel acquisition, divided by the average (**Figure 5.9c**). **Figure 5.9d** demonstrates which cells had transients, contractions or both during the consecutive transillumination and fluorescence acquisitions.

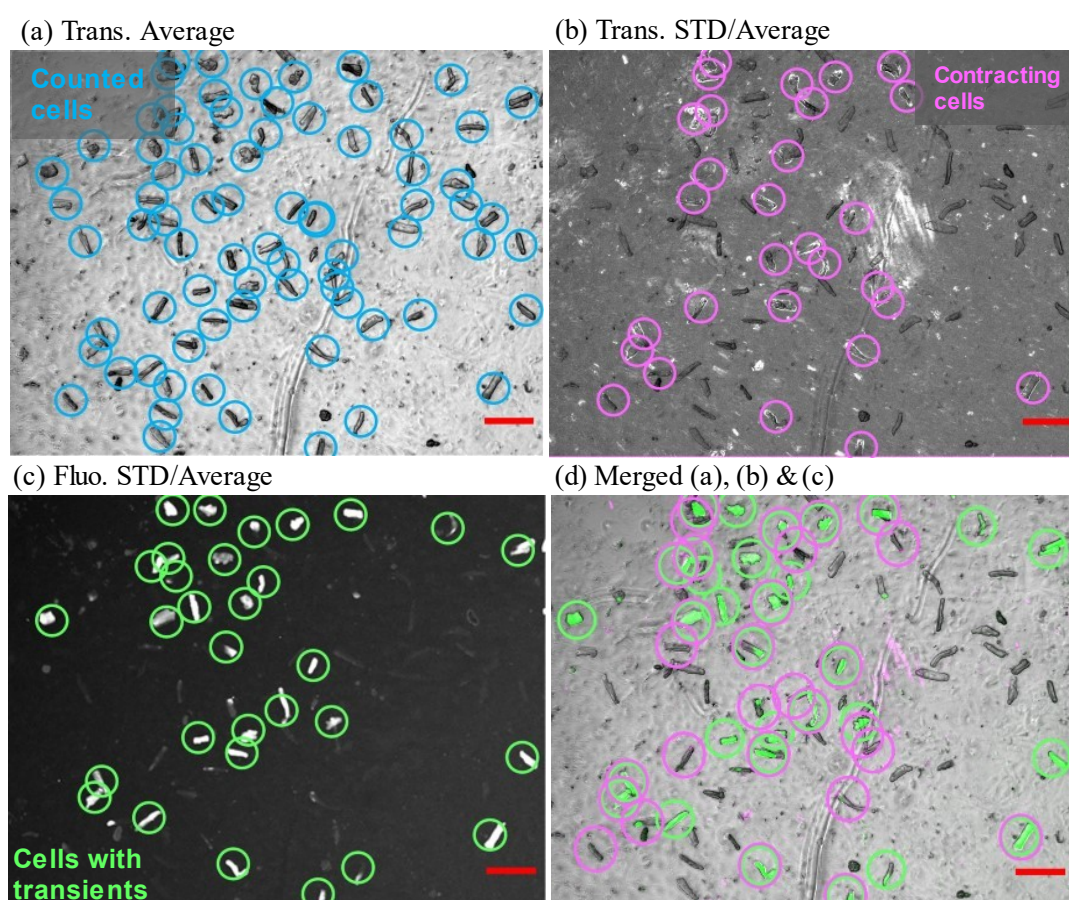


Figure 5.9 Counting adult-CM with transients and contraction from fluorescence and transillumination widefield images of co-culture. Average of 200 frames (40 s duration acquisition at 5 fps) using (a) widefield transillumination and (b) and fluorescence (Fluo-4 channel) microscopy of the same FOV for the day 1 no NBleb sample for co-culture B. Images (c) and (d) represent the average divided by the standard deviation over the whole acquisition for the transillumination and fluorescence channels respectively. The merged images (a), (b) and (c) are shown in (d). All counted adult-CM are encircled in blue in (a), those contracting in purple (b and d) and those with transients in green (c and d). Scalebar: 200 μ m.

The number of cells with contractions, transients for NBleb-treated and control (without NBleb) samples on Day 0 and Day 1 of co-culture are summarized in **Table 5.5**. Samples with NBleb had significantly fewer cells contracting than those not treated with NBleb: 2% compared to 22%

respectively on day 0 ($p = 0.0008$, Chi-squared test), and 6% compared to 39% respectively on day 1 ($p = 0.0007$, Chi-square test). Despite the mechanical decoupling, the samples with NBleb and without NBleb had no significant difference in the fraction of cells with calcium transients: 34% compared to 36% respectively on day 0 ($p = 0.84$ (n/s), Chi-square test) and 38% compared to 41% respectively on day 1 ($p = 0.71$ (n/s), Chi-squared test). This result confirms successful decoupling with NBleb, without any significant impact on transient prevalence.

Co-culture	Age (Days)	Decoupler	N _{CM}	Transillumination		Fluorescence	
				N _{contr}	%	N _{Tr}	%
B	0	—	137	30	22	47	34
		NBleb	53	1	2	19	36
	1	—	75	29	39	31	41
		NBleb	32	2	6	12	38

Table 5.5 Results from widefield transillumination and fluorescence imaging of Day 0 and Day 1 co-culture with and without NBleb. Summary of observations from wide-field transillumination and fluorescence imaging of the hiPSC-CM and adult-CM co-culture B after 4 and 24 hours of co-culture (Day 0 and Day 1) in samples prepared with and without decoupling (“—” and “NBleb” respectively). N_{CM} indicates the counted number of adult-CM within the FOV, while N_{contr} and N_{Tr} indicate how many of these cells contract and have calcium transients respectively, with the percentage indicated in the adjacent column.

Comparing the dynamics over the two days, the fraction of adult-CM with contraction in cells without NBleb was significantly higher for day 1 samples, compared to those imaged on day 0 (39% compared to 22% respectively, $p = 0.0092$, Chi-squared test). For NBleb samples, the increased number of contracting cells by day 1 was not statistically significant ($p = 0.29$, Chi-squared test), however, it is worth noting the small number of contracting cells in samples treated with NBleb. For calcium transients, the increase between day 0 and day 1 was not statistically significant for both control ($p = 0.31$, n/s, Chi-squared test) and NBleb-treated samples ($p = 0.89$, n/s, Chi-squared test). When interpreting the results, particularly the comparison between the two days, it is important to bear in mind that this widefield imaging was done on a small number of samples ($n = 4$), and that all samples were from a co-culture made with adult-CM from the same adult rat.

3D LSMF imaging of coupling events

Next, samples from both co-cultures A & B were imaged with 3D LSMF on day 0 and day 1 of co-culture, with and without NBleb, with twice the FOV along the y'-axis compared to experiment 3, at the cost of a decrease in volume acquisition rate from 8 Hz to 4 Hz due to an upper limit of a maximum frame rate of 199 fps for the readout of 1024 pixels in the vertical direction of the camera sensor. For each of the 8 samples, ≥ 5 FOVs containing unique cardiomyocytes were imaged over two consecutive acquisitions: first without electrical stimulation, and then with electrical pacing at 0.5 Hz. Each time-lapse acquisition was manually visualized as an image stack and through maximum intensity projections

along the detection axis for a full overview of the sample. The optically sectioned 3D data allowed manual selection of ROI within each cell, hence allowing analysis of changes in fluorescence emission within that region, with minimal contribution from out-of-focus fluorescence.

Figure 5.10 shows examples of synchronized dynamics in hiPSC-CM and adult-CM co-culture samples with and without mechanical decoupling. **Figures 5.10a&b** show orthogonal cuts through a volume from 15 s duration acquisitions of adult-CM and hiPSC-CM Day 1 co-culture without NBleb (a) and with NBleb (b), after co-registration, axial rescaling, and rotation into lab coordinates. The corresponding timelapses are displayed in **Videos 5.10a&b**. Three-dimensional $100 \times 100 \times 1$ -voxel ROI within the orthogonal cuts were used to sample the Fluo-4 intensity variation with time within hiPSC-CM and adult-CM. As can be seen from the $\Delta F/F_0$ variation with time for the two ROI in unpaced acquisitions in samples without and with NBleb (**Figure 5.10c&d** respectively), adult-CM and hiPSC-CM undergo synchronized spontaneous transients without external electrical stimulation at periods of $T = 5.5$ s and $T = 5$ s respectively. For the $\Delta F/F_0$ time-traces shown in **Figure 5.10d**, the transient decay slope for adult-CM is visibly steeper than that for hiPSC-CM.

Table 5.6 summarizes the samples prepared and imaged with 3D LSFM. Both unpaced and paced acquisitions for each FOV were manually screened for cell contraction (either by hiPSC-CM or adult-CM), presence of transients in hiPSC-CM and adult-CM, and coupled events between the two cell types. Coupled events were defined as calcium dynamics occurring synchronously in both the adult-CM and at least some of the underlying hiPSC-CM cells. For paced acquisitions, coupled events excluded synchronous transients at the pacing frequency for adult-CM which were not synchronized in the unpaced acquisition, as there is uncertainty as to whether the cells are coupled, or both only responding to the applied stimulation. Adult-CM which had coupled events in either the unpaced or paced acquisition were counted as “Coupled N_{CM} ” (last column).

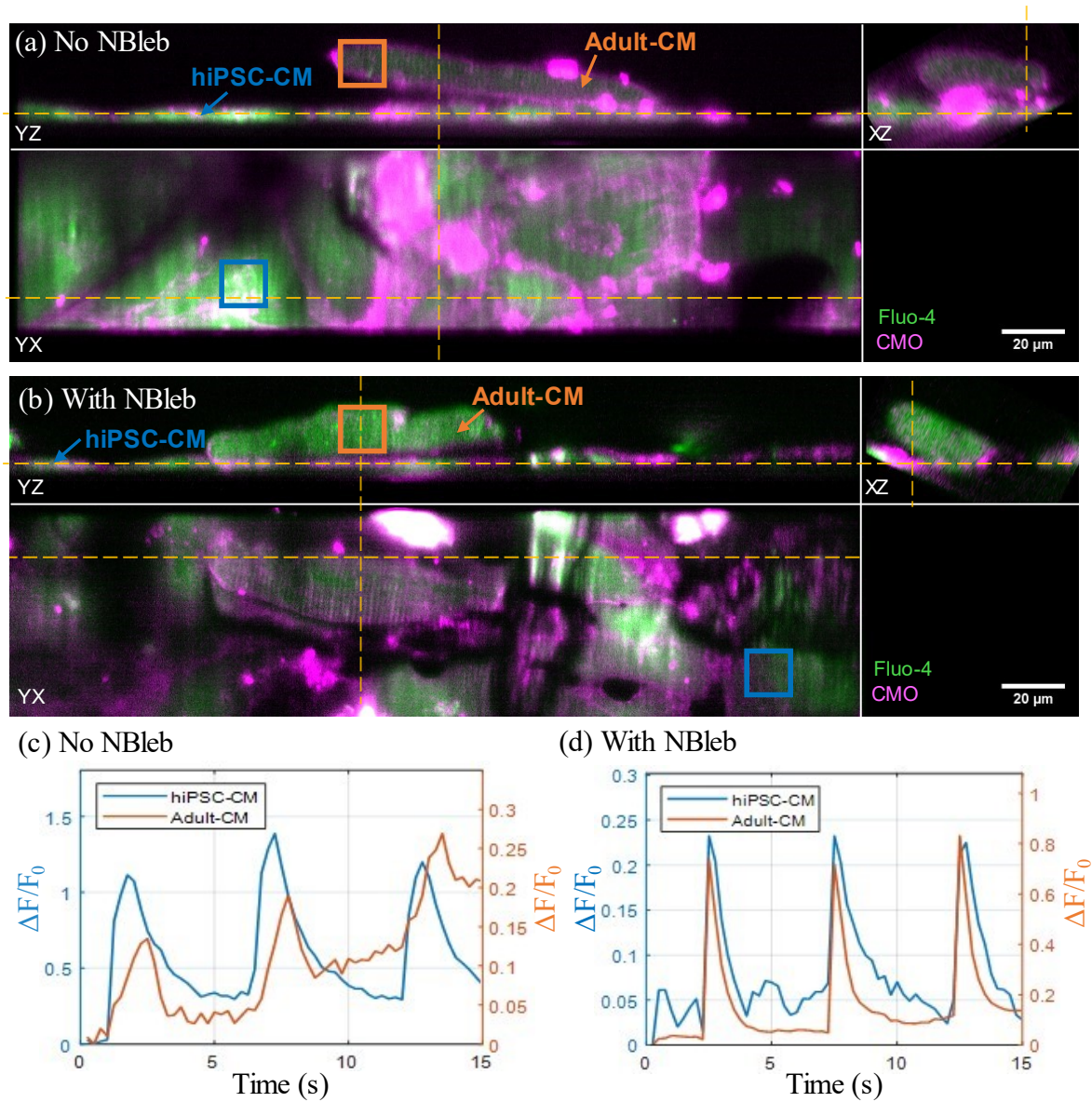


Figure 5.10 Synchronized spontaneous transients in co-culture in samples with and without NBleb. (a-b) Orthogonal cuts through the merged Fluo-4 (green) and CMO (purple) channels of hiPSC-CM and adult-CM co-culture imaged in 3D at 4 vps, 195 fps during unpaced acquisitions for samples (a) without NBleb and (b) with NBleb displayed at the peak of the first spontaneous transient ($t = 2$ s and $t = 2.5$ s for (a) and (b) respectively). The corresponding time-lapses are shown in **Video 5.10a&b**. Yellow lines indicated the intersecting planes of the displayed orthoslices. (c-d) Calcium transient $\Delta F/F_0$ time-traces calculated over the three-dimensional $100 \times 100 \times 1$ -voxel ROI within hiPSC-CM (blue) and adult-CM (orange) as indicated by the orange and blue rectangles respectively in (a) and (b).

Co-culture	Age (days)	Decoupler	N _{FOV}	N _{contr.}	Unpaced N _{Trans}		Paced N _{Trans}		Coupled N _{CM}
					hiPSC-CM	Adult-CM	hiPSC-CM	Adult-CM	
A	0	—	5	5	5	2	4	5	1
		NBleb	5	0	4	1	4	4	1
	1	—	5	2	4	3	3	4	3
		NBleb	6	0	5	4	4	5	4
B	0	—	6	4	1	1	6	6	1
		NBleb	5	0	0	0	4	5	1
	1	—	6	2	4	4	4	5	3
		NBleb	7	1	7	1	6	7	2
Total	Decoupler	—	22	13	14	10	17	20	8
		NBleb	23	1	16	6	18	21	8
	Age (days)	0	21	9	10	4	18	20	4
		1	24	5	20	12	17	21	12
		All	45	14	30	16	35	42	16

Table 5.6 Summary of the 3D LSM imaging of co-culture for Experiment 4. For each of the two co-cultures (referred to as A&B), two samples were imaged on the starting day of co-culture, while the other two were imaged the following day. Decoupling with para-Nitroblebbistatin is indicated by “NBleb”, with “—” indicating no decoupler used. The number of unique FOVs containing adult-CM imaged within each co-culture sample is indicated by N_{FOV}, and N_{contr} indicates how many FOVs with those adult-CM contained cells contracting during the acquisition. The next six columns indicate how many of the N_{CM} contained hiPSC-CM and adult-CM undergoing calcium transients in unpaced vs paced image acquisitions. Finally, the last column indicates how many out of the N_{CM} for each sample are considered coupled according to the criteria discussed above.

Across the two co-cultures, a total N_{CM} = 45 FOVs with unique adult-CM co-cultured with hiPSC-CM were imaged, with each one imaged with and without electrical stimulation. As can be seen from **Table 5.6**, for samples treated with NBleb, only 1 out of 23 (4%) FOVs contained contracting cells, compared to 13 out of 22 FOVs (59%) from samples without NBleb ($p = 0.0001$, Chi-square test), indicating successful decoupling, in agreement with the results from widefield imaging presented in **Table 5.5**. Overall, there was no significant difference in the number of adult-CM with coupled dynamics in samples with and without decoupler: 8 out of 22 FOVs (36%) from samples without NBleb, compared to 8 out of 23 FOVs in samples with NBleb ($p = 0.91$, n/s, Chi-square test), which indicates that the mechanical decoupling did not prevent coupling and synchronization of dynamics in the two cell types. Hence the second hypothesis (**Section 5.1.5**) is rejected.

In line with previous co-culture from Exp. 3, synchronized events were observed in samples co-cultured for only 4 hours, with 4 out of 21 CMs (19%) imaged on the same day that the co-culture was started being classified as coupled. Additionally, in agreement with earlier observations from Exp. 3 on increased coupling between hiPSC-CM and adult-CM with longer co-culture time, coupling improved

after 24 hours of co-culture, with 12 out of the 24 CMs (50%) imaged in samples co-cultured for 24 hours (i.e. day 1) being classified as coupled, significantly higher than the proportion for day 0 ($p = 0.0305$, Chi-square test). Hence the first hypothesis (see **Section 5.1.5**) is confirmed at the level of significance used here ($p < 0.05$).

5.3.4 Exp. 5: Imaging live myocardial slices

High speed 3D LSFM was used to image LV LMS using the same image acquisition settings as for 3D LSFM of hiPSC-CM co-culture, but with modified sample preparation and a different pacing chamber (**Section 5.2**). Electrical pacing at 0.5 Hz was applied and beating observed at the pacing frequency.

Figure 5.11(a-c) demonstrates orthogonal cuts through the (a) Fluo-4 channel, (b) CMO channel and (c) merged channels for a single point in time for an example 3D acquisition imaged at 4 Hz with electrical pacing at a frequency of 0.5 Hz. The orientation of individual cells seen in the XY orthoslice is diagonal, indicating LMS misalignment either during clip attachment to the slice, or sample mounting for imaging. Considering the YZ orthogonal cut through the Fluo-4 and CMO channels in **Figure 5.11a&b**, the CMO YZ-slice has a bright layer at the top surface of the sample, indicating higher level of staining of the cut surface. While there is some CMO staining within the cells, no clear staining of the t-tubules network was observed. The Fluo-4 staining is more homogenous throughout the first cell layer, however, the signal rapidly decays with imaging depth for both channels. One of the cells that appeared to have been bisected during the slicing (located at the intersection of the dashed yellow lines in **Fig 5.11a-c**) had a permanently high Fluo-4 signal. The time-lapse acquisition (**Video 5.11**) reveals regular tissue contraction, indicating unsuccessful decoupling with BDM.

Figure 5.11d shows the time variation in Fluo-4 emission within the two fixed $100 \times 20 \times 1$ -voxel ROI, with synchronized, but opposite variations in intensity. While the dip in $\Delta F/F_0$ (blue trace for ROI 1) every 2 seconds is likely due to a brighter region moving out of the ROI as the tissue contracts, it is unclear whether the synchronized regular peaks in $\Delta F/F_0$ in the orange intensity trace (ROI 2) are a result of localized stimulated calcium transients or a bright region moving into the fixed ROI at every contraction. While weaker calcium transients in LMS compared to other cardiomyocyte preparations have previously been noted (Watson et al., 2020), the low $\Delta F_{\max}/F_0$ is potentially a consequence of sub-optimal LMS health, sample preparation, or environmental control during imaging.

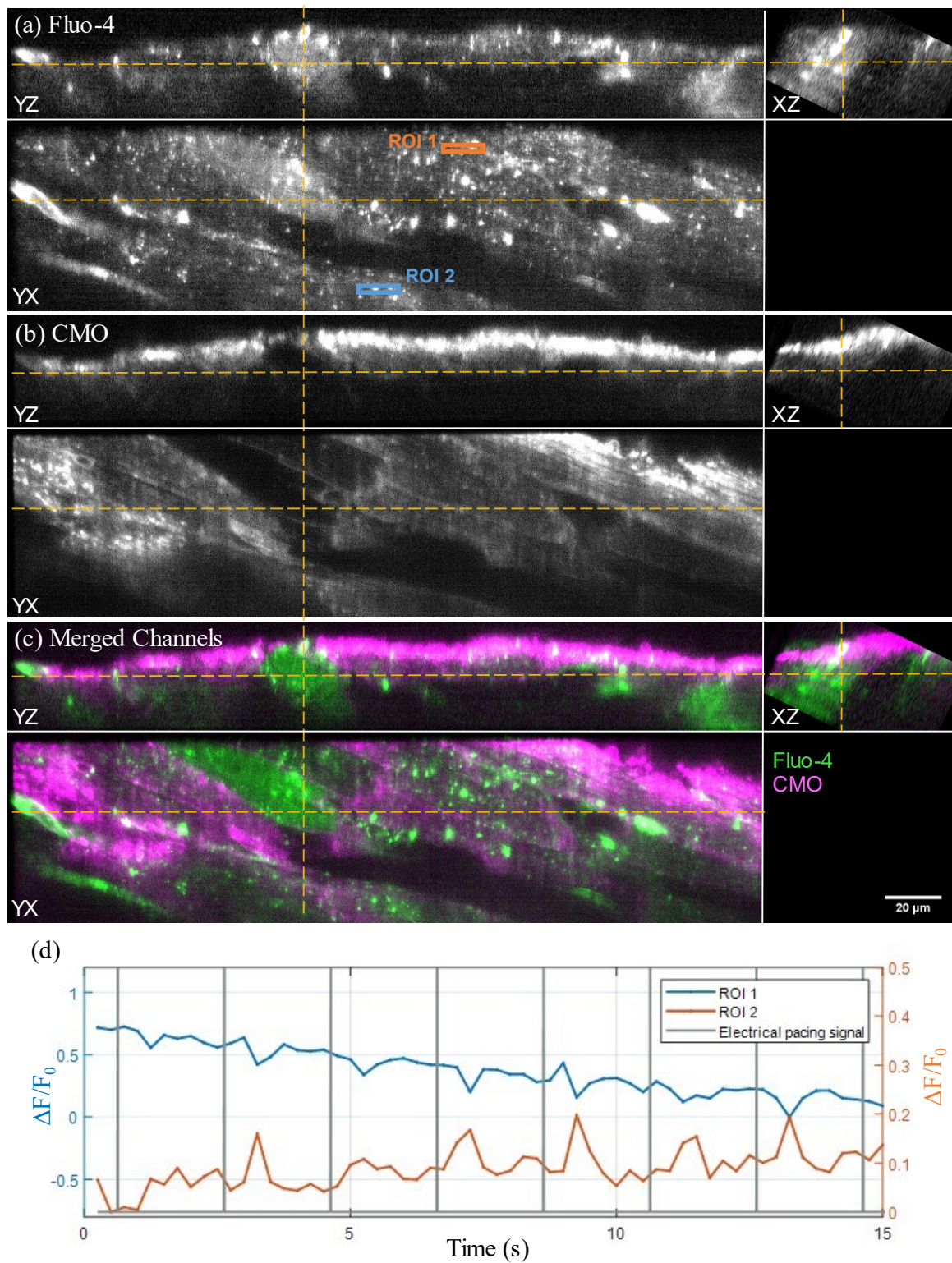


Figure 5.11 Stimulated LMS imaged over time in 3D. Orthogonal cuts through the (a) Fluo-4, (b) CMO and (c) merged channels of LMS imaged in 3D at 4 vps (at 195 fps, 40 planes per volume), with electrical pacing at 0.5 Hz, displayed at the $t = 2.5$ s timepoint of a 15 s acquisition. The yellow lines indicate the intersecting planes of the displayed orthoslices. The time-lapse acquisition is shown in **Video 5.11**. (d) $\Delta F/F_0$ time traces calculated over the three-dimensional $100 \times 20 \times 1$ -voxel ROI (orange and blue rectangles in (a)). As a result of motion artefacts due to LMS contraction, the change in $\Delta F/F_0$ over a fixed region in space cannot be used as a direct indicator of change in calcium concentration.

5.4 Discussion and conclusion

The imaging experiments described in this chapter implemented a custom-designed light-sheet fluorescence microscope for imaging calcium dynamics in hiPSC-CM culture and their co-culture with adult-CM for the first time. The 3D+t optically sectioned data at subcellular resolution and acquisition rates of 4 Hz and 8 Hz allowed analysis of the Ca dynamics within 2D ROI without contamination from out-of-focus fluorescence, hence enabling characterization of synchronized dynamics and coupling between hiPSC-CM and adult-CM, and quantification of the prevalence of coupled events in samples co-cultured for varying duration, with and without mechanical decoupling. Finally, 3D dual-channel LSFM was applied to imaging living myocardial slices.

2D and 3D dual-channel LSFM imaging of hiPSC-CM demonstrated spontaneous and stimulated calcium transients and contractions at electrical pacing periods between $T = 0-6$ s (Exp. 1-2). Larger FOV widefield transillumination and fluorescence imaging and 3D LSFM imaging of hiPSC-CM co-culture with adult-CM from a total of $n = 4$ rats (Exp. 3-4) revealed synchronized contraction and transients as early as 4 hours after start of co-culture, with a higher fraction of coupled adult-CM after 1 day of co-culture than on day 0 (12 out of 24 (50%) vs 4 out of 21 (19%) respectively, $p = 0.0305$).

With longer co-culture times of up to 2 days, the individual adult-CM experienced loss of their elongated shape and defined structure, which will reduce their contractile strength. While viability testing has demonstrated that the morphological alterations (inc. loss of t-tubule structure and rod-like shape, decrease in cell size) and electromechanical (including decrease in systolic shortening and calcium transient amplitude) of CM in culture are a non-apoptotic and non-necrotic adaptation to the culture conditions (Banyasz et al., 2008), the changes in phenotype limit the time that cultured cardiomyocytes can be reliably used as a model. One of the approaches to maintaining the original function and morphology of cardiac myocytes in culture is through continuous electric field stimulation (Berger et al., 1994). The effect of electromechanical stimulation in cardiac tissue environment on preserving structure and function is one of the main drivers for future use of LMS models.

While the presence of mechanical decoupler did inhibit contraction in most cells (with up to 6% of imaged CM contracting, compared to up to 60% in samples without NBleb), it did not prevent synchronized transient dynamics between hiPSC-CM and adult-CM, with no significant difference ($p = 0.91$, n/s) in the number of coupled adult-CM in samples without and with NBleb (8 out of 22 (36%) and 8 out of 23 (35%) respectively). This indicates that electrical coupling between the two cell types occurs without the need for mechanotransduction, suggesting the independence between the two forms of coupling in the heterogenous CM culture. Further investigation of the role of gap junction formation on the coupling of the two cell types can be done with live cell imaging of gap junction puncta, as done by Katoch and others (Katoch et al., 2015), or using gap junction uncouplers such as carbenoxolone (de Groot et al., 2003).

One limitation for the co-culture study was the number of unique animals ($n = 4$) used as a source for the adult-CM to create the biologically distinct co-cultures, due to logistical challenges and time constraints of simultaneous access to both hiPSC-CM and freshly isolated rat ventricle cardiomyocytes. A further limitation was the imaging and analysis throughput. While widefield low-NA imaging enables simultaneous imaging transients and contraction of up to the order of one hundred adult-CM, the lack of optical sectioning introduces contamination from out-of-focus fluorescence. The optical sectioning and high temporal resolution of 3D LSFM enables accurate determination of the spatial origin of the fluorescence in all three dimensions, however the sample size and throughput of the technique is limited by the manual acquisition and minimally automated analysis. The use of time and resources can be optimized by automating parts of the process – particularly sample pre-find and image acquisition.

Imaging LMS with 3D LSFM (Exp. 5) demonstrated only partial success in the trialled sample preparation and imaging protocol: no clear calcium transients were observed, and unsuccessful decoupling with BDM prevented optical mapping of Fluo-4 intensity variation due to motion artefacts from contraction. While time constraints and sample availability prevented direct further optimization of the LMS imaging protocol, it is likely that future experiments would benefit from modified sample preparation. To avoid motion artefacts, NBleb can be trialled for LMS decoupling. Another possible solution is motion tracking or the use of ratiometric dyes. While the stimulated beating of the tissue indicated sample viability during imaging, further experiments would benefit from optimizing the environment control during imaging, particularly by incorporating oxygenation of the immersion medium. In the future, deeper imaging into the sample can be achieved with improved illumination profiles and/or line illumination and 1D confocal slit detection. The experimental system already has the capability to achieve this, but the necessary acquisition software needs to be developed.

The insights and findings from this study are likely to raise further hypotheses about the coupling mechanism and efficiency between hiPSC-CM and adult-CM, and the time-evolution of the co-culture. In future work, the co-culture assay could also be used to test how the synchronization and coupling is influenced by other environmental parameters and drugs. A more realistic representation of the studied system would be achieved through 3D models, however, the preparation and imaging of these larger inhomogenous multi-layered samples comes with further challenges, as demonstrated in this chapter, and hopefully tackled in the future.

It is important to note that, while significant research effort is focused on treatment and management of cardiovascular diseases, the majority (86%) of CVD cases are attributable to modifiable risk factors such as high systolic blood pressure (hypertension) and poor diet. This estimate for coronary heart disease is even higher at 93.5% (British Heart Foundation, 2021), and hence, along with the medically-significant development of regenerative treatment, lifestyle and dietary interventions will remain key to preventing and managing cardiovascular disease.

6 Conclusion

The saying “seeing is believing” is particularly relevant in the context of biomedical imaging technology, where visualizing the underlying dynamics and structures is fundamental to quantification, biological understanding, and ultimately, the development of approaches for targeted treatment and prevention of diseases for an enhanced quality of life. During the last few decades, light-sheet fluorescence microscopy has established itself as one of the key techniques at the forefront of optical microscopy, with its gentle parallelized optically sectioned imaging compatible with the interrogation of dynamics in living cells.

In the multidisciplinary work presented in this thesis, the custom LSFM system was characterized, modified and applied to high-speed imaging of calcium release events in live adult and stem-cell derived cardiomyocytes, as well as live tissue slices, enabling the quantification of millisecond-timescale dynamics in correlation with cell structure, and qualitative characterization of the coupling of native and graft cardiomyocytes in culture.

Principles and operation of remote refocusing LSFM

While a range of approaches for high-speed volumetric imaging exist, aberration-free remote refocusing offers many unique advantages by enabling 3D imaging without sample disturbance and being compatible with high-NA microscopy. In this system, remote refocusing was not only used for detection, but also for the axial scanning of the light-sheet beam waist, to achieve a more uniform axial resolution over a larger FOV.

The high specificity of fluorescence microscopy allows functional imaging of biological structures and dynamics, and the ability to simultaneously image multiple spectral channels is often not only preferable, but also necessary for a more complete interrogation of the relevant processes. The system was modified to incorporate a spectral channel image splitter, with both colour-channels spatially separated on a single detector. Defocus in the Fluo-4 channel was corrected by introducing a pair of doublets with near-equal but opposite focal length.

A key design consideration for the system was acquisition speed: fast imaging at up to 390 fps for a $300 \times 38 \mu\text{m}$ FOV per spectral channel was achieved, enabling volumetric imaging for over a $40 \mu\text{m}$ axial range at up to 8 Hz. Inspired by recent and ongoing developments in the field, a potential system modification was discussed. By incorporating a galvo-scanning unit in real-space or Fourier space of the detection path and utilizing the shear warp transform from computer vision, sheared projections can be used for variable angle viewing of the sample, at acquisition speeds limited by the axial refocusing time, rather than the camera frame rate. Computational simulation was used to demonstrate how this principle can be used for 2D top-down projection viewing of the sample and faster computational rendering of 2D projections at different viewing angles than by using matrix rotation. While logistical

constraints prevented practical implementation within the scope of the project, the minor system modification required to achieve fast variable angle projection viewing may be a useful complementary extension to the system capabilities, improving sample navigation and overview for the microscope user.

Characterization of the spatially varying resolution

Imaging sub-cellular dynamics requires high spatial resolution over a sufficiently large FOV to study the regions of interest. The illumination confinement in LSFM modulates the detection PSF, improving the axial resolution, and introduces optical sectioning. However, increasing light-sheet thickness away from the waist limits the useable FOV. In **Chapter 3**, the system resolution was characterized using computational modelling and experimental PSF measurement. We showed that the spatially-varying resolution can be modelled using an “effective” system PSF that varies only along the illumination axis, and that the resultant axial PSF FWHM is consistent with that modelled using image formation. The light-sheet thickness and propagation lengths for each of the two illumination modes (DSLM and mSPIM) were characterized by modelling the two illumination paths in Zemax, and using the Physical Optics Propagation tool to account for aperture truncation and aberrations. The results demonstrated that the on-axis intensity distributions agree with the theoretical descriptions for a radially symmetric beam and 2D light-sheet.

Experimental PSF measurement was implemented through an automated MATLAB-based image analysis pipeline on bead image data. The analysis used Gaussian fitting of the intensity distribution in each of the three dimensions to estimate the lateral and axial resolution, and the laterally integrated axial intensity to quantify the optical sectioning. These parameters were used to compare the performance at different positions in the FOV, and at positive and negative remote refocus. The results demonstrated that the more tightly focused beam combined with the axial scanning of the waist in the DSLM + ASLM mode provided higher and more uniform resolution across the FOV. For the mSPIM mode, an axial resolution less than 2 μm was maintained over a $\pm 45 \mu\text{m}$ remote refocus range.

Overall, the measured lateral ($\sim 0.5 \mu\text{m}$) and axial resolution ($\sim 1.2 \mu\text{m}$ and $1.6 \mu\text{m}$) for the DSLM + ASLM and mSPIM illumination modes respectively was worse than the expected values, however, the achieved performance was appropriate for resolving the periodic structural features in cardiomyocytes, with sufficient contrast for quantitative image analysis. In the future, modification of the detection path, particularly the separation between the detection objective and the adjacent tube lens should improve the system performance.

High-speed 2D imaging of calcium dynamics in isolated cardiomyocytes

High-speed dual-objective LSFM was used for dual-channel 2D timelapse imaging of calcium dynamics in isolated left and right ventricle rat cardiomyocytes for the first time. A custom sample preparation, imaging protocol and data analysis pipeline was developed for the detection and

quantification of calcium sparks and transients in correlation to the cell's t-tubule microstructure. The fast acquisition rate, spatial resolution and the use of para-Nitroblebbistatin, a non-phototoxic, low-fluorescence decoupler enabled the 2D mapping of electrically stimulated calcium transient development dyssynchrony across the cell.

The novel technique and application resulted in new biological findings. The transient time-to-half-maximum was found to be shorter at the ends of the cell than the central region and longer in the nuclear regions compared to the rest of the cell. Detubulated regions of some cells were observed to have slower transient rise time compared to well-tubulated parts of the cell, however, the observation was not statistically significant across all cells, likely due to the majority of cells being well-tubulated. Most calcium sparks were found to be co-localized with t-tubules. While paired testing indicated that sparks not located on tubules had smaller areas, shorter durations, and less signal mass, the paired cell differences, when averaged for each heart, showed no statistical significance, and further investigation with a larger sample size or more complex statistical models is required for more robust statistical conclusions. Blinded comparison of calcium dynamics in left and right ventricle cardiomyocytes revealed brighter sparks in left ventricle cardiomyocytes, while differences in other quantified parameters were not statistically significant.

While the experiments carried out looked at cardiomyocyte physiology in healthy ventricular cells, in the future, the established imaging and analysis protocols can be extended to cardiomyocytes from diseased samples, as well as other cell types, such as atrial cardiomyocytes.

Volumetric imaging of calcium dynamics in hiPSC-CM and LMS

The remote refocusing LSFM system was applied to high-speed volumetric imaging of calcium dynamics in hiPSC-CM, their co-culture with adult cardiomyocytes, and in live myocardial slices for the first time. The high spatiotemporal resolution enabled visualization and qualitative characterization of electrically stimulated and spontaneous calcium transients. It was discovered that adult-CM and hiPSC-CM undergo synchronized calcium transients and contraction, with and without external electrical stimulation. This coupling began on the same day of the start of co-culture, was enhanced by the second day, and not prevented using motion uncoupler para-Nitroblebbistatin, despite successful inhibition of contraction. While the camera frame rate limited the volumetric imaging speed, in the future, the variable-angle projection method outlined in **Section 2.3** can be used to achieve faster 2D projection imaging with a top-down viewing angle, hence providing sufficient temporal sampling for the quantification of the calcium transient intensity time traces in hiPSC-CM monolayer culture. However, this approach would not be able to separate signal from cells overlapping in x and y.

Future research will be needed to establish and study the mechanism and development of the coupling between the two cell types. To overcome the structural adaptation of isolated adult-CM co-cultured with hiPSC-CM for longer durations, live myocardium slices were considered as a model more closely

resembling the native cardiac tissue environment and architecture. High-speed dual-channel LSFM was applied to volumetric imaging of LMS, enabling partial visualization of the multi-layered structure and contraction upon electrical stimulation, however, motion artefacts from slice movement prevented definitive observation, quantification and mapping of calcium transients. Additionally light scattering by the top layer of cells restricted the imaging depth. Further optimization of the slice imaging protocol is required, particularly by optimizing environmental control during imaging, and employing imaging regimes such as confocal slit detection for improved rejection of scattered light.

Concluding remarks

The remote refocusing LSFM system is a fast and versatile tool that, through the work presented in this thesis, has proven useful for studying both millisecond-timescale processes in single cells, and interactions and dynamics in multicellular culture and tissue. The potential impact of this thesis lies in the bridging of a developing technology with a range of potential imaging applications. The flexible system design enables customized imaging of a range of biological systems, with acquisition settings tailored to the demands of the specimen and experimental objective.

We expect that the sample preparation and imaging protocols developed during the course of this work will be useful and transferable to future experiments. The biological findings enabled by use of the optical system and presented in this thesis have opened new questions and directions for future work, particularly on the correlation between transient development and t-tubules in cardiomyocytes from disease samples, and the exact mechanism and development of coupling between host and graft cells.

In the last decade, a growing trend in biomedical imaging has been the automation of image acquisition and analysis, with the help of machine learning algorithms. Improvement in camera sensor speed and efficiency, the performance of optical and scanning components, the brightness and photostability of novel fluorophores, as well as microscopy community efforts to make the use of advanced microscopes easier and more accessible, indicates that microscope imaging technology will continue to generate impact across multiple disciplines within the biomedical sciences. With optical microscopy facilitating the quantification and understanding of cardiac physiology, the future of cardiovascular health and regeneration is brighter.

7 Research outputs

Publications

Dvinskikh L, Sparks H, Brito L, Harding S, MacLeod K, Dunsby C.

High-speed 2D imaging of calcium dynamics in left and right ventricle cardiomyocytes with light-sheet fluorescence microscopy. Manuscript in preparation for *Frontiers in Physiology* (2022)

Dvinskikh L, Sparks H, Brito L, Harding S, MacLeod K, Dunsby C. *Remote-refocusing light-sheet fluorescence microscopy enables 3D-imaging of hiPSC-CM and adult CM electromechanical coupling in co-culture*. Manuscript in preparation for *Scientific Reports* (2022)

Sparks H, Dvinskikh L, Firth J, Francis A, Harding S, Paterson C, MacLeod K, Dunsby C.

Development of a flexible light-sheet fluorescence microscope for high-speed 3D imaging of calcium dynamics and 3D imaging of cellular microstructure, *Journal of Biophotonics*, Vol 13, Issue 6 (2020)

Conference presentations

Joint BHF Regenerative Medicine UK Centres Symposium, (2021) Online – Oral presentation

Novel light-sheet fluorescence microscopy for imaging adult and pluripotent stem cell cardiomyocyte co-culture

OSA Biophotonics Congress – Optics in the Life Sciences, (2021) Online – Oral presentation

High-speed imaging of calcium dynamics in cardiomyocytes with a flexible light-sheet fluorescence microscope. Conference paper published in *OSA Technical Digest (Optical Society)*, pp NM2C.6

Focus on Microscopy (FoM) (2021) Online - Oral presentation

High-speed imaging of calcium dynamics in cardiomyocytes with a flexible light-sheet fluorescence microscope

Lightsheet Fluorescence Microscopy Conference, (2020) Online – Flash poster presentation

Development and application of a flexible light-sheet fluorescence microscope for high-speed 2D and 3D imaging of calcium dynamics in cardiomyocytes

International OSA Network of Students (IONS), (2019) Barcelona, Spain – Oral presentation

Development and application of a flexible light sheet fluorescence microscope for high-speed 2D and 3D imaging of calcium dynamics in cardiomyocytes.

Focus on Microscopy (FoM), (2019) London, UK – Poster presentation

Quantifying the spatial resolution of an inverted tilted light-sheet fluorescence microscope

8 References

- Abbe, E. (1881) On the estimation of aperture in the microscope. *JR Microsc.Soc.* 1 (3), 388-423.
- Abbe, E. (1873) Beiträge zur Theorie des Mikroskops und der mikroskopischen Wahrnehmung. *Archiv Für Mikroskopische Anatomie.* 9 (1), 413-468.
- Abrahamsson, S., Chen, J., Hajj, B., Stallinga, S., Katsov, A. Y., Wisniewski, J., Mizuguchi, G., Soule, P., Mueller, F. & Darzacq, C. D. (2013) Fast multicolor 3D imaging using aberration-corrected multifocus microscopy. *Nature Methods.* 10 (1), 60-63.
- Agard, D. A. (1984) Optical Sectioning Microscopy: Cellular Architecture in Three Dimensions. *Annual Review of Biophysics and Bioengineering.* 13 (1), 191-219. 10.1146/annurev.bb.13.060184.001203.
- Agard, D. A. & Sedat, J. W. (1983) Three-dimensional architecture of a polytene nucleus. *Nature.* 302 (5910), 676-681. 10.1038/302676a0.
- Airy, G. B. (1835) On the diffraction of an object-glass with circular aperture. *Transactions of the Cambridge Philosophical Society.* 5 283.
- Albert-Smet, I., Marcos-Vidal, A., Vaquero, J. J., Desco, M., Muñoz-Barrutia, A. & Ripoll, J. (2019) Applications of Light-Sheet Microscopy in Microdevices. *Frontiers in Neuroanatomy.* 13 10.3389/fnana.2019.00001.
- Amanfu, R. K., Muller, J. B. & Saucerman, J. J. (2011) Automated image analysis of cardiac myocyte Ca²⁺ dynamics. *2011 Annual International Conference of the IEEE Engineering in Medicine and Biology Society.* , IEEE. pp.4661-4664.
- Amat, F., Höckendorf, B., Wan, Y., Lemon, W. C., McDole, K. & Keller, P. J. (2015) Efficient processing and analysis of large-scale light-sheet microscopy data. *Nature Protocols.* 10 (11), 1679-1696.
- Ambrose, E. J. (1956) A surface contact microscope for the study of cell movements. *Nature.* 178 (4543), 1194.
- Aratyn-Schaus, Y., Pasqualini, F. S., Yuan, H., McCain, M. L., Ye, G. J., Sheehy, S. P., Campbell, P. H. & Parker, K. K. (2016) Coupling primary and stem cell-derived cardiomyocytes in an in vitro model of cardiac cell therapy. *Journal of Cell Biology.* 212 (4), 389-397.
- Axelrod, D. (1981) Cell-substrate contacts illuminated by total internal reflection fluorescence. *The Journal of Cell Biology.* 89 (1), 141-145.
- Banyasz, T., Lozinskiy, I., Payne, C. E., Edelmann, S., Norton, B., Chen, B., Chen-Izu, Y., Izu, L. T. & Balke, C. W. (2008) Transformation of adult rat cardiac myocytes in primary culture. *Experimental Physiology.* 93 (3), 370-382.
- Baumgart, E. & Kubitscheck, U. (2012) Scanned light sheet microscopy with confocal slit detection. *Optics Express.* 20 (19), 21805-21814.
- Beauchamp, P., Jackson, C. B., Ozhatil, L. C., Agarkova, I., Galindo, C. L., Sawyer, D. B., Suter, T. M. & Zuppinger, C. (2020) 3D co-culture of hiPSC-derived cardiomyocytes with cardiac fibroblasts improves tissue-like features of cardiac spheroids. *Frontiers in Molecular Biosciences.* 7 14.
- Becker, J. & Heintzmann, R. (2019) PSF broadening due to fluorescence emission. *bioRxiv.*

- Becker, K., Saghafi, S., Pende, M., Sabdyusheva-Litschauer, I., Hahn, C. M., Foroughipour, M., Jährling, N. & Dodt, H. (2019) Deconvolution of light sheet microscopy recordings. *Scientific Reports*. 9 (1), 1-14.
- Berger, H., Prasad, S. K., Davidoff, A. J., Pimental, D., Ellingsen, O., Marsh, J. D., Smith, T. W. & Kelly, R. A. (1994) Continual electric field stimulation preserves contractile function of adult ventricular myocytes in primary culture. *American Journal of Physiology-Heart and Circulatory Physiology*. 266 (1), H341-H349.
- Bergmann, O., Bhardwaj, R. D., Bernard, S., Zdunek, S., Barnabé-Heider, F., Walsh, S., Zupicich, J., Alkass, K., Buchholz, B. A., Druid, H., Jovinge, S. & Frisén, J. (2009) Evidence for Cardiomyocyte Renewal in Humans. *Science*. 10.1126/science.1164680.
- Bergmann, O., Zdunek, S., Felker, A., Salehpour, M., Alkass, K., Bernard, S., Sjöström, S. L., Szezechowska, M., Jackowska, T. & Dos Remedios, C. (2015) Dynamics of cell generation and turnover in the human heart. *Cell*. 161 (7), 1566-1575.
- Berlin, J. R. (1995) Spatiotemporal changes of Ca²⁺ during electrically evoked contractions in atrial and ventricular cells. *American Journal of Physiology-Heart and Circulatory Physiology*. 269 (3), H1165-H1170.
- Bers, D. M. (2002) Cardiac excitation-contraction coupling. *Nature* 415 (198-205)
- Bers, D. M. (2006) Altered cardiac myocyte Ca regulation in heart failure. *Physiology (Bethesda, Md.)*. 21 380-387. 10.1152/physiol.00019.2006.
- Betzig, E., Patterson, G. H., Sougrat, R., Lindwasser, O. W., Olenych, S., Bonifacino, J. S., Davidson, M. W., Lippincott-Schwartz, J. & Hess, H. F. (2006) Imaging intracellular fluorescent proteins at nanometer resolution. *Science*. 313 (5793), 1642-1645.
- Betzig, E. & Trautman, J. K. (1992) Near-field optics: microscopy, spectroscopy, and surface modification beyond the diffraction limit. *Science*. 257 (5067), 189-195.
- Blanchard, P. M. & Greenaway, A. H. (1999) Simultaneous multiplane imaging with a distorted diffraction grating. *Applied Optics*. 38 (32), 6692-6699.
- Born, M. & Wolf, E. (1980) *Principles of optics: electromagnetic theory of propagation, interference and diffraction of light*. 6th edition. Oxford; New York, Pergamon Press.
- Botcherby, E. J., Juskaitis, R., Booth, M. J. & Wilson, T. (2007) Aberration-free optical refocusing in high numerical aperture microscopy. *Optics Letters*. 32 (14), 2007-2009. 10.1364/OL.32.002007.
- Botcherby, E. J., Booth, M. J., Juškaitis, R. & Wilson, T. (2009) Real-time slit scanning microscopy in the meridional plane. *Optics Letters*. 34 (10), 1504-1506.
- Botcherby, E. J., Juškaitis, R., Booth, M. J. & Wilson, T. (2008) An optical technique for remote focusing in microscopy. *Optics Communications*. 281 (4), 880-887.
- Botcherby, E. J., Smith, C. W., Kohl, M. M., Débarre, D., Booth, M. J., Juškaitis, R., Paulsen, O. & Wilson, T. (2012) Aberration-free three-dimensional multiphoton imaging of neuronal activity at kHz rates. *Proceedings of the National Academy of Sciences*. 109 (8), 2919-2924.
- Bouchard, M. B., Voleti, V., Mendes, C. S., Lacefield, C., Grueber, W. B., Mann, R. S., Bruno, R. M. & Hillman, E. M. (2015) Swept confocally-aligned planar excitation (SCAPE) microscopy for high-speed volumetric imaging of behaving organisms. *Nature Photonics*. 9 (2), 113-119.

- Boukens, B. J., Christoffels, V. M., Coronel, R. & Moorman, A. F. (2009) Developmental basis for electrophysiological heterogeneity in the ventricular and outflow tract myocardium as a substrate for life-threatening ventricular arrhythmias. *Circulation Research*. 104 (1), 19-31.
- Brakenhoff, G. J., Blom, P. & Barends, P. (1979) Confocal scanning light microscopy with high aperture immersion lenses. *Journal of Microscopy*. 117 (2), 219-232.
- Bray, M., Geisse, N. A. & Parker, K. K. (2007) Multidimensional detection and analysis of Ca² sparks in cardiac myocytes. *Biophysical Journal*. 92 (12), 4433-4443.
- Breckwoldt, K., Weinberger, F. & Eschenhagen, T. (2016) Heart regeneration. *Biochimica Et Biophysica Acta (BBA) - Molecular Cell Research*. 1863 (7, Part B), 1749-1759. 10.1016/j.bbamcr.2015.11.010.
- British Heart Foundation, (. (2021) *Heart and Circulatory Disease Statistics 2021*. United Kingdom, British Heart Foundation.
- Brochet, D. X., Xie, W., Yang, D., Cheng, H. & Lederer, W. J. (2011) Quarky calcium release in the heart. *Circulation Research*. 108 (2), 210-218.
- Bromiley, P. (2003) Products and convolutions of Gaussian probability density functions. *Tina-Vision Memo*. 3 (4), 1.
- Broxton, M., Grosenick, L., Yang, S., Cohen, N., Andalman, A., Deisseroth, K. & Levoy, M. (2013) Wave optics theory and 3-D deconvolution for the light field microscope. *Optics Express*. 21 (21), 25418-25439.
- Chakraborty, T., Driscoll, M. K., Jeffery, E., Murphy, M. M., Roudot, P., Chang, B., Vora, S., Wong, W. M., Nielson, C. D., Zhang, H., Zhemkov, V., Hiremath, C., De La Cruz, Estanislao Daniel, Yi, Y., Bezprozvanny, I., Zhao, H., Tomer, R., Heintzmann, R., Meeks, J. P., Marciano, D. K., Morrison, S. J., Danuser, G., Dean, K. M. & Fiolka, R. (2019) Light-sheet microscopy of cleared tissues with isotropic, subcellular resolution. *Nature Methods*. 16 (11), 1109-1113. 10.1038/s41592-019-0615-4.
- Chandler, W. K., Hollingworth, S. & Baylor, S. M. (2003) Simulation of calcium sparks in cut skeletal muscle fibers of the frog. *The Journal of General Physiology*. 121 (4), 311-324.
- Chang, B., Manton, J. D., Sapoznik, E., Pohlkamp, T., Terrones, T. S., Welf, E. S., Murali, V. S., Roudot, P., Hake, K. & Whitehead, L. (2021) Real-time multi-angle projection imaging of biological dynamics. *Nature Methods*. 18 (7), 829-834.
- Chen, Y., Chen, M., Zhu, L., Wu, J. Y., Du, S. & Li, Y. (2018) Measure and model a 3-D space-variant PSF for fluorescence microscopy image deblurring. *Optics Express*. 26 (11), 14375-14391.
- Cheng, H., Lederer, W. J. & Cannell, M. B. (1993) Calcium sparks: elementary events underlying excitation-contraction coupling in heart muscle. *Science*. 262 (5134), 740-744.
<https://science.sciencemag.org/content/262/5134/740>.
- Cheng, H. & Lederer, W. J. (2008) Calcium Sparks. *Physiological Reviews*. 88 (4), 1491-1545. 10.1152/physrev.00030.2007.
- Cheng, H., Song, L., Shirokova, N., González, A., Lakatta, E. G., Ríos, E. & Stern, M. D. (1999) Amplitude Distribution of Calcium Sparks in Confocal Images: Theory and Studies with an Automatic Detection Method. *Biophysical Journal*. 76 (2), 606-617. 10.1016/S0006-3495(99)77229-2.
- Chesler, N. C., Roldan, A., Vanderpool, R. R. & Naeije, R. (2009) How to measure pulmonary vascular and right ventricular function. *2009 Annual International Conference of the IEEE Engineering in Medicine and Biology Society*. , IEEE. pp.177-180.

- Choi, C. H. J., Alabi, C. A., Webster, P. & Davis, M. E. (2010) Mechanism of active targeting in solid tumors with transferrin-containing gold nanoparticles. *Proceedings of the National Academy of Sciences of the United States of America*. 107 (3), 1235-1240. 10.1073/pnas.0914140107.
- Chong, J. J. H., Yang, X., Don, C. W., Minami, E., Liu, Y., Weyers, J. J., Mahoney, W. M., Van Biber, B., Cook, S. M., Palpant, N. J., Gantz, J. A., Fugate, J. A., Muskheli, V., Gough, G. M., Vogel, K. W., Astley, C. A., Hotchkiss, C. E., Baldessari, A., Pabon, L., Reinecke, H., Gill, E. A., Nelson, V., Kiem, H., Laflamme, M. A. & Murry, C. E. (2014) Human embryonic-stem-cell-derived cardiomyocytes regenerate non-human primate hearts. *Nature*. 510 (7504), 273-277. 10.1038/nature13233.
- Chong, J. J. H. & Murry, C. E. (2014) Cardiac regeneration using pluripotent stem cells—Progression to large animal models. *Stem Cell Research*. 13 (3, Part B), 654-665. 10.1016/j.scr.2014.06.005.
- Chow, A., Stuckey, D. J., Kidher, E., Rocco, M., Jabbour, R. J., Mansfield, C. A., Darzi, A., Harding, S. E., Stevens, M. M. & Athanasiou, T. (2017) Human Induced Pluripotent Stem Cell-Derived Cardiomyocyte Encapsulating Bioactive Hydrogels Improve Rat Heart Function Post Myocardial Infarction. *Stem Cell Reports*. 9 (5), 1415-1422. 10.1016/j.stemcr.2017.09.003.
- Chroma. (2021a) *ET525/50m*. <https://www.chroma.com/products/parts/et525-50m> [Accessed Mar 1, 2022].
- Chroma. (2021b) *ET630/75m*. <https://www.chroma.com/products/parts/et630-75m> [Accessed Mar 1, 2022].
- Chu, A. J., Zhao, E. J., Chiao, M. & Lim, C. J. (2020) Co-culture of induced pluripotent stem cells with cardiomyocytes is sufficient to promote their differentiation into cardiomyocytes. *PloS One*. 15 (4), e0230966.
- Chu, J., Wang, Q. (., Lehan, J. P., Griesmann, U. & Gao, G. (2008) Measuring the Phase Transfer Function of a Phase-Shifting Interferometer. 7064 70640C-8. <https://www.nist.gov/publications/measuring-phase-transfer-function-phase-shifting-interferometer>.
- Cleemann, L., Wang, W. & Morad, M. (1998) Two-dimensional confocal images of organization, density, and gating of focal Ca² release sites in rat cardiac myocytes. *Proceedings of the National Academy of Sciences*. 95 (18), 10984-10989.
- Cole, R. W., Jinadasa, T. & Brown, C. M. (2011) Measuring and interpreting point spread functions to determine confocal microscope resolution and ensure quality control. *Nature Protocols*. 6 (12), 1929-1941. 10.1038/nprot.2011.407.
- Conchello, J. & Lichtman, J. W. (2005) Optical sectioning microscopy. *Nature Methods*. 2 (12), 920-931.
- Corbett, A. (2021) *PyCalibrate*. <https://www.psfcheck.com/psfcheck-processing> [Accessed Mar 11, 2022].
- Corbett, A. D., Shaw, M., Yacoot, A., Jefferson, A., Schermelleh, L., Wilson, T., Booth, M. & Salter, P. S. (2018) Microscope calibration using laser written fluorescence. *Optics Express*. 26 (17), 21887-21899.
- Costa, E. C., Silva, D. N., Moreira, A. F. & Correia, I. J. (2019) Optical clearing methods: An overview of the techniques used for the imaging of 3D spheroids. *Biotechnology and Bioengineering*. 116 (10), 2742-2763. 10.1002/bit.27105.
- Costantini, I., Cicchi, R., Silvestri, L., Vanzi, F. & Pavone, F. S. (2019) In-vivo and ex-vivo optical clearing methods for biological tissues. *Biomedical Optics Express*. 10 (10), 5251-5267.

- Courty, S., Bouzigues, C., Luccardini, C., Ehrensperger, M., Bonneau, S. & Dahan, M. (2006) Tracking individual proteins in living cells using single quantum dot imaging. In: Anonymous *Methods in enzymology*. , Elsevier. pp. 211-228.
- D'Agostino, R. & Pearson, E. S. (1973) Tests for departure from normality. Empirical results for the distributions of b^2 and \sqrt{b} . *Biometrika*. 60 (3), 613-622.
- Dal Maschio, M., De Stasi, A. M., Benfenati, F. & Fellin, T. (2011) Three-dimensional in vivo scanning microscopy with inertia-free focus control. *Optics Letters*. 36 (17), 3503-3505.
- Davidovits, P. & Egger, M. D. (1969) Scanning laser microscope. *Nature*. 223 (5208), 831.
- de Groot, J. R., Veenstra, T., Verkerk, A. O., Wilders, R., Smits, J. P. P., Wilms-Schopman, F. J. G., Wiegerinck, R. F., Bourier, J., Belterman, C. N. W., Coronel, R. & Verheijck, E. E. (2003) Conduction slowing by the gap junctional uncoupler carbenoxolone. *Cardiovascular Research*. 60 (2), 288-297. 10.1016/j.cardiores.2003.07.004.
- Dean, K. M. & Fiolka, R. (2014) Uniform and scalable light-sheets generated by extended focusing. *Optics Express*. 22 (21), 26141-26152.
- Dean, K. M., Roudot, P., Welf, E. S., Danuser, G. & Fiolka, R. (2015) Deconvolution-free subcellular imaging with axially swept light sheet microscopy. *Biophysical Journal*. 108 (12), 2807-2815.
- Demchenko, A. P. (2020) Photobleaching of organic fluorophores: quantitative characterization, mechanisms, protection. *Methods and Applications in Fluorescence*. 8 (2), 022001. 10.1088/2050-6120/ab7365.
- Digman, M. A., Caiolfa, V. R., Zama, M. & Gratton, E. (2008) The phasor approach to fluorescence lifetime imaging analysis. *Biophysical Journal*. 94 (2), L14-L16.
- Dong, C., Koenig, K. & So, P. T. (2003) Characterizing point spread functions of two-photon fluorescence microscopy in turbid medium. *Journal of Biomedical Optics*. 8 (3), 450-459.
- Dries, E., Bardi, I., Nunez-Toldra, R., Meijlink, B. & Terracciano, C. M. (2021) CaMKII inhibition reduces arrhythmogenic Ca²⁺ events in subendocardial cryoinjured rat living myocardial slices. *Journal of General Physiology*. 153 (6), .
- Dries, E., Bito, V., Lenaerts, I., Antoons, G., Sipido, K. R. & Macquaide, N. (2013) Selective modulation of coupled ryanodine receptors during microdomain activation of calcium/calmodulin-dependent kinase II in the dyadic cleft. *Circulation Research*. 113 (11), 1242-1252.
- Du, D. T., Hellen, N., Kane, C. & Terracciano, C. M. (2015) Action potential morphology of human induced pluripotent stem cell-derived cardiomyocytes does not predict cardiac chamber specificity and is dependent on cell density. *Biophysical Journal*. 108 (1), 1-4.
- Du, S., Zhao, T. & Zhao, L. (2019) Light sheets with extended length. *Optics Communications*. 450 166-171.
- Dunsby, C. (2008) Optically sectioned imaging by oblique plane microscopy. *Optics Express*. 16 (25), 20306. 10.1364/OE.16.020306.
- Duocastella, M., Sancataldo, G., Saggau, P., Ramoino, P., Bianchini, P. & Diaspro, A. (2017) Fast inertia-free volumetric light-sheet microscope. *ACS Photonics*. 4 (7), 1797-1804.

- Dürig, U., Pohl, D. W. & Rohner, F. (1986) Near-field optical-scanning microscopy. *Journal of Applied Physics*. 59 (10), 3318-3327.
- Dvinskikh, L. (2022) Cardiomyocyte timelapse videos. Zenodo. <https://doi.org/10.5281/zenodo.6917163>
- Egger, M. D. & Petrán, M. (1967) New reflected-light microscope for viewing unstained brain and ganglion cells. *Science*. 157 (3786), 305-307.
- Engelbrecht, C. J. & Stelzer, E. H. (2006) Resolution enhancement in a light-sheet-based microscope (SPIM). *Optics Letters*. 31 (10), 1477-1479. 10.1364/OL.31.001477.
- Eschenhagen, T., Bolli, R., Braun, T., Field, L. J., Fleischmann, B. K., Frisé, J., Giacca, M., Hare, J. M., Houser, S., Lee, R. T., Marbán, E., Martin, J. F., Molkentin, J. D., Murry, C. E., Riley, P. R., Ruiz-Lozano, P., Sadek, H. A., Sussman, M. A. & Hill, J. A. (2017) Cardiomyocyte Regeneration. *Circulation*. 136 (7), 680-686. 10.1161/CIRCULATIONAHA.117.029343.
- Ettinger, A. & Wittmann, T. (2014) Chapter 5 - Fluorescence live cell imaging. In: Waters, J. C. & Wittman, T. (eds.). *Methods in Cell Biology*. , Academic Press. pp. 77-94. <https://www.sciencedirect.com/science/article/pii/B9780124201385000057>.
- Ewald, P. P. (1969) Introduction to the dynamical theory of X-ray diffraction. *Acta Crystallographica Section A: Crystal Physics, Diffraction, Theoretical and General Crystallography*. 25 (1), 103-108.
- Fabiato, A. (1983) Calcium-induced release of calcium from the cardiac sarcoplasmic reticulum. *The American Journal of Physiology*. 245 (1), 1.
- Fabiato, A. & Fabiato, F. (1979) Use of chlorotetracycline fluorescence to demonstrate Ca²⁺-induced release of Ca²⁺ from the sarcoplasmic reticulum of skinned cardiac cells. *Nature (London)*. 281 (5727), 146-148. 10.1038/281146a0.
- Fahrbach, F. O. & Rohrbach, A. (2010) A line scanned light-sheet microscope with phase shaped self-reconstructing beams. *Optics Express*. 18 (23), 24229-24244.
- Fahrbach, F. O., Voigt, F. F., Schmid, B., Helmchen, F. & Huisken, J. (2013) Rapid 3D light-sheet microscopy with a tunable lens. *Optics Express*. 21 (18), 21010-21026. 10.1364/OE.21.021010.
- Favro, L. D., Thomas, R. L., Kuo, P. & Chen, L. (1992) *Confocal microscope*. 5,162,941 (Patent).
- Feffer, S. M. (1996) ernst Abbe, Carl Zeiss, and the transformation of microscopical optics. In: Anonymous *Scientific Credibility and Technical Standards in 19th and early 20th century Germany and Britain*. , Springer. pp. 23-66.
- Fiolka, R., Stemmer, A. & Belyaev, Y. (2007) Virtual slit scanning microscopy. *Histochemistry and Cell Biology*. 128 (6), 499-505.
- Fish, K. N. (2009) Total internal reflection fluorescence (TIRF) microscopy. *Current Protocols in Cytometry*. 50 (1), 12.18. 1-12.18. 13.
- Fisher, S. A., Brunskill, S. J., Doree, C., Mathur, A., Taggart, D. P. & Martin-Rendon, E. (2014) Stem cell therapy for chronic ischaemic heart disease and congestive heart failure. *Cochrane Database of Systematic Reviews*. (4), 10.1002/14651858.CD007888.pub2.
- Fisher, S. A., Doree, C., Mathur, A. & Martin-Rendon, E. (2015) Meta-Analysis of Cell Therapy Trials for Patients With Heart Failure. *Circulation Research*. 116 (8), 1361-1377. 10.1161/CIRCRESAHA.116.304386.

- Gao, L. (2015) Extend the field of view of selective plan illumination microscopy by tiling the excitation light sheet. *Optics Express*. 23 (5), 6102-6111.
- Garrett, W. K. C. & Kaiser, W. (1961) Two-photon excitation in CaF₂: Eu²⁺. *Phys.Rev.Lett.* 7 229-231.
- Gaskill, J. D. (1978) *Linear systems, Fourier transforms, and optics*. Wiley.
- Gee, K. R., Brown, K. A., Chen, W. U., Bishop-Stewart, J., Gray, D. & Johnson, I. (2000) Chemical and physiological characterization of fluo-4 Ca²⁺ -indicator dyes. *Cell Calcium*. 27 (2), 97-106.
- Germanguz, I., Sedan, O., Zeevi-Levin, N., Shtrichman, R., Barak, E., Ziskind, A., Eliyahu, S., Meiry, G., Amit, M. & Itskovitz-Eldor, J. (2011) Molecular characterization and functional properties of cardiomyocytes derived from human inducible pluripotent stem cells. *Journal of Cellular and Molecular Medicine*. 15 (1), 38-51.
- Gherghiceanu, M., Barad, L., Novak, A., Reiter, I., Itskovitz-Eldor, J., Binah, O. & Popescu, L. (2011) Cardiomyocytes derived from human embryonic and induced pluripotent stem cells: comparative ultrastructure. *Journal of Cellular and Molecular Medicine*. 15 (11), 2539-2551.
- Gibson, S. F. & Lanni, F. (1991) Experimental test of an analytical model of aberration in an oil-immersion objective lens used in three-dimensional light microscopy. *Josa A*. 8 (10), 1601-1613.
- Gintoli, M., Mohanan, S., Salter, P., Williams, E., Beard, J. D., Jekely, G. & Corbett, A. D. (2020) Spinning disk-remote focusing microscopy. *Biomedical Optics Express*. 11 (6), 2874-2888.
- Göppert-Mayer, M. (1931) Über elementarakte mit zwei quantensprüngen. *Annalen Der Physik*. 401 (3), 273-294.
- Guo, A. & Song, L. (2014) AutoTT: Automated Detection and Analysis of T-Tubule Architecture in Cardiomyocytes. *Biophysical Journal*. 106 (12), 2729-2736. 10.1016/j.bpj.2014.05.013.
- Gustafsson, M. G. (2005) Nonlinear structured-illumination microscopy: wide-field fluorescence imaging with theoretically unlimited resolution. *Proceedings of the National Academy of Sciences*. 102 (37), 13081-13086.
- Gustafsson, M. G. (2000) Surpassing the lateral resolution limit by a factor of two using structured illumination microscopy. *Journal of Microscopy*. 198 (2), 82-87.
- Gustafsson, M. G., Agard, D. A. & Sedat, J. W. (1999) I5M: 3D widefield light microscopy with better than 100nm axial resolution. *Journal of Microscopy*. 195 (1), 10-16.
- Hamamatsu Photonics. (2019) ORCA-Fusion Digital CMOS Camera C14440-20UP/C14440-20UP01 Instruction manual. Ver 1.3 https://www.hamamatsu.com/content/dam/hamamatsu-photonics/sites/static/sys/en/manual/C14440-20UP_IM_En.pdf
- Hammer, K. P., Hohendanner, F., Blatter, L. A., Pieske, B. M. & Heinzel, F. R. (2015) Variations in local calcium signaling in adjacent cardiac myocytes of the intact mouse heart detected with two-dimensional confocal microscopy. *Frontiers in Physiology*. 5 10.3389/fphys.2014.00517.
- Hanley, Q. S., Verveer, P. J., Gemkow, M. J., Arndt-Jovin, D. & Jovin, T. M. (1999) An optical sectioning programmable array microscope implemented with a digital micromirror device. *Journal of Microscopy*. 196 (Pt 3), 317-331.
- Hecht, E. (2002) *Optics*. 4th edition. Addison-Wesley.

- Heidbreder, M., Endesfelder, U., van de Linde, S., Hennig, S., Widera, D., Kaltschmidt, B., Kaltschmidt, C. & Heilemann, M. (2010) Subdiffraction fluorescence imaging of biomolecular structure and distributions with quantum dots. *Biochimica Et Biophysica Acta (BBA)-Molecular Cell Research*. 1803 (10), 1224-1229.
- Heintzmann, R. (2007) Estimating missing information by maximum likelihood deconvolution. *Micron*. 38 (2), 136-144.
- Heintzmann, R. & Cremer, C. G. (1999) Laterally modulated excitation microscopy: improvement of resolution by using a diffraction grating. *Optical biopsies and microscopic techniques III.*, SPIE. pp.185-196.
- Heintzmann, R., Jovin, T. M. & Cremer, C. (2002) Saturated patterned excitation microscopy—a concept for optical resolution improvement. *Josa A*. 19 (8), 1599-1609. 10.1364/JOSAA.19.001599.
- Heinzel, F. R., MacQuaide, N., Biesmans, L. & Sipido, K. (2011) Dyssynchrony of Ca²⁺ release from the sarcoplasmic reticulum as subcellular mechanism of cardiac contractile dysfunction. *Journal of Molecular and Cellular Cardiology*. 50 (3), 390-400.
- Hell, S. (1990) *Abbildung transparenter Mikrostrukturen im konfokalen Mikroskop*. Heidelberg University.
- Hell, S. W. & Wichmann, J. (1994) Breaking the diffraction resolution limit by stimulated emission: stimulated-emission-depletion fluorescence microscopy. *Optics Letters*. 19 (11), 780-782.
- Hell, S. & Stelzer, E. H. K. (1992a) Properties of a 4Pi confocal fluorescence microscope. *Josa A*. 9 (12), 2159-2166. 10.1364/JOSAA.9.002159.
- Hell, S. & Stelzer, E. H. (1992b) Fundamental improvement of resolution with a 4Pi-confocal fluorescence microscope using two-photon excitation. *Optics Communications*. 93 (5-6), 277-282.
- Helmchen, F. & Denk, W. (2005) Deep tissue two-photon microscopy. *Nature Methods*. 2 (12), 932-940.
- Herron, T. J., Lee, P. & Jalife, J. (2012) Optical Imaging of Voltage and Calcium in Cardiac Cells & Tissues. *Circulation Research*. 110 (4), 609-623. 10.1161/CIRCRESAHA.111.247494.
- Hoffmann, M. & Judkewitz, B. (2019) Diffractive oblique plane microscopy. *Optica*. 6 (9), 1166-1170.
- Hollingworth, S., Peet, J., Chandler, W. K. & Baylor, S. M. (2001) Calcium sparks in intact skeletal muscle fibers of the frog. *The Journal of General Physiology*. 118 (6), 653-678.
- Hooke, R. (1665) *Micrographia: or some physiological descriptions of minute bodies made by magnifying glasses, with observations and inquiries thereupon*. Great Britain, The Royal Society.
- Huisken, J. & Stainier, D. Y. R. (2007) Even fluorescence excitation by multidirectional selective plane illumination microscopy (mSPIM). *Optics Letters*. 32 (17), 2608-2610. 10.1364/OL.32.002608.
- Huisken, J., Swoger, J., Del Bene, F., Wittbrodt, J. & Stelzer, E. H. (2004) Optical Sectioning Deep Inside Live Embryos by Selective Plane Illumination Microscopy. *Science*. 305 (5686), 1007-1009.
- Hurley, M. E., Sheard, T. M., Norman, R., Kirton, H. M., Shah, S. S., Pervolaraki, E., Yang, Z., Gamper, N., White, E. & Steele, D. (2021) A correlative super-resolution protocol to visualise structural underpinnings of fast second-messenger signalling in primary cell types. *Methods*. 193 27-37.

- Hüser, J., Lipsius, S. L. & Blatter, L. A. (1996) Calcium gradients during excitation-contraction coupling in cat atrial myocytes. *The Journal of Physiology*. 494 (3), 641-651.
- Hwang, H. S., Kryshnal, D. O., Feaster, T. K., Sánchez-Freire, V., Zhang, J., Kamp, T. J., Hong, C. C., Wu, J. C. & Knollmann, B. C. (2015) Comparable calcium handling of human iPSC-derived cardiomyocytes generated by multiple laboratories. *Journal of Molecular and Cellular Cardiology*. 85 79-88.
- Ibrahim, M., Gorelik, J., Yacoub, M. H. & Terracciano, C. M. (2011) The structure and function of cardiac t-tubules in health and disease. *Proceedings of the Royal Society B: Biological Sciences*. 278 (1719), 2714-2723.
- Icha, J., Weber, M., Waters, J. C. & Norden, C. (2017) Phototoxicity in live fluorescence microscopy, and how to avoid it. *BioEssays*. 39 (8), 1700003. 10.1002/bies.201700003.
- Illaste, A., Wullschlegel, M., Fernandez-Tenorio, M., Niggli, E. & Egger, M. (2019) Automatic detection and classification of Ca² release events in line-and frame-scan images. *Biophysical Journal*. 116 (3), 383-394.
- Im, K., Han, S., Park, H., Kim, D. & Kim, B. (2005) Simple high-speed confocal line-scanning microscope. *Optics Express*. 13 (13), 5151-5156.
- Iribe, G., Ward, C. W., Camelliti, P., Bollensdorff, C., Mason, F., Burton, R. A., Garny, A., Morpew, M. K., Hoenger, A. & Lederer, W. J. (2009) Axial stretch of rat single ventricular cardiomyocytes causes an acute and transient increase in Ca² spark rate. *Circulation Research*. 104 (6), 787-795.
- Itzhaki, I., Rapoport, S., Huber, I., Mizrahi, I., Zwi-Dantsis, L., Arbel, G., Schiller, J. & Gepstein, L. (2011) Calcium Handling in Human Induced Pluripotent Stem Cell Derived Cardiomyocytes. *Plos One*. 6 (4), e18037. 10.1371/journal.pone.0018037.
- Jabbour, R. J., Owen, T. J., Pandey, P., Reinsch, M., Wang, B., King, O., Couch, L. S., Pantou, D., Pitcher, D. S. & Chowdhury, R. A. (2021) In vivo grafting of large engineered heart tissue patches for cardiac repair. *JCI Insight*. 6 (15), .
- Jabłoński, A. (1935) Über den mechanismus der photolumineszenz von farbstoffphosphoren. *Zeitschrift Für Physik*. 94 (1), 38-46.
- Jaimes, R., Walton, R. D., Pasdois, P., Bernus, O., Efimov, I. R. & Kay, M. W. (2016) A technical review of optical mapping of intracellular calcium within myocardial tissue. *American Journal of Physiology-Heart and Circulatory Physiology*. 310 (11), H1388-H1401. 10.1152/ajpheart.00665.2015.
- Jemielita, M., Taormina, M. J., DeLaurier, A., Kimmel, C. B. & Parthasarathy, R. (2013) Comparing phototoxicity during the development of a zebrafish craniofacial bone using confocal and light sheet fluorescence microscopy techniques. *Journal of Biophotonics*. 6 (11-12), 920-928. 10.1002/jbio.201200144.
- Jeon, Y. K., Jang, J. H., Youm, J. B., Zhang, Y. H. & Kim, S. J. (2019) Difference in Calcium Sensitivity Between Right and Left Ventricles With Lower Expression of Calcium Binding Proteins in Right Ventricular Myocytes. *Circulation Research*. 125 (Suppl_1), A191.
- Jin, R., Yu, Y., Shen, D., Luo, Q., Gong, H. & Yuan, J. (2021) Flexible, video-rate, and aberration-compensated axial dual-line scanning imaging with field-of-view jointing and stepped remote focusing. *Photonics Research*. 9 (8), 1477-1485.

- Jones, J. S., Small, D. M. & Nishimura, N. (2018) In Vivo Calcium Imaging of Cardiomyocytes in the Beating Mouse Heart With Multiphoton Microscopy. *Frontiers in Physiology*. 9 10.3389/fphys.2018.00969.
- Jungmann, R., Avendaño, M. S., Woehrstein, J. B., Dai, M., Shih, W. M. & Yin, P. (2014) Multiplexed 3D cellular super-resolution imaging with DNA-PAINT and Exchange-PAINT. *Nature Methods*. 11 (3), 313-318.
- Kane, C., Couch, L. & Terracciano, C. M. N. (2015) Excitation–contraction coupling of human induced pluripotent stem cell-derived cardiomyocytes. *Frontiers in Cell and Developmental Biology*. 3 10.3389/fcell.2015.00059.
- Kaneko, T., Tanaka, H., Oyamada, M., Kawata, S. & Takamatsu, T. (2000) Three distinct types of Ca(2+) waves in Langendorff-perfused rat heart revealed by real-time confocal microscopy. *Circulation Research*. 86 (10), 1093-1099.
- Kang, S., Duocastella, M. & Arnold, C. B. (2020) Variable optical elements for fast focus control. *Nature Photonics*. 14 (9), 533-542.
- Kasha, M. (1950) Characterization of electronic transitions in complex molecules. *Discussions of the Faraday Society*. 9 14-19.
- Katoch, P., Mitra, S., Ray, A., Kelsey, L., Roberts, B. J., Wahl, J. K., Johnson, K. R. & Mehta, P. P. (2015) The Carboxyl Tail of Connexin32 Regulates Gap Junction Assembly in Human Prostate and Pancreatic Cancer Cells. *The Journal of Biological Chemistry*. 290 (8), 4647-4662. 10.1074/jbc.M114.586057.
- Keller, P. & Ahrens, M. (2015) Visualizing Whole-Brain Activity and Development at the Single-Cell Level Using Light-Sheet Microscopy. *Neuron (Cambridge, Mass.)*. 85 (3), 462-483. 10.1016/j.neuron.2014.12.039.
- Keller, P. J., Schmidt, A. D., Wittbrodt, J. & Stelzer, E. H. (2008) Reconstruction of zebrafish early embryonic development by scanned light sheet microscopy. *Science*. 322 (5904), 1065-1069.
- Képiró, M., Várkuti, B. H., Végner, L., Vörös, G., Hegyi, G., Varga, M. & Málnási-Csizmadia, A. (2014) para-Nitroblebbistatin, the non-cytotoxic and photostable myosin II inhibitor. *Angewandte Chemie International Edition*. 53 (31), 8211-8215.
- Kikuchi, K. & Poss, K. D. (2012) Cardiac Regenerative Capacity and Mechanisms. *Annual Review of Cell and Developmental Biology*. 28 (1), 719-741. 10.1146/annurev-cellbio-101011-155739.
- Kim, B. & Naemura, T. (2015) Blind depth-variant deconvolution of 3D data in wide-field fluorescence microscopy. *Scientific Reports*. 5 (1), 1-9.
- Kim, J. J., Yang, L., Lin, B., Zhu, X., Sun, B., Kaplan, A. D., Bett, G. C., Rasmusson, R. L., London, B. & Salama, G. (2015) Mechanism of automaticity in cardiomyocytes derived from human induced pluripotent stem cells. *Journal of Molecular and Cellular Cardiology*. 81 81-93.
- Kimbrel, E. A. & Lanza, R. (2016) Pluripotent stem cells: the last 10 years. *Regenerative Medicine*. 11 (8), 831-847. 10.2217/rme-2016-0117.
- Kirshner, H., Aguet, F., Sage, D. & Unser, M. (2013) 3-D PSF fitting for fluorescence microscopy: implementation and localization application. *Journal of Microscopy*. 249 (1), 13-25.
- Klán, P. & Wirz, J. (2009) *Photochemistry of organic compounds: from concepts to practice*. John Wiley & Sons.

- Klimanskaya, I., Chung, Y., Becker, S., Lu, S. & Lanza, R. (2006) Human embryonic stem cell lines derived from single blastomeres. *Nature*. 444 (7118), 481-485.
- Kner, P., Sedat, J. W., Agard, D. A. & Kam, Z. (2010) High-resolution wide-field microscopy with adaptive optics for spherical aberration correction and motionless focusing. *Journal of Microscopy*. 237 (2), 136-147.
- Kockskämper, J., Seidlmayer, L., Walther, S., Hellenkamp, K., Maier, L. S. & Pieske, B. (2008) Endothelin-1 enhances nuclear Ca²⁺ transients in atrial myocytes through Ins (1, 4, 5) P 3-dependent Ca²⁺ release from perinuclear Ca²⁺ stores. *Journal of Cell Science*. 121 (2), 186-195.
- Kockskämper, J., Sheehan, K. A., Bare, D. J., Lipsius, S. L., Mignery, G. A. & Blatter, L. A. (2001) Activation and propagation of Ca²⁺ release during excitation-contraction coupling in atrial myocytes. *Biophysical Journal*. 81 (5), 2590-2605.
- Köhler, A. (1894) New method of illumination for photomicrographical purposes. *Journal of the Royal Microscopical Society*. 14 261-262.
- Kolstad, T. R., van den Brink, J., MacQuaide, N., Lunde, P. K., Frisk, M., Aronsen, J. M., Norden, E. S., Cataliotti, A., Sjaastad, I. & Sejersted, O. M. (2018) Ryanodine receptor dispersion disrupts Ca²⁺ release in failing cardiac myocytes. *Elife*. 7 e39427.
- Kondo, R. P., Dederko, D. A., Teutsch, C., Chrast, J., Catalucci, D., Chien, K. R. & Giles, W. R. (2006) Comparison of contraction and calcium handling between right and left ventricular myocytes from adult mouse heart: a role for repolarization waveform. *The Journal of Physiology*. 571 (1), 131-146.
- Kumar, M., Kishore, S., Nasenbeny, J., McLean, D. L. & Kozorovitskiy, Y. (2018) Integrated one-and two-photon scanned oblique plane illumination (SOPi) microscopy for rapid volumetric imaging. *Optics Express*. 26 (10), 13027-13041.
- Kumar, M. & Kozorovitskiy, Y. (2020) Tilt (in) variant lateral scan in oblique plane microscopy: a geometrical optics approach. *Biomedical Optics Express*. 11 (6), 3346-3359.
- Kumar, S., Wilding, D., Sikkil, M. B., Lyon, A. R., MacLeod, K. T. & Dunsby, C. (2011) High-speed 2D and 3D fluorescence microscopy of cardiac myocytes. *Optics Express*. 19 (15), 13839. 10.1364/OE.19.013839.
- Kurtenbach, S., Kurtenbach, S. & Zoidl, G. (2014) Gap junction modulation and its implications for heart function. *Frontiers in Physiology*. 5 82.
- Laasmaa, M., Karro, N., Birkedal, R. & Vendelin, M. (2019) Iocbio sparks detection and analysis software. *PeerJ*. 7 e6652.
- Lacroute, P. & Levoy, M. (1994) Fast volume rendering using a shear-warp factorization of the viewing transformation. *Proceedings of the 21st annual conference on Computer graphics and interactive techniques*. pp.451-458.
- Lakowicz, J. R. (2006) *Principles of fluorescence spectroscopy*. Springer.
- Landry, J. R., Itoh, R., Li, J. M., Hamann, S. S., Mandella, M., Contag, C. H. & Solgaard, O. (2019) Tunable structured illumination light sheet microscopy for background rejection and imaging depth in minimally processed tissues. *Journal of Biomedical Optics*. 24 (4), 046501.

- Lane, N. (2015) The unseen world: reflections on Leeuwenhoek (1677) 'Concerning little animals'. *Philosophical Transactions of the Royal Society B: Biological Sciences*. 370 (1666), 20140344. 10.1098/rstb.2014.0344.
- Laser 2000 Photonics. *560 nm edge BrightLine® single-edge image-splitting dichroic beamsplitter for standard microscopy*. <https://photonics.laser2000.co.uk/products/light-delivery-and-control/microscopy-filters/individual-filters/dichroic-beamsplitter-filters-individual-filters-microscopy-filters/560-nm-edge-brightline-single-edge-image-splitting-dichroic-beamsplitter-for-standard-microscopy/> [Accessed Mar 1, 2022].
- Laurila, E., Ahola, A., Hyttinen, J. & Aalto-Setälä, K. (2016) Methods for in vitro functional analysis of iPSC derived cardiomyocytes—Special focus on analyzing the mechanical beating behavior. *Biochimica Et Biophysica Acta (BBA)-Molecular Cell Research*. 1863 (7), 1864-1872.
- Lee, Y., Ng, K., Lai, W., Chan, Y., Lau, Y., Lian, Q., Tse, H. & Siu, C. (2011) Calcium homeostasis in human induced pluripotent stem cell-derived cardiomyocytes. *Stem Cell Reviews and Reports*. 7 (4), 976-986.
- Lemon, W. C. & McDole, K. (2020) Live-cell imaging in the era of too many microscopes. *Current Opinion in Cell Biology*. 66 34-42. 10.1016/j.ceb.2020.04.008.
- Leung, C. & Donnelly, T. D. (2017) Measuring the spatial resolution of an optical system in an undergraduate optics laboratory. *American Journal of Physics*. 85 (6), 429-438.
- Levoy, M., Ng, R., Adams, A., Footer, M. & Horowitz, M. (2006) Light field microscopy. In: Anonymous *ACM SIGGRAPH 2006 Papers*. pp. 924-934.
- Li, J., Xue, F., Qu, F., Ho, Y. & Blu, T. (2018) On-the-fly estimation of a microscopy point spread function. *Optics Express*. 26 (20), 26120-26133.
- Li, T., Ota, S., Kim, J., Wong, Z. J., Wang, Y., Yin, X. & Zhang, X. (2014) Axial plane optical microscopy. *Scientific Reports*. 4 (1), 1-6.
- Li, X., Wei, X., Qin, Y., Chen, Y., Duan, C. & Yin, M. (2016) The emission rise time of BaY₂ZnO₅:Eu³⁺ for non-contact luminescence thermometry. *Journal of Alloys and Compounds*. 657 353-357. 10.1016/j.jallcom.2015.10.101.
- Liew, L. C., Ho, B. X. & Soh, B. (2020) Mending a broken heart: current strategies and limitations of cell-based therapy. *Stem Cell Research & Therapy*. 11 (1), 1-15.
- Lindek, S., Salmon, N., Cremer, C. & Stelzer, E. H. (1994) Theta microscopy allows phase regulation in 4Pi (A)-confocal two-photon fluorescence microscopy. *Optik-Stuttgart*. 98 15.
- Lindek, S. & Stelzer, E. H. (1994) Confocal theta microscopy and 4Pi-confocal theta microscopy. *Three-dimensional microscopy: image acquisition and processing*. , SPIE. pp.188-194.
- Ljubojevic, S. & Bers, D. M. (2015) Nuclear Calcium in Cardiac Myocytes. *Journal of Cardiovascular Pharmacology*. 65 (3), 211-217. 10.1097/FJC.000000000000174.
- Ljubojević, S., Walther, S., Asgarzoei, M., Sedej, S., Pieske, B. & Kockskämper, J. (2011) In situ calibration of nucleoplasmic versus cytoplasmic Ca²⁺ concentration in adult cardiomyocytes. *Biophysical Journal*. 100 (10), 2356-2366.

- Louch, W. E., Mork, H. K., Sexton, J., Stromme, T. A., Laake, P., Sjaastad, I. & Sejersted, O. M. (2006) T-tubule disorganization and reduced synchrony of Ca^{2+} release in murine cardiomyocytes following myocardial infarction. *Journal of Physiology*. 574 (2), 519. 10.1113/jphysiol.2006.107227.
- Lyon, A. R., MacLeod, K. T., Zhang, Y., Garcia, E., Kanda, G. K., Korchev, Y. E., Harding, S. E. & Gorelik, J. (2009) Loss of T-tubules and other changes to surface topography in ventricular myocytes from failing human and rat heart. *Proceedings of the National Academy of Sciences*. 106 (16), 6854-6859.
- Mackenzie, L., Bootman, M. D., Berridge, M. J. & Lipp, P. (2001) Predetermined recruitment of calcium release sites underlies excitation-contraction coupling in rat atrial myocytes. *The Journal of Physiology*. 530 (3), 417-429.
- Mahajan, V. N. (2001) *Optical Imaging and Aberrations, Part II. Wave Diffraction Optics*. SPIE Press.
- Maioli, V. (2016) *High-speed 3-D fluorescence imaging by oblique plane microscopy: multi-well plate-reader development, biological application and image analysis*. Imperial College London.
- Mann, H. B. & Whitney, D. R. (1947) On a test of whether one of two random variables is stochastically larger than the other. *The Annals of Mathematical Statistics*. 50-60.
- Marchena, M. & Echebarria, B. (2020) Influence of the tubular network on the characteristics of calcium transients in cardiac myocytes. *Plos One*. 15 (4), e0231056. 10.1371/journal.pone.0231056.
- Maurer, C. R., Qi, R. & Raghavan, V. (2003) A linear time algorithm for computing exact Euclidean distance transforms of binary images in arbitrary dimensions. *IEEE Transactions on Pattern Analysis and Machine Intelligence*. 25 (2), 265-270.
- Maurice, D. M. (1974) A scanning slit optical microscope. *Investigative Ophthalmology & Visual Science*. 13 (12), 1033-1037.
- Maxwell, J. C. (1858) On the general laws of optical instruments. *The Quarterly Journal of Pure and Applied Mathematics*. 2 233-246.
- McCain, M. L., Yuan, H., Pasqualini, F. S., Campbell, P. H. & Parker, K. K. (2014) Matrix elasticity regulates the optimal cardiac myocyte shape for contractility. *American Journal of Physiology-Heart and Circulatory Physiology*. 306 (11), H1525-H1539.
- McCutchen, C. W. (1964) Generalized aperture and the three-dimensional diffraction image. *Josa*. 54 (2), 240-244.
- McDole, K., Guignard, L., Amat, F., Berger, A., Malandain, G., Royer, L. A., Turaga, S. C., Branson, K. & Keller, P. J. (2018) In toto imaging and reconstruction of post-implantation mouse development at the single-cell level. *Cell*. 175 (3), 859-876. e33.
- McGorty, R., Liu, H., Kamiyama, D., Dong, Z., Guo, S. & Huang, B. (2015) Open-top selective plane illumination microscope for conventionally mounted specimens. *Optics Express*. 23 (12), 16142-16153.
- McNally, J. G., Preza, C., Conchello, J. & Thomas, L. J. (1994) Artifacts in computational optical-sectioning microscopy. *Josa A*. 11 (3), 1056-1067.
- Medvedev, R. (2020) *Structural and functional differences between cardiomyocytes from right and left ventricles in health and disease*. University of Verona.
- Medvedev, R., Sanchez-Alonso, J. L., Alvarez-Laviada, A., Rossi, S., Dries, E., Schorn, T., Abdul-Salam, V. B., Trayanova, N., Wojciak-Stothard, B. & Miragoli, M. (2021) Nanoscale Study of Calcium Handling

- Remodeling in Right Ventricular Cardiomyocytes Following Pulmonary Hypertension. *Hypertension*. 77 (2), 605-616.
- Mermillod-Blondin, A., McLeod, E. & Arnold, C. B. (2008) High-speed varifocal imaging with a tunable acoustic gradient index of refraction lens. *Optics Letters*. 33 (18), 2146-2148.
- Mertz, J. (2019) Strategies for volumetric imaging with a fluorescence microscope. *Optica*. 6 (10), 1261-1268.
- Metra, M. & Teerlink, J. R. (2017) Heart failure. *The Lancet*. 390 (10106), 1981-1995. 10.1016/S0140-6736(17)31071-1.
- Millett-Sikking, A., Thayer, N. H., Bohnert, A. & York, A. G. (2018) *Remote refocus enables class-leading spatiotemporal resolution in 4D optical microscopy*. https://andrewgyork.github.io/remote_refocus/ [Accessed 27.02.2021].
- Minsky, M. (1961) Microscopy apparatus US patent 3013467. *USP Office, Ed.US*.
- Mitchell, J. (2019) *Heart patches set for human trials*. <https://www.bhf.org.uk/what-we-do/news-from-the-bhf/news-archive/2019/june/heart-patches-set-for-human-trials> [Accessed September 20th, 2019].
- Mohan, S. & Corbett, A. D. (2021) Sensitivity of remote focusing microscopes to magnification mismatch. *Journal of Microscopy*.
- Molina, C. E., Heijman, J. & Dobrev, D. (2016) Differences in Left Versus Right Ventricular Electrophysiological Properties in Cardiac Dysfunction and Arrhythmogenesis. *Arrhythmia & Electrophysiology Review*. 5 (1), 14-9. 10.15420/aer.2016.8.2.
- Monici, M. (2005) Cell and tissue autofluorescence research and diagnostic applications. *Biotechnology Annual Review*. , Elsevier. pp. 227-256. <https://www.sciencedirect.com/science/article/pii/S1387265605110072>.
- Morizane, A., Doi, D., Kikuchi, T., Okita, K., Hotta, A., Kawasaki, T., Hayashi, T., Onoe, H., Shiina, T. & Yamanaka, S. (2013) Direct comparison of autologous and allogeneic transplantation of iPSC-derived neural cells in the brain of a nonhuman primate. *Stem Cell Reports*. 1 (4), 283-292.
- Mosterd, A., Hoes, A. W., de Bruyne, M. C., Deckers, J. W., Linker, D. T., Hofman, A. & Grobbee, D. E. (1999) Prevalence of heart failure and left ventricular dysfunction in the general population; The Rotterdam Study. *European Heart Journal*. 20 (6), 447-455. 10.1053/euhj.1998.1239.
- Mosterd, A. & Hoes, A. W. (2007) Clinical epidemiology of heart failure. *Heart*. 93 (9), 1137-1146. 10.1136/hrt.2003.025270.
- Muellerbroich, C., Kelly, A., Acker, C., Bub, G., Breugmann, T., Di Bona, A., Entcheva, E., Ferrantini, C., Kohl, P. & Lehnart, S. E. (2021) Novel optics-based approaches for cardiac electrophysiology: a review. *Frontiers in Physiology*. 1971.
- Mukamel, E. A., Nimmerjahn, A. & Schnitzer, M. J. (2009) Automated analysis of cellular signals from large-scale calcium imaging data. *Neuron*. 63 (6), 747-760.
- Nakai, J., Ohkura, M. & Imoto, K. (2001) A high signal-to-noise Ca²⁺ probe composed of a single green fluorescent protein. *Nature Biotechnology*. 19 (2), 137-141. 10.1038/84397.
- Neil, M. a. A., Juškaitis, R. & Wilson, T. (1997) Method of obtaining optical sectioning by using structured light in a conventional microscope. *Optics Letters*. 22 (24), 1905-1907. 10.1364/OL.22.001905.

- Niggli, E. (1999) Localized intracellular calcium signaling in muscle: calcium sparks and calcium quarks. *Annual Review of Physiology*. 61 311-335. 10.1146/annurev.physiol.61.1.311.
- Niggli, E. & Egger, M. (2002) Calcium quarks. *Front Biosci*. 7 d1288-d1297.
- Nyquist, H. (1928) Certain topics in telegraph transmission theory. *Transactions of the American Institute of Electrical Engineers*. 47 (2), 617-644.
- Ogier, A., Dorval, T. & Genovesio, A. (2008) Inhomogeneous deconvolution in a biological images context. *2008 5th IEEE International Symposium on Biomedical Imaging: From Nano to Macro*. , IEEE. pp.744-747.
- Oku, H., Hashimoto, K. & Ishikawa, M. (2004) Variable-focus lens with 1-kHz bandwidth. *Optics Express*. 12 (10), 2138-2149.
- Oshikane, Y., Kataoka, T., Okuda, M., Hara, S., Inoue, H. & Nakano, M. (2007) Observation of nanostructure by scanning near-field optical microscope with small sphere probe. *Science and Technology of Advanced Materials*. 8 (3), 181.
- Otsu, N. (1979) A Threshold Selection Method from Gray-Level Histograms. *IEEE Transactions on Systems, Man, and Cybernetics*. 9 (1), 62-66. 10.1109/TSMC.1979.4310076.
- Øyehaug, L., Loose, K. Ø, Jølle, G. F., Røe, Å T., Sjaastad, I., Christensen, G., Sejersted, O. M. & Louch, W. E. (2013) Synchrony of cardiomyocyte Ca² release is controlled by T-tubule organization, SR Ca² content, and ryanodine receptor Ca² sensitivity. *Biophysical Journal*. 104 (8), 1685-1697.
- Pasqualin, C., Gannier, F., Malécot, C. O., Bredeloux, P. & Maupoil, V. (2015) Automatic quantitative analysis of t-tubule organization in cardiac myocytes using ImageJ. *American Journal of Physiology-Cell Physiology*. 308 (3), C237-C245.
- Passier, R., van Laake, L. W. & Mummery, C. L. (2008) Stem-cell-based therapy and lessons from the heart. *Nature*. 453 (7193), 322-329.
- Patrick Theer, Cyril Mongis & Michael Knop. (2014) PSFj: know your fluorescence microscope. *Nature Methods*. 11 (10), 981-982. 10.1038/nmeth.3102.
- Patterson, G. H. & Piston, D. W. (2000) Photobleaching in Two-Photon Excitation Microscopy. *Biophysical Journal*. 78 (4), 2159-2162. 10.1016/S0006-3495(00)76762-2.
- Perbellini, F., Watson, S. A., Scigliano, M., Alayoubi, S., Tkach, S., Bardi, I., Quaife, N., Kane, C., Dufton, N. P. & Simon, A. (2018) Investigation of cardiac fibroblasts using myocardial slices. *Cardiovascular Research*. 114 (1), 77-89.
- Picht, E., Zima, A. V., Blatter, L. A. & Bers, D. M. (2007) SparkMaster: automated calcium spark analysis with ImageJ. *American Journal of Physiology-Cell Physiology*. 293 (3), C1073-C1081.
- Planchon, T. A., Gao, L., Milkie, D. E., Davidson, M. W., Galbraith, J. A., Galbraith, C. G. & Betzig, E. (2011) Rapid three-dimensional isotropic imaging of living cells using Bessel beam plane illumination. *Nature Methods*. 8 (5), 417-423. 10.1038/nmeth.1586.
- Poland, S. P., Wright, A. J. & Girkin, J. M. (2008) Active focus locking in an optically sectioning microscope utilizing a deformable membrane mirror. *Optics Letters*. 33 (5), 419-421.

- Prabhat, P., Ram, S., Ward, E. S. & Ober, R. J. (2004) Simultaneous imaging of different focal planes in fluorescence microscopy for the study of cellular dynamics in three dimensions. *IEEE Transactions on Nanobioscience*. 3 (4), 237-242.
- Preibisch, S., Saalfeld, S., Schindelin, J. & Tomancak, P. (2010) Software for bead-based registration of selective plane illumination microscopy data. *Nature Methods*. 7 (6), 418-419.
- Preza, C., Ollinger, J. M., McNally, J. G. & Thomas, L. J. (1992) Point-spread sensitivity analysis for computational optical-sectioning microscopy. *Micron and Microscopica Acta*. 23 (4), 501-513. 10.1016/0739-6260(92)90024-8.
- Psaras, Y., Margara, F., Cicconet, M., Sparrow, A. J., Repetti, G. G., Schmid, M., Steeples, V., Wilcox, J. A. L., Bueno-Orovio, A., Redwood, C. S., Watkins, H. C., Robinson, P., Rodriguez, B., Seidman, J. G., Seidman, C. E. & Toepfer, C. N. (2021) CalTrack: High-Throughput Automated Calcium Transient Analysis in Cardiomyocytes. *Circulation Research*. 129 (2), 326-341. 10.1161/CIRCRESAHA.121.318868.
- Rao, C., Prodromakis, T., Kolker, L., Chaudhry, U. A., Trantidou, T., Sridhar, A., Weekes, C., Camelliti, P., Harding, S. E. & Darzi, A. (2013) The effect of microgrooved culture substrates on calcium cycling of cardiac myocytes derived from human induced pluripotent stem cells. *Biomaterials*. 34 (10), 2399-2411.
- Rayleigh, L. (1879) XXXI. Investigations in optics, with special reference to the spectroscope. *The London, Edinburgh, and Dublin Philosophical Magazine and Journal of Science*. 8 (49), 261-274.
- Reddy, G. D., Kelleher, K., Fink, R. & Saggau, P. (2008) Three-dimensional random access multiphoton microscopy for functional imaging of neuronal activity. *Nature Neuroscience*. 11 (6), 713-720.
- Redington, A. N., Gray, H. H., Hodson, M. E., Rigby, M. L. & Oldershaw, P. J. (1988) Characterisation of the normal right ventricular pressure-volume relation by biplane angiography and simultaneous micromanometer pressure measurements. *Heart*. 59 (1), 23-30.
- Reynaud, E. G., Kržič, U., Greger, K. & Stelzer, E. H. K. (2008) Light sheet-based fluorescence microscopy: more dimensions, more photons, and less photodamage. *HFSP Journal*. 2 (5), 266-275. 10.2976/1.2974980.
- Reynaud, E. G., Peychl, J., Huiskens, J. & Tomancak, P. (2015) Guide to light-sheet microscopy for adventurous biologists. *Nature Methods*. 12 (1), 30-34. 10.1038/nmeth.3222.
- Richards, B. (1956) Diffraction in systems of high relative aperture. *Astronomical Optics and Related Subjects*. 352.
- Rust, M. J., Bates, M. & Zhuang, X. (2006) Sub-diffraction-limit imaging by stochastic optical reconstruction microscopy (STORM). *Nature Methods*. 3 (10), 793-796.
- Sathish, V., Xu, A., Karmazyn, M., Sims, S. M. & Narayanan, N. (2006) Mechanistic basis of differences in Ca²⁺-handling properties of sarcoplasmic reticulum in right and left ventricles of normal rat myocardium. *American Journal of Physiology-Heart and Circulatory Physiology*. 291 (1), H88-H96.
- Sato, M., O'Gara, P., Harding, S. E. & Fuller, S. J. (2005) Enhancement of adenoviral gene transfer to adult rat cardiomyocytes in vivo by immobilization and ultrasound treatment of the heart. *Gene Therapy*. 12 (11), 936-941.
- Schermelleh, L., Heintzmann, R. & Leonhardt, H. (2010) A guide to super-resolution fluorescence microscopy. *Journal of Cell Biology*. 190 (2), 165-175.

Scherschel, J. A. & Rubart, M. (2008) Cardiovascular imaging using two-photon microscopy. *Microscopy and Microanalysis*. 14 (6), 492-506.

Schneckenburger, H. & Richter, V. (2021) Challenges in 3D Live Cell Imaging. *Photonics*. , Multidisciplinary Digital Publishing Institute. pp.275.

Scientific Volume Imaging, B. V. (2022) *Huygens PSF Distiller* | *Scientific Volume Imaging*. <https://svi.nl/Huygens-PSF-Distiller> [Accessed Mar 11, 2022].

Senyo, S. E., Steinhäuser, M. L., Pizzimenti, C. L., Yang, V. K., Cai, L., Wang, M., Wu, T., Guérquin-Kern, J., Lechene, C. P. & Lee, R. T. (2013) Mammalian heart renewal by pre-existing cardiomyocytes. *Nature*. 493 (7432), 433-436.

Shacklock, P. S., Wier, W. G. & Balke, C. W. (1995) Local Ca² transients (Ca² sparks) originate at transverse tubules in rat heart cells. *The Journal of Physiology*. 487 (3), 601-608.

Shain, W. J., Vickers, N. A., Goldberg, B. B., Bifano, T. & Mertz, J. (2017) Extended depth-of-field microscopy with a high-speed deformable mirror. *Optics Letters*. 42 (5), 995-998.

Sheppard, C. J. R. & Choudhury, A. (1977) Image Formation in the Scanning Microscope. *Optica Acta: International Journal of Optics*. 24 (10), 1051-1073. 10.1080/713819421.

Sheppard, C. J. R. & Matthews, H. J. (1987) Imaging in high-aperture optical systems. *Josa A*. 4 (8), 1354-1360. 10.1364/JOSAA.4.001354.

Sheppard, C. (1997) Aberrations in high aperture optical systems. *Optik*. 105 (1), 29-33.

Sheppard, C. (1989) General considerations of diffraction theory of 3-D imaging. *European J.Cell Biology Suppl*. 25 29-32.

Sheppard, C. & Gong, Y. (1991) Improvement in axial resolution by interference confocal microscopy. *Optik*. 87 (3), 129-132.

Sheppard, C. & Wilson, T. (1986) On the equivalence of scanning and conventional microscopes. *Optik (Stuttgart)*. 73 (1), 39-43.

Sheppard, C. & Wilson, T. (1978) Depth of field in the scanning microscope. *Optics Letters*. 3 (3), 115-117.

Sheppard, C. J. & Gu, M. (1991) Aberration compensation in confocal microscopy. *Applied Optics*. 30 (25), 3563-3568.

Shiba, Y., Gomibuchi, T., Seto, T., Wada, Y., Ichimura, H., Tanaka, Y., Ogasawara, T., Okada, K., Shiba, N., Sakamoto, K., Ido, D., Shiina, T., Ohkura, M., Nakai, J., Uno, N., Kazuki, Y., Oshimura, M., Minami, I. & Ikeda, U. (2016) Allogeneic transplantation of iPS cell-derived cardiomyocytes regenerates primate hearts. *Nature (London)*. 538 (7625), 388-391. 10.1038/nature19815.

Shkryl, V. M., Blatter, L. A. & Rios, E. (2012) Properties of Ca² sparks revealed by four-dimensional confocal imaging of cardiac muscle. *Journal of General Physiology*. 139 (3), 189-207.

Siedentopf, H. & Zsigmondy, R. (1902) Über Sichtbarmachung und Größenbestimmung ultramikroskopischer Teilchen, mit besonderer Anwendung auf Goldrubingläser. *Annalen Der Physik*. 315 (1), 1-39. 10.1002/andp.19023150102.

Siegman, A. E. (1986) *Wave optics and Gaussian beams*, University Science Books

- Sikkel, M. (2015) *Arrhythmogenic sarcoplasmic reticulum calcium leak in isolated ventricular cardiomyocytes - changes in heart failure and mechanisms of pharmacological modulation*. Imperial College London.
- Sikkel, M. B., Kumar, S., Maioli, V., Rowlands, C., Gordon, F., Harding, S. E., Lyon, A. R., MacLeod, K. T. & Dunsby, C. (2016a) High speed sCMOS-based oblique plane microscopy applied to the study of calcium dynamics in cardiac myocytes. *Journal of Biophotonics*. 9 (3), 311-323. 10.1002/jbio.201500193.
- Sikkel, M. B., Kumar, S., Maioli, V., Rowlands, C., Gordon, F., Harding, S. E., Lyon, A. R., MacLeod, K. T. & Dunsby, C. (2016b) High speed sCMOS-based oblique plane microscopy applied to the study of calcium dynamics in cardiac myocytes. *Journal of Biophotonics*. 9 (3), 311-323. 10.1002/jbio.201500193.
- Silvestri, L., Bria, A., Sacconi, L., Iannello, G. & Pavone, F. S. (2012) Confocal light sheet microscopy: micron-scale neuroanatomy of the entire mouse brain. *Optics Express*. 20 (18), 20582-20598.
- Sines, G. & Sakellarakis, Y. A. (1987) Lenses in Antiquity. *American Journal of Archaeology*. 91 (2), 191-196. 10.2307/505216.
- Smith, P. J., Taylor, C. M., Shaw, A. J. & McCabe, E. M. (2000) Programmable array microscopy with a ferroelectric liquid-crystal spatial light modulator. *Applied Optics*. 39 (16), 2664-2669.
- Soeller, C. & Cannell, M. B. (1999) Examination of the transverse tubular system in living cardiac rat myocytes by 2-photon microscopy and digital image-processing techniques. *Circulation Research*. 84 (3), 266-275.
- Song, L., Sobie, E. A., McCulle, S., Lederer, W. J., Balke, C. W. & Cheng, H. (2006) Orphaned ryanodine receptors in the failing heart. *Proceedings of the National Academy of Sciences*. 103 (11), 4305-4310.
- Sorenson, A. L., Tepper, D., Sonnenblick, E., Robinson, T. & Capasso, J. (1985) Size and shape of enzymatically isolated ventricular myocytes from rats and cardiomyopathic hamsters. *Cardiovascular Research*. 19 (12), 793-799. 10.1093/cvr/19.12.793.
- Sparks, H., Dent, L., Bakal, C., Behrens, A., Salbreux, G. & Dunsby, C. (2020) Dual-view oblique plane microscopy (dOPM). *Biomedical Optics Express*. 11 (12), 7204-7220.
- Sparks, H., Dvinskikh, L., Firth, J., Francis, A., Harding, S., Paterson, C., MacLeod, K. & Dunsby, C. (2020) Development a flexible light-sheet fluorescence microscope for high-speed 3D imaging of calcium dynamics and 3D imaging of cellular microstructure. *Journal of Biophotonics*. 13 (6), e201960239. 10.1002/jbio.201960239.
- Sparrow, C. M. (1916) On spectroscopic resolving power. *The Astrophysical Journal*. 44 76.
- Steele, E. M. & Steele, D. S. (2014) Automated detection and analysis of Ca²⁺ sparks in xy image stacks using a thresholding algorithm implemented within the open-source image analysis platform ImageJ. *Biophysical Journal*. 106 (3), 566-576.
- Stelzer, E. H. K. (2015) Light-sheet fluorescence microscopy for quantitative biology. *Nature Methods*. 12 (1), 23-26. 10.1038/nmeth.3219.
- Stelzer, E. H. K., Strobl, F., Chang, B., Preusser, F., Preibisch, S., McDole, K. & Fiolka, R. (2021) Light sheet fluorescence microscopy. *Nature Reviews Methods Primers*. 1 (1), 1-25. 10.1038/s43586-021-00069-4.
- Stelzer, E. H. (2006) The intermediate optical system of laser-scanning confocal microscopes. *Handbook of biological confocal microscopy*, Springer. pp. 207-220.

- Stelzer, E. H. (1998) Contrast, resolution, pixelation, dynamic range and signal-to-noise ratio: fundamental limits to resolution in fluorescence light microscopy. *Journal of Microscopy*. 189 (1), 15-24.
- Stelzer, E. H. & Lindek, S. (1994) Fundamental reduction of the observation volume in far-field light microscopy by detection orthogonal to the illumination axis: confocal theta microscopy. *Optics Communications*. 111 (5-6), 536-547.
- Steward, G. C. (1927) On Herschel's Condition and the Optical Cosine Law. *Mathematical Proceedings of the Cambridge Philosophical Society*, Cambridge University Press. pp.703-712.
- Stokes, G. G. (1852) XXX. On the change of refrangibility of light. *Philosophical Transactions of the Royal Society of London*. (142), 463-562.
- Strehl, K. (1894) *Theorie des fernrohrs: auf grund der beugung des Lichts*. JA Barth (A. Meiner).
- Student. (1908) The probable error of a mean. *Biometrika*. 1-25.
- Sun, X., Callamaras, N., Marchant, J. S. & Parker, I. (1998) A continuum of InsP3-mediated elementary Ca²⁺ signalling events in *Xenopus* oocytes. *The Journal of Physiology*. 509 (1), 67-80.
- Sutanto, H., Lyon, A., Lumens, J., Schotten, U., Dobrev, D. & Heijman, J. (2020) Cardiomyocyte calcium handling in health and disease: Insights from in vitro and in silico studies. *Progress in Biophysics and Molecular Biology*. 157 54-75.
- Svelto, O. (2010) Ray and wave propagation through optical media. In: Anonymous *Principles of lasers*. , Springer. pp. 131-161.
- Swoger, J., Verveer, P., Greger, K., Huiskens, J. & Stelzer, E. H. (2007) Multi-view image fusion improves resolution in three-dimensional microscopy. *Optics Express*. 15 (13), 8029-8042.
- Takahashi, K. & Yamanaka, S. (2006) Induction of Pluripotent Stem Cells from Mouse Embryonic and Adult Fibroblast Cultures by Defined Factors. *Cell*. 126 (4), 663-676. 10.1016/j.cell.2006.07.024.
- Takahashi, N., Sasaki, T., Matsumoto, W., Matsuki, N. & Ikegaya, Y. (2010) Circuit topology for synchronizing neurons in spontaneously active networks. *Proceedings of the National Academy of Sciences*. 107 (22), 10244-10249.
- Tatian, B. (1965) Method for obtaining the transfer function from the edge response function. *Josa*. 55 (8), 1014-1019.
- ThermoFisher Scientific. (2022) *Fluorescence SpectraViewer*. <https://www.thermofisher.com/order/fluorescence-spectraviewer> [Accessed Mar 1, 2022].
- ThermoFisher Scientific. *Fluorescence SpectraViewer*. <https://www.thermofisher.com/order/fluorescence-spectraviewer> [Accessed Feb 18, 2022].
- Tian, Q., Kaestner, L. & Lipp, P. (2012) Noise-Free Visualization of Microscopic Calcium Signaling by Pixel-Wise Fitting. *Circulation Research*. 111 (1), 17-27. 10.1161/CIRCRESAHA.112.266403.
- Tian, Q., Schröder, L., Flockerzi, A., Zeug, A., Kaestner, L. & Lipp, P. (2015) Large-Scale, Automated Calcium Spark Analysis using iSpark Reveals Functional and Spatial Remodeling During Cardiac Hypertrophy. *Biophysical Journal*. 108 (2), 340a.

- Tian, Q., Schröder, L., Schwarz, Y., Flockerzi, A., Kaestner, L., Zeug, A., Bruns, D. & Lipp, P. (2019) Large scale, unbiased analysis of elementary calcium signaling events in cardiac myocytes. *Journal of Molecular and Cellular Cardiology*. 135 79-89.
- Tiburcy, M., Hudson, J. E., Balfanz, P., Schlick, S., Meyer, T., Chang Liao, M., Levent, E., Raad, F., Zeidler, S. & Wingender, E. (2017) Defined engineered human myocardium with advanced maturation for applications in heart failure modeling and repair. *Circulation*. 135 (19), 1832-1847.
- Toader, B., Boulanger, J., Korolev, Y., Lenz, M. O., Manton, J., Schonlieb, C. & Muresan, L. (2021) Image reconstruction in light-sheet microscopy: spatially varying deconvolution and mixed noise. *arXiv Preprint arXiv:2108.03642*.
- Van der Voort, H. & Strasters, K. C. (1995) Restoration of confocal images for quantitative image analysis. *Journal of Microscopy*. 178 (2), 165-181.
- Verdeyen, J. T. (2000) *Laser Electronics*. Prentice-Hall series in solid state physical electronics. 3rd edition. Upper Saddle River, N.J. : Prentice Hall.
- Vettenburg, T., Dalgarno, H. I. C., Nylk, J., Coll-Lladó, C., Ferrier, D. E. K., Čížmár, T., Gunn-Moore, F. J. & Dholakia, K. (2014) Light-sheet microscopy using an Airy beam. *Nature Methods*. 11 (5), 541-544. 10.1038/nmeth.2922.
- Vilkov, L. V. & Pentin, Y. A. (1987) Physical Research Methods in Chemistry. *Structural Methods and Optical Spectroscopy*. 1-683.
- Vliet, V. (1998) Theory of confocal fluorescence imaging in the programmable array microscope (PAM). *Journal of Microscopy*. 189 (3), 192-198.
- Voie, A. H., Burns, D. H. & Spelman, F. A. (1993) Orthogonal-plane fluorescence optical sectioning: Three-dimensional imaging of macroscopic biological specimens. *Journal of Microscopy*. 170 (3), 229-236. 10.1111/j.1365-2818.1993.tb03346.x.
- Voleti, V., Patel, K. B., Li, W., Perez Campos, C., Bharadwaj, S., Yu, H., Ford, C., Casper, M. J., Yan, R. W. & Liang, W. (2019) Real-time volumetric microscopy of in vivo dynamics and large-scale samples with SCAPE 2.0. *Nature Methods*. 16 (10), 1054-1062.
- Wagner, M., Weber, P., Bruns, T., Strauss, W. S., Wittig, R. & Schneckenburger, H. (2010) Light dose is a limiting factor to maintain cell viability in fluorescence microscopy and single molecule detection. *International Journal of Molecular Sciences*. 11 (3), 956-966.
- Wang, K., Lee, P., Mirams, G. R., Sarathchandra, P., Borg, T. K., Gavaghan, D. J., Kohl, P. & Bollensdorff, C. (2015) Cardiac tissue slices: preparation, handling, and successful optical mapping. *American Journal of Physiology-Heart and Circulatory Physiology*. 308 (9), H1112-H1125.
- Wapcaplet. (2006) *Diagram of the human heart*.
[https://en.wikipedia.org/wiki/Heart#/media/File:Diagram_of_the_human_heart_\(cropped\).svg](https://en.wikipedia.org/wiki/Heart#/media/File:Diagram_of_the_human_heart_(cropped).svg) [Accessed Mar 8, 2022].
- Wartmann, R. (2007) *Optisches Abbildungssystem, insbesondere für Mikroskope*. DE102005051026A1 (Patent).
- Watson, S. A., Dendorfer, A., Thum, T. & Perbellini, F. (2020) A practical guide for investigating cardiac physiology using living myocardial slices. *Basic Research in Cardiology*. 115 (6), 1-12.

- Watson, S. A., Duff, J., Bardi, I., Zabielska, M., Atanur, S. S., Jabbour, R. J., Simon, A., Tomas, A., Smolenski, R. T. & Harding, S. E. (2019) Biomimetic electromechanical stimulation to maintain adult myocardial slices in vitro. *Nature Communications*. 10 (1), 1-15.
- Watson, S. A., Scigliano, M., Bardi, I., Ascione, R., Terracciano, C. M. & Perbellini, F. (2017) Preparation of viable adult ventricular myocardial slices from large and small mammals. *Nature Protocols*. 12 (12), 2623-2639.
- Watson, S. A., Terracciano, C. M. & Perbellini, F. (2019) Myocardial slices: an intermediate complexity platform for translational cardiovascular research. *Cardiovascular Drugs and Therapy*. 33 (2), 239-244.
- Weinberger, F., Mannhardt, I. & Eschenhagen, T. (2017) Engineering cardiac muscle tissue: a maturing field of research. *Circulation Research*. 120 (9), 1487-1500.
- Welch, B. L. (1947) The generalization of 'STUDENT'S' problem when several different population variances are involved. *Biometrika*. 34 (1-2), 28-35.
- Welford, W. T. (1960) Use of annular apertures to increase focal depth. *Josa*. 50 (8), 749-753.
- Wicker, K. & Heintzmann, R. (2007) Interferometric resolution improvement for confocal microscopes. *Optics Express*. 15 (19), 12206-12216.
- Wilcoxon, F. (1992) Individual comparisons by ranking methods. In: Anonymous *Breakthroughs in statistics*. , Springer. pp. 196-202.
- Williams, C. S. & Becklund, O. A. (2002) *Introduction to the optical transfer function*. SPIE Press.
- Wilson, T. (1989) Optical sectioning in confocal fluorescent microscopes. *Journal of Microscopy*. 154 (2), 143-156.
- Wilson, T. (2011) Resolution and optical sectioning in the confocal microscope. *Journal of Microscopy*. 244 (2), 113-121.
- Wilson, T. & Sheppard, C. (1984) *Theory and practice of scanning optical microscopy*. Academic press London.
- Woo, S., Cleemann, L. & Morad, M. (2002) Ca²⁺ current-gated focal and local Ca²⁺ release in rat atrial myocytes: evidence from rapid 2-D confocal imaging. *The Journal of Physiology*. 543 (2), 439-453.
- Wright, T., Sparks, H., Paterson, C. & Dunsby, C. (2021) Video-rate remote refocusing through continuous oscillation of a membrane deformable mirror. *Journal of Physics: Photonics*. 3 (4), 045004.
- Wu, Y., Chandris, P., Winter, P. W., Kim, E. Y., Jaumouillé, V., Kumar, A., Guo, M., Leung, J. M., Smith, C., Rey-Suarez, I., Liu, H., Waterman, C. M., Ramamurthi, K. S., La Riviere, P. J. & Shroff, H. (2016) Simultaneous multiview capture and fusion improves spatial resolution in wide-field and light-sheet microscopy. *Optica*. 3 (8), 897-910. 10.1364/OPTICA.3.000897.
- Wu, Y., Ghitani, A., Christensen, R., Santella, A., Du, Z., Rondeau, G., Bao, Z., Colón-Ramos, D. & Shroff, H. (2011) Inverted selective plane illumination microscopy (iSPIM) enables coupled cell identity lineaging and neurodevelopmental imaging in *Caenorhabditis elegans*. *Proceedings of the National Academy of Sciences*. 108 (43), 17708-17713.
- Wu, Y., Wawrzusin, P., Senseney, J., Fischer, R. S., Christensen, R., Santella, A., York, A. G., Winter, P. W., Waterman, C. M., Bao, Z., Colón-Ramos, D. A., McAuliffe, M. & Shroff, H. (2013) Spatially

isotropic four-dimensional imaging with dual-view plane illumination microscopy. *Nature Biotechnology*. 31 (11), 1032-1038. 10.1038/nbt.2713.

Yang, Y., Chen, W., Fan, J. L. & Ji, N. (2021) Adaptive optics enables aberration-free single-objective remote focusing for two-photon fluorescence microscopy. *Biomedical Optics Express*. 12 (1), 354-366.

Yordanov, S., Neuhaus, K., Hartmann, R., Díaz-Pascual, F., Vidakovic, L., Singh, P. K. & Drescher, K. (2021) Single-objective high-resolution confocal light sheet fluorescence microscopy for standard biological sample geometries. *Biomedical Optics Express*. 12 (6), 3372-3391.

Zemax, L. (2016) Physical Optics Propagation. *OpticStudio 16.5 SP1 Help Files*. pp. 1027-1084.

Zhang, B., Zerubia, J. & Olivo-Marin, J. (2007) Gaussian approximations of fluorescence microscope point-spread function models. *Applied Optics*. 46 (10), 1819-1829.

Zhang, G. Q., Wei, H., Lu, J., Wong, P. & Shim, W. (2013a) Identification and characterization of calcium sparks in cardiomyocytes derived from human induced pluripotent stem cells. *PloS One*. 8 (2), e55266.

Zhang, X., Haviland, S., Wei, H., Šarić, T., Fatima, A., Hescheler, J., Cleemann, L. & Morad, M. (2013b) Ca²⁺ signaling in human induced pluripotent stem cell-derived cardiomyocytes (iPS-CM) from normal and catecholaminergic polymorphic ventricular tachycardia (CPVT)-afflicted subjects. *Cell Calcium*. 54 (2), 57-70.

Zhao, G., Qiu, Y., Zhang, H. M. & Yang, D. (2019) Intercalated discs: cellular adhesion and signaling in heart health and diseases. *Heart Failure Reviews*. 24 (1), 115-132.

Zheng, Q., Jockusch, S., Zhou, Z. & Blanchard, S. C. (2014) The contribution of reactive oxygen species to the photobleaching of organic fluorophores. *Photochemistry and Photobiology*. 90 (2), 448-454.

Zhong, Q., Li, A., Jin, R., Zhang, D., Li, X., Jia, X., Ding, Z., Luo, P., Zhou, C. & Jiang, C. (2021) High-definition imaging using line-illumination modulation microscopy. *Nature Methods*. 18 (3), 309-315.

Zimmermann, W., Melnychenko, I., Wasmeier, G., Didié, M., Naito, H., Nixdorff, U., Hess, A., Budinsky, L., Brune, K. & Michaelis, B. (2006) Engineered heart tissue grafts improve systolic and diastolic function in infarcted rat hearts. *Nature Medicine*. 12 (4), 452-458.

Žurauskas, M., Barnstedt, O., Frade-Rodriguez, M., Waddell, S. & Booth, M. J. (2017) Rapid adaptive remote focusing microscope for sensing of volumetric neural activity. *Biomedical Optics Express*. 8 (10), 4369-4379.

9 Appendix

A1. Video captions

1. **Video 4.3: 2D LSFM timelapse of a single ventricular cardiomyocyte** undergoing stimulated calcium transients and spontaneous sparks, imaged at 390 fps. The cell is electrically paced for around half of the acquisition. Video has been downsampled by 8x in time through bilinear interpolation. Playback at 2× real-time speed. Scalebar: 10 μm .
2. **Video 5.5: 3D LSFM timelapse of hiPSC-CM undergoing spontaneous calcium transients.** Orthogonal cuts through the merged Fluo-4 (green) and CMO (magenta) channels of hiPSC-CM culture imaged at 4 vps, 195 fps during an unpaced acquisition. FOV: $302 \times 76 \times 40 \mu\text{m}$. Playback at 2× real-time speed.
3. **Video 5.6: Widefield transillumination timelapse of hiPSC-CM and adult-CM** day 0 (left), day 1 (middle) and day 2 (right) of co-culture, with synchronized spontaneous contraction. Playback at 4× real-time speed. Scalebar: 100 μm .
4. **Video 5.7: Widefield fluorescence timelapse of hiPSC-CM and adult-CM** on day 0 (left), day 1 (middle) and day 2 (right) of co-culture, with synchronized spontaneous calcium transients. Playback at 4× real-time speed. Scalebar: 100 μm .
5. **Video 5.8: 3D LSFM timelapse of hiPSC-CM and adult-CM co-culture undergoing synchronized spontaneous transients.** Orthogonal cuts through the merged Fluo-4 (green) and CMO (magenta) channels of hiPSC-CM culture, imaged at 8 vps, 390 fps during an unpaced acquisition. FOV: $302 \times 38 \times 40 \mu\text{m}$. Playback at 2× real-time speed.
6. **Video 5.10a: 3D LSFM timelapse of hiPSC-CM and adult-CM co-culture undergoing synchronized spontaneous transients** in a sample without NBleb. Orthogonal cuts through the merged Fluo-4 (green) and CMO (magenta) channels, imaged at 4 vps, 195 fps during an unpaced acquisition. FOV: $302 \times 76 \times 40 \mu\text{m}$. Playback at 2× real-time speed.
7. **Video 5.10b: 3D LSFM timelapse of hiPSC-CM and adult-CM co-culture undergoing synchronized spontaneous transients** in a sample treated with NBleb. Orthogonal cuts through the merged Fluo-4 (green) and CMO (magenta) channels, imaged at 4 vps, 195 fps during an unpaced acquisition. FOV: $302 \times 76 \times 40 \mu\text{m}$. Playback at 2× real-time speed.
8. **Video 5.11: 3D LSFM timelapse of live myocardial slices undergoing stimulated contraction.** Orthogonal cuts through the merged Fluo-4 (green) and CMO (magenta) channels, imaged at 4 vps, 195 fps during an unpaced acquisition. FOV: $302 \times 76 \times 40 \mu\text{m}$. Playback at 2× real-time speed.

A2. System design and operation

Figure A1.1: Photo of optical system with a vertically positioned breadboard, including marked illumination and detection paths (green and blue respectively) and key components. The system diagram (Figure 2.9) is provided in Section 2.2.1

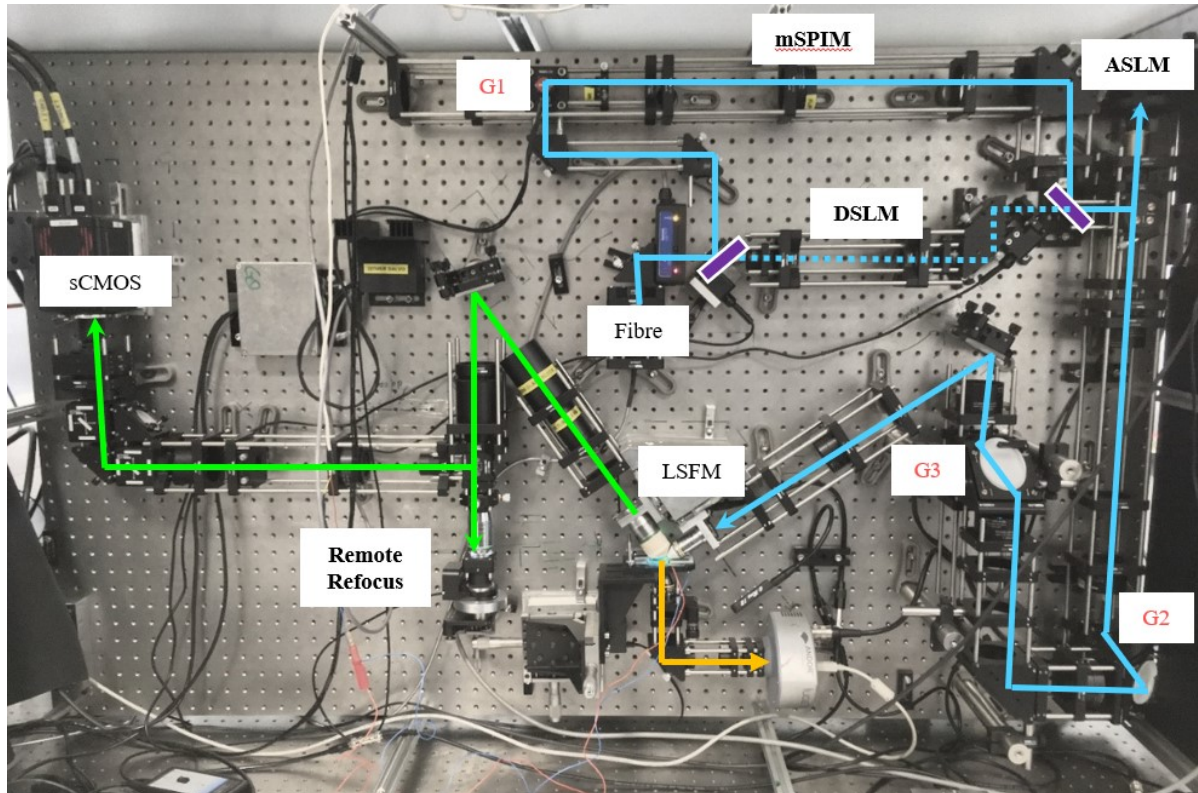


Table A2.1: Parts list for the LSMF system

Laser engine	Omicron, LightHUB®			
	Wavelength (nm)	Model		
	488	Omicron LuxX488-100		
	561	Cobalt JIVE 561-75		
PM-SMF	Kineflex Fibre System			
Optomechanics	Label	Description	Supplier	Part ID
Collimating objective	O1	Air objective, 10x, 0.3 NA	Thorlabs	N10X-PF
mSPIM	M2 & M3	1" mirrors, dielectric	Thorlabs	BB1-E02
	FM1 & FM2	1" mirrors, dielectric	Thorlabs	BB1-E02
		Motorized flipper mirrors	Newport	8892-K-M
	G1	1D Galvo system, dielectric mirror	Thorlabs	GVS001
	C1	1" cylindrical lens, 50 mm focal length	Thorlabs	LJ1567RM-A
	P1	2" plössl (pair of achromats), 200 mm focal length	Thorlabs	AC508-400-A-ML
	M4	2" mirror	Thorlabs	BB2-E02
	P2	2" plössl (pair of achromats), 200 mm focal length	Thorlabs	AC508-400-A-ML
DSLM	D1	1" achromat, 40 mm focal length	Thorlabs	AC254-040-A-ML
	D2	1" achromat, 200 mm focal length	Thorlabs	AC254-200-A-ML
	M5 & M6	1" mirrors, dielectric	Thorlabs	BB1-E02
ASLM + light-sheet positioning	PBS1	Polarsing beam splitter	Thorlabs	PBS251
	QWP1	Quarter-wave plate	Thorlabs	AQWP05M-600
	O2	Air objective, 10x, 0.3 NA	Thorlabs	N10X-PF
	RM1	7 mm diameter mirror, dielectric	Thorlabs	BB03-E02
	x'-scan	Linear stage	PI	V-522
	P3	2" plössl (pair of achromats), 200 mm focal length	Thorlabs	AC508-400-A-ML
	P4	2" plössl (pair of achromats), 100 mm focal length	Thorlabs	AC508-200-A-ML
	G2 (z'-scan) & G3 (y'-scan)	2D Galvo system, dielectric mirrors	Thorlabs	GVS202
	M7-M9	2" elliptical mirror, dielectric	Thorlabs	BBE2-E02
	P5	2" plössl (pair of achromats), 150 mm focal length	Thorlabs	AC508-300-A-ML
	P6	2" plössl (pair of achromats), 150 mm focal length	Thorlabs	AC508-300-A-ML
	P7	2" plössl (pair of achromats), 75 mm focal length	Thorlabs	AC508-150-A-ML
	M10	2" mirror, dielectric	Thorlabs	BBE2-E02
	P8	2" plössl (pair of achromats), 200 mm focal length	Thorlabs	AC508-400-A-ML

	O3	Water immersion dipping objective, 10x, 0.3 NA	Thorlabs	N10XW-PF
Remote refocus	O4	Water immersion dipping objective, 20x, 1 NA	Zeiss	421452-9900-000
	HWP	Half-wave plate	Newport	10RP52-1B
	T1	Tube lens, 165 mm focal length	Zeiss	423731-8246-000
	GB	80 mm NBK7 rod that tube lens T1 is designed to work with, see patent DE 102005051026A1	Zeiss	N/A
	M11	2" mirror, dielectric	Thorlabs	BB2-E02
	P9	2" plössl (pair of achromats), 150.4 mm focal length	Linos	322295000, 322311000
	PBS2	Polarsing beam splitter	Thorlabs	PBS251
	QWP2	Quarter-wave plate	Thorlabs	AQWP05M-600
	O5	Air objective, 20x, .75 NA	Nikon	MRD00205
	RM2	7 mm diameter mirror, silver + #1.5 coverslip epoxied on	Thorlabs	PF03-03-P01
	z'scan	Linear stage	PI	P-725 PIFOC
Dual channel imaging	T2	Tube lens	Thorlabs	TTL165-A
	2DS	Rectangular aperture	Ealing	74-1137-000
	T3	Tube lens	Thorlabs	TTL100-A
	DM1 & DM2	Dichroic mirrors	Semrock	FF560-FDi01-25x36
	F1	Emission bandpass filter	Chroma	ET525/50
	F2	Emission bandpass filter	Semrock	ET630/75
	M12 & M13	2" mirror, dielectric	Thorlabs	TTL100-A
	L+	Achromatic doublet	Edmund Optics	67-334
	L-	Negative doublet	Edmund Optics	45-423
Final tube lens	T4	Higher spatial resolution imaging of t-tubule network in cardiomyocytes	Thorlabs	TTL200-A
Camera	sCMOS	mSPIM +remote refocus bead data acquisition	Hamamatsu	ORCA-Lightning Digital CMOS camera C14120-20P
		DSLM +ASLM illumination Bead Data acquisition, high-speed 2D and 3D imaging of calcium dynamics in cardiomyocytes	Hamamatsu	ORCA-Fusion Digital CMOS camera C14440-20UP

A3. Resolution characterization

Figure A3.1: Zemax lens data for the DSLM+ASLM illumination path optical relay

	Surface Type	Comment	Radius	Thickness	Material	Coating	Clear Semi-Dia	Mech Semi-Dia	Par 1 (unused)
0	OBJECT	Standard ▾	Infinity	Infinity			0.000	0.000	
1		Standard ▾	Infinity	38.283			6.000 U	6.000	
2	(aper)	Standard ▾	AC254-040-A-ML	23.660	10.000	N-BK7	THORA	12.700 U	12.700
3	(aper)	Standard ▾		-20.090	2.500	SF5		12.700 U	12.700
4	(aper)	Standard ▾		-57.680	227.322		NULL	12.700 U	12.700
5	(aper)	Standard ▾		-291.070	2.500	LAFN7	NULL	12.700 U	12.700
6	(aper)	Standard ▾	AC254-200-A-ML	87.570	4.000	N-SSK5		12.700 U	12.700
7	(aper)	Standard ▾		-77.400	202.323		NULL	12.700 U	12.700
8	STOP	Standard ▾	Infinity	20.000				6.000 U	6.000
9	Paraxial ▾	refocusing objectives		40.000			6.000 U	-	20.000
10	Paraxial ▾			20.000			6.000 U	-	20.000
11		Standard ▾	Infinity	195.722			6.000 U	6.000	
12	(aper)	Standard ▾	760.000	2.000	SF2	THORA	25.400 U	25.400	
13	(aper)	Standard ▾	PL1 186.750	5.000	N-BK7		25.400 U	25.400	
14	(aper)	Standard ▾	AC508-400-A-ML	-219.800	0.000		THORA	25.400 U	25.400
15	(aper)	Standard ▾	AC508-400-A-ML	219.800	5.000	N-BK7	THORA	25.400 U	25.400
16	(aper)	Standard ▾		-186.750	2.000	SF2		25.400 U	25.400
17	(aper)	Standard ▾	focal sep	-760.000	289.103		THORA	25.400 U	25.400
18	(aper)	Standard ▾		376.250	2.000	SF2	THORA	25.400 U	25.400
19	(aper)	Standard ▾	PL2 93.110	8.500	N-BK7		25.400 U	25.400	
20	(aper)	Standard ▾	AC508-200-A-ML	-109.860	0.000		THORA	25.400 U	25.400
21	(aper)	Standard ▾	AC508-200-A-ML	109.860	8.500	N-BK7	THORA	25.400 U	25.400
22	(aper)	Standard ▾		-93.110	2.000	SF2		25.400 U	25.400
23	(aper)	Standard ▾	afocal sep	-376.250	0.000		THORA	25.400 U	25.400
24		Standard ▾	GZ start	Infinity	93.381		24.400 U	24.400	
25	Coordinate Break ▾			0.000	-		0.000	-	0.000
26	Coordinate Break ▾	Element Tilt		0.000	-		0.000	-	0.000
27	(aper)	Standard ▾	z galvo	Infinity	0.000	MIRROR	3.540 U	3.540	
28	Coordinate Break ▾	Element Tilt: return		0.000	-		0.000	-	0.000 P
29	Coordinate Break ▾			0.000	-		0.000	-	0.000
30		Standard ▾	GZ end	Infinity	145.131		3.001	3.001	
31	(aper)	Standard ▾		580.800	2.000	SF2	THORA	25.400 U	25.400
32	(aper)	Standard ▾	PL3 134.000	6.000	N-BK7		25.400 U	25.400	
33	(aper)	Standard ▾	AC508-300-A-ML	-161.500	0.000		THORA	25.400 U	25.400
34	(aper)	Standard ▾	AC508-300-A-ML	161.500	6.000	N-BK7	THORA	25.400 U	25.400
35	(aper)	Standard ▾		-134.000	2.000	SF2		25.400 U	25.400
36	(aper)	Standard ▾	focal sep	-580.800	290.262		THORA	25.400 U	25.400
37	(aper)	Standard ▾		580.800	2.000	SF2	THORA	25.400 U	25.400
38	(aper)	Standard ▾	PL4 134.000	6.000	N-BK7		25.400 U	25.400	
39	(aper)	Standard ▾	AC508-300-A-ML	-161.500	0.000		THORA	25.400 U	25.400
40	(aper)	Standard ▾	AC508-300-A-ML	161.500	6.000	N-BK7	THORA	25.400 U	25.400
41	(aper)	Standard ▾		-134.000	2.000	SF2		25.400 U	25.400
42	(aper)	Standard ▾	afocal sep	-580.800	0.000		THORA	25.400 U	25.400
43		Standard ▾	Gy start	Infinity	145.131		2.997	2.997	
44	Coordinate Break ▾			0.000	-		0.000	-	0.000
45	Coordinate Break ▾	Y-Galvo		0.000	-		0.000	-	0.000
46	(aper)	Standard ▾		Infinity	0.000	MIRROR	3.540 U	3.540	
47	Coordinate Break ▾	Y-Galvo: return		0.000	-		0.000	-	0.000 P
48	Coordinate Break ▾			0.000	-		0.000	-	0.000
49		Standard ▾	Gy end	Infinity	65.244		12.700 U	12.700	
50	(aper)	Standard ▾		247.700	3.000	SF5	NULL	25.400 U	25.400
51	(aper)	Standard ▾	PL5 72.120	12.000	N-BK7		25.400 U	25.400	
52	(aper)	Standard ▾	AC508-150-A-ML	-83.180	0.000		THORA	25.400 U	25.400
53	(aper)	Standard ▾	AC508-150-A-ML	83.180	12.000	N-BK7	THORA	25.400 U	25.400
54	(aper)	Standard ▾		-72.120	3.000	SF5		25.400 U	25.400
55	(aper)	Standard ▾	focal sep	-247.700	260.937		NULL	25.400 U	25.400
56	(aper)	Standard ▾		760.000	2.000	SF2	THORA	25.400 U	25.400
57	(aper)	Standard ▾	PL6 186.750	5.000	N-BK7		25.400 U	25.400	
58	(aper)	Standard ▾	AC508-400-A-ML	-219.800	0.000		THORA	25.400 U	25.400
59	(aper)	Standard ▾	AC508-400-A-ML	219.800	5.000	N-BK7	THORA	25.400 U	25.400
60	(aper)	Standard ▾		-186.750	2.000	SF2		25.400 U	25.400
61	(aper)	Standard ▾	afocal sep	-760.000	215.693		THORA	25.400 U	25.400
62	(aper)	Paraxial ▾		26.600 V	1.33.0.0 M		6.000 U	-	20.000
63	IMAGE	Standard ▾	Infinity	-			8.430E-04	8.430E-04	

Figure A3.2: Zemax lens data for the mSPIM illumination path optical relay

	Surface Type	Comment	Radius	Thickness	Material	Coating	Clear Semi-Dia	Mech Semi-Dia	Par 1 (unused)
0	Standard ▾		Infinity	Infinity			0.000	0.000	
1	Standard ▾		Infinity	100.000			6.000 U	6.000	
2	Coordinate Break ▾			0.000	-		0.000	-	0.000
3	Toroidal ▾	LJ1695RM-A	25.840	6.800	N-BK7	THORA	11.700 U	-	0.000
4	Toroidal ▾		Infinity	45.003		THORA	11.700 U	-	0.000
5	Coordinate Break ▾			195.769	-		0.000	-	0.000
6	Standard ▾		760.000	2.000	SF2	THORA	25.400 U	25.400	
7	Standard ▾		186.750	5.000	N-BK7		25.400 U	25.400	
8	Standard ▾	AC508-400-A-ML	-219.800	0.000		THORA	25.400 U	25.400	
9	Standard ▾	PL3	Infinity	0.000			5.990	5.990	
10	Standard ▾	AC508-400-A-ML	219.800	5.000	N-BK7	THORA	25.400 U	25.400	
11	Standard ▾		-186.750	2.000	SF2		25.400 U	25.400	
12	Standard ▾		-760.000	391.521		THORA	25.400 U	25.400	
13	Standard ▾		760.000	2.000	SF2	THORA	25.400 U	25.400	
14	Standard ▾	PL4	186.750	5.000	N-BK7		25.400 U	25.400	
15	Standard ▾	AC508-400-A-ML	-219.800	0.000		THORA	25.400 U	25.400	
16	Standard ▾		Infinity	0.000			5.996	5.996	
17	Standard ▾	AC508-400-A-ML	219.800	5.000	N-BK7	THORA	25.400 U	25.400	
18	Standard ▾		-186.750	2.000	SF2		25.400 U	25.400	
19	Standard ▾		-760.000	195.722		THORA	25.400 U	25.400	
20	Standard ▾		Infinity	20.000			6.000 U	6.000	
21	Paraxial ▾	refocusing objectives		40.000			10.000 U	-	20.000
22	Paraxial ▾			20.000			10.000 U	-	20.000
23	Standard ▾		Infinity	195.722			6.000 U	6.000	
24	Standard ▾		760.000	2.000	SF2	THORA	25.400 U	25.400	
25	Standard ▾	PL1	186.750	5.000	N-BK7		25.400 U	25.400	
26	Standard ▾	AC508-400-A-ML	-219.800	0.000		THORA	25.400 U	25.400	
27	Standard ▾	AC508-400-A-ML	219.800	5.000	N-BK7	THORA	25.400 U	25.400	
28	Standard ▾		-186.750	2.000	SF2		25.400 U	25.400	
29	Standard ▾	focal sep	-760.000	289.103		THORA	25.400 U	25.400	
30	Standard ▾		376.250	2.000	SF2	THORA	25.400 U	25.400	
31	Standard ▾	PL2	93.110	8.500	N-BK7		25.400 U	25.400	
32	Standard ▾	AC508-200-A-ML	-109.860	0.000		THORA	25.400 U	25.400	
33	Standard ▾	AC508-200-A-ML	109.860	8.500	N-BK7	THORA	25.400 U	25.400	
34	Standard ▾		-93.110	2.000	SF2		25.400 U	25.400	
35	Standard ▾	afocal sep	-376.250	0.000		THORA	25.400 U	25.400	
36	Standard ▾	GZ start	Infinity	93.381			24.400 U	24.400	
37	Coordinate Break ▾			0.000	-		0.000	-	0.000
38	Coordinate Break ▾	Element Tilt		0.000	-		0.000	-	0.000
39	Standard ▾	z qalvo	Infinity	0.000	MIR...		3.540 U	3.540	
40	Coordinate Break ▾	Element Tiltreturn		0.000	-		0.000	-	0.000 P
41	Coordinate Break ▾			0.000	-		0.000	-	0.000
42	Standard ▾	GZ end	Infinity	145.131			3.003	3.003	
43	Standard ▾		580.800	2.000	SF2	THORA	25.400 U	25.400	
44	Standard ▾	PL3	134.000	6.000	N-BK7		25.400 U	25.400	
45	Standard ▾	AC508-300-A-ML	-161.500	0.000		THORA	25.400 U	25.400	
46	Standard ▾	AC508-300-A-ML	161.500	6.000	N-BK7	THORA	25.400 U	25.400	
47	Standard ▾		-134.000	2.000	SF2		25.400 U	25.400	
48	Standard ▾	focal sep	-580.800	290.262		THORA	25.400 U	25.400	
49	Standard ▾		580.800	2.000	SF2	THORA	25.400 U	25.400	
50	Standard ▾	PL4	134.000	6.000	N-BK7		25.400 U	25.400	
51	Standard ▾	AC508-300-A-ML	-161.500	0.000		THORA	25.400 U	25.400	
52	Standard ▾	AC508-300-A-ML	161.500	6.000	N-BK7	THORA	25.400 U	25.400	
53	Standard ▾		-134.000	2.000	SF2		25.400 U	25.400	
54	Standard ▾	afocal sep	-580.800	0.000		THORA	25.400 U	25.400	
55	Standard ▾	Gy start	Infinity	145.131			2.991	2.991	
56	Coordinate Break ▾			0.000	-		0.000	-	0.000
57	Coordinate Break ▾	Y-Galvo		0.000	-		0.000	-	0.000
58	Standard ▾		Infinity	0.000	MIR...		3.540 U	3.540	
59	Coordinate Break ▾	Y-Galvo:return		0.000	-		0.000	-	0.000 P
60	Coordinate Break ▾			0.000	-		0.000	-	0.000
61	Standard ▾	Gy end	Infinity	65.244			12.700 U	12.700	
62	Standard ▾		247.700	3.000	SF5	THORA	25.400 U	25.400	
63	Standard ▾	PL5	72.120	12.000	N-BK7		25.400 U	25.400	
64	Standard ▾	AC508-150-A-ML	-83.180	0.000		THORA	25.400 U	25.400	
65	Standard ▾	AC508-150-A-ML	83.180	12.000	N-BK7	THORA	25.400 U	25.400	
66	Standard ▾		-72.120	3.000	SF5		25.400 U	25.400	
67	Standard ▾	focal sep	-247.700	260.937		THORA	25.400 U	25.400	
68	Standard ▾		760.000	2.000	SF2	THORA	25.400 U	25.400	
69	Standard ▾	PL6	186.750	5.000	N-BK7		25.400 U	25.400	
70	Standard ▾	AC508-400-A-ML	-219.800	0.000		THORA	25.400 U	25.400	
71	Standard ▾	AC508-400-A-ML	219.800	5.000	N-BK7	THORA	25.400 U	25.400	
72	Standard ▾		-186.750	2.000	SF2		25.400 U	25.400	
73	Standard ▾	afocal sep	-760.000	215.693		THORA	25.400 U	25.400	
74	Paraxial ▾			26.600	V 1.33.... M		6.000 U	-	20.000
75	Standard ▾		Infinity	-			1.248E-03	1.248E-03	

A4. Single-cell 2D imaging

Figure A4.1. T-tubule maps across all analyzed cells with the cell membrane outline shown in grey and identified nuclei in orange (n = 60). Scalebar: 100 μm

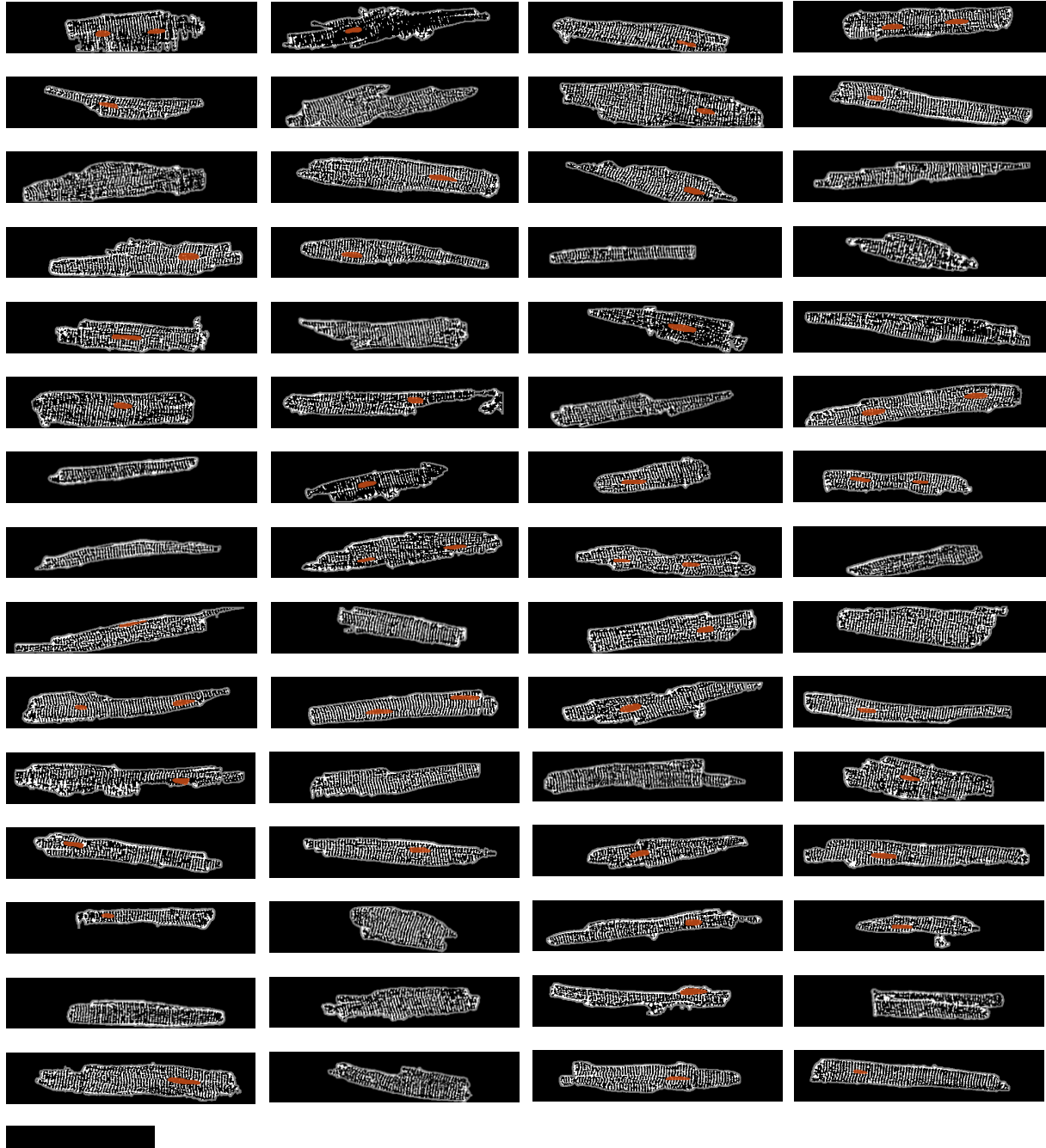
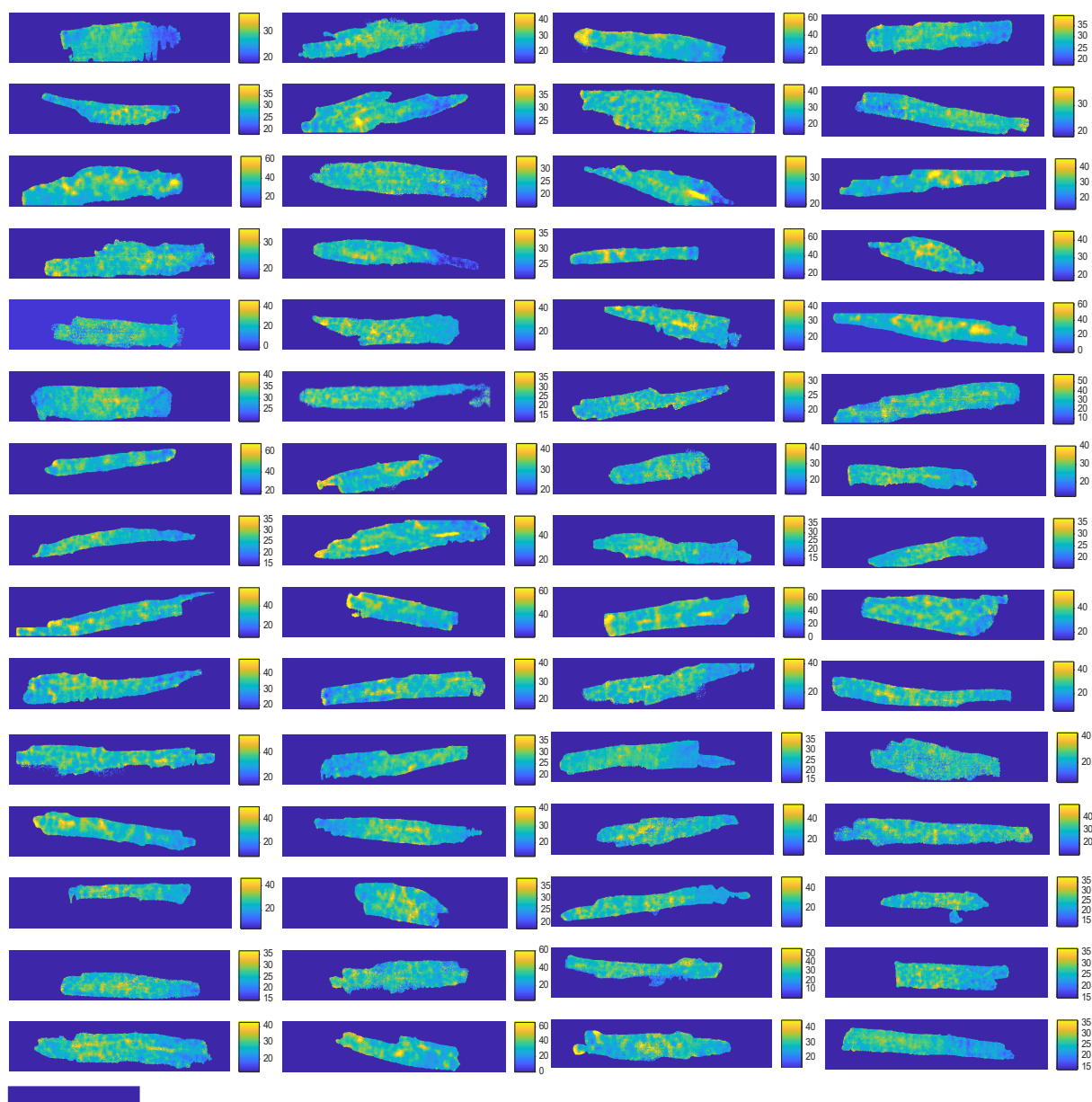


Figure A4.2 Time-to-half-maximum (T50, ms) maps for all $n = 60$ analyzed cells, with the colormap auto-scaled between the median \pm IQR values. Scalebar: 100 μm



A5. Permission to reproduce third-party works

SPRINGER NATURE LICENSE TERMS AND CONDITIONS

Feb 02, 2022

This Agreement between Ms. Liuba Dvinskikh ("You") and Springer Nature ("Springer Nature") consists of your license details and the terms and conditions provided by Springer Nature and Copyright Clearance Center.

License Number	5234200541608
License date	Jan 22, 2022
Licensed Content Publisher	Springer Nature
Licensed Content Publication	Nature Methods
Licensed Content Title	Real-time multi-angle projection imaging of biological dynamics
Licensed Content Author	Bo-Jui Chang et al
Licensed Content Date	Jun 28, 2021
Type of Use	Thesis/Dissertation
Requestor type	non-commercial (non-profit)
Format	electronic
Portion	figures/tables/illustrations
Number of figures/tables/illustrations	1
High-res required	no
Will you be translating?	no
Circulation/distribution	1 - 29
Author of this Springer Nature content	no
Title	Remote refocusing light-sheet fluorescence microscopy for high-speed 2D and 3D imaging of calcium dynamics in cardiomyocytes
Institution name	Imperial College London
Expected presentation date	Feb 2022
Portions	Extended Data Fig. 4 Equivalence of projections from rotated and sheared volumes. - adapted for different formatting
Requestor Location	Ms. Liuba Dvinskikh Imperial College London Blackett Laboratory South Kensington Campus London, SW7 2AZ United Kingdom
Total	Attn: Ms. Liuba Dvinskikh 0.00 GBP

**Springer Nature Customer Service Centre GmbH
Terms and Conditions**

This agreement sets out the terms and conditions of the licence (the **Licence**) between you and **Springer Nature Customer Service Centre GmbH** (the **Licensor**). By clicking 'accept' and completing the transaction for the material (**Licensed Material**), you also confirm your acceptance of these terms and conditions.

1. Grant of License

1. The Licensor grants you a personal, non-exclusive, non-transferable, world-wide licence to reproduce the Licensed Material for the purpose specified in your order only. Licences are granted for the specific use requested in the order and for no other use, subject to the conditions below.
2. The Licensor warrants that it has, to the best of its knowledge, the rights to license reuse of the Licensed Material. However, you should ensure that the material you are requesting is original to the Licensor and does not carry the copyright of another entity (as credited in the published version).
3. If the credit line on any part of the material you have requested indicates that it was reprinted or adapted with permission from another source, then you should also seek permission from that source to reuse the material.

2. Scope of Licence

1. You may only use the Licensed Content in the manner and to the extent permitted by these Ts&Cs and any applicable laws.
2. A separate licence may be required for any additional use of the Licensed Material, e.g. where a licence has been purchased for print only use, separate permission must be obtained for electronic re-use. Similarly, a licence is only valid in the language selected and does not apply for editions in other languages unless additional translation rights have been granted separately in the licence. Any content owned by third parties are expressly excluded from the licence.
3. Similarly, rights for additional components such as custom editions and derivatives require additional permission and may be subject to an additional fee. Please apply to Journalpermissions@springernature.com/bookpermissions@springernature.com for these rights.
4. Where permission has been granted **free of charge** for material in print, permission may also be granted for any electronic version of that work, provided that the material is incidental to your work as a whole and that the electronic version is essentially equivalent to, or substitutes for, the print version.
5. An alternative scope of licence may apply to signatories of the [STM Permissions Guidelines](#), as amended from time to time.

☐ **Duration of Licence**

1. A licence for is valid from the date of purchase ('Licence Date') at the end of the relevant period in the below table:

Scope of Licence	Duration of Licence
Post on a website	12 months
Presentations	12 months
Books and journals	Lifetime of the edition in the language purchased

☐ Acknowledgement

1. The Licensor's permission must be acknowledged next to the Licenced Material in print. In electronic form, this acknowledgement must be visible at the same time as the figures/tables/illustrations or abstract, and must be hyperlinked to the journal/book's homepage. Our required acknowledgement format is in the Appendix below.

☐ Restrictions on use

1. Use of the Licensed Material may be permitted for incidental promotional use and minor editing privileges e.g. minor adaptations of single figures, changes of format, colour and/or style where the adaptation is credited as set out in Appendix 1 below. Any other changes including but not limited to, cropping, adapting, omitting material that affect the meaning, intention or moral rights of the author are strictly prohibited.
2. You must not use any Licensed Material as part of any design or trademark.
3. Licensed Material may be used in Open Access Publications (OAP) before publication by Springer Nature, but any Licensed Material must be removed from OAP sites prior to final publication.

☐ Ownership of Rights

1. Licensed Material remains the property of either Licensor or the relevant third party and any rights not explicitly granted herein are expressly reserved.

☐ Warranty

IN NO EVENT SHALL LICENSOR BE LIABLE TO YOU OR ANY OTHER PARTY OR ANY OTHER PERSON OR FOR ANY SPECIAL, CONSEQUENTIAL, INCIDENTAL OR INDIRECT DAMAGES, HOWEVER CAUSED, ARISING OUT OF OR IN CONNECTION WITH THE DOWNLOADING, VIEWING OR USE OF THE MATERIALS REGARDLESS OF THE FORM OF ACTION, WHETHER FOR BREACH OF CONTRACT, BREACH OF WARRANTY, TORT, NEGLIGENCE, INFRINGEMENT OR OTHERWISE (INCLUDING, WITHOUT LIMITATION, DAMAGES BASED ON LOSS OF PROFITS, DATA, FILES, USE, BUSINESS OPPORTUNITY OR CLAIMS OF THIRD PARTIES), AND WHETHER OR NOT THE PARTY HAS BEEN ADVISED OF THE POSSIBILITY OF SUCH DAMAGES. THIS LIMITATION SHALL APPLY NOTWITHSTANDING ANY FAILURE OF ESSENTIAL PURPOSE OF ANY LIMITED REMEDY PROVIDED HEREIN.

☐ Limitations

1. **BOOKS ONLY:** Where 'reuse in a dissertation/thesis' has been selected the following terms apply: Print rights of the final author's accepted manuscript (for clarity, NOT the

published version) for up to 100 copies, electronic rights for use only on a personal website or institutional repository as defined by the Sherpa guideline (www.sherpa.ac.uk/romeo/).

2. For content reuse requests that qualify for permission under the [STM Permissions Guidelines](#), which may be updated from time to time, the STM Permissions Guidelines supersede the terms and conditions contained in this licence.

☐ **Termination and Cancellation**

1. Licences will expire after the period shown in Clause 3 (above).
2. Licensee reserves the right to terminate the Licence in the event that payment is not received in full or if there has been a breach of this agreement by you.

Appendix 1 — Acknowledgements:

For Journal Content:

Reprinted by permission from [the Licensor]: [Journal Publisher (e.g. Nature/Springer/Palgrave)] [JOURNAL NAME] [REFERENCE CITATION (Article name, Author(s) Name), [COPYRIGHT] (year of publication)]

For Advance Online Publication papers:

Reprinted by permission from [the Licensor]: [Journal Publisher (e.g. Nature/Springer/Palgrave)] [JOURNAL NAME] [REFERENCE CITATION (Article name, Author(s) Name), [COPYRIGHT] (year of publication), advance online publication, day month year (doi: 10.1038/sj.[JOURNAL ACRONYM].)]

For Adaptations/Translations:

Adapted/Translated by permission from [the Licensor]: [Journal Publisher (e.g. Nature/Springer/Palgrave)] [JOURNAL NAME] [REFERENCE CITATION (Article name, Author(s) Name), [COPYRIGHT] (year of publication)]

Note: For any republication from the British Journal of Cancer, the following credit line style applies:

Reprinted/adapted/translated by permission from [the Licensor]: on behalf of Cancer Research UK: : [Journal Publisher (e.g. Nature/Springer/Palgrave)] [JOURNAL NAME] [REFERENCE CITATION (Article name, Author(s) Name), [COPYRIGHT] (year of publication)]

For Advance Online Publication papers:

Reprinted by permission from The [the Licensor]: on behalf of Cancer Research UK: [Journal Publisher (e.g. Nature/Springer/Palgrave)] [JOURNAL NAME] [REFERENCE CITATION (Article name, Author(s) Name), [COPYRIGHT] (year of publication), advance online publication, day month year (doi: 10.1038/sj.[JOURNAL ACRONYM].)]

For Book content:

Reprinted/adapted by permission from [the Licensor]: [Book Publisher (e.g. Palgrave Macmillan, Springer etc)] [Book Title] by [Book author(s)] [COPYRIGHT] (year of publication)

Other Conditions:

Version 1.3

Questions? customercare@copyright.com or +1-855-239-3415 (toll free in the US) or +1-978-646-2777.